REPUBLIQUE ALGERIENNE DEMOCRATIQUE ET POPULAIRE

Ministère de l'Enseignement Supérieur et de la Recherche Scientifique

Université Blida 1

Faculté de Technologie

Département de Mécanique

جـــــامعة البـــــليدة 1

كـــــــلية التكنولوجيـــا

قـــــسم الـميكانيـــــك

This dissertation is submitted for the degree of Doctor in Sciences

Specialty« Mechanical Engineering »

Option « Energetic »

presented by

MAHALLEM Abderrahmane

Contribution to the Numerical Modeling and Simulation of Fluid-Structure Interaction Using a Smoothed Particle Hydrodynamics (SPH) Approach

Supervisor : **Prof. ROUDANE Mohamed**
Department of Mechanics, Faculty of Technology, Blida-1 University, Algeria

Jury :

Prof. BENAROUS Abdellah, Blida 1 University, Algeria	President
Prof. HANINI Salah, Médéa University, Algeria	Examinator
Dr. SALHI Merouane, Blida 1 University, Algeria	Examinator
Dr. DANOUNI Samir, Tipaza University Center, Algeria	Examinator
Dr. BOUZEFOUR Fatih, UDES Bousmail, Tipaza, Algeria	Examinator

November 2023

Acknowledgements

I would like to begin by expressing my deepest gratitude to Prof. **Mohamed Roudane**. He has not only served as an exceptional supervisor, advisor, scientist, and engineer, but has also demonstrated unwavering support, patience, and kindness throughout my research journey. I am profoundly thankful for the opportunity to work alongside him, as his guidance has been invaluable in the development of my research and the writing of scientific papers, culminating in the completion of this Ph.D. thesis.

I am grateful to Dr. **Abdelkader KRIMI** for providing me with the opportunity to embark on this significant chapter of my career and for granting me access to the realm of real-world research. Without their invaluable support, the completion of this thesis would not have been possible.

I am equally indebted to Prof. **Sofiane KHELLADI** for his continuous support throughout my Ph.D. studies and related research endeavors. His patience, motivation, and the privilege of working with him and his esteemed Laboratory of Fluid and Energy Systems Engineering (LIFSE) at ENSAM-Paris, France, have significantly contributed to my academic and research growth.

I extend my deepest gratitude to the esteemed members of my thesis committee, who also served as examiners. Prof. **BENAROUS Abdellah** from Blida 1 University graciously accepted the role of the thesis discussion's president, providing insightful comments and leveraging expertise in the field of CFD, significantly enriching the depth of my research. Additionally, I am profoundly thankful for the invaluable contributions of Prof. **HANINI Salah** from Médéa University, Dr. **SALHI Merouane** from Blida 1 University, Dr. **DANOUNI Samir** from Tipaza University Center, and Dr. **BOUZEFOUR Fatih** from UDES Bousmail. As examiners, their encouragement and thought-provoking questions broadened the scope of my work from diverse perspectives. Their collective guidance and feedback significantly contributed to refining the methodology and enhancing the overall quality of this thesis.

Special thanks are also due to my professors at the University of BLIDA-Algeria and EPEA Oran-Algeria. Their guidance and teachings in the multidisciplinary fields of Mathematics,

Computer Science, and Physics have been instrumental in nurturing my passion for these subjects.

Lastly, my heartfelt gratitude goes to my family. To my parents, Taher and Zohra "rahimahum Allah," who have given me everything they could in life to shape me into the person I am today. To my siblings, for their unwavering spiritual support, particularly during challenging times.

I extend my special thanks to my wife, who has shown remarkable patience throughout this arduous journey. Her support has been the cornerstone of my perseverance. I am also grateful to my two daughters, Ines and Rym, who are the light of my life, as well as to my mother-in-law, Naziha, and father-in-law, Mahmoud, and my brothers-in-law, for their unwavering support.

Finally, I would like to express my deepest appreciation to all my friends and colleagues who have stood by me and provided invaluable support. Each one of them, including Sid Ahmed, Omar, Khaled, Ali, Noureddine, Hamza, Bilel, Oussama, Kheldoune, Taki, Bahi, Djamal, Merouane, Ramzi, Rachid, Said, Yacine, Hichem, Amine, Salim, and many others, has played a unique and cherished role in my journey.

ملخص

تقدم هذه الرسالة دراسة شاملة حول نمذجة ومحاكاة التفاعل بين الموائع والهياكل باستخدام طريقة الجسيمات الهيدروديناميكية الملساء. التركيز الرئيسي للأطروحة هو على التفاعل بين سائل ومواد حبيبية، حيث يتم وصف المواد الحبيبية باستخدام نماذج ريولوجية غير نيوتونية مختلفة، مثل قوانين كاسون و بينغهام الأساسية. تقدم هذه الدراسة عرضاً شاملاً للأدبيات الحالية في مجال نمذجة التفاعل بين السوائل والهياكل والمحاكاة، مع التركيز على طريقة الجسيمات الهيدروديناميكية الملساء وتطبيقاتها في نمذجة المواد الحبيبية. يتم أيضًا مناقشة النماذج الريولوجية المختلفة المستخدمة لوصف سلوك المواد الحبيبية بالتفصيل.

أحد المساهمات الرئيسية لهذا البحث هو تعميم هذه النماذج الريولوجية غير النيوتونية لتجنب الانقطاعات الرقمية الموروثة من القوانين الأصلية. يتم ذلك من خلال إدخال نهج جديد لتنفيذ هذه القوانين في معادلات الجسيمات الهيدروديناميكية الملساء الحاكمة، مما يحسن بشكل كبير دقة وقوة نتائج المحاكاة. يتم وصف هذه النماذج و طريقة دمجها بالتفصيل، بما في ذلك المعادلات والطرق الرقمية المستخدمة.

بعد ذلك، يتم اختبار صحة النماذج المنفذة من خلال سلسلة من المحاكاة الرقمية تتضمن التفاعل بين سائل ومواد حبيبية. تتم مقارنة نتائج المحاكاة الرقمية بالبيانات التجريبية ونتائج من أساليب رقمية أخرى. تقدم الرسالة مناقشة مفصلة للنتائج، محددة مزايا وعيوب طريقة الجسيمات الهيدروديناميكية الملساء لنمذجة تفاعل السوائل بالمواد الحبيبية.

تتضمن الأطروحة أيضاً تحليل حساسية للمعاملات الرقمية المستخدمة في طريقة الجسيمات الهيدروديناميكية الملساء، لفهم تأثير هذه للمعاملات على نتائج المحاكاة. يوضح البحث أن طريقة الجسيمات الهيدروديناميكية الملساء يمكن استخدامها بنجاح لنمذجة التفاعل بين سائل ومواد حبيبية، وأن تعميم النماذج الريولوجية غير النيوتونية، مثل قوانين كاسون و بينغهام، يمكن أن يحسن من دقة وقوة نتائج المحاكاة الرقمية. تقدم الرسالة مساهمة قيمة في مجال نمذجة ومحاكاة تفاعل الموائع بالهياكل، ومن المتوقع أن يكون لها تأثير كبير على البحوث المستقبلية في هذا المجال.

الكلمات المفتاحية: تفاعل الموائع والهياكل، مواد حبيبية، نموذج بينغهام، نموذج كاسون، النمذجة والمحاكاة الرقمية، ريولوجيا، هيدروديناميكا الجسيمات الملساء، التحقق والتطبيقات.

Abstract

This thesis presents a comprehensive study on the modeling and numerical simulation of Fluid-Structure Interaction (FSI) using the Smoothed Particle Hydrodynamics (SPH) method. The main focus of the dissertation is on the interaction between a fluid and granular material, where the granular material is described using different non-Newtonian rheological models, such as the Bingham and Casson constitutive laws. This work presents a thorough literature review of the current state of the art in FSI modeling and simulation, with a focus on the SPH method and its applications in granular material modeling. The various rheological models used to describe the behavior of granular materials are also discussed in detail. One of the key contributions of this research is the generalization of these non-Newtonian rheological models to avoid numerical discontinuities inherited from the original laws. This is achieved by introducing a new approach for the implementation of these laws into the SPH governing equations, which significantly improves the accuracy and robustness of the simulation results. The implementation process is described in detail, including the equations used and the numerical methods employed. The validity of the implemented models is then tested through a series of numerical simulations involving the interaction between a fluid and granular material. The simulation results are compared to experimental data and results from other numerical methods. The thesis presents a detailed discussion of the results, identifying the advantages and limitations of the SPH method for modeling fluid-granular material interaction. The dissertation also includes a sensitivity analysis of the numerical parameters used in the SPH method, to understand the effect of these parameters on the simulation results. The research demonstrates that the SPH method can be successfully used to model the interaction between a fluid and granular material, and that the generalization of non-Newtonian rheological models, such as the Bingham and Casson laws, can improve the accuracy and robustness of the simulation results. The thesis provides a valuable contribution to the field of fluid-structure interaction modeling and simulation, and is expected to have a significant impact on future research in this area.

Keywords: Fluid-Structure Interaction, Granular materials, Bingham Model, Casson Model, Modeling and numerical simulation, Rheology, Smoothed Particle Hydrodynamics, Validation and Applications.

Résumé

Cette thèse présente une étude détaillée sur la modélisation et la simulation numérique de l'Interaction Fluide-Structure (IFS) en utilisant la méthode Smoothed Particle Hydrodynamics (SPH). L'accent principal de la dissertation est mis sur l'interaction entre un fluide et un matériau granulaire, où le matériau granulaire est décrit en utilisant différents modèles rhéologiques non-newtoniens, tels que les lois constitutives de Bingham et de Casson. Ce travail présente une revue approfondie de l'état actuel de l'art dans la modélisation et la simulation de l'IFS, en mettant l'accent sur la méthode SPH et ses applications dans la modélisation des matériaux granulaires. Les différents modèles rhéologiques utilisés pour décrire le comportement des matériaux granulaires sont également discutés en détail. Une des contributions clés de cette recherche est la généralisation de ces modèles rhéologiques non-newtoniens pour éviter les discontinuités numériques héritées des lois originales. Cela est réalisé en introduisant une nouvelle approche pour l'implémentation de ces lois dans les équations gouvernant la méthode SPH, ce qui améliore considérablement la précision et la robustesse des résultats de simulation. Le processus d'implémentation est décrit en détail, y compris les équations utilisées et les méthodes numériques employées. La validité des modèles implémentés est ensuite testée par une série de simulations numériques impliquant l'interaction entre un fluide et un matériau granulaire. Les résultats de la simulation sont comparés aux données expérimentales et aux résultats d'autres méthodes numériques. La thèse présente une discussion détaillée des résultats, identifiant les avantages et les limites de la méthode SPH pour la modélisation de l'interaction fluide-matériau granulaire. La dissertation comprend également une analyse de sensibilité des paramètres numériques utilisés dans la méthode SPH, afin de comprendre l'effet de ces paramètres sur les résultats de simulation. La recherche démontre que la méthode SPH peut être utilisée avec succès pour modéliser l'interaction entre un fluide et un matériau granulaire, et que la généralisation des modèles rhéologiques non-newtoniens, tels que les lois de Bingham et de Casson, peut améliorer la précision et la robustesse des résultats de simulation. La thèse apporte une contribution précieuse au domaine de la modélisation et de la simulation de l'interaction fluide-structure, et devrait avoir un impact significatif sur les futures recherches dans ce domaine.

Mots clés: Interaction Fluide-Structure, matériaux granulaire, Modèle de Bingham, Modèle de Casson, Modélisation et la simulation numérique, Rhéologie, Smoothed Particle Hydrodynamics, Validation et Applications.

Table of contents

List of figures x

Nomenclature xvi

1 State of the art overview 5

1.1 Background on Fluid-Structure Interaction (FSI) 5

1.1.1 Definition, description, and Importance of FSI 5

1.1.2 Overview of different modeling and simulation methods for FSI . . 6

1.2 The Smoothed Particle Hydrodynamics (SPH) Method 8

1.2.1 Description of the SPH method 8

1.2.2 Fundamentals of SPH Method 9

1.2.3 Smoothing kernel functions 10

1.2.4 Software Packages Utilizing Smoothed Particle Hydrodynamics . . 15

1.2.5 Applications of the SPH Method 16

2 Numerical Techniques for Modeling with Smooth Particle Hydrodynamics 41

2.1 Principle governing equations 41

2.1.1 The continuity equation 42

2.1.2 The momentum conservation equation 42

2.1.3 Pressure determination in SPH method 43

2.1.4 Stress determination and rheological models for describing constitutive laws 47

2.1.5 The displacement equation 50

2.2 Approximation of Governing Equations through SPH Discretization 51

2.2.1 Formulations for SPH continuity equation Approximation 51

2.2.2 Formulations for SPH Density Approximation 52

2.2.3 Pressure approximation 53

2.2.4 Cauchy stress tensor approximation 55

2.2.5 Viscous stress tensor approximation . . . 55
2.3 Recent advancements in the SPH method . . . 58
2.3.1 Shepard Correction . . . 58
2.3.2 The Damping Method for Reducing Oscillations in SPH Simulations. 59
2.3.3 Enhancement of the Gradient Calculation in the Kernel Function . . 59
2.3.4 Enhancement of the Laplacian operator in the Kernel Function . . . 60
2.3.5 SPH enhancing by particle approximation in governing equations . 61
2.4 Neighboring particles search in SPH simulations . . . 65
2.4.1 Brute Force Method . . . 65
2.4.2 Linked-list Method . . . 65
2.4.3 Tree-based Method . . . 65
2.4.4 Adaptive Kernel Method . . . 66
2.5 Boundary conditions in SPH simulations . . . 66
2.5.1 Fixed boundary conditions . . . 66
2.5.2 Free boundary conditions . . . 68
2.5.3 Moving boundary conditions . . . 69
2.5.4 Treatment of Free Surface boundary Conditions . . . 70
2.5.5 Reflecting boundary conditions . . . 70
2.5.6 Periodic Boundary Conditions . . . 71
2.5.7 Combination of boundary conditions . . . 71
2.6 Solid-Fluid Interaction in SPH . . . 72
2.6.1 Rigid bodies . . . 72
2.6.2 Fluid-Structure Interaction (FSI) Approaches . . . 73
2.7 Advanced time integration algorithms in SPH Simulations . . . 74
2.7.1 Verlet Algorithm . . . 74
2.7.2 Leapfrog Algorithm . . . 74
2.7.3 Predictor-Corrector Algorithms . . . 74
2.7.4 Symplectic Integrators . . . 75
2.7.5 Runge-Kutta Algorithms . . . 75
2.7.6 Forward Euler method . . . 75
2.7.7 Multi-Step Algorithms . . . 75
2.8 Numerical stability criteria . . . 75
2.8.1 Courant-Friedrichs-Lewy (CFL) condition . . . 76
2.8.2 Artificial viscosity condition . . . 76
2.8.3 Viscous-Diffusion Condition . . . 77
2.8.4 Body force condition . . . 77

2.8.5 Surface tension condition 77

3 Modelling of fluid-granular material interaction using Smoothed Particle Hydrodynamics 79

3.1 Mathematical models 81

3.1.1 Governing equations 81

3.1.2 Viscoplastic constitutive laws 83

3.2 SPH approximation forms of governing equations 89

3.2.1 SPH discretization 90

3.2.2 Boundary conditions and time integration techniques 93

4 Validation of the SPH Model for Fluid-Granular Material Interaction: Applications, Results, and Discussion 95

4.1 Dam-break benchmark 96

4.2 Granular material collapse 99

4.3 Water-granular material interaction 103

4.3.1 Subaerial landslide induced generated water waves 103

4.3.2 Submarine landslide induced generated water waves 110

References 125

Appendix A Determination of the yield stress τ_y 155

Appendix B Frobenius norm of the shear rate tensor 157

List of figures

1.1 Schematic representation of mesh-based methods (a) the finite element method (FEM), and (b) the finite volume method (FVM) 7
1.2 Schematic representation of the SPH method: 2D sketch of the fluid and solid computational domains 8
1.3 Physical domain description using smothing kernel function in the SPH method framework 10
1.4 Snapshots of 2D dam-break flow on a wet bed 17
1.5 SPH snapshots of the coalescence of two spheres colored by pressure at increasing time instants 17
1.6 DEM-SPH simulation of flow generated in a pool of water by spray impingement: Photograph of the experimental flow (left) and the simulation results colored by the fluid speed (right) 18
1.7 Comparison of lid-driven cavity for Reynolds Re = 100 (top panels) and Re = 1000 (bottom panels). The snapshots are colored by pressure field and streamlines (left) and by vorticity field (right) 19
1.8 SPH simulation snapshots of the interaction between two rising bubbles through a fluid column. representation of the pressure (right column), the magnitude velocity (middle column), and the magnitude velocity with particle direction vector of isolated bubble, respectively 20
1.9 SPH simulation of the airflow around a circular cylinder for different Reynolds number Re= 20, 50, 100, and 200. The snapshots are colored by the magnitude vilocity field 21
1.10 Airflow around a circular cylinder: convergence of drag and lift coefficients CD and CL at different spatial resolutions at Re=100 and 200, respectively . 22
1.11 Different simulation results in the context of bridging classical and quantum mechanics for the dynamics of cryogenic liquid helium-4 using SPH model 23

1.12 SPH simulation of an oscillating plate: the deformed configuration is colored by Von Mises stress $\bar{\sigma}$ at different time instants 24
1.13 Time history of the vertical position y observed at the midpoint of the oscillating plate using different particle resolutions 24
1.14 SPH 3D simulation of a twisting column: the large elastic deformations is colored by pressure at different time instants 25
1.15 Notched plate with hole: Snapshots of the final crack pattern under different prescribed velocity loading using the SPH method compared to the experimental results 25
1.16 Chip thickness Comparison during a machining procedure of aluminum alloy Al6061-T6: experimental snapshot (left), simulation results using LAG method (middle), and simulation results using SPH method 26
1.17 SPH simulation of synthetic diamond grit scratching on steel: the snapshots are colored by plastic strain distribution at different penetration depths and grain orientations 26
1.18 Comparison of experimental and numerical SPH results of material flow patterns during an operation of Shear Assisted Processing and Extrusion (ShAPE) 27
1.19 Comparison between SPH failure results and the experimental results of the sandstone with different dip angles. Snapshots are colored by: tensile (green) and shear cracks (brown), respectively 27
1.20 Comparison between SPH and experimental results of the progressive failure of a granular column. SPH results are colored by the velocity filed 28
1.21 Comparison between SPH and experimental results of the progressive failure of column of glass beads constrained by two parallel gate sheets. SPH results are colored by the velocity filed 29
1.22 SPH simulation of the magnitude of the fluid velocity field and the deformation of a flexible beam attached to a rigid cylinder for a periodic cycle at four equidistant points in time 30
1.23 Comparison between SPH simulation and experimental results of dam-break flow through an elastic gate at different time instants. The fluid particles in the SPH snapshots are colored by the velocity field in the x flow direction v_x 31
1.24 Comparison between SPH simulation and experimental results of dam-break flow impacting an elastic gate at different time instants. The structure particles in the SPH snapshots are colored by the Von Mises stress contour . . . 32

1.25 Comparison between SPH simulation and experimental results of sloshing with an elastic baffle hanging from the top tank wall at different time instants. The fluid particles in the SPH snapshots are colored by the pressure field . 33
1.26 Comparison between SPH (right) and FEM (left) simulation results of flow through complex geometry blood vessels sloshing with an elastic baffle hanging from the top tank wall at different time instants. The fluid particles in the SPH snapshots are colored by the velocity field 33
1.27 Comparison between SPH (left) and FE method (right) simulation results of Ogden rubber material and its surrounding fluid in the brain. The snapshots are colored by the strain 34
1.28 SPH 3D simulation of a vertical ditching of a helicopter into sea surface at different time instants with the fuselage hitting the crest of the water wave . 35
1.29 Comparison between SPH simulation (right) and experimental results of the water entry of a cylindrical shell at different time instants. The snapshots are colored by the pressure field 36
1.30 SPH simulation of the interaction between floating breakwaters and water waves. The snapshots are colored by the velocity field 37
1.31 SPH simulation of the hydrodynamic evolution of a complex floating body upon immersion within a reservoir of water. The snapshots are colored by the initial vertical position of particles 37
1.32 Comparison between SPH simulation and experimental results of rigid subaerial landslide generated impulse water waves at different time instants. The snapshots are colored by the pressure field 38
1.33 SPH simulation of deformable subaerial landslide generated impulse water waves at different time instants. The snapshots shows the simulated velocity of the water flow and the deformation of the sand sliding along the slope . . 38
1.34 SPH simulation of the hydrodynamic evolution of water free surface due to the motion of rigid submarine landslide at different time instants 39
1.35 SPH simulation of deformable submarine landslide generating impulse water waves at different time instants. The snapshots are colored by the velocity field (left) and the vorticity (right) 40

3.1 Shear stress vs. shear rate for Newtonian fluids, Bingham and Casson rheological models 84

4.1 Geometrical details and material descriptions of dam break configuration . 96

4.2 Dam-break problem: comparison between our numerical results (left column) and the experimental results of Lobovskỳ et al. (right column) at t: (A)=0 s, (B)=0.32 s, (C)=0.41 s, (D)=0.46 s 97
4.3 Dam-break problem: comparison between the water wave front evolution obtained by our numerical results (blue points), numerical results of Vaucorbeil et al. (red dashed circles) and experimental results of Lobovskỳ et al. (black line) 98
4.4 Dam break problem: Snapshots of numerical results presenting the pressure (left side) and velocity (right) fields 98
4.5 Granular material collapse: Geometrical details of the experimental configuration 99
4.6 Granular material collapse: comparison between the numerical results from R_C_RCL rheological model (left column), R_B_RCL rheological model (right column) and the experimental results of Lajeunesse et al. (middle column), at t: (A)=0 s, (B)=0.08 s, (C)=0.16 s, (D)=0.24 s, and (E)=0.32 s . 100
4.7 Granular material collapse: Comparison of R_B_RCL (red) and R_C_RCL (blue) rheological models presented in this work, along with Herschel-Bulkley (green) and $\mu(I)$ (brown) models used by Kheirkhahan and Hosseini, overlaid on the original experiment PIV snapshots by Lajeunesse et al. The snapshots were taken at two different instants: (a) t = 0.08 s and (b) t = 0.32 s. 101
4.8 Granular material collapse: comparison between the distance traveled by the material obtained with the numerical results from R_C_RCL (blue dash-dotted line), R_B_RCL (red dashed line) rheological models , and the experimental results of Lajeunesse et al. (black plus sign) 102
4.9 Water-granular material interaction: Geometrical details and material descriptions of subaerial landslide-tsunami experimental benchmark 104
4.10 Water-granular material interaction: comparison between the numerical results from R_C_RCL rheological model (left column), R_B_RCL rheological model (right column) and the experimental results of Fritz et al. (middle column), at T: (A)=0.18 , (B)=0.56 , (C)=1.33 , (D)=3.61 107
4.11 Water-granular material interaction: confrontation between R_C_RCL (red point) and R_B_RCL (blue circle) rheological models overlaid on the original experiment PIV snapshot of Fritz et al. at $T = 3.61$. (A): represent the granular material profile and (B) the water wave profile 107

4.11 Subaerial landslide-tsunamis: comparison between the numerical results of R_C_RCL model (right column) and the experimental results of (left column) at relative time $t(gh)^{0.5}$: (a)=0.18, (b)=0.56, (c)=1.33, (d)=3.61; with: (A) Velocity vector fields; (B) Horizontal particle velocity fields; (C) Vertical particle velocity fields; (D) Absolute particle velocity fields 109
4.12 Water-granular material interaction: Geometrical details and material descriptions of submarine landslide-tsunami experimental benchmark 111
4.13 Submarine landslide-tsunamis: comparison between the numerical results of the present work (middle column), the experimental results of Grilli et al. (left column), and the numerical results of Ghaitanellis et al. (right column) at t: (A)=0 s, (B)=0.02 s, (C)=0.17 s, (D)=0.32 s and (E)=0.47 s 113
4.14 Description of the initial configuration of the submarine landslide along an inclined plane 114
4.15 Submarine landslide: comparison between the experimental sequences ((A) row) and the numerical results achieved using the generalized Casson rheological model of the current study, with $\tau_y = 0$ pa ((B) row), $\tau_y = 200$ pa ((C) row), and $\tau_y = 1000$ pa ((D) row), at t=0.4 s (left) and t=0.8 s (right) . . 115
4.16 Submarine landslide: comparison between the experimental water waves profiles (black circles) and the numerical results achieved using the generalized Casson rheological model of the current study, with $\tau_y = 0$ pa (green line), $\tau_y = 200$ pa (dashed blue line), and $\tau_y = 1000$ pa (dotted red line), at t=0.4 s (left) and t=0.8 s (right) 116
4.17 Submarine landslide: comparison between the numerical granular material profiles achieved using the generalized Casson rheological model of the current study (brown points), the $\mu(I)$ rhological model of Hosseini et al. (blue stars), and the Herschel-Bulkley rhological model of Shi and Huang (black circles), with $\tau_y = 1000$ pa at t=0.4 s (left) and t=0.8 s (right) 116
4.18 Description of the initial configuration of the immersed granular column collapse benchmark 117
4.19 Immersed granular column collapse: Comparison between the temporal evolution of the experimental results of Jandaghian et al. (left column),the numerical results of Jandaghian et al. using MPS model (right column), and the present SPH model results (middle column) at times t: (A)=0 s, (B)=0.17 s, (C)=0.33s, and (D)=0.49 s 119

4.20 Immersed granular column collapse: Comparison between the temporal evolution of the normalized traveled distance by the front of the granular material obtained in the experimental results of Jandaghian et al. (black circles),the numerical results of Jandaghian et al. using MPS model (the red lines with + signs), and the present SPH model results (dashed blue line) . . 120
4.21 Immersed granular column collapse: comparison between the experimental granular material profiles of Jandaghian et al. (black circles), the numerical results of Jandaghian et al. using MPS model (the red + signs), and the present SPH model results (blue diamond) at times t: (A)=0.17 s, and (B)=0.33 s 121
4.22 Immersed granular column collapse: Comparison between the evolution of the water free surface obtained in the experimental results of (black circles),the numerical results of using MPS model (the red lines with + signs), and the present SPH model results (dashed blue line) at t: (A)=0.17 s, (B)=0.33 s, and (C)=0.49 s 122

A.1 Mohr-Coulomb yield criterion. The Mohr circle is based on the principal stresses σ_1 and σ_2. Yielding occurs when the Mohr circle is tangent to the failure envelope. 156

Nomenclature

Greek Symbols

Π_{ij}	Artificial viscosity term
σ	Cauchy stress tensor (Pa)
ε_D	Corrective deformation term
ρ	Density (kg/m^3)
δ	Dirac delta function
μ	Dynamic viscosity (Pa·s)
Ω	Global domain
∇	Gradient operator
Δx_0	Initial inter-particle distance (m)
ϕ	Internal friction angle
Δ	Laplacian operator
γ	Ratio of specific heats
ρ_0	Reference density (kg/m^3)
τ	Viscous stress tensor (Pa)
τ_y	Yield stress (Pa)

Superscripts

$\overline{f}$	Average function

*	Intermediate positions

Subscripts

i	Central particle
$_f$	Fluid phase
j	Neighborhood of the particle i
$_s$	Solid phase

Other Symbols

μ_{eff}	Effective dynamic viscosity (Pa.s)
$\|.\|_F$	Frobenius norm
$\mathscr{D}^{\delta-MSPH}$	Multiphase diffusive term
δ-SPH	Single phase diffusive term

Acronyms / Abbreviations

T	Adimensional time
p_b	Background pressure (Pa)
K	Bulk modulus (Pa)
c	Cohesion (Pa)
kh	Compact support radius (m)
CFD	Computational Fluid Dynamics
CFL	Courant-Friedrichs-Lewy
DEM	Discrete Element Method
r_{ij}	Distance between position vectors r_i and r_j (m)
EISPH	Explicit ISPH
FEM	Finite Element Method
FVM	Finite Volume Method

FSI	Fluid-structure interaction
F	Froude number
g	Gravitational acceleration vector (m/s^2)
I	Identity tensor
ISPH	Incompressible SPH
m	Mass (kg)
MPMs	Meshfree Particle Methods
MPS	Moving Particle Semi-implicit
$\mathscr{D}^{\delta-MSPH}$	Multiphase diffusive term
n_b	Total number of particles j
V	Volume (m^3)
n_{por}	Porosity term
r	Position vector (m)
p	Pressure (Pa)
PPE	Pressure Poisson equation
R_B_RCL	Regularized Bingham Rheological Constitutive Law
R_C_RCL	Regularized Casson Rheological Constitutive Law
Re	Reynolds number
SPH	Smoothed Particle Hydrodynamics
W	Smoothing kernel function
h	Smoothing length (m)
D	Strain tensor
t	Time (s)
v	Velocity vector (m/s)

τ	Viscous stress tensor (Pa)
WCSPH	Weakly Compressible Smoothed Particle Hydrodynamics

Introduction

Fluid-structure interaction (FSI) is a complex and multi-disciplinary field that is of great importance in various engineering and scientific applications [1–5]. Understanding the dynamics of fluid-structure interaction is essential for the design and optimization of various systems, such as offshore structures, aircraft, and industrial processes [6]. One of the most significant examples of (FSI) is the interaction between fluids and granular materials, which is of great importance in many natural and industrial processes [7–9].

One example of fluid-granular material interaction is submarine landslides, which occur when a mass of sediment slides down the slope of the seafloor and into the ocean [10–14]. These landslides can have a significant impact on the ocean environment, as they can generate tsunamis, disrupt shipping lanes, and damage offshore structures. For example, The 2015 Taan Fjord submarine landslide, which occurred in Alaska, caused a tsunami that damaged a nearby fishing village [15]. Another example is subaerial landslides, which occur when a mass of rock, soil, or debris slides down a slope of a mountain, hill, or other upland area and into a valley or other low-lying water area [16–19, 10]. Subaerial landslides can have a devastating impact on human settlements and infrastructure. For example, the 2019 Mindanao subaerial landslide, which happened in the Philippines, killed at least 82 people and caused widespread damage to homes and other structures [20]. In addition, a significant illustration of fluid-granular interaction relates to the behavior of granular materials in industrial processes, such as mining, oil and gas production, and soil treatment [21–23]. The granular materials in these processes exhibit a wide range of mechanical and rheological behavior, and the accurate representation of granular materials is crucial for simulating fluid-structure interaction problems [24].

The main objective of this thesis is to model and simulate the interaction between fluids and structures, with a specific focus on fluid-granular material interaction [10]. The meshless Smoothed Particle Hydrodynamics (SPH) approach will be used to model individual physical particles in the fluid and granular material, where their interactions are governed using various rheological models [25, 26]. This approach allows for a better understanding of granular media as non-Newtonian fluids, where constitutive laws such as the Bingham and

Casson models are examined to characterize the behavior of granular materials [27]. Due to the capability of these models in capturing the yield stress and viscosity of granular materials, a range of applications can be simulated to serve various research and engineering fields [28]. By incorporating these modeling and simulation techniques, the present research makes significant contributions to the field of smoothed particle hydrodynamics (SPH) and its application in modeling complex fluid-structure interaction (FSI), specifically focusing on the interaction between fluids and granular materials. These contributions can be summarized as follows:

- **Advances in SPH Method Improvement Algorithms:** This work presents an overview of both historical and recent advancements in SPH method improvement algorithms, providing valuable insights into the evolution of this numerical technique.
- **Variety of SPH Algorithms for Governing Equation Discretization:** The thesis discusses various SPH algorithms employed for discretizing the governing equations, offering a comprehensive understanding of the options available for SPH simulations.
- **Development of Weakly Compressible SPH Code:** A dedicated weakly compressible smoothed particle hydrodynamics (WCSPH) numerical code has been developed. This code is tailored for modeling complex scenarios involving water-granular material interactions, enhancing the capability to address real-world problems.
- **New Constitutive Laws for Coupled Dynamics:** The thesis introduces novel constitutive laws designed to concurrently address the behavior of landslides and water dynamics. These laws establish a robust and natural coupling between both physical phases, enabling more accurate simulations.
- **Incorporation of Multiphase Diffusive Term:** The implementation of a multiphase diffusive term $\mathscr{D}^{\delta-MSPH}$, as proposed in [29], is discussed. This addition is instrumental in reducing pressure oscillations within the context of the weakly compressible SPH approach.
- **Generalized Wall Boundary Conditions:** The thesis presents the implementation of generalized wall boundary conditions, as outlined in [21]. These conditions enable the simulation of fluid-granular material coupled flows, expanding the applicability of SPH simulations.
- **Comprehensive Rheological Model Comparison:** A thorough comparison is conducted between the generalization and incorporation of Bingham and Casson rheologi-

cal models into SPH. The utilization of the pressure-dependent Mohr-Coulomb yield criterion is explored, providing valuable insights into the behavior of these models.

- **Validation and Verification:** The proposed SPH model is rigorously validated through its application to a variety of challenging test cases involving fluids, granular flows, and their interactions. Experimental and numerical verification studies are presented to demonstrate the applicability and accuracy of the developed SPH model.

The significance of this research is underscored by its contribution to the scientific community through publications and conference presentations. Specifically, this work has been published and presented as follows:

– Abderrahmane Mahallem, Mohamed Roudane, Abdelkader Krimi, and Sid Ahmed Gouri. Smoothed Particle Hydrodynamics for modelling landslide–water interaction problems. *Landslides* 19, 1249–1263 (2022). https://doi.org/10.1007/s10346-021-01807-1

– Abderrahmane Mahallem, Mohamed Roudane, Abdelkader Krimi, Sid Ahmed Gouri, and Abderrazak Allali. Smoothed Particle Hydrodynamics Approach for Modeling Submerged Granular Flows and the Induced Water Wave Propagation. Submitted to *Geophysical and Astrophysical Fluid Dynamics*

– Abderrahmane Mahallem, Mohamed Roudane, Abdelkader Krimi, Sofiane Khelladi, Sid Ahmed Gouri, and Abderrazak Allali. Advancing Granular Material Behavior Simulations: Comparative Analysis of Bingham and Casson Models in WCSPH. Submitted to *Acta Mechanica Sinica*

– Mohamed Roudane, Sid Ahmed Gouri, Abdelkader Krimi, and Abderrahmane Mahallem. Evolution of Free Surface of 3-D shematic Dam Break using Smoothed Particle Hydromechanics. *17th PORTUGAL International Conference on Innovations in "Engineering and Technology" (PIET-19)* Oct. 16-18 2019 Lisbon (Portugal). https://doi.org/10.17758/EIRAI7.F1019104

This thesis is organized into five main parts. The first part serves as the introduction, offering background information on fluid-structure interaction, granular materials, and the specific case of fluid-granular material interaction. It also provides an overview of the main objectives and research questions of the thesis. In the subsequent first chapter, a comprehensive literature review is presented, focusing on the current state of the art in fluid-structure interaction modeling and simulation, with an emphasis on the Smoothed Particle Hydrodynamics (SPH) method and its applications. The second chapter is dedicated to the

development of the SPH approach and the numerical techniques employed for modeling. The third chapter specifically addresses the implementation of the Bingham and Casson constitutive laws into the SPH governing equations, providing a detailed account of the process, including the equations used and the numerical methods applied. Moving to the fourth chapter, it examines the validity of the implemented models, subjecting them to a series of numerical simulations involving fluid-granular material interactions. These simulation results are then meticulously compared to experimental data and findings from other numerical methods, facilitating a thorough discussion of the advantages and limitations of the SPH method for modeling fluid-granular material interaction. Finally, the thesis concludes with a summary of the key findings and a discussion of potential avenues for future research in this field.

Chapter 1

State of the art overview

This chapter will provide an overview of the current state of the art in modeling and simulating fluid-structure interaction (FSI) using the Smoothed Particle Hydrodynamics (SPH) method. We will cover the fundamental principles of SPH, its strengths and weaknesses, and its applications in various fields. By the end of this chapter, readers will have a solid understanding of the current state of FSI modeling using SPH and the opportunities for future research in this field.

1.1 Background on Fluid-Structure Interaction (FSI)

1.1.1 Definition, description, and Importance of FSI

Fluid-structure interaction (FSI) is a multidisciplinary field that studies the interactions between fluid flows and solid structures [30]. The fluid can be either a gas or a liquid, and the structure can be either a solid object or a flexible body [6]. The interactions between the fluid and the structure can occur in a variety of ways, such as the flow of air or water over a solid object [31], or the movement of a structure through a fluid [32] . In FSI, the motion of the fluid is governed by the laws of fluid dynamics, while the motion of the structure is governed by the laws of solid mechanics [33]. The interactions between the fluid and the structure are determined by the boundary conditions at the fluid-structure interface. These boundary conditions can include the transfer of momentum, energy, and mass between the fluid and the structure [34].

The study of FSI is important in a variety of fields, including engineering, physics, biology, geophysics, and many other domains [33, 35]. In engineering, FSI is used to study the behavior of fluid-structure systems, such as aircraft [36, 37], ships [38], and offshore structures [39]. In physics, FSI is used to study the behavior of natural systems, such as the

flow of water over a riverbed or the movement of a bird through the air [40]. In biology, FSI is used to study the behavior of living organisms, such as fish and whales, as they move through water [41]. In geophysics, FSI is used to study the behavior of fluid-structure systems and understand the interactions between fluids and solid structures in geophysical systems. For example, it is used to study geo-disasters, such as tsunamis occurred after subaerial and submarine landslides [42, 43].

1.1.2 Overview of different modeling and simulation methods for FSI

Modeling and simulation methods for fluid-structure interaction (FSI) can be broadly classified into two categories: mesh-based methods and mesh-free methods [44–46].

Mesh-based Methods

Mesh-based methods involve the discretization of the fluid and structural domains through the use of a mesh. The most widely used mesh-based methods for FSI are the finite element method (FEM) and the finite volume method (FVM) [34, 47].

FEM is a robust technique for simulating FSI, offering versatility in handling diverse geometries and boundary conditions. It finds extensive application in the analysis of solid structures like bridges, buildings, and aircraft components [48]. The method revolves around subdividing the structure into small elements and subsequently solving the equations of motion for each element.

In contrast, FVM excels in simulating fluid flows, demonstrating proficiency across a broad spectrum of fluid dynamics and geometries. It is commonly employed in the analysis of phenomena such as water flow in rivers, airflow over aircraft, and oil flow in pipelines [49]. This method is based on partitioning the fluid domain into small control volumes, followed by solving the equations of motion for each control volume.

When simulating FSI using FEM and FVM, the equations of motion for the fluid and structure are coupled using either a two-way coupling approach or a monolithic approach [50]. The two-way coupling approach entails solving the equations of motion for the fluid and structure separately, and then exchanging information between the two solutions at each time step [51]. On the other hand, the monolithic approach involves solving the equations of motion for the fluid and structure simultaneously [52].

The main drawback of these methods lies in their substantial computational requirements and the need for expertise in specialized software usage [53]. Additionally, grid-based approaches exhibit limitations when applied to simulations involving large deformations, moving material interfaces, significant inhomogeneities, deformable boundaries, or free

surfaces [54, 55]. These methods may struggle to accurately represent such complex scenarios. In Fig. 1.1, we provide a schematic illustration of discretization using FEM and FVM mesh-based methods.

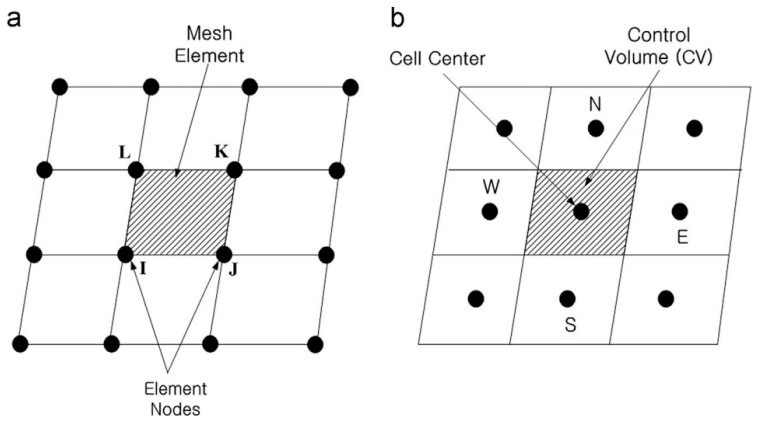

Fig. 1.1 Schematic representation of mesh-based methods (a) the finite element method (FEM), and (b) the finite volume method (FVM). (image from [56])

Mesh-free Methods

In order to circumvent issues arising from node connectivity, a distinct class of numerical techniques, known as Meshfree (or meshless) methods, was developed [46, 57]. These methods revolutionize the traditional discretization process by allowing the continuum to be represented as a set of independent particles without interconnecting nodes. This feature significantly simplifies the handling of large deformation problems and facilitates precise representation of free-moving interfaces, all while maintaining a reasonable level of computational efficiency [46, 58].

When these nodes are conceived as substantial elements, effectively simulating particles within the material domain and bearing its physical properties, the approach is aptly termed "meshfree particle methods (MPMs)" [59]. This paradigm generally adopts a Lagrangian framework [60].

The Meshfree Particle Methods (MPMs) encompass a range of techniques, including Reproducing Kernel Particle Method (RKPM) [62, 63], Marker-and-Cell (MAC) [64], Element-Free Galerkin (EFG) method [65, 66], Dissipative Particle Dynamics (DPD) [67, 68], Local Maximum Entropy (LME) method [69, 70], Particle-Mesh (PM) [71], Radial Point Interpolation Method (RPIM) [72, 73], lattice gas Cellular Automata (CA) [74, 75], Moving Least Squares (MLS) method [76, 77], Natural Element Method (NEM) [78, 79], Finite Pointset Method (FPM) [80, 81], Particle-in-Cell (PIC) [82, 64], Fluid-In-Cell (FLIC) [83],

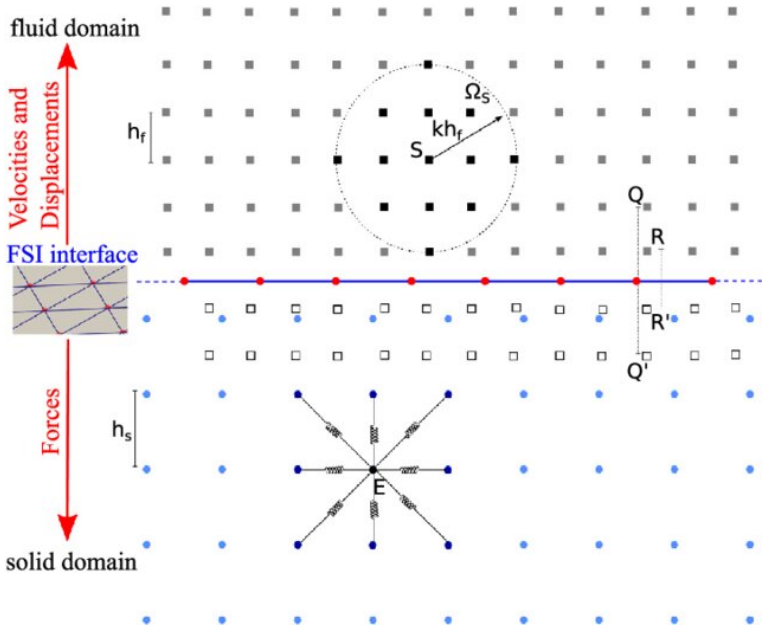

Fig. 1.2 Schematic representation of the SPH method: 2D sketch of the fluid and solid computational domains. (image from [61])

Particle-Particle-Mesh (P^M), Moving Particle Semi-implicit (MPS) [84], Smoothed Particle Hydrodynamics (SPH) [85, 86], and various other meshfree particle methods. Each of these methods has its own strengths and weaknesses, and the choice of method depends on the specific problem being studied, as well as the available computational resources.

1.2 The Smoothed Particle Hydrodynamics (SPH) Method

1.2.1 Description of the SPH method

In this thesis, we place a prominent emphasis on the Smoothed Particle Hydrodynamics (SPH) method, a meshfree, Lagrangian approach renowned for its efficiency and robustness. This technique represents the continuum through discrete particles, with their movements tracked over time. SPH employs interpolation and kernel functions to estimate physical properties throughout space, facilitating a smooth distribution of fluid properties [85, 87].

Within the SPH framework, properties like density, velocity, and pressure are computed for each particle. Interactions between particles are determined using smoothing kernels, which approximate local fluid properties, ensuring a more accurate representation. These interactions are computed by aggregating contributions from all particles within the smoothing kernel [88].

The versatility of the SPH method extends to simulating a wide array of scenarios, including liquid and gas flows, as well as fluid-structure interactions. Its applicability spans intricate geometries, like those found in porous media and multiphase flows. Beyond, SPH finds valuable utility in astrophysical, oceanographic, and meteorological studies. Furthermore, it can be coupled with other physical models to simulate a diverse range of phenomena, including combustion, explosions, and solid-fluid interactions [55, 89–91].

One notable advantage of the SPH method lies in its capacity to handle topological changes and moving boundaries without necessitating laborious remeshing or re-gridding, which can pose a substantial computational burden in grid-based methods. Additionally, the SPH method lends itself well to parallel computing, enabling large-scale simulations on supercomputers [92–95]. However, it is important to note that the SPH method can incur computational expenses, warranting judicious consideration of resources in its application [96, 97].

1.2.2 Fundamentals of SPH Method

In 1977, the Smoothed Particle Hydrodynamics (SPH) method emerged, initially devised by researchers [85] and [87] for simulating astrophysical phenomena. Over time, its applications expanded into the domains of solid and fluid mechanics, finding utility in a diverse array of scenarios. This is owed to its capacity to effectively address the intricacies inherent in various physical problems (discussed in section 1.2.5).

Fundamentally, this Lagrangian technique involves discretizing the continuous domain into a finite assembly of particles. These particles assume the relevant physical attributes through weighted interpolations of neighboring particles. It's important to note that only those particles falling within the domain of influence (bounded by a maximum distance of (kh) from the focal particle under consideration) exert an influence on the behavior of physical properties within said focal particle.

SPH relies on a mathematical identity that holds true for a well-defined and continuous function f, as elucidated in the equation below:

$$f(r_i) = \int_{\Omega} \delta(r_i - r_j) f(r_j) \mathrm{d}r_j^n \tag{1.1}$$

Here, $\mathrm{d}r_j^n$ represents the elemental volume located at position r_j, and $\delta(r_i - r_j)$ stands for the Dirac or delta function. However, due to the lack of continuity and differentiability of the delta function, Substituting the Dirac delta function with a kernel or smoothing function W , we derive an approximation for the function f at position r_i leading to:

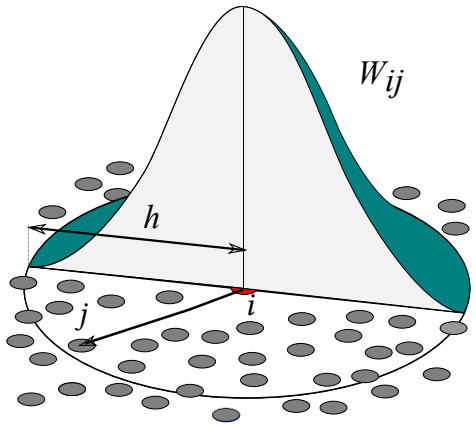

Fig. 1.3 Physical domain description using smothing kernel function in the SPH method framework

$$f(r_i) \approx \int_{\Omega(kh)} W(r_i - r_j, h) f(r_j) \mathrm{d}r_j^n \tag{1.2}$$

Here, h denotes the smoothing length, commonly defined as a constant relative to the initial inter-particle distance Δx_0 [98]. It is important to highlight that h can be customized for individual particles, thereby augmenting the precision of the SPH method [92, 99].

The kernel function operates within a compact support of radius kh, where a particle at position r_i interacts solely with neighboring particles r_j. This confines the global domain Ω to the compact support domain $\Omega(kh)$, subsequently reducing computation time. The constant k is contingent on the choice of the smoothing kernel function. Figure 1.3 provides a visual depiction of the Lagrangian particles positioned within the domain of influence, delineated by a circumference with a smoothing length equivalent to (h).

1.2.3 Smoothing kernel functions

In the Smooth Particle Hydrodynamics (SPH) method, a smoothing kernel function is used to calculate the spatial derivatives of continuum properties, such as density and velocity [88]. The smoothing kernel is a function that is used to smooth the properties of the fluid over a small region around each particle. There are several different smoothing kernel functions that can be used in the SPH method, each with their own advantages and disadvantages [94]. The smoothing kernel function can be represented in a general form as :

$$W(r_{ij}, h) = W(r, h) = \frac{\eta_n}{h^n} Q\left(\frac{r}{h}\right) = \frac{\eta_n}{h^n} Q(q) \tag{1.3}$$

Where n is the number of space dimension, Q is function of dimensionless distance $q = \frac{r}{h}$, and η_n is constant depends of the choice of kernel function and the space dimension n. The letter r denotes the variable distance between two points ($r = r_{ij} = \|r_i - r_j\|$).

One of the most commonly used smoothing kernel functions is the cubic spline kernel [100]. The mathematical form of the cubic spline kernel is given by:

$$Q(q) = \begin{cases} 1 - \frac{3}{2}q^2 + \frac{3}{4}q^3 & 0 \leq q < 1 \\ \frac{1}{4}(2-q)^3 & 1 \leq q < 2 \\ 0 & q \geq 2 \end{cases} \tag{1.4}$$

Where the constants $\eta_1 = \frac{2}{3}$, $\eta_2 = \frac{10}{7\pi}$ and $\eta_3 = \frac{10}{\pi}$ are used for 1, 2 and 3 dimensions, respectively.

Another popular smoothing kernel is the quintic spline kernel [101, 102], which is a more complex kernel that is able to accurately approximate spatial derivatives. This kernel function is defined as:

$$Q(q) = \begin{cases} (3-q)^5 - 6(2-q)^5 + 15(1-q)^5 & 0 \leq q < 1 \\ (3-q)^5 - 6(2-q)^5 & 1 \leq q < 2 \\ (3-q)^5 & 2 \leq q < 3 \\ 0 & q \geq 3 \end{cases} \tag{1.5}$$

Where $\eta_1 = \frac{1}{120}$, $\eta_2 = \frac{7}{478\pi}$ and $\eta_3 = \frac{1}{120\pi}$ are used for 1, 2 and 3 dimensions, respectively.

Other examples of smoothing kernel functions include the Gaussian kernel [87], which is defined as:

$$Q(q) = e^{-q^2} \tag{1.6}$$

Where the constants $\eta_1 = \frac{1}{\sqrt{\pi}}$, $\eta_2 = \frac{1}{\pi}$ and $\eta_3 = \frac{1}{\pi\sqrt{\pi}}$ are used for 1, 2 and 3 dimensions, respectively.

We find also the Wendland kernel [103], which is defined as:

- Wendland $C2$:

$$Q(q) = (1 - \frac{q}{2})^4(2q+1) \tag{1.7}$$

Where $\eta_2 = \frac{7}{4\pi}$ and $\eta_3 = \frac{21}{16\pi}$ are used for 2 and 3 dimensions, respectively.

- Wendland $C4$:

$$Q(q) = (1-\frac{q}{2})^6(\frac{35}{12}q^2+3q+1) \tag{1.8}$$

  Where $\eta_2 = \frac{9}{4\pi}$ and $\eta_3 = \frac{495}{256\pi}$ are used for 2 and 3 dimensions, respectively.

- Wendland $C6$:

$$Q(q) = (1-\frac{q}{2})^8(4q^3+\frac{25}{4}q^2+4q+1) \tag{1.9}$$

  Where $\eta_2 = \frac{39}{14\pi}$ and $\eta_3 = \frac{1365}{512\pi}$ are used for 2 and 3 dimensions, respectively.

The choice of smoothing kernel function depends on the specific application and can affect the accuracy and stability of the SPH method [104]. For example, the cubic spline kernel is a good choice for many SPH simulations due to its simplicity, while the quintic spline kernel is often used for high-resolution simulations [105]. Moreover in the context of the SPH method, the smoothing kernel function W guarantees a more substantial influence from the closest neighboring particles on the value of the physical property in the reference particle. The kernel should fulfill some specific properties to ensure accurate and stable simulations [106]. These properties include:

Smoothness: The function should be smooth, meaning that it should have continuous derivatives of all orders. This is important for ensuring that the interpolation of particle data is accurate and does not introduce any unwanted artifacts or noise.

Spherical symmetry: The function should be radially symmetric, meaning that it should only depend on the distance between two particles and not on their relative positions. This ensures that the interpolation of particle data is isotropic. Mathematically, it means that: $W(r_i - r_j, h) = W(r_j - r_i, h) = W(r_{ij}, h)$, where r_{ij} signifies the distance between position vectors r_i and r_j ($r_{ij} = \|r_i - r_j\|$).

Normalization: The function should have a total integral of 1 over the smoothing length, h. This ensures that the interpolated values are in the same scale as the original values. Mathematically, it means that: $\int_{\Omega(kh)} W(r_i - r_j, h)\mathrm{d}r_j = 1$

Compact support: The function should have compact support $\Omega(kh)$, meaning that its value should be non-zero only within a finite range $W(r,h) = 0$ for $r \geq kh$. This ensures that the interpolation of particle data is localized and does not affect particles far away from the point being interpolated. Mathematically, it means that: $W(r_i - r_j, h) \geq 0$ for $r < kh$

Continuity: The function should be continuous, meaning that the function and its derivatives should be continuous over the support of the kernel. Mathematically, it means that: $W(r_i)$ and $\frac{dW(r_i)}{dr_i}$ are continuous in the range of support.

W should monotonically decrease from position r_i.

The gradient of kernel W is given by:

Efficiency: The kernel function W should accurately approximate the Dirac delta function δ as $h \longrightarrow 0$. Additionally, W should monotonically decrease from position r_i. Moreover, the gradient of kernel (W) is given by: $\nabla_{r_i} W(r_i - r_j, h) = \frac{\partial W(r,h)}{\partial r} \frac{r_i - r_j}{r} = -\nabla_{r_j} W(r_j - r_i, h)$

Any function that adheres to the aforementioned properties is suitable for use as a smoothing function in the SPH method [44, 107].

Smoothing kernel approximation of a function

The smoothing kernel function is used to approximate a function in Smoothed Particle Hydrodynamics by interpolating the values of the function at the neighboring particles. The basic idea is to use the kernel function to weight the contribution of each neighboring particle to the value of the function at a given point [108, 59, 109]. The interpolation of a function at a point i can be written as:

$$f(r_i) \approx \sum_{j}^{n_b} f(r_j) W_{ij} V_j \tag{1.10}$$

Where, n_b is the number of particles j in the neighborhood of the particle i, the volume V_j of particle j is defined as $V_j = \frac{m_j}{\rho_j}$, with m_j and ρ_j the mass and the density of the particle j, respectively. The notation W_{ij} denotes $W_{ij} = W(r_{ij}, h) = W(r_i - r_j, h)$.

Smoothing kernel approximation of a function first deravatives

In SPH Smoothed Particle Hydrodynamics, the smoothing kernel function is also used to approximate the derivatives of a function. The basic idea is to use the kernel function to weight the contribution of each neighboring particle to the value of the function derivative at a given point [92].

The gradient of a function f at a point i can be written as:

$$\nabla f(r_i) \approx \sum_{j}^{n_b} f(r_j)\ \nabla W_{ij}\ V_j \tag{1.11}$$

Where $f(r_i)$ is the value of the function at point i, $f(r_j)$ is the value of the function at the neighboring point j, m_j is the mass of the neighboring point j, r_{ij} is the vector pointing from point i to j, h is the smoothing length and $W(r_{ij},h)$ is the smoothing kernel function.

Similarly, the divergence of a vector function at a point i can be written as:

$$\nabla \cdot \mathbf{F}_i = \sum_{j=1}^{N} m_j \frac{\mathbf{F}_j - \mathbf{F}_i}{\|r_{ij}\|} \cdot \mathbf{r}_{ij} W(r_{ij},h) \tag{1.12}$$

Where $\mathbf{F}_i$ is the vector function at point i, $\mathbf{F}_j$ is the vector function at the neighboring point j, m_j is the mass of the neighboring point j, $\mathbf{r}_{ij}$ is the vector pointing from point i to j, h is the smoothing length and $W(r_{ij},h)$ is the smoothing kernel function.

As discussed above, the choice of the smoothing kernel function affects the accuracy of the approximation. As with the function approximation, kernel functions like the cubic spline kernel and the Gaussian kernel are commonly used, but the Gaussian kernel is typically more accurate for approximating derivatives due to its infinite differentiability.

It is important to note that the accuracy of the derivative approximations also depends on the choice of the smoothing length h and the number of particles in the simulation. As the number of particles increases and h decreases, the accuracy of the derivative approximations improves [110].

Smoothing kernel approximation of a function second deravatives

The smoothing kernel approximation of function second derivatives involves approximating the Laplacian of a function, denoted as $\nabla^2 f(r_i)$, at a point i in a continuous space using a set of discrete points [111, 112]. The Laplacian is a measure of the rate of change of the function's curvature, and is defined as the divergence of the gradient of the function, mathematically represented as:

$$\Delta f(r_i) = \nabla^2 f(r_i) = \nabla \cdot \nabla f(r_i) \approx \sum_{j}^{n_b} f(r_j) \nabla^2 W_{ij} V_j \tag{1.13}$$

Where ∇ is the gradient operator, and the dot represents the dot product.

The kernel approximation approach is based on a convolution of the function with a smoothing kernel, $W(r_{ij})$, where r_{ij} is the distance between the point of interest j and the point where the value is known i. The kernel is used as a weighting factor to estimate the Laplacian function.

Alternative expression for approximating a function second derivatives was proposed in [113] and it is expressed as:

$$\Delta f(r_i) \approx 2\sum_{j}^{n_b} \frac{f(r_i) - f(r_j)}{\|r_i - r_j\|^2}(r_i - r_j) \cdot \nabla W_{ij} V_j \tag{1.14}$$

The equation 1.14 allows for the efficient approximation of the Laplacian of a function in a continuous space using a set of discrete points, providing a balance between computational efficiency and accuracy [112, 114, 115].

1.2.4 Software Packages Utilizing Smoothed Particle Hydrodynamics

There are various software packages available that implement the SPH method for different applications. These software packages provide tools and algorithms to simulate and analyze fluid dynamics, including fluid-structure interactions, multiphase flows, and even astrophysical phenomena. Some popular software packages that use the SPH method include:

DualSPHysics: It is an open-source software package that focuses on simulating free-surface flows, such as water waves and coastal engineering problems. It provides a user-friendly interface and supports parallel computing for efficient simulations [116].

SPHysics: This is another open-source software package that is designed to simulate a wide range of fluid flow problems, including multiphase flows, compressible flows, and fluid-structure interactions. It offers various numerical algorithms and boundary conditions to handle complex fluid dynamics scenarios [117].

SPH-flow: Developed by FlowKit Ltd., this commercial software package specializes in simulating complex fluid flows, including turbulent flows and multiphase flows. It provides advanced features like particle clustering and adaptive resolution to enhance the accuracy and efficiency of simulations [89].

LS-DYNA: Although primarily known as a general-purpose finite element analysis software, LS-DYNA also includes an SPH module for simulating fluid flows. It can handle various fluid-structure interaction problems and supports parallel computing for large-scale simulations [118].

These software packages typically provide pre-processing tools to create the initial particle distribution, define boundary conditions, and specify physical properties. They also offer post-processing capabilities to visualize and analyze simulation results, including generating animations, extracting flow statistics [119]. While these software packages provide a convenient way to simulate fluid flows using the SPH method, it is important to note that proper validation and calibration against experimental data are crucial for accurate and reliable

results. Additionally, understanding the underlying numerical algorithms and limitations of the SPH method is essential to ensure appropriate use and interpretation of the simulations [120].

1.2.5 Applications of the SPH Method

Smoothed Particle Hydrodynamics (SPH) is a versatile and powerful numerical method that has a wide range of applications in simulating fluid, solid, and fluid-structure interactions [121]. It is particularly useful in modeling complex and multi-physics problems that involve free-surface flows, moving boundaries, and non-linear dynamics. The method represents computational domains as a set of discrete particles, which are smoothed over a certain region to calculate the fluid properties [95]. This approach allows for a high degree of flexibility and adaptability, making it ideal for simulating a wide range of problems in various fields, such as computational mechanics, computer graphics, astrophysics, and geophysics [122]. In the field of computational mechanics, SPH is a powerful tool for simulating a wide range of problems involving fluid-structure interactions, such as simulating the behavior of liquid-filled structures, and simulating the impact of fluid flow on solid structures, as well as simulating natural hazards like tsunamis, landslides and other geohazards. In the following, some of the applications of Smoothed Particle Hydrodynamics (SPH) are examined and discussed.

Applications for fluids

Many examples of the applications of SPH in fluid dynamics can be found in the literature, such as simulation of dam-break flows with free surface and large deformation[123]. The SPH method ability to handle these complexities is one of the reasons why it is so effective in simulating fluid flows. As depicted in Figure 1.4, Yang et al. [123] have illustrated a simulation of a dam-break flow on a wet bed using the SPH method with an adaptive spatial resolution (ASR) method, particle shifting, and variable smoothing length. Their work has shown the ability of the method to model such complex flow scenarios effectively.

Additionally, the SPH has been used for modeling the behavior of liquids, such as droplet collisions , splashing and spray formation. For instance, we show via Fig. 1.5 snapshots of the pressure field obtained by Blank et Al. [124] to simulate the coalescence of spherical droplets introducing a surface tension model for the SPH method using a Young-Laplace pressure boundary condition. Furthermore, Cleary and Serizawa [125] have described a combined DEM-SPH model for simulating spray impingement into a pool of water as it is shown in Fig. 1.6.

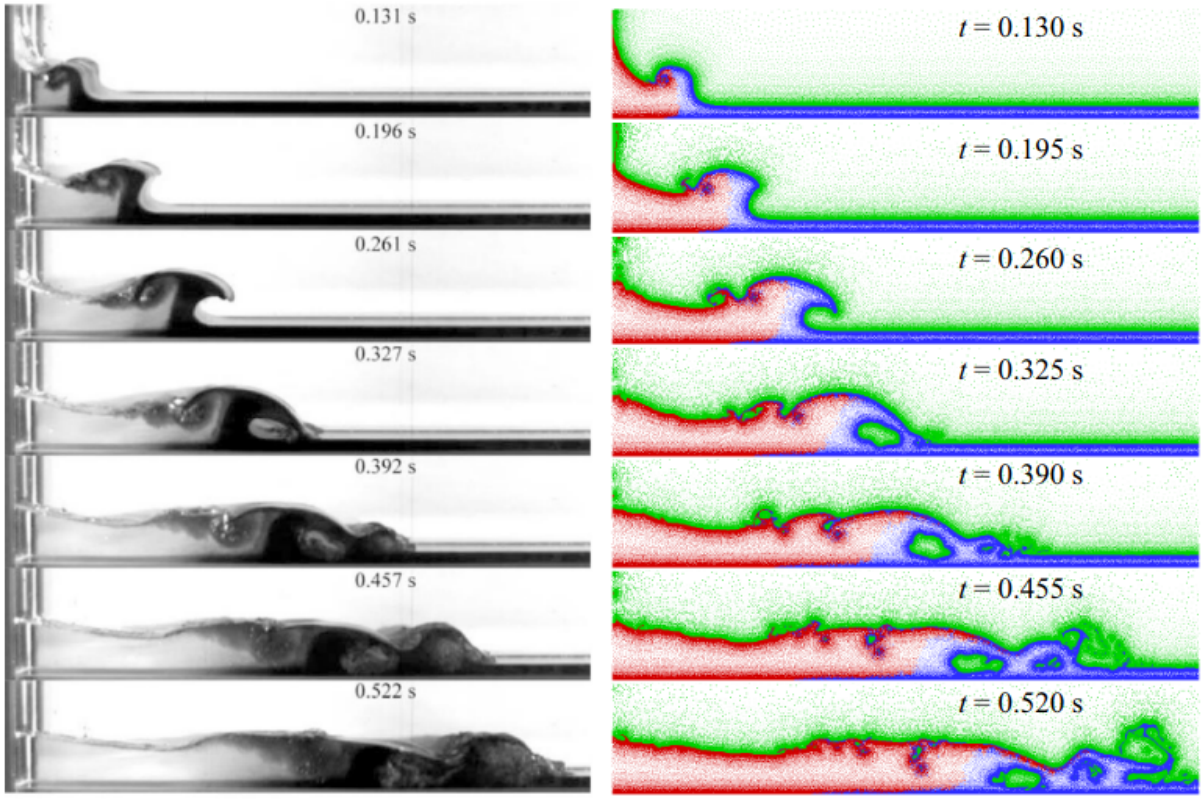

Fig. 1.4 Snapshots of 2D dam-break flow on a wet bed (Yang et al. [123]).

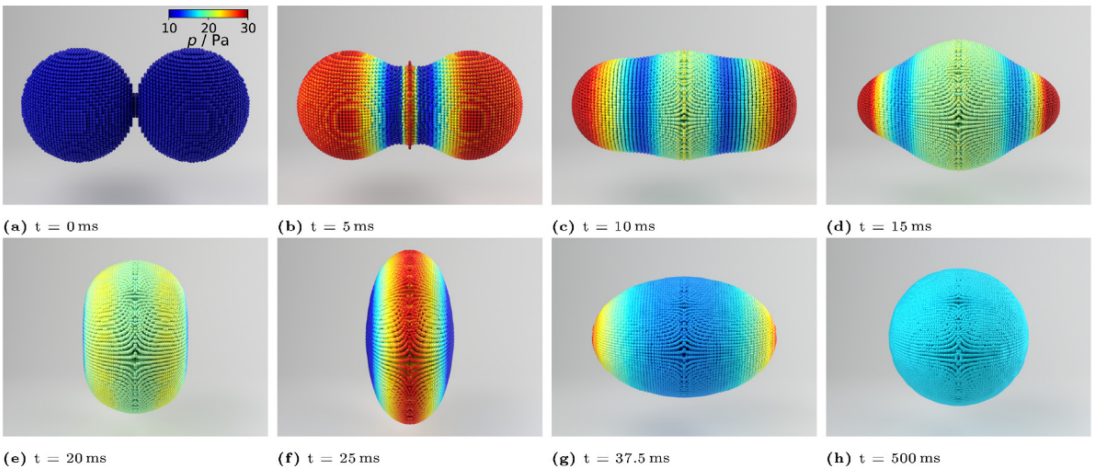

Fig. 1.5 SPH snapshots of the coalescence of two spheres colored by pressure at increasing time instants (Blank et al. [124]).

The SPH method has also been applied to study the dynamics of multiphase flows, including flows containing bubbles and particle-laden flows. We present in Fig. 1.7 the lid-driven cavity problem studied by Antuono et al. [126] through a proposed δALE-SPH

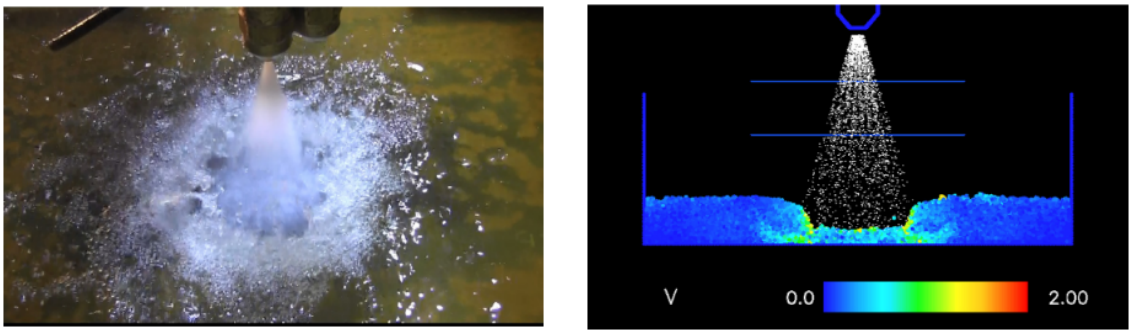

Fig. 1.6 DEM-SPH simulation of flow generated in a pool of water by spray impingement: Photograph of the experimental flow (left) and the simulation results colored by the fluid speed (right) (Cleary et al. [125]).

model. In particular, the pressure field and streamlines (left) and the vorticity field (right) are depicted at two different Reynolds number Re = 100 (top panels) and Re = 1000 (bottom panels).

Krimi et al. [29] conducted a study on the interaction of two rising bubbles through a fluid column using a modified version of the Continuum Stress Surface formulation (CSS) in the Smoothed Particle Hydrodynamics (SPH) method. The purpose of this modification was to improve stability near the fluid interface. The results of their study are depicted in Figure 1.8 at three different times: $t = 0, 0.25, 0.5$ [s]. In the figure, the left and middle columns show the pressure and velocity magnitude, respectively. The right column illustrates the velocity magnitude along with the particle direction vector of an isolated bubble.

In aerodynamics, Zhang et al. [127] have simulated the airflow past a circular cylinder based on free-stream boundary conditions in a purely Lagrangian Weakly-Compressible Smoothed Particle Hydrodynamics (WCSPH). Fig. 1.9 presents their achieved results exhibiting the velocity contours at different Reynolds numbers.

Other applications can be quoted, such as in cryogenics. Tsuzuki et al. [128] have discussed the equivalence of a fully classical mechanical approximation of the two-fluid model of superfluid helium-4 based on the SPH method to solving a many-body quantum mechanical equation under specific conditions, as depicted in Fig. 1.11.

Applications for solids and structures

In addition to its application in fluid dynamics, The versatility of the Smoothed Particle Hydrodynamics (SPH) method extends to structure dynamics and solid mechanics. In the following, some of these applications will be explored and discussed. For instance, Wu et al. [129] have successfully modeled oscillating plates. The elastic deformation with Von

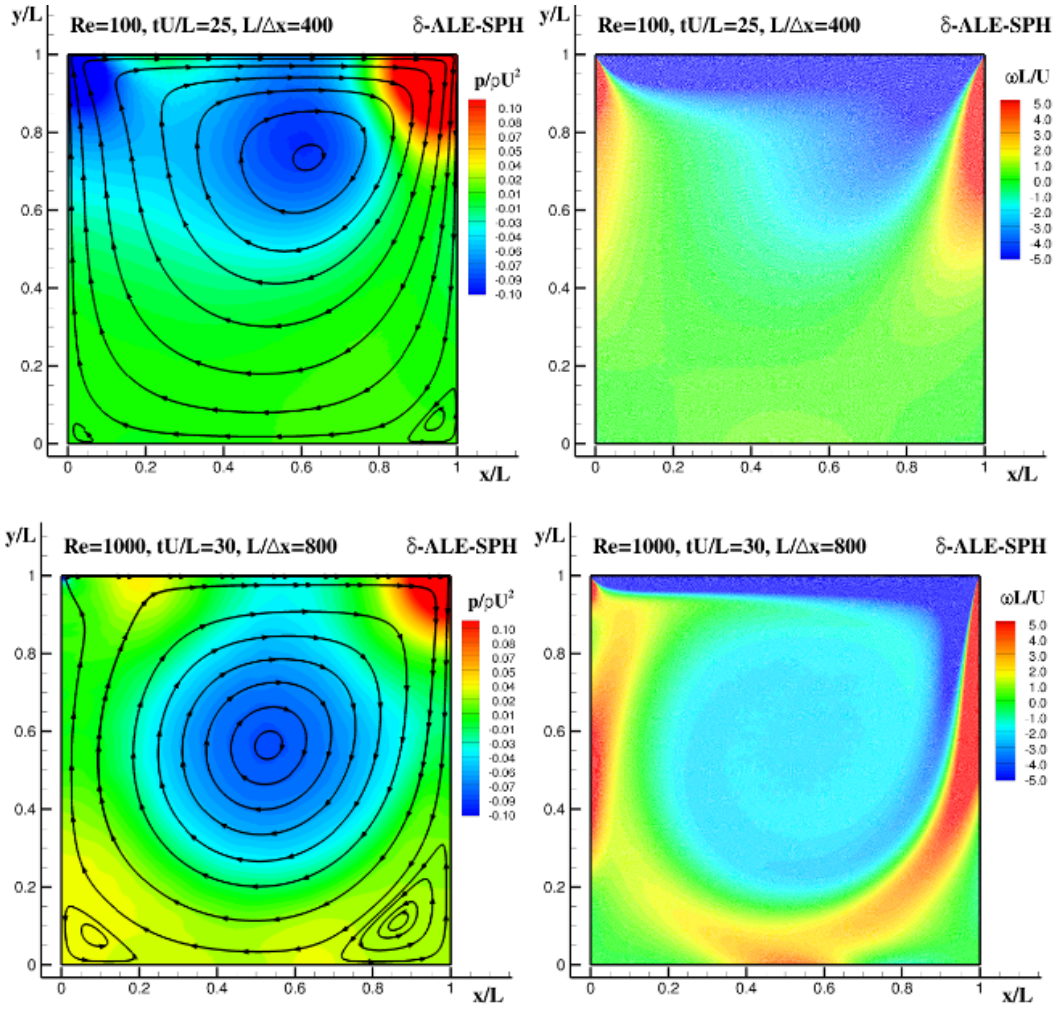

Fig. 1.7 Comparison of lid-driven cavity for Reynolds $Re = 100$ (top panels) and $Re = 1000$ (bottom panels). The snapshots are colored by pressure field and streamlines (left) and by vorticity field (right) (Antuono et al. [126]).

Mises stress $\bar{\sigma}$ of the particle configuration obtained by total Lagrangian-Smoothed Particle Hydrodynamics (TL-SPH) model is presented in Fig. 1.12. The period and amplitude of oscillations convergence with enhanced resolution are exhibited by Figure 1.13, depicting the vertical position y of the end-of-strip midpoint against time t and initial particle spacing dp.

Moreover, Kincl et al. [130] have integrated the Symmetric Hyperbolic Thermodynamically Compatible equations (SHTC) with the SPH method to investigate structure dynamical problems. Their proposed SHTC-SPH method was tested on a benchmark of a twisting column, and Fig. 1.14 presents a color plot of pressure. The obtained results indicate that the SPH method is capable of accurately simulating large elastic deformations in three dimensions. Rahimi et al. [131] have proposed an SPH model for simulating dynamic of

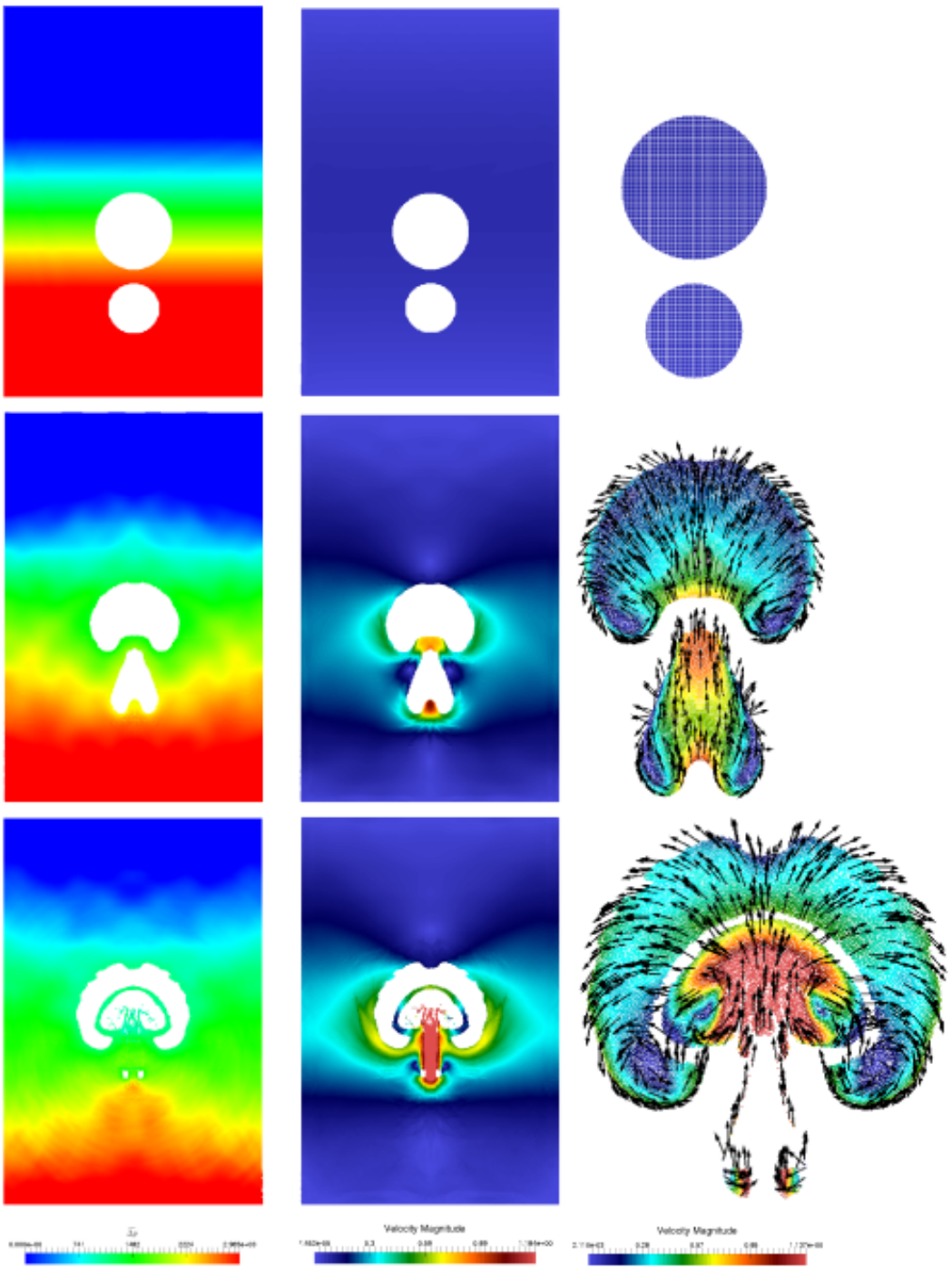

Fig. 1.8 SPH simulation snapshots of the interaction between two rising bubbles through a fluid column. representation of the pressure (right column), the magnitude velocity (middle column), and the magnitude velocity with particle direction vector of isolated bubble, respectively (Krimi et al [29]).

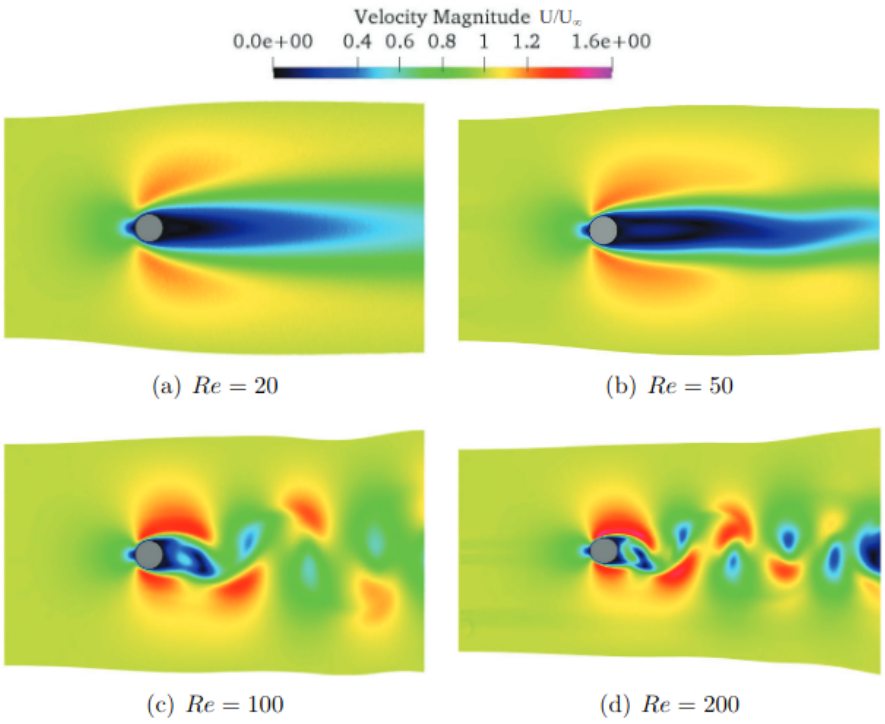

Fig. 1.9 SPH simulation of the airflow around a circular cylinder for different Reynolds number *Re*= 20, 50, 100, and 200. The snapshots are colored by the magnitude vilocity field (Zhang et al. [127]).

brittle fracture and solid mechanics. The convergence of the SPH model can be shown in Fig. 1.15, which presents their results obtained from modeling the interaction of cracks with other structural defects in a porous plate with an eccentric hole. The SPH method has been also applied in to simulate machining procedure in the manufacture of industrial components. For instance, Nawaz et al. [132] have used the SPH method to model the orthogonal dry machining of aluminum alloy Al6061-T6 using the SPH method. Fig. 1.16 compared the SPH simulated chip thickness with the experimental work and Lagrangian (LAG) finite element method at cutting speed of 250 m/min. Furthermore, Fabbro et al. [133] conducted a single diamond grain scratch test experiment and used the SPH method to model grains scratching a rebar base material. Fig. 1.17 shows the top view of deformations and equivalent plastic strain distribution simulated with SPH at different penetration depths and grain orientations.

In the same framework, Li et al. [134] have proposed for the first time an SPH model for simulating Shear Assisted Processing and Extrusion (ShAPE) of Aluminum alloy 7075 tubes. Fig. 1.18 shows a comparison between experimental samples and SPH numerical material flow patterns of extruded tubes with various processing parameters. The results were

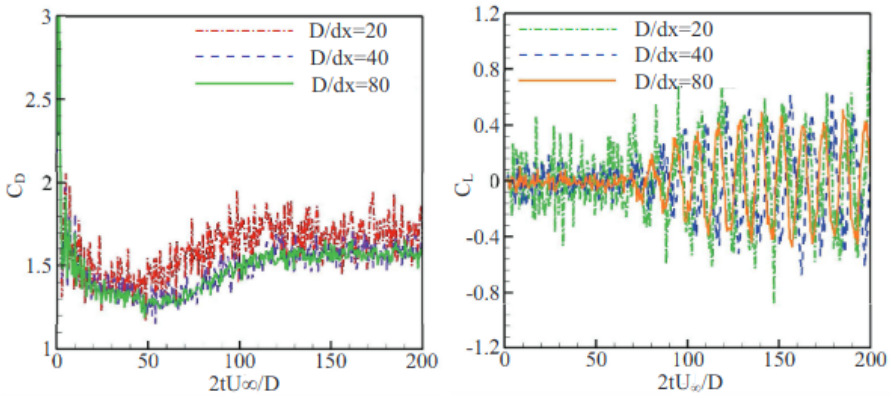

(b) $Re = 100$

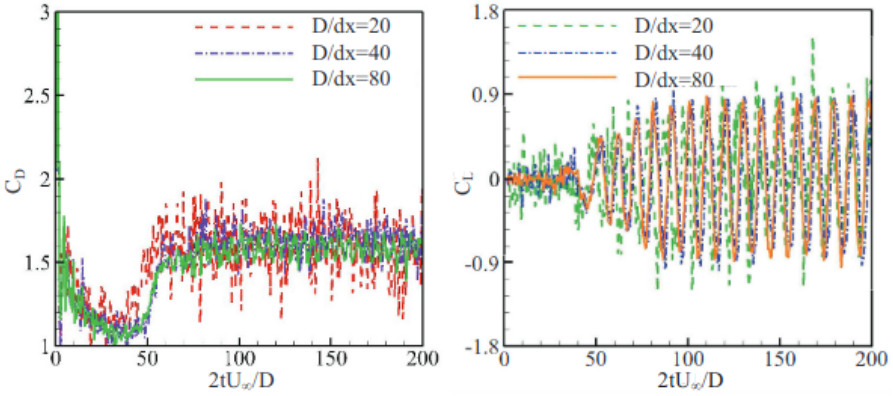

(c) $Re = 200$

Fig. 1.10 Airflow around a circular cylinder: convergence of drag and lift coefficients *CD* and *CL* at different spatial resolutions at *Re*=100 and 200, respectively (Zhang et al. [127]).

very similar, which demonstrates the strength of the SPH model in predicting this kind of material flows. In geomaterials engineering fields, the SPH method demonstrates its validity for the simulation of the fracture process of brittle solids and the flow behavior of granular materials. For instance, Xia et al. [135] have developed Kernel Broken Smoothed Particle Hydrodynamics (KBSPH) method for modeling the crack propagation and deformation of layered rock cells. Fig. 1.19 exhibits a comparison between experimental and numerical results of an unconfined compression tests on layered sandstone samples. The brittle behavior of these specimens at different dip angles and crack distributions were accurately predicted using the SPH method. Another important application of the SPH method is in the simulation of gravitational flows of granular materials. This type of simulation is particularly useful in geotechnical engineering, where the behavior of soil and rocks under different gravitational forces needs to be understood. For example, Nguyen al. [136] have used the SPH method to investigate the dynamics of granular column collapse. Fig. 1.20 shows a simulation of

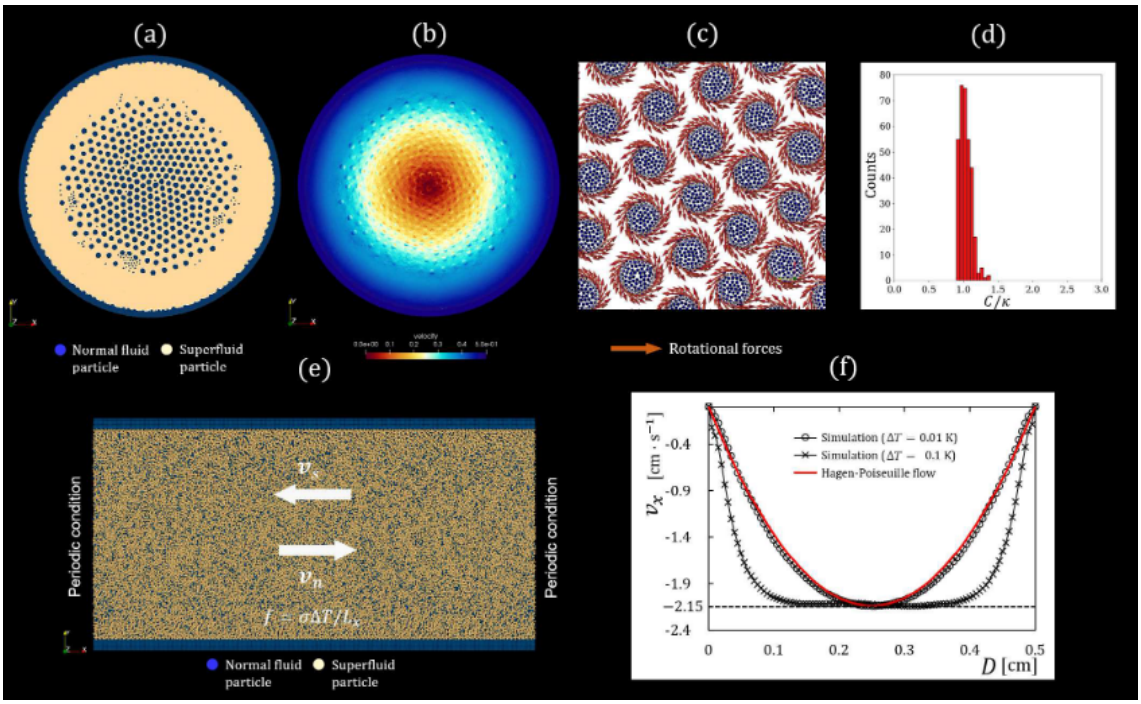

Fig. 1.11 Different simulation results in the context of bridging classical and quantum mechanics for the dynamics of cryogenic liquid helium-4 using SPH model (Tsuzuki et al. [128]).

Aluminum granular bars flow using the SPH method, where the color map represents the flow velocity. The results of this simulation provide valuable insights into the behavior of granular materials flows. Zhu et al. [137] used the SPH method to simulate the collapse of a granular column with asymmetric walls, where the column is confined by two vertical walls. Fig. 1.21 shows snapshots of the simulation at different times, demonstrating the ability of the SPH method to accurately capture the dynamics of granular collapse and the formation of characteristic features such as the failure velocity and the final deposit shape.

Applications for fluid-structure interactions

Since it is capable of modeling both fluids and structures, the SPH method can also be applied to problems involving fluid-structure interaction (FSI). The ability of the SPH method to handle large deformations and complex geometries makes it a powerful tool for simulating FSI problems in a wide range of applications. Several examples of the application of the SPH method for modeling fluid-structure interaction problems have been reported in the literature. For instance, Fuchs et al. [138] have used an SPH model to simulate flow-induced oscillations of a flexible beam attached to a rigid cylinder. In this application, the SPH

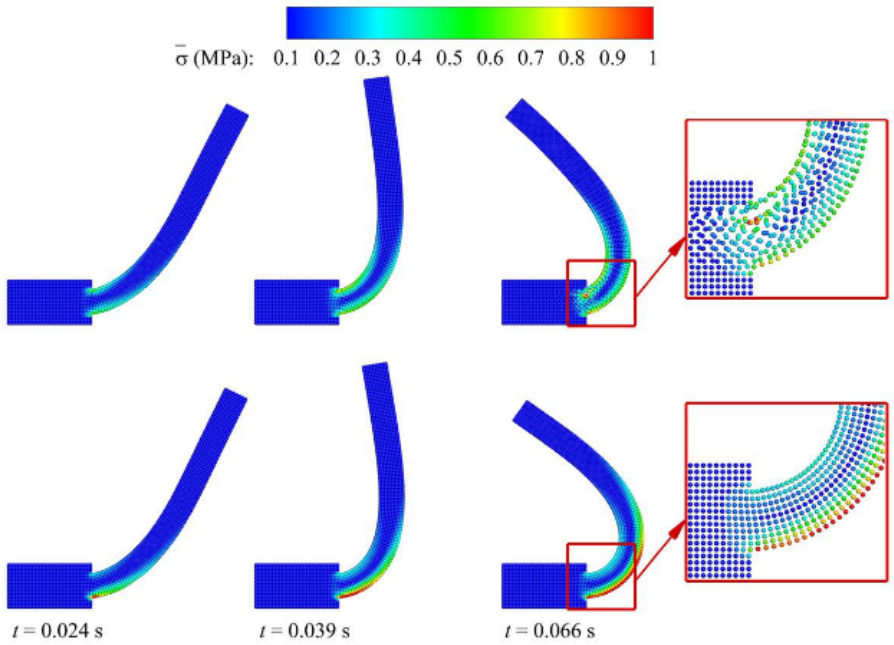

Fig. 1.12 SPH simulation of an oscillating plate: the deformed configuration is colored by Von Mises stress $\bar{\sigma}$ at different time instants (Wu et al. [129]).

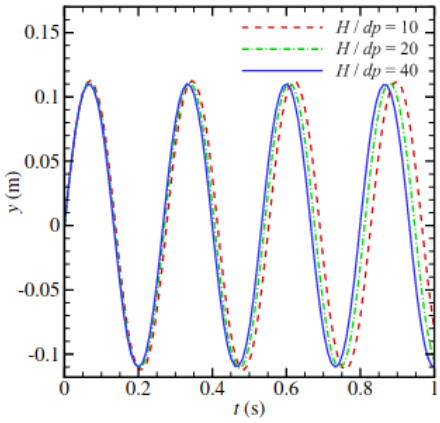

Fig. 1.13 Time history of the vertical position y observed at the midpoint of the oscillating plate using different particle resolutions (Wu et al. [129]).

method was used to model both the fluid flow and the flexible structure, allowing for accurate prediction of the dynamic response of the system. The magnitude of the fluid velocity field and the deformation of the structure are depicted in Fig. 1.22.

In other examples, Zhang et al. [139, 140] employed an SPH model to simulate a dam-break flow through an elastic gate. The elastic gate and the fluid were both modeled using the SPH method. The Fluid-elastic structure interaction was taken into account through a multi-

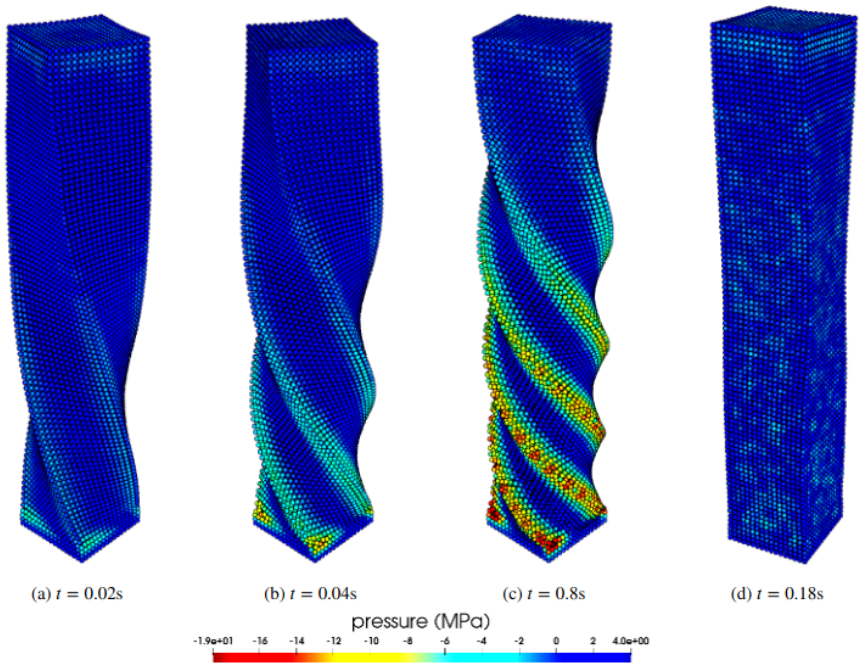

Fig. 1.14 SPH 3D simulation of a twisting column: the large elastic deformations is colored by pressure at different time instants (Kincl et al. [130]).

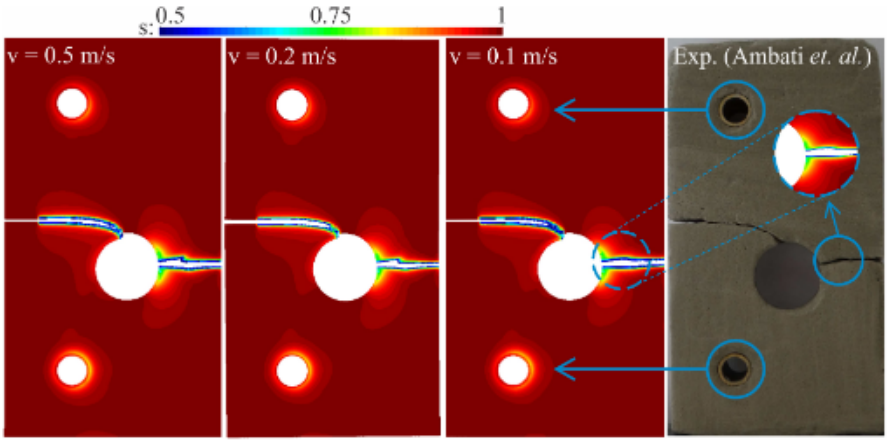

Fig. 1.15 Notched plate with hole: Snapshots of the final crack pattern under different prescribed velocity loading using the SPH method compared to the experimental results (Rahimi et al. [131]).

resolution coupling between the fluid and the structure, allowing for accurate prediction of the gate's deformation and the fluid flow pattern. The simulation results were validated against experimental data, as shown in Fig. 1.23 and 1.24, demonstrating the effectiveness of the SPH method in modeling FSI problems involving complex geometries and large deformations. Similarly, the SPH method has been applied to model fluid-structure interaction in sloshing

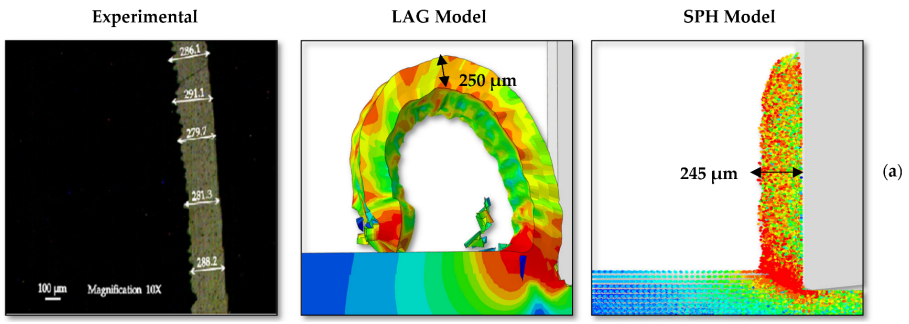

Fig. 1.16 Chip thickness Comparison during a machining procedure of aluminum alloy Al6061-T6: experimental snapshot (left), simulation results using LAG method (middle), and simulation results using SPH method (Nawaz et al. [132]).

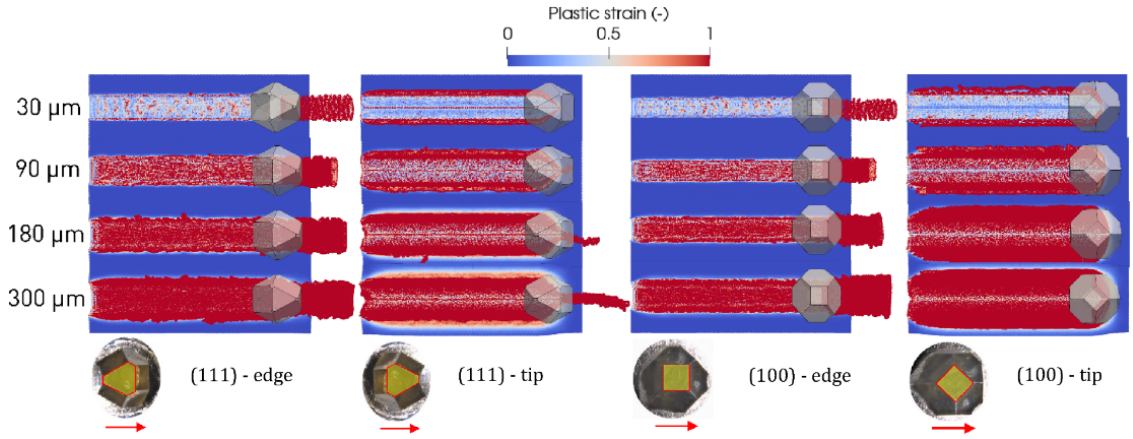

Fig. 1.17 SPH simulation of synthetic diamond grit scratching on steel: the snapshots are colored by plastic strain distribution at different penetration depths and grain orientations (Fabbro et al. [133]).

tanks. For example, Zhang et al. [141] developed an SPH model to simulate the sloshing motion of a liquid with a hanging elastic baffle. The baffle is modeled as a thin, flexible structure that is attached to the top of the tank, and the SPH method is used to model both the fluid flow and the deformation of the baffle. The results of the simulation are shown in Fig. 1.25, where the deformation of the baffle and the fluid flow pattern are clearly visible. The accuracy of the SPH model in predicting the behavior of the liquid and the baffle demonstrates its potential for simulating a wide range of fluid-structure interaction problems.

In addition to the applications mentioned above, the SPH method has also been applied to model FSI in biomedical engineering. For instance, Topalovic et al. [142] have used an SPH model to investigate the flow through complex geometry blood vessels. The results are illustrated in Fig. 1.26 comparing FEM and SPH simulation and showing that the SPH

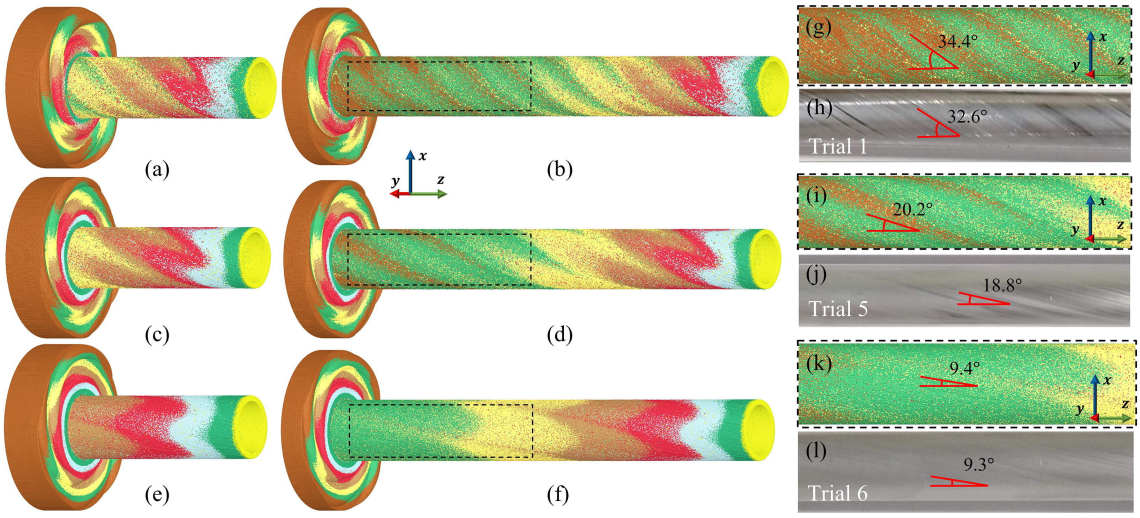

Fig. 1.18 Comparison of experimental and numerical SPH results of material flow patterns during an operation of Shear Assisted Processing and Extrusion (ShAPE) (Li et al. [134]).

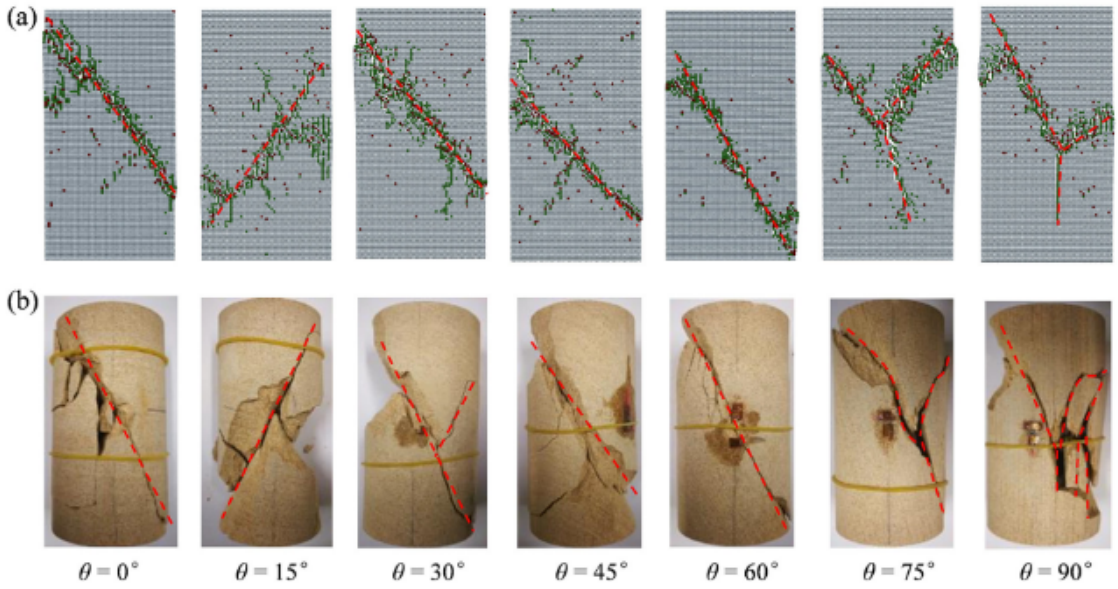

Fig. 1.19 Comparison between SPH failure results and the experimental results of the sandstone with different dip angles. Snapshots are colored by: tensile (green) and shear cracks (brown), respectively (Xia et al. [135]).

method can accurately predict this kind of complex flow patterns. Another application of the SPH method is in the field of brain biomechanics, where it has been used to model the cerebrospinal fluid and its interaction with the brain tissue. For example, Duckworth et al. [143] have proposed an SPH model to simulate the dynamics of the cerebrospinal fluid in the

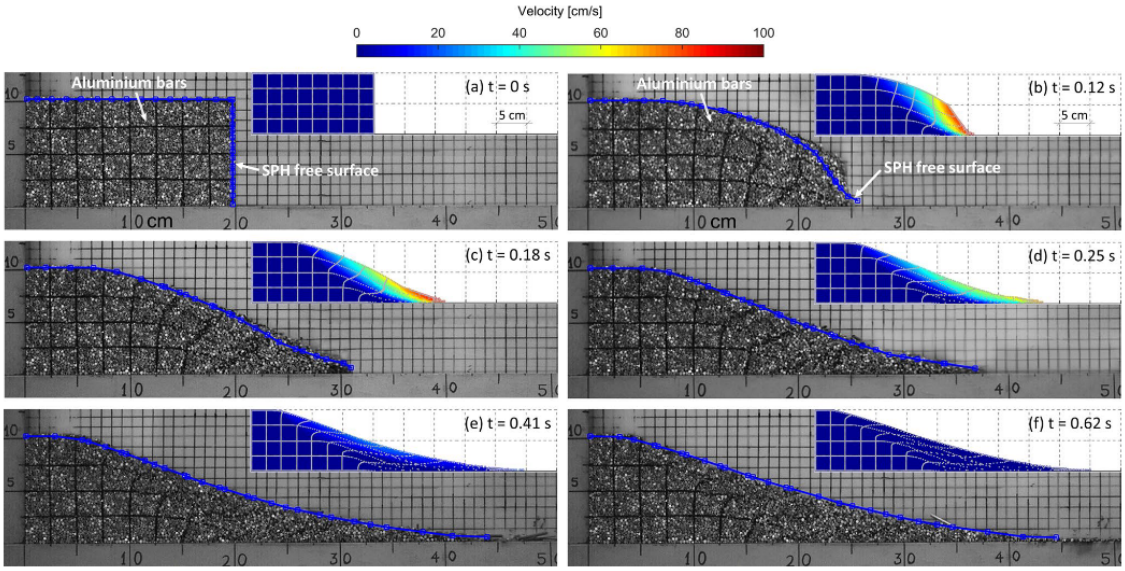

Fig. 1.20 Comparison between SPH and experimental results of the progressive failure of a granular column. SPH results are colored by the velocity filed (Nguyen et al. [136]).

brain ventricles. The model has been validated against MRI scan data and has shown good agreement in terms of flow patterns and pressure distribution as it is shown in Fig. 1.27.

Furthermore, the SPH method has been applied to the simulation of fluid-structure interaction (FSI) problems in the context of aircraft ditching scenarios. For example, Woodgate et al. [144] have used an SPH model for predicting the complex fluid-structure interactions that occur during helicopter ditching, including the interaction between the water and the helicopter structure. Fig. 1.28 shows the dynamic response of a regional jet during a ditching event at different instances. The SPH method has been also applied to simulate the water entry of a rigid bodies. For example, Peng et al. [145] provided detailed information about the complex free surface flows, as well as the hydrodynamic forces acting on the cylinder during the water entry of a vertical cylinder, and the numerical results showed good agreement with experimental data. The deformation of the free surface and the pressure distribution on the water are shown in Fig. 1.29. In a similar manner, the SPH method has been successfully used to model the interaction between fluids and floating bodies. For example, Cui et al. [146] have utilized an SPH method to simulate the interaction between fluids and a floating box then they have proposed new designed breakwaters that have better performance than fixed breakwaters in deep water conditions (see Fig. 1.30). The SPH model was also able to capture the behavior of the fluid flow around complex floating structure, and the dynamic response of the structure due to the fluid-structure interaction [147]. Figure 1.31 shows an example of a simulation of the interaction between fluids and a floating complex

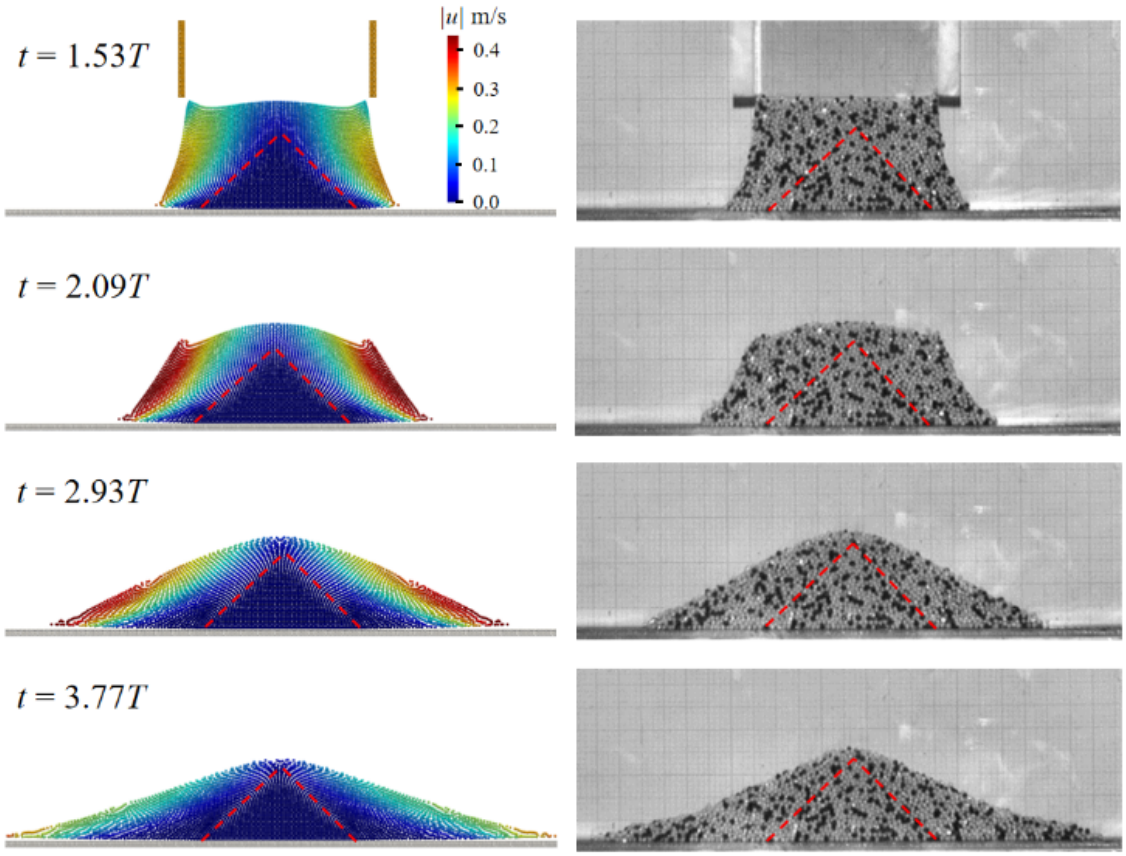

Fig. 1.21 Comparison between SPH and experimental results of the progressive failure of column of glass beads constrained by two parallel gate sheets. SPH results are colored by the velocity filed (Zhu et al. [137]).

structure using SPH. Such simulations can provide valuable insights into the behavior of floating structures in different flow conditions, which is important in a variety of engineering applications such as ship design and offshore structures.

The smoothed particle hydrodynamics (SPH) method has also been widely used to simulate various natural phenomena, including landslides. In recent studies, the SPH method has been employed to simulate both subaerial and submarine landslides, considering both sliding deformable and rigid masses [148, 16, 149, 150, 10]. For subaerial landslides, the SPH method can be used to simulate the movement of a sliding mass along a slope, taking into account the effects of gravity, friction, and other external forces (see Fig. 1.32). The SPH method is particularly useful for simulating the complex behavior of landslides, such as the formation of tsunamis and the interaction between the sliding mass and the surrounding water (see Fig. 1.33). In the case of submarine landslides, the SPH method can be used to simulate the movement of a sliding mass underwater, taking into account the effects of

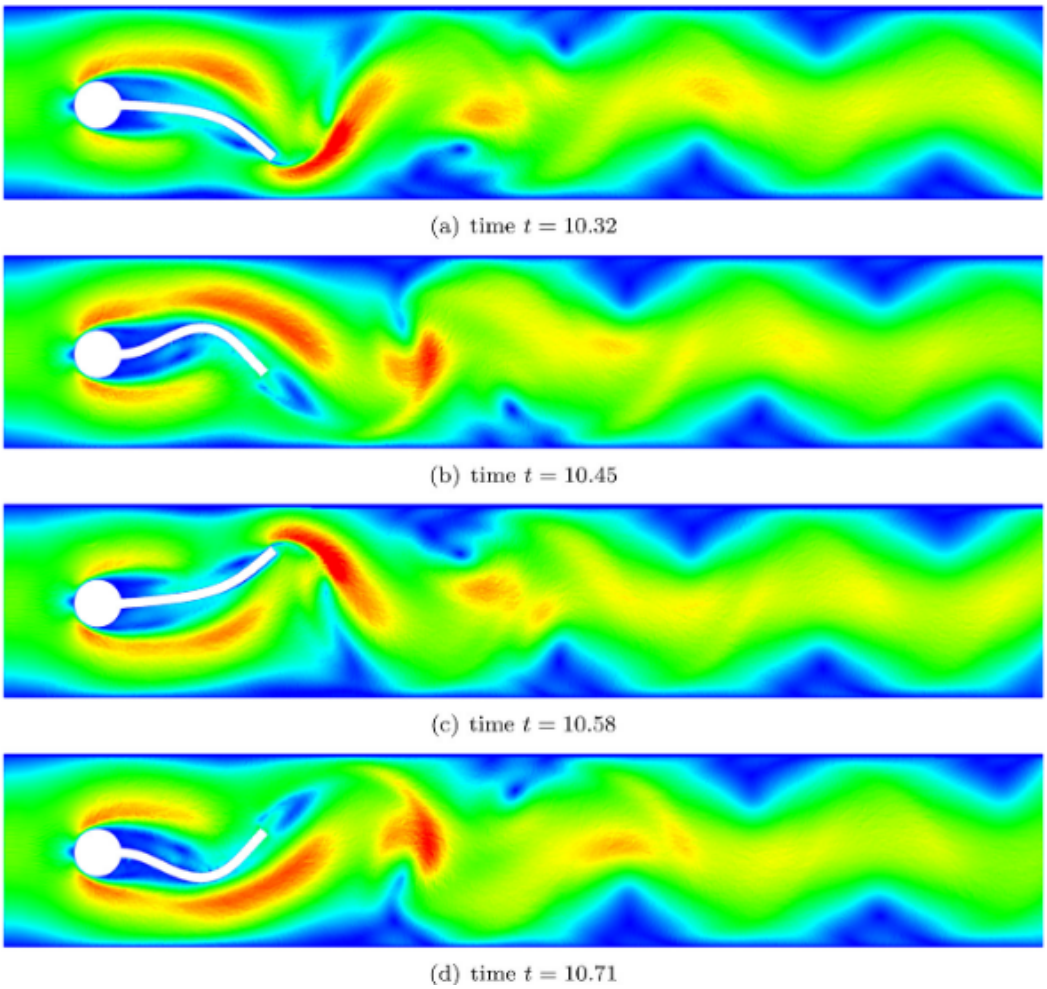

(a) time $t = 10.32$

(b) time $t = 10.45$

(c) time $t = 10.58$

(d) time $t = 10.71$

Fig. 1.22 SPH simulation of the magnitude of the fluid velocity field and the deformation of a flexible beam attached to a rigid cylinder for a periodic cycle at four equidistant points in time (Fuchs et al. [138]).

buoyancy, hydrodynamic forces, and sediment transport (see Fig. 1.34). The SPH method is particularly useful for simulating the complex behavior of submarine landslides, such as the formation of turbidity currents and the interaction between the sliding mass and the seafloor (see Fig. 1.35).

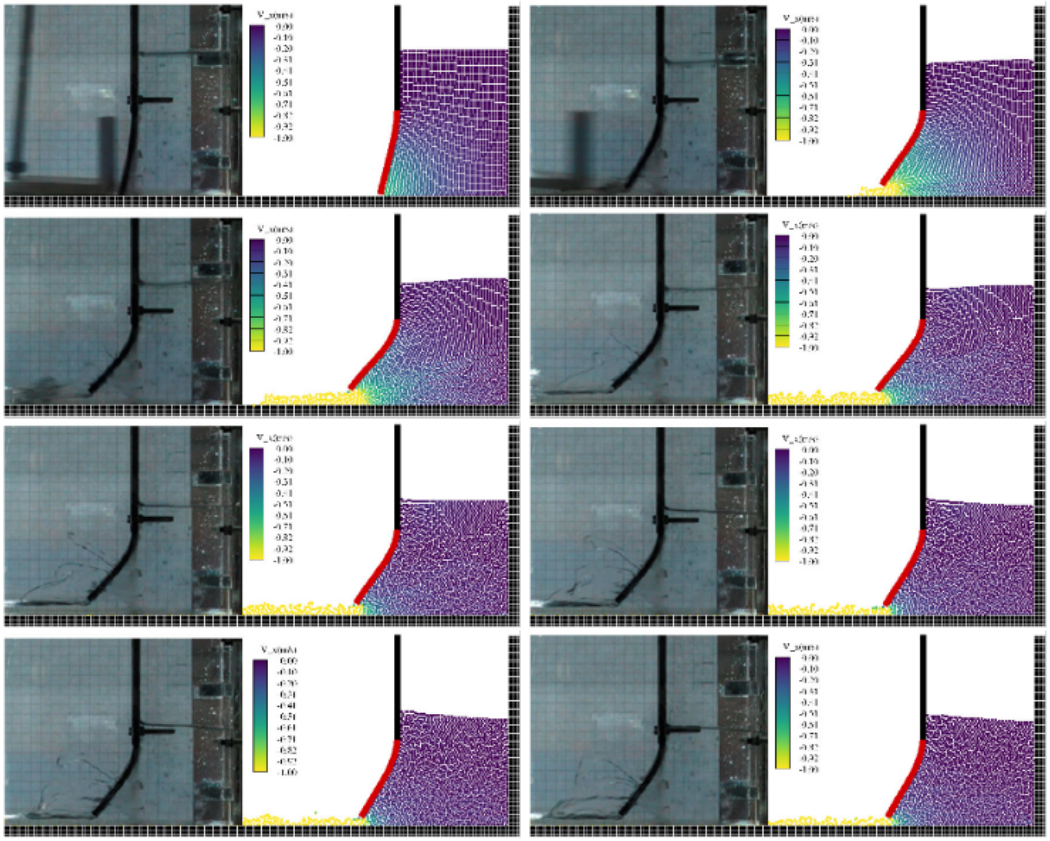

Fig. 1.23 Comparison between SPH simulation and experimental results of dam-break flow through an elastic gate at different time instants. The fluid particles in the SPH snapshots are colored by the velocity field in the x flow direction v_x (Zhang et al. [139]).

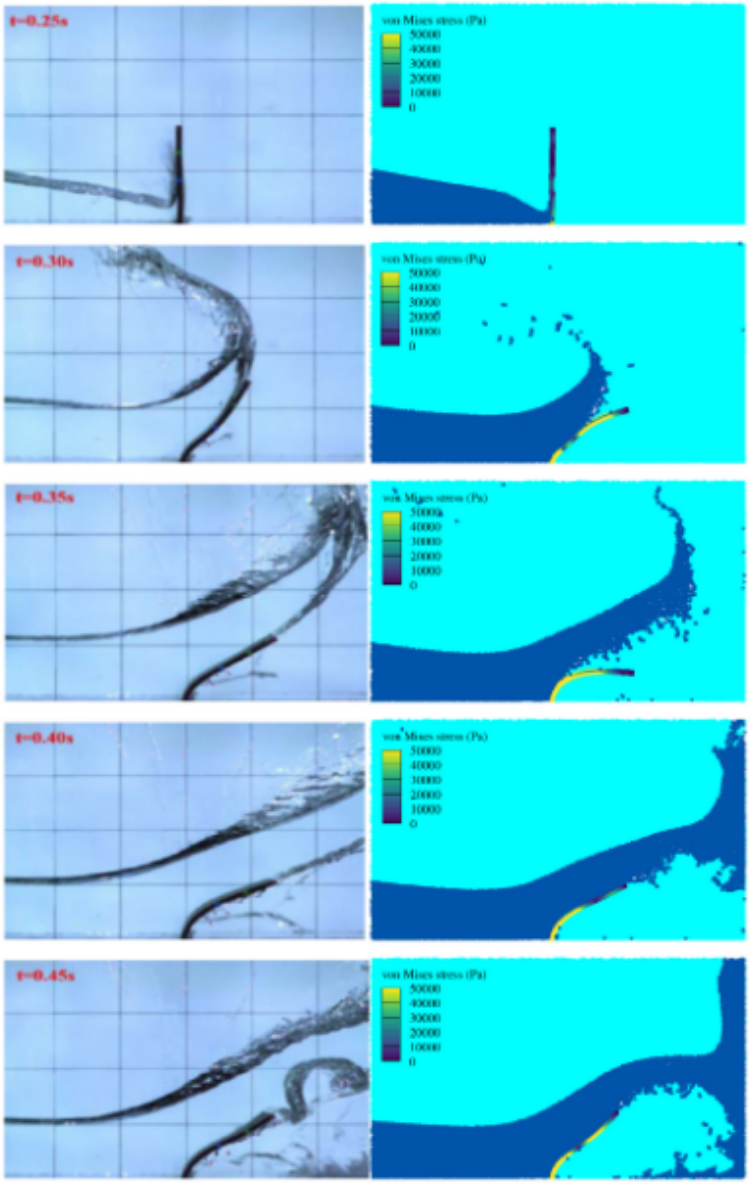

Fig. 1.24 Comparison between SPH simulation and experimental results of dam-break flow impacting an elastic gate at different time instants. The structure particles in the SPH snapshots are colored by the Von Mises stress contour (Zhang et al [140]).

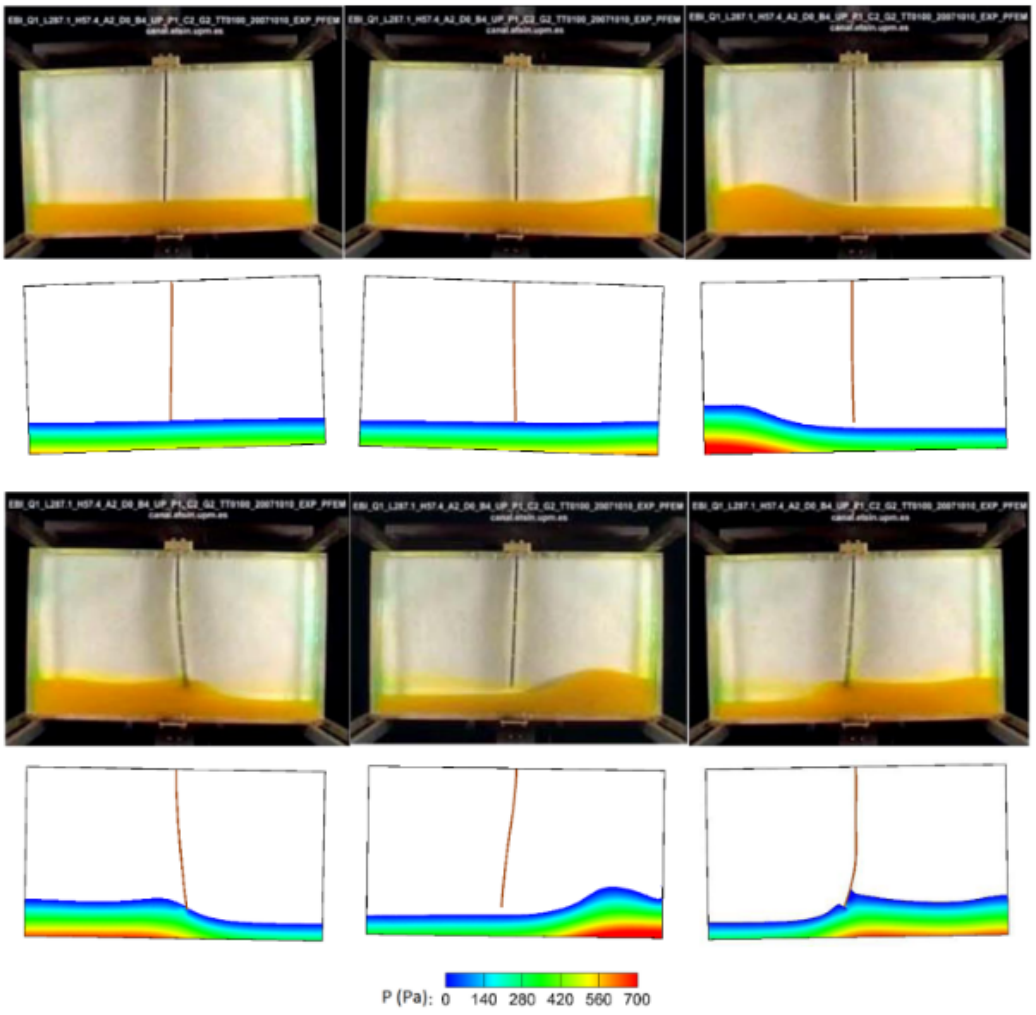

Fig. 1.25 Comparison between SPH simulation and experimental results of sloshing with an elastic baffle hanging from the top tank wall at different time instants. The fluid particles in the SPH snapshots are colored by the pressure field (Zhang et al [141]).

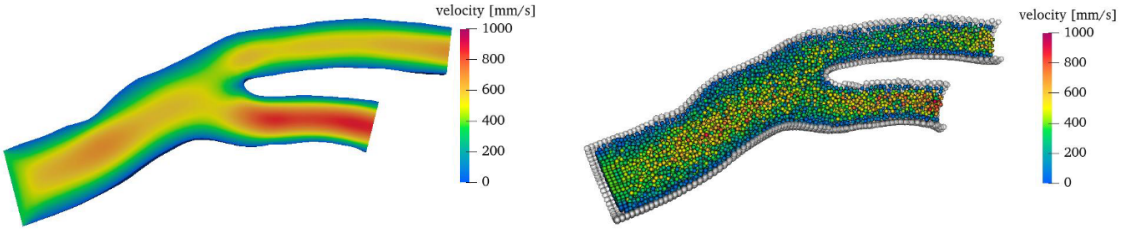

Fig. 1.26 Comparison between SPH (right) and FEM (left) simulation results of flow through complex geometry blood vessels sloshing with an elastic baffle hanging from the top tank wall at different time instants. The fluid particles in the SPH snapshots are colored by the velocity field (Topalovic et al. [142]).

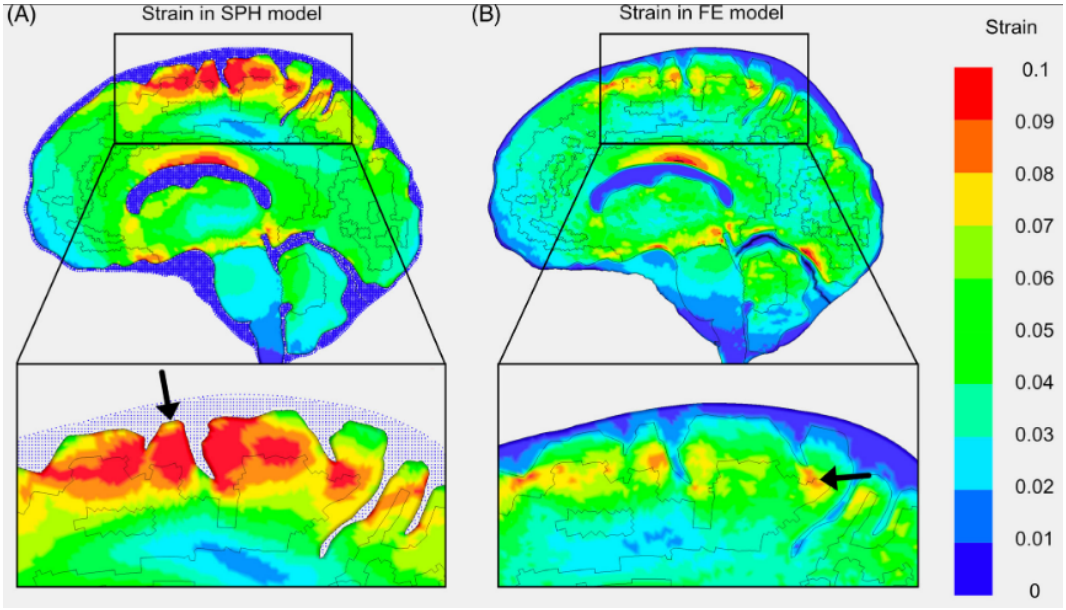

Fig. 1.27 Comparison between SPH (left) and FE method (right) simulation results of Ogden rubber material and its surrounding fluid in the brain. The snapshots are colored by the strain (Duckworth et al. [143]).

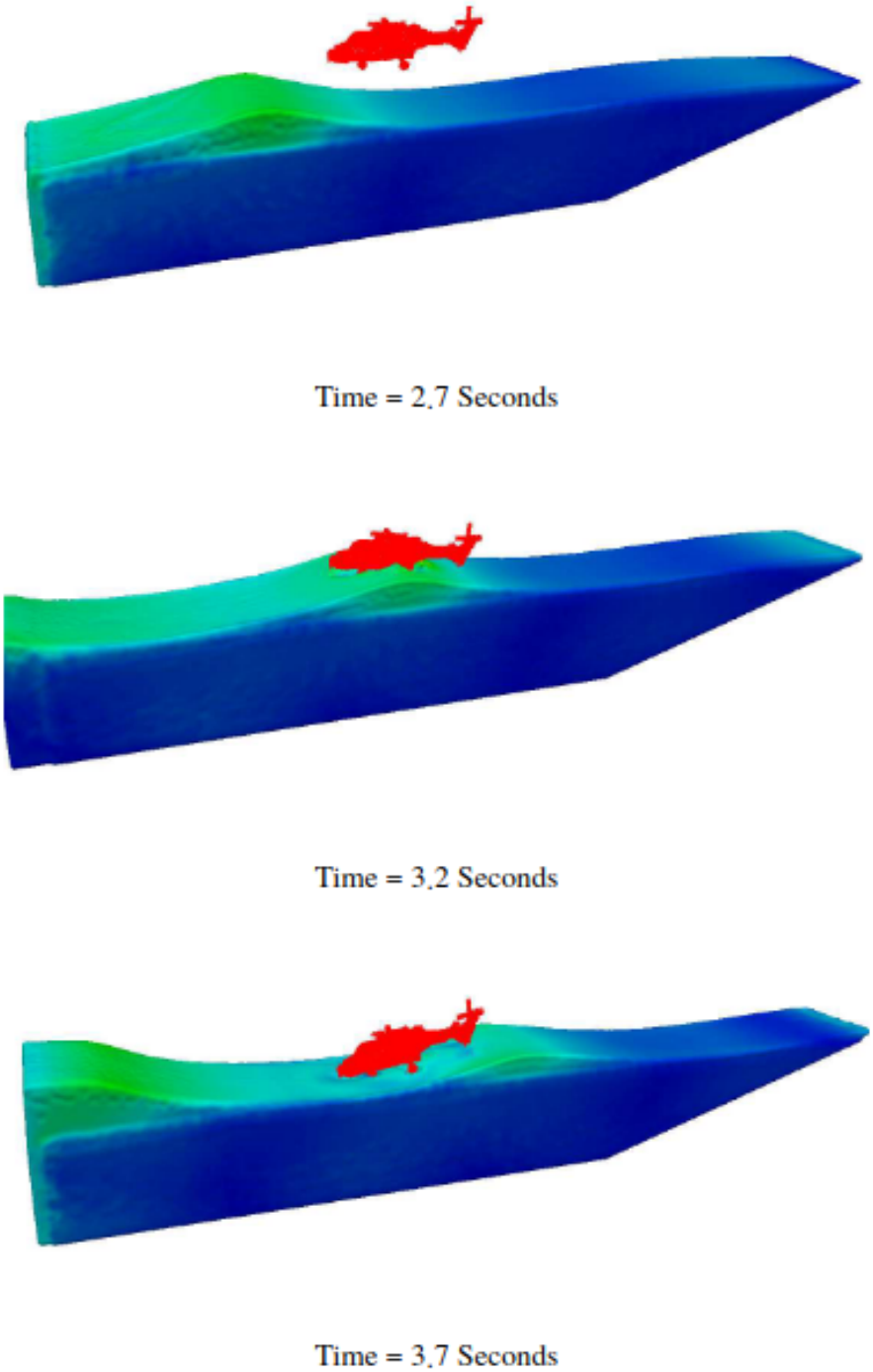

Fig. 1.28 SPH 3D simulation of a vertical ditching of a helicopter into sea surface at different time instants with the fuselage hitting the crest of the water wave (Woodgate et al. [144]).

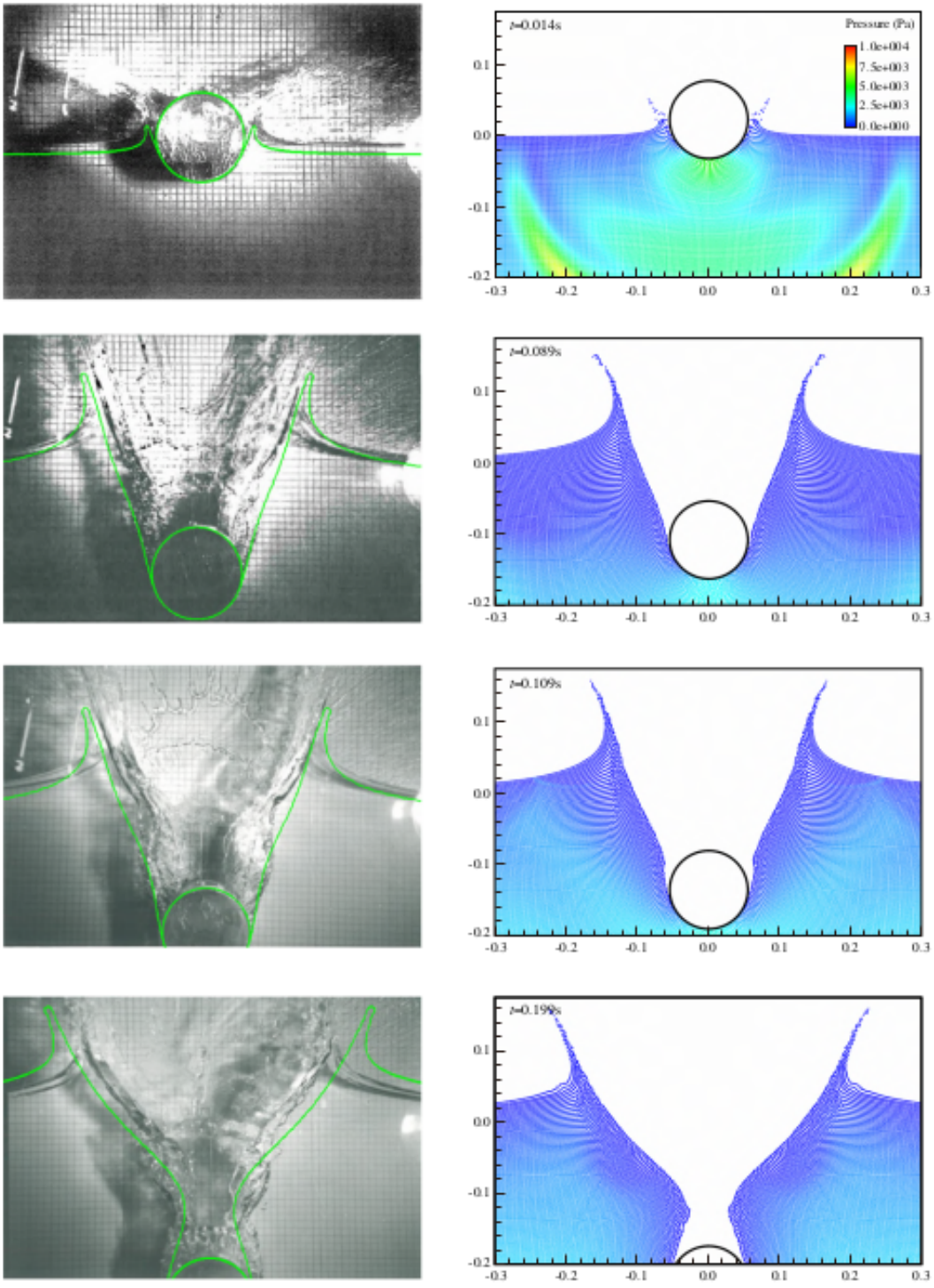

Fig. 1.29 Comparison between SPH simulation (right) and experimental results of the water entry of a cylindrical shell at different time instants. The snapshots are colored by the pressure field (Peng et al [145]).

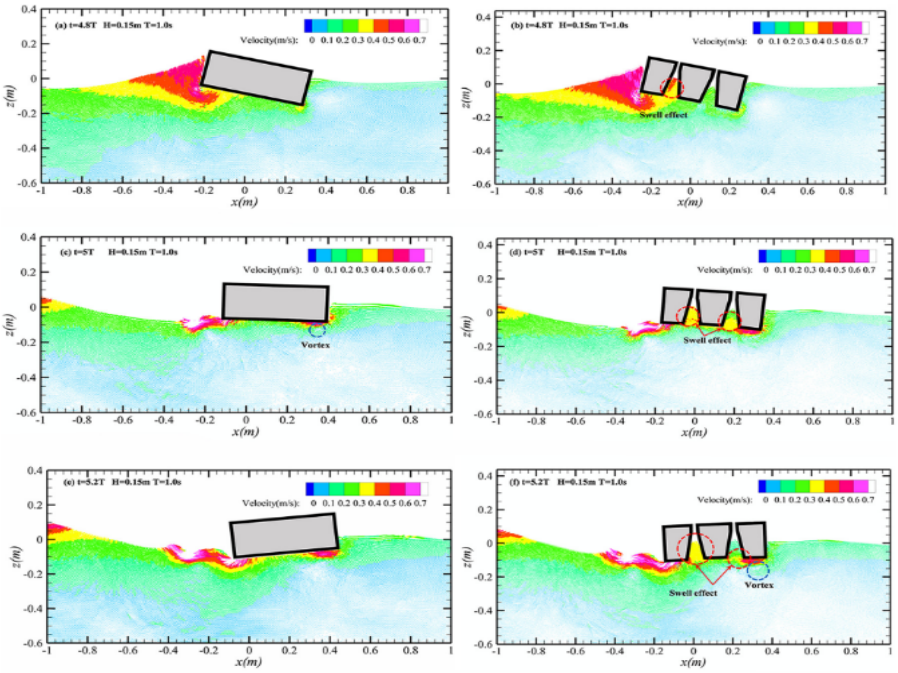

Fig. 1.30 SPH simulation of the interaction between floating breakwaters and water waves. The snapshots are colored by the velocity field (Cui et al. [146]).

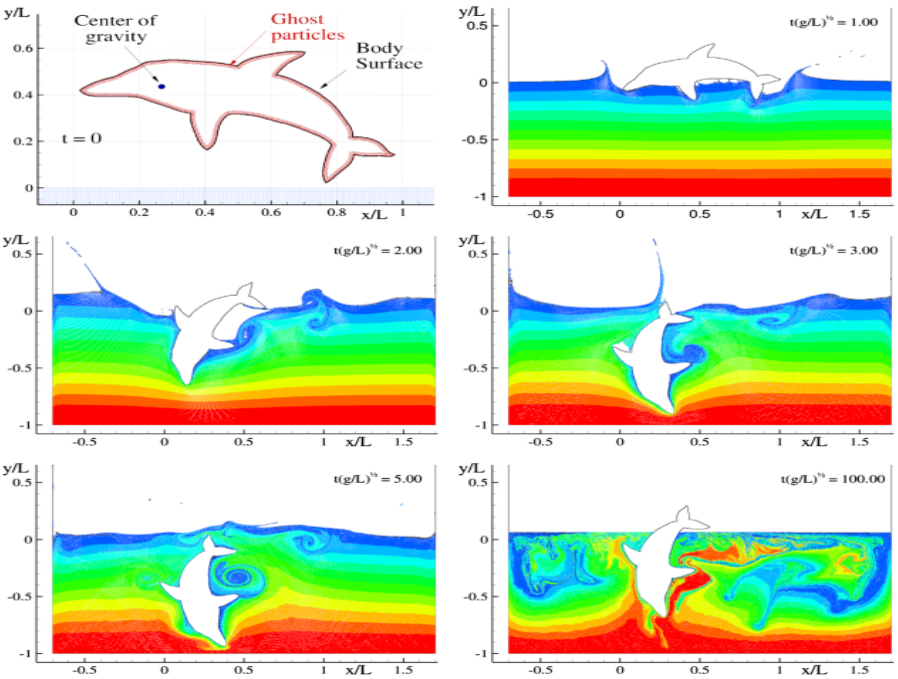

Fig. 1.31 SPH simulation of the hydrodynamic evolution of a complex floating body upon immersion within a reservoir of water. The snapshots are colored by the initial vertical position of particles (Bouscasse et al. [147]).

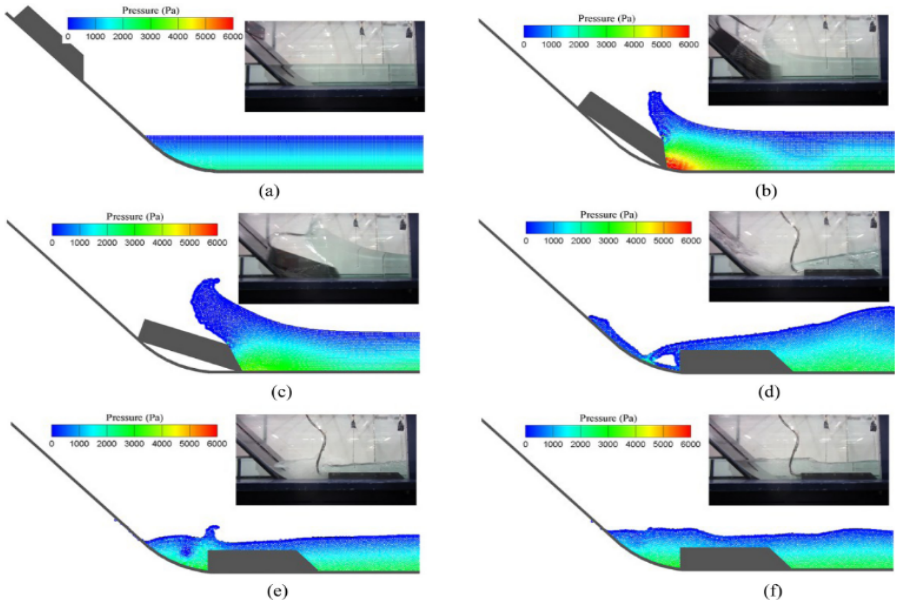

Fig. 1.32 Comparison between SPH simulation and experimental results of rigid subaerial landslide generated impulse water waves at different time instants. The snapshots are colored by the pressure field (Zhang et al. [148]).

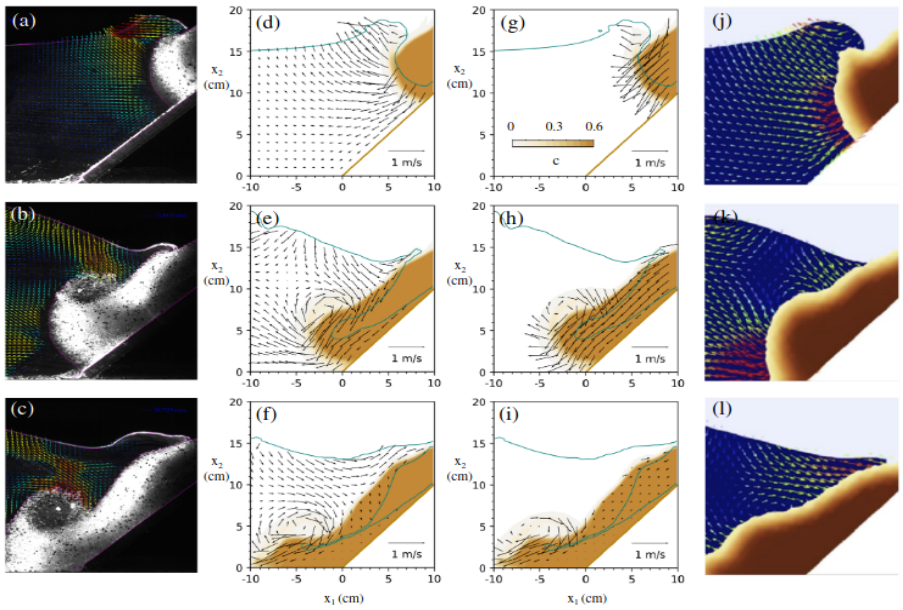

Fig. 1.33 SPH simulation of deformable subaerial landslide generated impulse water waves at different time instants. The snapshots shows the simulated velocity of the water flow and the deformation of the sand sliding along the slope (Lee et al. [16]).

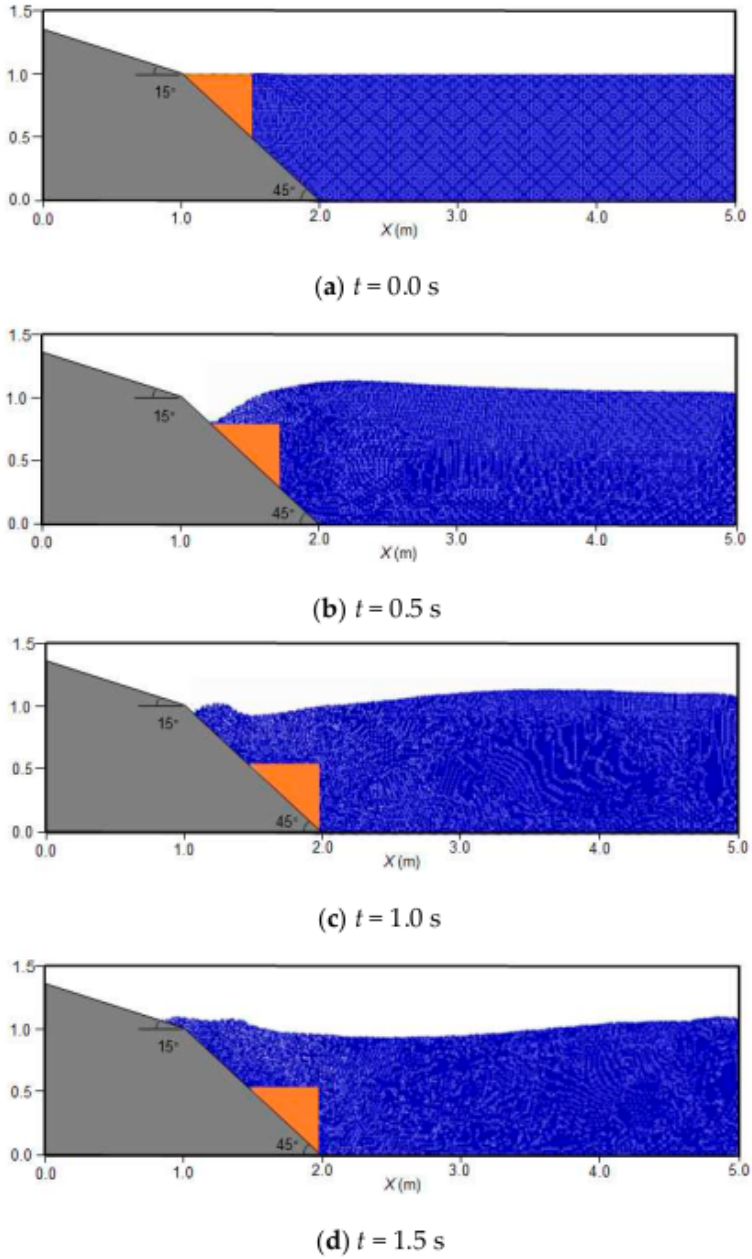

(a) $t = 0.0$ s

(b) $t = 0.5$ s

(c) $t = 1.0$ s

(d) $t = 1.5$ s

Fig. 1.34 SPH simulation of the hydrodynamic evolution of water free surface due to the motion of rigid submarine landslide at different time instants (Dai et al. [149]).

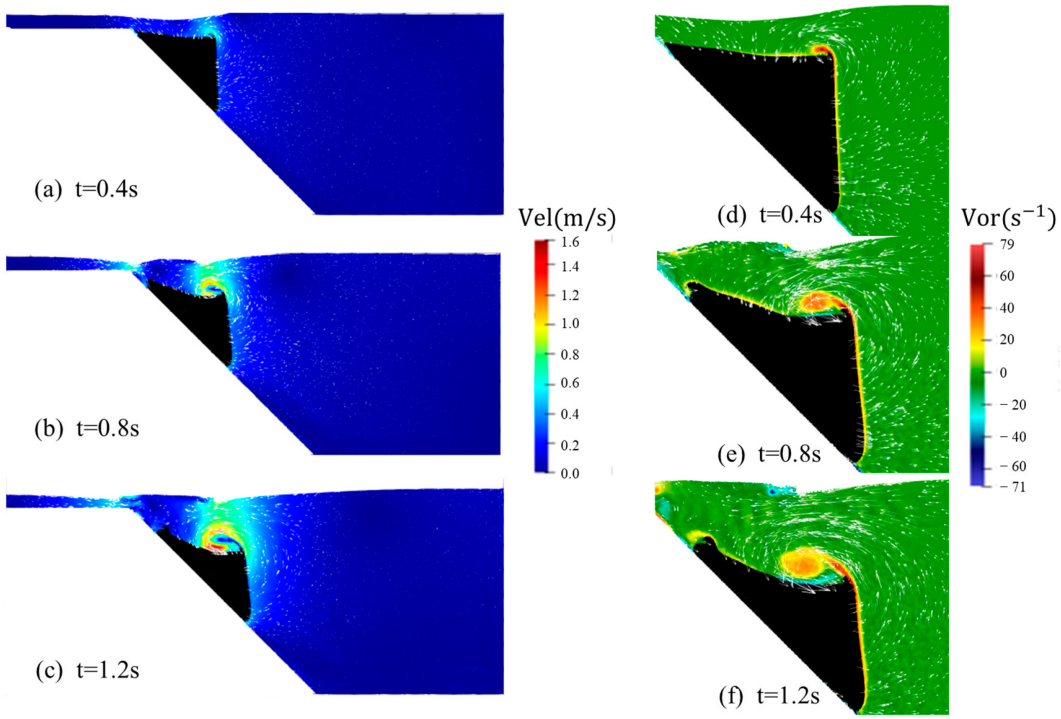

Fig. 1.35 SPH simulation of deformable submarine landslide generating impulse water waves at different time instants. The snapshots are colored by the velocity field (left) and the vorticity (right) (Shi et al. [150]).

In conclusion, this chapter has presented an overview of the state-of-the-art in modeling and simulating fluid-structure interaction (FSI) using the Smooth Particle Hydrodynamics (SPH) method. The chapter has highlighted the utility of SPH in simulating FSI problems, as it can effectively handle large deformations and complex geometries. The wide range of applications in which SPH can be applied, including simulating the interaction between fluids and granular materials. The advantages of using SPH for FSI problems, such as its ability to handle large deformations, ease of handling complex geometries, and ability to simulate problems with high dynamic range, have been outlined. However, it has also been noted that there are some challenges and limitations when using SPH for FSI problems, such as the need for a large number of particles and the quality of the interpolation kernel function. It has been acknowledged that the state-of-the-art in FSI using SPH is still developing and there are many opportunities for future research in this field. As the method continues to evolve and improve, it is expected that it will become an increasingly powerful tool for solving FSI problems in a wide range of applications. Overall, the SPH method is a promising approach for simulating FSI problems and continues to receive attention from researchers in various fields and industries.

Chapter 2

Numerical Techniques for Modeling with Smoothed Particle Hydrodynamics method

In this chapter, we will delve into the world of numerical techniques for modeling complex problems using Smooth Particle Hydrodynamics (SPH). SPH is a powerful method for simulating a wide range of problems, particularly those involving fluid-structure interaction (FSI). The method is known for its ability to handle large deformations and complex geometries easily, making it an attractive option for a variety of applications. However, to effectively use SPH for FSI, it is crucial to understand the numerical techniques and methods used to model these problems. We will explore the various numerical techniques used in SPH, including the governing equations and their discretized forms, the different multiphysics coupling strategies between fluids and structures, the use of interpolation smoothing kernels, the treatment of boundary conditions, the SPH accuracy and stability improving methods and time integration schemes.

2.1 Principle governing equations

Herein, we will focus on the application of the SPH method in the study of fluid-structure interactions. When the fluid and solid are in isothermal conditions, the evolution of the system can be fully described by the continuity, momentum conservation, and displacement equations. These equations are represented in the Lagrangian form and will be discussed in detail.

2.1.1 The continuity equation

The continuity equation is a fundamental equation in fluid dynamics that describes the conservation of mass in a fluid system. It states that the rate of change of mass in a fixed volume is equal to the rate of flow of mass into and out of that volume. Mathematically, it is represented as:

$$\frac{\mathrm{d}\rho}{\mathrm{d}t} = -\rho \nabla \cdot v \tag{2.1}$$

Where ρ is the density, t is time, ∇ is the gradient operator, and v is the velocity vector. The left-hand side of the equation represents the rate of change of mass within the volume, while the right-hand side represents the net rate of mass flow into and out of the volume. This equation is known as a continuity equation, since it expresses the conservation of mass over time [151–153].

2.1.2 The momentum conservation equation

The momentum conservation equation, also known as the Navier-Stokes equation, describes how the momentum of a fluid changes over time. It is a fundamental equation in fluid dynamics and is used to predict the motion of fluids, such as liquids and gases [154, 155]. The equation is typically written in the form:

$$\frac{\mathrm{d}v}{\mathrm{d}t} = \frac{1}{\rho}\nabla \cdot \sigma + f \tag{2.2}$$

where ρ is the density of the fluid, v is the velocity vector, fluid forces $f = F^s + F^b$ with F^s and F^b represent surface force vector and volumetric body force vector respectively, and σ is the stress tensor. This equation forms the basis for simulating fluid dynamics using the SPH method.

The Cauchy stress tensor σ is a measure of the internal forces within the fluid and includes both the pressure forces and the viscous forces. The pressure forces are isotropic and depend only on the pressure, while the viscous forces are anisotropic and depend on the gradient of velocity.

The viscous forces are modeled by the constitutive law, such as the Newton's law of viscosity, which relates the shear stress to the velocity gradient. The constitutive law is written as

$$\sigma = -pI + \tau \tag{2.3}$$

where τ is the deviatoric part of the Cauchy stress tensor. For the flow of a Newtonian fluid, it is essential to consider the stress tensor, which exhibits a direct proportionality to the rate of strain tensor, characterized by the constant coefficient known as dynamic viscosity (μ) [156, 157]. Consequently, the viscous stress tensor (often referred to as the deviatoric tensor) for Newtonian fluid flow can be mathematically represented in term of the strain tensor as

$$\tau = \mu\, D \tag{2.4}$$

Here, D stands for the rate of strain tensor, defined as $D = \nabla v + (\nabla v)^T$, where ∇v denotes the velocity gradient tensor. μ is the dynamic viscosity of the fluid. This leads to

$$\sigma = -pI + \mu(\nabla v + (\nabla v)^T) \tag{2.5}$$

where p is the pressure, I is the identity tensor, and the superscript T represents the tensor transpose operation. For an incompressible Newtonian fluid, as $\nabla \cdot v = 0$, the divergence of the viscous stress tensor $\nabla \cdot \tau$ simplifies to:

$$\tau = \mu \nabla^2 v \tag{2.6}$$

By including this constitutive law into the momentum conservation equation, the second Navier-Stokes equation can be rewritten as:

$$\frac{\mathrm{d}v}{\mathrm{d}t} = -\frac{\nabla p}{\rho} + \frac{\nabla \cdot \tau}{\rho} + f \tag{2.7}$$

This equation describes the motion of a fluid and the forces $f = F^s + F^b$ acting upon it, including the effects of viscosity and pressure.

In the context of SPH method, the use of constitutive laws, which describe the relationship between stress and strain in a material, is important in simulations to accurately model the behavior of both fluid and solid materials.

2.1.3 Pressure determination in SPH method

Pressure determination is an essential aspect in various fields, including computational fluid dynamics, engineering, and physics. In the context of Smoothed Particle Hydrodynamics (SPH) simulations, pressure determination is crucial for accurately modeling fluid behavior. There are several methods for determining pressure in SPH simulations, including Weakly Compressible SPH (WCSPH), Incompressible SPH (ISPH), Explicit Incompressible SPH

(EISPH), and others. In this section, we will discuss in detail the various methods of pressure determination in SPH simulations, including their mathematical formulations, algorithms, and applications.

Incompressible SPH approach

The technique so-called Incompressible SPH (ISPH) is an SPH method that is used for pressure determination in fluid simulations where the fluid is considered incompressible. Unlike WCSPH, ISPH does not make use of an equation of state to determine pressure, but rather solves for the pressure directly from the Navier-Stokes equations. This approach involves solving Poisson's equation through the utilization of the projection method. This method was initially formulated within the framework of grid-based techniques by Chorin [158, 159] and later adapted by Cummins and Rudman [160] to address incompressible Smoothed Particle Hydrodynamics flow problems. In the ISPH method, the continuity equation is streamlined to yield a divergence-free velocity field, considering the constant nature of density. This can be expressed as:

$$\nabla \cdot v = 0 \tag{2.8}$$

In the context of the ISPH method, a variant known as the ISPH divergence-free velocity field (ISPH_DF method) is often used [161]. In this method, the density and mass of particles remain constant, and their positions, denoted as r_i^n, are advected to intermediate positions r_i^* using the following equation:

$$r_i^* = r_i^n + \delta t \; v_i^n \tag{2.9}$$

At these intermediate positions r_i^*, an intermediate velocity v_i^* is calculated based on various forces governing the movement of particle i at time n, except for pressure-related forces:

$$v_i^* = v_i^n + \delta t \left(\frac{\nabla \cdot \tau}{\rho} + F^s + F^b \right) \tag{2.10}$$

Pressure at time $n+1$ is determined by solving a pressure Poisson equation (PPE) given by:

$$\nabla \cdot \left(\frac{1}{\rho} \nabla p^{n+1} \right)_i = \frac{1}{\delta t} \nabla \cdot v_i^* \tag{2.11}$$

The final velocity v_i^{n+1} at the time step $n+1$ results from the projection of v_i^* as follows:

$$v_i^{n+1} = v_i^* - \frac{\delta t}{\rho} \nabla p_i^{n+1} \tag{2.12}$$

The particle positions at the final time step are then calculated using:

$$r_i^{n+1} = r_i^n + \delta t \left(\frac{v_i^{n+1} + v_i^n}{2} \right) \tag{2.13}$$

The ISPH_DF method is known for providing accurate and smooth pressure fields but can lead to particle arrangement instabilities [162]. To address this issue, particle shifting algorithms, as proposed by Xu et al. [163] and improved by Lind et al. [162], or the one proposed by Fatehi and Manzari [164], can be employed.

To enhance the accuracy and stability of the ISPH_DF method, two alternative methods have been developed. The first method, known as ISPH_DI (Incompressible Smoothed Particle Hydrodynamics based on keeping density invariance) [165], is similar to ISPH_DF in most steps, except for the solving of the Poisson equation. In ISPH_DI, the right-hand side of the Pressure Poisson Equation is expressed in terms of relative density difference, rather than the velocity divergence as in ISPH_DF, resulting in a Pressure Poisson Equation given by:

$$\nabla \cdot \left(\frac{1}{\rho^*} \nabla p^{n+1} \right)_i = \frac{\rho_0 - \rho^*}{\rho_0 \delta t^2} \tag{2.14}$$

Here, ρ^* represents the intermediate particle density approximated through the continuity equation.

According to Xu et al. [163], the ISPH_DI scheme offers more stable simulations than ISPH_DF but may suffer from reduced accuracy. To combine the advantages of both ISPH_DF and ISPH_DI, Hu and Adams [166] proposed a combined scheme known as ISPH_DFDI. This scheme requires solving two pressure Poisson equations, leading to higher computational costs.

In ISPH, the fluid is considered truly incompressible, meaning that the density of the fluid is constant and the pressure is only used to balance the forces acting on the fluid. This approach results in more accurate simulations of incompressible fluids compared to the use of an equation of state as in WCSPH. However, it is computationally more expensive as the pressure must be computed directly from the Navier-Stokes equations.

Weakly Compressible SPH approach

In the context of pressure determination using Weakly Compressible SPH (WCSPH), the pressure is calculated using an explicit equation of state (EOS) based on the density of fluid particles and the reference speed of sound, c_0 [10]. The reference pressure, p_r, is calculated as follows:

$$p_r = \frac{\rho_0 c_0^2}{\gamma} \tag{2.15}$$

where ρ_0 is the reference density and γ is the ratio of specific heats. The pressure, p, is then calculated using the equation of state called also MacDonald equation as[167]:

$$p = p_r \left\{ \left(\frac{\rho}{\rho_0} \right)^{\gamma} - 1 \right\} + p_b \tag{2.16}$$

In this equation, ρ is the current density of fluid particles and p_b is the atmospheric pressure. This method is suitable for fluid simulations where the fluid density changes slightly and the speed of sound remains constant.

For instance, the reference speed of sound, c_0, in fluid flow simulations can be calculated based on the reference velocity U_0, reference length L_0, and effective dynamic viscosity μ_{eff} [168, 169]. It is typically determined based on the density variations relative to the initial density, set at 1% ($\delta\rho = 0.01$) [170]. The equation can be written as follows:

$$c_0^2 \approx \max \left\{ \frac{U_0^2}{\delta\rho}, \frac{\|g\| L_0}{\delta\rho}, \frac{\mu_{eff} U_0}{\rho_0 L_0 \delta\rho} \right\} \tag{2.17}$$

where ρ is the current density. The reference velocity, length, and viscosity can be set based on the specific requirements of the simulation and the properties of the fluid being modeled.

In the context of simulating solid deformation, it is customary to utilize the linear equation of state (Equation (2.16)) with $\gamma = 1$. The artificial speed of sound is typically computed using the following equation [171–173]:

$$c_0^2 \approx \frac{K}{\rho_0} \tag{2.18}$$

Here, K represents the bulk modulus which is a material property that characterizes its response to uniform compression. It measures the material's resistance to changes in volume when subjected to an external pressure. For solids, a higher bulk modulus indicates greater stiffness and less compressibility.

In numerical scenarios involving single-phase free surface fluid flows and solid dynamics, it is a common practice to set the background pressure to zero ($p_b = 0$). Moreover, in simulations of single or multiphase confined fluid flows, the pressure is selected to be a positive value that ensures the positivity of the calculated pressure field according to the equation of state, thus preventing tensile instability [174]. Various formulations for the background pressure have been employed in the literature. For instance, Marrone et al. [174] use $p_b = 3\rho_0 U_0^2$ for confined single fluid flow, while Krimi et al. [21] use $p_b \propto 0.05 p_r$ for simulating confined multiphase flow. To enhance the numerical stability of multiphase fluid flow simulations, Colagrossi and Landrini [175] recommend employing a common reference pressure for all fluid phases.

Explicit Incompressible SPH approach

The Explicit Incompressible SPH (EISPH) method is a variation of the Incompressible SPH (ISPH) method used for pressure determination in fluid simulations where the fluid is considered incompressible. Unlike the traditional ISPH method, EISPH uses an explicit time integration scheme to update the pressure field, rather than a pressure-correction method. The reader is advised to refer to [176–180] for more details. Thus, in the EISPH method, the pressure is updated explicitly using the following equation:

$$p^{n+1} = p^n - \frac{\rho}{\Delta t}(d - d_0) \cdot v^{n+1} \tag{2.19}$$

where n is the iteration number, Δt is the time step, d is the SPH smoothing length, d_0 is the initial smoothing length, and v^{n+1} is the updated velocity field.

In the EISPH method, the fluid is considered truly incompressible, meaning that the density of the fluid is constant and the pressure is only used to balance the forces acting on the fluid. This approach results in more accurate simulations of incompressible fluids compared to the use of an equation of state, such as in WCSPH. The EISPH method is computationally efficient compared to traditional ISPH, as it does not require the solution of a Poisson equation.

2.1.4 Stress determination and rheological models for describing constitutive laws

Rheological models are mathematical descriptions of the deformation and flow of materials. They are used to model the behavior of a wide range of materials, including liquids, gases, and solids. In the context of the momentum equation in the Lagrangian form, rheological

models are used to describe the constitutive laws that govern the deformation of a material. These laws describe how the material deforms in response to an applied stress or force.

There are many different types of rheological models, each of which is suited to a specific class of materials. In particular, they are used to describe constitutive laws for both Newtonian and non-Newtonian fluids.

A Newtonian fluid is a fluid whose viscosity is constant and independent of the applied stress. The constitutive equation for a Newtonian fluid is given by the equation 3.7. This equation states that the ratio of stress to strain rate is constant and independent of the magnitude of the stress, which is the defining characteristic of a Newtonian fluid [156, 157, 181].

On the other hand, a non-Newtonian fluid is a fluid whose viscosity changes depending on the applied stress. There are several different types of rheological models that can be used to describe the behavior of non-Newtonian fluids, including power-law, Bingham plastic, Casson, and Herschel-Bulkley models [172, 176, 182].

Bingham plastic model

The Bingham plastic model, also known as the viscoplastic model and discussed in [183] and [184], stands out as one of the simplest and most frequently employed representations within the category of viscous time-dependent fluids. Within this model, materials exhibit a unique behavior: they behave as a Newtonian fluid only when the applied stress surpasses a specified yield stress limit (τ_y); otherwise, they act as rigid bodies. The Bingham plastic model is given by the equation:

$$\begin{cases} \tau = \left\{ \frac{\tau_y}{\|D\|_F} + \mu \right\} D & \|\tau\|_F \geq \tau_y \\ D = 0 & \|\tau\|_F < \tau_y \end{cases} \tag{2.20}$$

where τ_y is the yield stress and μ is the plastic viscosity.The symbol $\|.\|_F$ denotes the Frobenius norm, as detailed in equations (3.9) and (3.10). Equation (3.8) introduces the yield criterion for soil materials, utilizing the Von Mises criterion [185]. The expression in equation (3.8) can be reformulated into a continuous form to mitigate the numerical challenges associated with its discontinuous representation. For instance, the exponential model [186] and the Bercovier and Engelman (BE) model [187] are often employed for this purpose.

This model is often used to describe fluids that exhibit a yield stress, such as toothpaste or drilling mud.

$$\|D\|_F = \left(\frac{1}{2}D : D\right)^{\frac{1}{2}} \tag{2.21}$$

$$\|\tau\|_F = \left(\frac{1}{2}\tau : \tau\right)^{\frac{1}{2}} \tag{2.22}$$

Casson model

The Casson equation is a rheological model that is often used to describe the behavior of non-Newtonian fluids, specifically those that exhibit yield stress [188, 189]. The equation is given by:

$$\begin{cases} \tau^{\frac{1}{2}} = \left\{ \dfrac{\tau_{y_c}^{\frac{1}{2}}}{\|D\|_F^{\frac{1}{2}}} + \mu_c^{\frac{1}{2}} \right\} D^{\frac{1}{2}} & \|\tau\|_F \geq \tau_{y_c} \\ D = 0 & \|\tau\|_F < \tau_{y_c} \end{cases} \tag{2.23}$$

where τ is the stress, D is the strain rate, τ_y is the yield stress, and μ is the plastic viscosity.

The Casson model is often used to describe the flow behavior of certain types of non-Newtonian fluids, especially those that exhibit both yield stress and shear-thinning properties. One of the typical applications of the Casson model is in describing the flow behavior of blood [190].

Herschel-Bulkley model

The Herschel-Bulkley model [191] is given by the equation:

$$\tau = \tau_y + kD^n \tag{2.24}$$

where τ_y is the yield stress, k is the consistency index, and n is the flow behavior index. This model is often used to describe fluids that exhibit both a yield stress and shear-thinning behavior, such as some types of food products [192].

It is important to note that there are many other models out there, like the Power Law Model, the Cross Model, the Carreau Model, the Power-law+Yield stress Model, the Cross-power Law Model, etc [193–195] . each of these models have their own specific characteristics, advantages and disadvantages. The selection of a specific model depends on the specific properties of the fluid being studied and the type of deformation it is undergoing.

In general, it is important to note that these rheological models are based on empirical data and may not always accurately predict the behavior of a fluid in all situations. Additionally, it is important to keep in mind that these models are only valid for certain ranges of deformation, and their predictions may become less accurate outside of these ranges.

Time-dependent fluids exhibit a hysteresis loop that is contingent upon the rate of shear stress application. In this category, two models, the pseudoplastic time-dependent fluid (thixotropic) [196] and the dilatant time-dependent fluid (rheopectic), are noteworthy. Thixotropic fluids include examples like waxy crude oil [197], while rheopectic fluids are exemplified by Bentonite clay suspensions [198].

Viscoelastic fluids [199], as the name implies, possess a combination of both viscous and elastic properties. Examples of viscoelastic fluids include egg whites and polymer melts [200].

2.1.5 The displacement equation

In the context of smoothed particle hydrodynamics (SPH), the displacement equation is a mathematical representation of the movement of fluid or solid particles in a computational domain over time [201, 152, 153]. The equation can be expressed as follows:

$$\frac{\mathrm{d}r}{\mathrm{d}t} = v \tag{2.25}$$

Where $\frac{\mathrm{d}r}{\mathrm{d}t}$ is the derivative of the position vector, r, with respect to time, t, and v is the velocity vector of the particle.

In SPH, the fluid or solid is represented by a set of discrete particles, and the motion of each particle is described by its position and velocity. The displacement equation is used to calculate the change in position of a particle over time, based on its velocity.

The displacement equation is an important component of SPH simulations, as it provides the information necessary to update the position of each particle and maintain a continuous representation of the fluid or solid. It is also a key factor in ensuring the accuracy and stability of the simulation, as the calculation of the displacement must take into account the various physical and computational constraints that are present in the system.

In this study, a weakly compressible SPH approach is adopted since it is well suited to water-granular material interaction scenarios involving significant deformations and multi-phase flows including different densities and viscosities [202]. With this fully explicit method, including an equation of state, the governing equations can be summarized as follows:

$$\begin{cases} \frac{d\rho}{dt} = -\rho \nabla . v \\ \frac{dv}{dt} = \frac{-\nabla p}{\rho} + \frac{\nabla . \tau}{\rho} + g \\ \frac{dr}{dt} = v \\ p = \rho_0 c_0^2 \left\{ \left(\frac{\rho}{\rho_0} \right) - 1 \right\} \end{cases} \tag{2.26}$$

2.2 Approximation of Governing Equations through SPH Discretization

In the SPH method, the discrete governing equations are approximated by evaluating the properties of the fluid or solid body at the locations of the particles. The particle properties are used to calculate the local values of physical quantities such as velocity, density, and pressure, which are then used to solve the governing equations. The aim of this section is to provide a detailed explanation of the process of approximating the governing equations in SPH, including the use of SPH discretization, and the mathematical equations involved.

2.2.1 Formulations for SPH continuity equation Approximation

In the SPH discrete form, the continuity equation can be approximated in different ways, each with its own advantages and disadvantages.Typically, the non-symmetric variant of the SPH first derivative is used to formulate the terms on the right-hand side of the continuity equation. The following are some of the most commonly used formulations for SPH continuity equation approximation. The standard SPH formulation is given as follows [92].

$$\frac{d\rho_i}{dt} = \rho_i \sum_j^{n_b} \frac{m_j}{\rho_i} (v_i - v_j) \cdot \nabla i W i j (r_i - r_j, h) \tag{2.27}$$

Where, nb is the number of particles j in the neighborhood of the particle i. This is the most commonly used formulation of the continuity equation in SPH, which is based on the density interpolation between particles. The gradient of the smoothing kernel is used to approximate the fluid velocity, and the mass of each particle is used to weight the contribution of each particle to the density change.

in the other hand, the volume-preserving SPH formulation stands as follows [92]:

$$\frac{d\rho_i}{dt} = \sum_j^{n_b} m_j (v_i - v_j) \cdot \nabla i W i j (r_i - r_j, h) \tag{2.28}$$

This formulation of the continuity equation is based on the volume-conserving property of the smoothing kernel. It is similar to the standard SPH formulation, but without the density of each particle in the calculation. This formulation is less accurate than the density-conserving SPH formulation, but it is computationally more efficient.

It exists another approaches to approximating the continuity equation in the SPH discrete form. For instance, some formulations involve modifying the smoothing length estimation. This approach is more complex and involves iteratively solving for the smoothing length to ensure that the continuity equation is satisfied.

The choice of which formulation to use will depend on the specific application and the desired properties of the simulation. For example, the volume-preserving SPH density estimation is often preferred for simulating incompressible flows, while the standard SPH density estimation is preferred for simulating compressible flows.

2.2.2 Formulations for SPH Density Approximation

In Smoothed Particle Hydrodynamics (SPH), the density of fluid particles is a crucial quantity that needs to be estimated in order to calculate various fluid properties such as pressure, velocity, and acceleration. There are several different formulations that can be used to approximate the density in SPH, each with its own strengths and weaknesses.

The standard density summation formulation is one of the simplest and most widely used methods for density approximation in SPH [203]. In this method, the density of particle i is directly approximated via the basic SPH interpolation applied on the density ρ at the particle i. This summation form is expressed as as follows:

$$\rho_i = \sum_{j=1}^{n_b} m_j W(r_i - r_j, h) \tag{2.29}$$

Where m_j is the mass of particle j, W_{ij} is a smoothing kernel function, and h_i is the smoothing length for particle i. The smoothing kernel function is used to interpolate the density of particle i based on the densities of its neighboring particles.

The density summation formulation (2.29) offers a distinct advantage over formulations (2.27) in that it precisely conserves mass [92]. An alternative version of the density summation formulation, as presented by Hu and Adams [203] (equation (2.30)), also conserves mass accurately, as in (2.29). Additionally, it allows for density discontinuities when particle i interacts with neighboring particles j exhibiting significant differences in particle mass. This property makes it well-suited for simulating multiphase fluid flows with substantial density variations.

$$\rho_i = m_i \sum_j^{n_b} W_{ij} \tag{2.30}$$

However, the density summation formulations (2.29) and (2.30) are less suitable for scenarios involving free surface flows. They struggle to reproduce a zero pressure at free surface particles. In contrast, using density divergence equation (2.28) naturally reproduces zero pressure at free surface particles. The formulation (2.29) is particularly recommended over equation (2.28) when dealing with multiphase fluid flows characterized by high density ratios (≥ 2) [204, 88]. This preference arises because in the summation on the right-hand side of equation (2.28), neighboring particle mass directly influences the calculation, whereas in the formulation (2.27), it is the volumes that have the primary impact. The choice of the appropriate formulation depends on the particular requirements of a simulation and the type of physical problem being modeled.

2.2.3 Pressure approximation

The pressure gradient is an important component in the simulation, as it drives the fluid motion. There are several formulations for calculating the pressure gradient in SPH simulations [92, 205, 206]. These formulations are based on different physical concepts and mathematical models, and each has its own advantages and disadvantages.

In the standard SPH formulation, the pressure gradient using this model is given in a discrete form by [92, 205, 206]:

$$-\frac{1}{\rho_i}\nabla p_i = -\sum_j^{n_b} m_j \left(\frac{p_i}{\rho_i^2} + \frac{p_j}{\rho_j^2}\right) \nabla W_{ij} \tag{2.31}$$

This equation calculates the pressure gradient of particle i based on the pressure of all its neighboring particles j and their contributions to the gradient of the smoothing kernel between particles i and j. The pressure force between particles i and j is proportional to the pressure difference between them, which is taken into account by the term $\left(\frac{p_i}{\rho_i^2} + \frac{p_j}{\rho_j^2}\right)$. The formulation is based on the ideal gas law, which states that the pressure of a gas is proportional to its density.

In addition to the standard SPH formulation given by Eq. (2.31), two other commonly used formulations are [92, 205, 206]:

The pressure balance formulation:

$$-\frac{1}{\rho_i}\nabla p_i = -\sum_j^{n_b} \frac{m_j}{\rho_i \rho_j}\left(p_i + p_j\right)\nabla W_{ij} \tag{2.32}$$

The pressure continuity formulation:

$$-\frac{1}{\rho_i}\nabla p_i = -\sum_j^{n_b} \frac{m_j}{\rho_i \rho_j}\left(p_j - p_i\right)\nabla W_{ij} \tag{2.33}$$

For multiphase fluid flow scenarios, Hu and Adams [203, 207] introduced a novel approach that approximates spatial derivatives using particle-averaged quantities. In this method, neighboring particles j of particle i contribute to the summation based on their specific volumes rather than their masses. This technique ensures exact mass conservation and naturally accommodates density discontinuities across phase interfaces. Consequently, the pressure gradient can be expressed as follows:

$$-\frac{1}{\rho_i}\nabla p_i = -\frac{1}{m_i}\sum_j^{n_b}\left(V_i^2 p_i + V_j^2 p_j\right)\nabla W_{ij} \tag{2.34}$$

This expression closely resembles the pressure gradient form favored by Monaghan [92]. Importantly, this formulation conserves linear momentum precisely because the exchange of particle positions i and j within the summation results in opposing pressure forces. Another formulation for the pressure gradient is as follows [208, 209]:

$$-\frac{1}{\rho_i}\nabla p_i = -\frac{1}{m_i}\sum_j^{n_b}\left(V_i^2 + V_j^2\right)\widetilde{p_{ij}}\nabla W_{ij} \tag{2.35}$$

Here, $\widetilde{p_{ij}}$ represents the density-weighted inter-particle averaged pressure and is defined as:

$$\widetilde{p_{ij}} = \frac{\rho_i p_j + \rho_j p_i}{\rho_i + \rho_j} \tag{2.36}$$

This form, $\widetilde{p_{ij}}$, ensures that $\frac{1}{\rho}\nabla p$ remains continuous even when a density discontinuity is present within the fluid field.

Each formulation has its own advantages and disadvantages and the choice of the appropriate formulation depends on the specific problem being simulated. For example, the standard SPH formulation is widely used for simulating ideal gases, while the pressure continuity formulation may be more suitable for simulating high-density liquids.

2.2.4 Cauchy stress tensor approximation

To ensure the conservation of momentum, one can choose from several symmetric expressions for calculating the divergence operator of the Cauchy stress tensor σ [92]:

$$\frac{1}{\rho_i}\nabla\cdot\sigma_i=\sum_j^{n_b}\left(m_j\left(\frac{\sigma_i}{\rho_i^2}+\frac{\sigma_j}{\rho_j^2}\right)\nabla W_{ij}\right) \tag{2.37}$$

In cases of significant density variation, Monaghan [167] recommends using another discrete symmetric form for Cauchy stress divergence [205]:

$$\frac{1}{\rho_i}\nabla\cdot\sigma_i=\sum_j^{n_b}\left(\frac{m_j}{\rho_i\rho_j}\left(\sigma_i+\sigma_j\right)\nabla W_{ij}\right) \tag{2.38}$$

Here, σ_i is expressed as $\sigma_i=-p_iI+\tau_i$.

An asymmetric expression for discretizing the divergence of the Cauchy stress tensor is used in some cases [210, 206]:

$$\frac{1}{\rho_i}\nabla\cdot\sigma_i=\sum_j^{n_b}\left(\frac{m_j}{\rho_i\rho_j}\left(\sigma_j-\sigma_i\right)\nabla W_{ij}\right) \tag{2.39}$$

Typically, these three formulations of the Cauchy stress tensor divergence $\nabla\cdot\sigma_i$ are used in solid mechanics to model elastic behavior, where the deviatoric part τ is determined by Hooke laws, as discussed in [211]. For fluid dynamics applications, the momentum equation form (2.7) is preferred, with pressure gradient and viscous tensor divergence τ being discretized differently [44].

2.2.5 Viscous stress tensor approximation

In SPH simulations, the calculation of the viscous stress tensor is an important component in modeling fluid flow and capturing the effects of viscosity on the fluid motion. There are several different formulations that can be used to calculate the viscous stress tensor, including:

Morris formulation which is based on the idea of representing the viscous stress tensor as the product of the viscosity and the velocity gradient tensor. The Morris formulation [112] is expressed as:

$$\frac{1}{\rho_i}\nabla\cdot\tau_i=\sum_j^{n_b}m_j\frac{(\mu_i+\mu_j)}{\rho_i\rho_j}\frac{r_{ij}\cdot\nabla W_{ij}}{r_{ij}^2}v_{ij} \tag{2.40}$$

where τ_i is the viscous stress tensor, μ is the viscosity, m_j is the mass of particle j, ρ_i and ρ_j are the densities of particles i and j, respectively, r_{ij} is the vector pointing from particle j to particle i, v_{ij} is the relative velocity between particles i and j, and W_{ij} is the smoothing kernel. The formulation given by Equation (2.40) precisely conserves linear momentum, although it approximately preserves angular momentum [212].

The artificial Viscosity Formulation which uses an artificial viscosity term to introduce the viscous effects in the simulation. The viscous stress tensor is calculated as:

$$\tau_i = \sum_j^{n_b} m_j \cdot \frac{\mu_{ij}}{\rho_{ij}} (v_{ij} \cdot r_{ij}) r_{ij} W_{ij} \tag{2.41}$$

where μ_{ij} is the artificial viscosity term calculated using a specific formula such as the Monaghan's artificial viscosity formula [213]. For instance, the approximation of the divergence of the viscous stress tensor has been derived from the artificial viscosity term used in the work of Monaghan and Gingold [213] by Violeau and Issa [96] as follows:

$$\frac{1}{\rho_i} \nabla \cdot \tau_i = \sum_j^{n_b} m_j \frac{8}{\rho_i + \rho_j} \left(\frac{\mu_i}{\rho_i} + \frac{\mu_j}{\rho_j} \right) \frac{r_{ij} \cdot v_{ij}}{r_{ij}^2 + \eta^2} \nabla W_{ij} \tag{2.42}$$

Another approach to calculating the divergence of the viscous stress tensor was introduced by Cleary in [214]. This formulation provides an alternative method for accurately determining the amount of viscous force in a fluid simulation.

$$\frac{1}{\rho_i} \nabla \cdot \tau_i = \sum_j^{n_b} m_j \frac{\xi}{\rho_i \rho_j} \frac{4 \mu_i \mu_j}{\mu_i + \mu_j} \frac{r_{ij} \cdot v_{ij}}{r_{ij}^2 + \eta^2} \nabla W_{ij} \tag{2.43}$$

The formulation developed by Cleary [214] offers a unique solution that combines elements from traditional finite difference methods with the smoothed particle hydrodynamics (SPH) framework, which has become widely adopted in fluid simulation.

In order to accurately approximate the viscous stress tensor divergence, a suitable value must be chosen for the parameter ξ. In a study by Basa et al [212], it was determined that the previously established value of $\xi = 4.96333$, which was calibrated through comparison to known solutions in a Couette flow, resulted in highly inaccurate velocity predictions for simulations of Poiseuille flow. Instead, the authors found that setting $\xi = 4.24$ produced much better results. Additionally, the parameter η^2 is usually set to a small value, such as $(0.1h)^2$, to avoid potential singularities (or division by zero) that could occur if two particles were to get too close to each other.

In the context of simulating multiphase flows, the expression for the divergence of the viscous tensor in the pressure approximation equation (2.34) is given by:

$$\frac{1}{\rho_i}\nabla\cdot\tau_i = \frac{1}{m_i}\sum_j^{n_b}\left(V_i^2+V_j^2\right)\widetilde{\mu_{ij}}\frac{v_{ij}}{r_{ij}}\frac{\partial W}{\partial r_{ij}} \tag{2.44}$$

Here, $\widetilde{\mu_{ij}}$ is the inter-particle-averaged shear viscosity:

$$\widetilde{\mu_{ij}} = \frac{2\mu_i\mu_j}{\mu_i+\mu_j} \tag{2.45}$$

This form of the viscous force conserves linear momentum. Angular momentum conservation can be achieved using other formulations, such as the one used by Hu and Adams [215] and extended for multiphase flow applications by Krimi et al [21]:

$$\frac{1}{\rho_i}\nabla\cdot\tau_i = \frac{\zeta}{m_i}\sum_j^{n_b}\left(V_i^2+V_j^2\right)\widetilde{\mu_{ij}}\frac{v_{ij}\cdot r_{ij}}{r_{ij}^2}\nabla W_{ij} \tag{2.46}$$

Here, $\zeta = n+2$, where n is the space dimension number.

It's important to note that the volume is calculated as $V_i = \frac{m_i}{\rho_i}$, with mass m_i held constant during the simulation, and density ρ_i computed using the summation formulation (2.30).

Various SPH discretization principles for multiphase flow can be found in the literature. For example, Grenier et al [216] derived governing equations using a Lagrangian variational principle, leading to a Hamiltonian system of particles, which is suitable for modeling flows with interfaces and free surfaces. Detailed formulations can be found in [216–219].

When modeling non-Newtonian fluids using the Generalized Newtonian Fluids (GNL) technique [183, 220], alternative formulations for the divergence of the viscous stress tensor (deviatoric tensor 2.47) are commonly used in the literature [221, 222]. Krimi et al [21] extended this formulation for use in the context of non-Newtonian multiphase fluids and fluid-like mass frameworks 2.48:

$$\frac{1}{\rho_i}\nabla\cdot\tau_i = \sum_j^{n_b}\frac{m_j}{\rho_j}\frac{\mu_i+\mu_j}{r_{ij}^2+\eta^2}\left(v_{ij}\left(r_{ij}\cdot\nabla W_{ij}\right)+r_{ij}\left(v_{ij}\cdot\nabla W_{ij}\right)\right) \tag{2.47}$$

$$\frac{1}{\rho_i}\nabla\cdot\tau_i = \frac{1}{m_i}\sum_j^{n_b}\left\{\frac{V_i^2+V_j^2}{r_{ij}^2}\right\}\frac{\rho_i\mu_j+\rho_j\mu_i}{\rho_i+\rho_j}\left\{v_{ij}\left(r_{ij}\cdot\nabla W_{ij}\right)+r_{ij}\left(v_{ij}\cdot\nabla W_{ij}\right)\right\} \tag{2.48}$$

Each of these formulations has its own advantages and disadvantages, and the choice of the appropriate formulation depends on the specific problem being simulated and the desired level of accuracy. The main criteria is to find a formulation that accurately captures the continuum behavior and reduces computational errors.

2.3 Recent advancements in the SPH method

The conventional SPH method has been widely used for simulation of various physical phenomena, however, there are several limitations and challenges that need to be addressed to improve its accuracy and efficiency . Some of the key challenges faced by the traditional SPH method are the following:

- One of the major limitations of the traditional SPH method is the conservation of volume [223]. The particle distribution in SPH method may lead to some irregular shapes and variations in the particle density, which can result in inaccuracies in the calculation of physical properties.
- Another major challenge of the SPH method is its numerical instability, especially in cases involving high velocity gradients, complex geometries, and high particle concentrations [168, 224]. This can lead to oscillations, convergence problems, and divergence of the simulation.
- Regarding the lack of accuracy in certain applications [117, 225], the SPH method may not provide accurate results in certain applications, such as in simulating sharp interfaces, high Reynolds number flows, or multi-phase flows with strong inter-particle interactions.

To overcome these challenges and limitations, several advancements have been proposed and developed in recent years , including improved particle distributions, new formulations for gradient approximation, and adaptive time stepping methods. The enhancement of the accuracy, stability, and consistency of the SPH method can be approached through two fundamental avenues [55]: Firstly, by refining the approximation of the kernel function and its derivatives, and secondly, by reestablishing the SPH particle representation of the governing equations. These advancements aim to improve the accuracy and stability of the SPH method in various applications.

2.3.1 Shepard Correction

The Shepard correction formulation [226] in the SPH method involves approximating a continuous function, $f(r_i)$, at the i^{th} particle position, r_i, using a weighted sum of values from neighboring particles j in the set n_b, also called Shepard filter:

$$f(r_i) \approx \sum_{j}^{n_b} f(r_j) W_{ij}^{S} V_j \tag{2.49}$$

Where V_j is the volume of particle j, and the Shepard kernel, W_{ij}^S, is given by:

$$W_{ij}^S = \frac{W_{ij}}{\sum_j^{n_b} W_{ij}^S V_j} \tag{2.50}$$

The Shepard kernel, W_{ij}^S, is a normalization of the standard SPH kernel, W_{ij}, that ensures the sum of the weighted values over all neighboring particles is equal to the value of $f(r_i)$ at that particle's position. The Shepard correction allows for improved smoothing of the particle distribution, reducing the noise present in the traditional SPH method [227, 106, 228, 21].

2.3.2 The Damping Method for Reducing Oscillations in SPH Simulations.

The smoothed particle hydrodynamics (SPH) method can sometimes produce high-frequency oscillations due to artificial sound waves in the simulation domain, which can be a result of the imposition of initial conditions. To address this issue, Monaghan et al. proposed a damping technique that can be applied during a predefined time period to reduce such artifacts. The technique involves smoothing the particle distribution and accelerating particles.

The duration of the damping period is defined by the damping time T_D [229]. During this time, the acceleration due to the body force is mitigated by the damping factor $\xi_D(t)$, which is defined as[209]:

$$\xi_D(t) = \begin{cases} \left(\sin\left(\frac{t}{T_D} - 0.5\right)\pi + 1\right) & t \leqslant T_D \\ 1 & t > T_D \end{cases} \tag{2.51}$$

According to this equation, the damping factor starts at zero, increases to a maximum of 2 during the first half of the damping time period, and then decreases back to zero during the second half. The damping factor remains equal to 1 once the damping time period has ended. This approach allows for a smooth transition from the damping period to the normal simulation, which reduces the impact of the damping on the overall results.

2.3.3 Enhancement of the Gradient Calculation in the Kernel Function

In SPH, a smoothed approximation of a physical field is obtained by interpolating the field values of a set of particles. The smoothed field value at a particle position, r_i, is estimated by considering the contribution of all other neighboring particles within a smoothing length, h. The smoothing kernel, W_{ij}, is a weighting function that determines the contribution of

each neighboring particle to the field value at r_i. The gradient of the smoothed field is then estimated using the gradient of the kernel function, ∇W_{ij}. However, the standard gradient estimate using ∇W_{ij} can result in unphysical behavior, such as artificial over-diffusion or undershoot of gradients, due to the discrete and non-uniform distribution of particles. To address this issue, Monaghan [230] introduced the concept of gradient correction, where the gradient of the kernel function is multiplied by a correction term, $L(r_i)$, to improve the gradient estimate.

The correction term is a function of the particle position and is designed to correct for the non-uniform distribution of particles. The equation for the gradient correction of the kernel function is given by:

$$\nabla W_{ij}^{C} = L(r_i)\ \nabla \cdot W_{ij} \tag{2.52}$$

where ∇W_{ij}^{C} is the corrected gradient of the kernel function and $L(r_i)$ is the correction term. The specific form of the correction term can vary depending on the choice of kernel function and the desired level of accuracy.

2.3.4 Enhancement of the Laplacian operator in the Kernel Function

The Laplacian approximation in Smoothed Particle Hydrodynamics is only of zero-order consistency. While attempting to improve its consistency through correction of the kernel function is challenging, a more consistent method was proposed by Schwaiger in [231] that provides an approximation of second-order consistency. Fatehi and Manzari [232] later presented an even more improved formulation that guarantees a second-order consistency, albeit with the cost of a more complex computation. This formulation, as expressed by Equation (2.53), involves the calculation of a fourth-order tensor, B_i, which is dependent on the first-order consistent gradient formulation given by Equation (2.54).

$$\nabla \cdot \nabla f(r_i) \approx B_i : [2 \sum_{j}^{n_b} V_j r_{ij} \otimes \nabla W_{ij} \left(\frac{f_{ij}}{r_{ij}^2} - \frac{r_{ij}}{r_{ij}^2} \cdot \nabla f(r_i) \right) .] \tag{2.53}$$

With $\nabla f(r_i)$ is the first order consistent gradient formulation given through the equation (2.52), and $B_i = B(r_i)$ is a fourth-order symmetric that can be determined from the following equation:

$$B_i : \left\{ \sum_j^{n_b} V_j \frac{r_{ij}}{r_{ij}^2} \otimes r_{ij} \otimes r_{ij} \otimes \nabla W_{ij} + \left(\sum_j^{n_b} \frac{V_j}{r_{ij}^2} r_{ij} \otimes r_{ij} \otimes \nabla W_{ij} \right) \cdot L_i \cdot \left(\sum_j^{n_b} V_j r_{ij} \otimes r_{ij} \otimes \nabla W_{ij} \right) \right\} = -I \tag{2.54}$$

2.3.5 SPH enhancing by particle approximation in governing equations

Artificial viscosity terms

The implementation of artificial viscosity in the context of Smoothed Particle Hydrodynamics (SPH) is a crucial step in achieving stability in numerical simulations. The SPH method is a popular approach in the field of computational fluid dynamics, where the fluid is represented by a large number of particles, each with its own physical properties. However, this method can be prone to numerical instabilities when dealing with high-speed flow and strong shockwaves. To tackle this issue, an additional term, referred to as the artificial viscosity, was introduced to the SPH momentum equation.

The artificial viscosity term was first proposed by Lucy [85] and later improved by Monaghan and Gingold [233], who emphasized the importance of linear and angular momentum conservation in numerical simulations. The viscous term, denoted by Π_{ij}, is added to the pressure terms in the SPH momentum equation, which can be written as:

$$\frac{\mathrm{d}v_i}{\mathrm{d}t} = -\sum_j^{n_b} m_j \left(\frac{p_i}{\rho_i^2} + \frac{p_j}{\rho_j^2} + \Pi_{ij} \right) \nabla W_{ij} \tag{2.55}$$

Alternatively, it can also be added to the stress terms and it can be written as:

$$\frac{\mathrm{d}v_i}{\mathrm{d}t} = \sum_j^{n_b} m_j \left(\frac{\sigma_i}{\rho_i^2} + \frac{\sigma_j}{\rho_j^2} - \Pi_{ij} I \right) \nabla W_{ij} \tag{2.56}$$

where the artificial viscosity term Π_{ij} is defined as follows:

$$\Pi_{ij} = -\alpha \frac{\overline{h_{ij}}\,\overline{c_{0_{ij}}}}{\overline{\rho_{ij}}} \left(\frac{v_{ij} \cdot r_{ij}}{r_{ij}^2 + \eta^2} \right) \tag{2.57}$$

Here, $\eta^2 = (0.1h)^2$ is used to ensure a non-zero denominator, $\overline{\rho_{ij}}$ represents the average density of particles i and j, $\overline{h_{ij}}$ denotes the average smoothing length, and $\overline{c_{0_{ij}}}$ represents the average speed of sound of the two particles. The identity matrix I is also used in the equation.

The implementation of this artificial viscosity in Smoothed Particle Hydrodynamics (SPH) has been widely used and studied, and it is established that the formulation of the artificial viscosity term Π_{ij} works effectively for moderate strength shocks (Monaghan, 1983). However, when the Mach number becomes very high, the standard formulation is found to be insufficient (Monaghan, 2005). To address this issue, Monaghan (1992) proposed an additional term to the artificial viscosity, as given by Equation (2.58).

$$\Pi_{ij} = \begin{cases} \frac{-\alpha\overline{c_{0_{ij}}}\Phi_{ij}+\beta\Phi_{ij}^2}{\overline{\rho_{ij}}} & v_{ij}\cdot r_{ij} < 0 \\ 0 & v_{ij}\cdot r_{ij} \geq 0 \end{cases} \tag{2.58}$$

This expression is derived from the dissipative term in shock solutions based on Riemann solvers, where Φ_{ij} is defined as in Equation (2.59).

$$\Phi_{ij} = \frac{\overline{h_{ij}}\, v_{ij}\cdot r_{ij}}{r_{ij}^2+\eta^2} \tag{2.59}$$

The free parameters α and β are chosen based on the specific problem to be simulated, with good results obtained with the choice of $\alpha = 1$ and $\beta = 2$ (Monaghan, 2005).

In terms of the dissipative term, Equation (2.60) describes the contribution of Φ_{ij} as a product of the signal velocity, v_{sig}, and a factor $K = 0.5$.

$$\Phi_{ij} = -K\, v_{sig}\frac{v_{ij}\cdot r_{ij}}{\overline{\rho_{ij}}\, r_{ij}} \tag{2.60}$$

The signal velocity, defined in Equation (2.61), accounts for the sum of the individual sound speeds c_{0_i} and c_{0_j}, and is modulated by the relative velocity of the particle pair, v_{ij}, with a coefficient $\beta = 4$.

$$v_{sig} = c_{0_i} + c_{0_j} - \beta v_{ij}\cdot e_{ij} \tag{2.61}$$

In summary, the use artificial viscosity term helps to keep particles from getting too close to each other, ensuring the stability of the simulation and the accuracy of the results.

XSPH correction

XSPH, or Extended Smoothed Particle Hydrodynamics, is a modification of the classical Smoothed Particle Hydrodynamics (SPH) method for simulating fluid dynamics[234]. The main difference between XSPH and SPH is that XSPH takes into account the relative movement of particles in order to improve the accuracy of the simulation. This correction is applied to the equation of motion in the simulation, and it has two primary objectives.

Firstly, the XSPH correction helps to order the movement of particles, thereby stabilizing the free surface of liquids in the simulation. Secondly, the XSPH correction helps to prevent unphysical penetration of particles through each other, which can be a major issue in classical SPH simulations. By incorporating the XSPH correction into the simulation, the results produced by the simulation are more accurate and physically realistic. The XSPH method adjusts the governing equation as following:

$$\frac{\mathrm{d}r_i}{\mathrm{d}t} = v_i + \varepsilon_{XSPH} \sum_j^{n_b} m_j \frac{v_{ji}}{\overline{\rho_{ij}}} W_{ij} \tag{2.62}$$

More accurately, The XSPH method involves the modification of the displacement equation in the governing equations system by the addition of a correction term. The constant ε_{XSPH}, which governs the magnitude of the correction, is typically taken to be within the range of 0 to 1. A commonly used value for ε is 0.5, as noted in previous studies such as [235, 173]. However, when simulating incompressible flows, a value of $\varepsilon = 0.3$ has been found to be effective, as stated by Liu and Liu in [59]. The average density between particles i and j, denoted as $\overline{\rho_{ij}}$, is calculated as $\overline{\rho_{ij}} = \frac{\rho_i + \rho_j}{2}$.

Diffusive terms correction

The addition of numerical diffusive terms in the continuity equation is a common technique in SPH simulations, especially for weakly-compressible fluids, with the purpose of minimizing the noise in the density and pressure fields.In this context, several diffusive terms have been introduced.For instance, Ferrari et al.[236] utilized the Riemann solver theory to construct a numerical diffusive term based on a Rusanov flux, which was added to the continuity equation to minimize numerical noise in the density field. This diffusive term is described as following:

$$D_i^{Ferr} = \sum_j^{n_b} m_j \left(\frac{\max\{c_{0_i}, c_{0_j}\}}{\rho_j} (\rho_j - \rho_i) \right) e_{ij} \cdot \nabla W_{ij} \tag{2.63}$$

Where e_{ij} is the inter-particles unite vector that is expressed as $e_{ij} = \frac{r_{ij}}{r_{ij}}$.

The inclusion of the diffusive term D_i^{Ferr} into weakly-compressible schemes leads to a smoother pressure field due to the calculation of the pressure field from the density field through an equation of state. A smoother density field results in a smoother pressure field.

Similarly, Fatehi and Manzari [164] introduced a new term through a numerical investigation of pressure evolution for a checker-board problem [237]. This model, which is based

on the Laplacian of the pressure field instead of the density field, was the first of its kind. This diffusive term is written as:

$$D_i^{Fat} = -\rho_i \delta t \left\{ \left\langle \nabla \cdot \left\langle \frac{\nabla p}{\rho} \right\rangle \right\rangle_i - \left\langle \nabla \cdot \frac{\nabla p}{\rho} \right\rangle_i \right\} \tag{2.64}$$

Where,

$$\left\langle \nabla \cdot \left\langle \frac{\nabla p}{\rho} \right\rangle \right\rangle_i = \sum_j^{n_b} V_j \left(\nabla \nabla W_{ij} \right) \cdot \left(\left\langle \frac{\nabla p}{\rho} \right\rangle_j - \left\langle \frac{\nabla p}{\rho} \right\rangle_i \right) \tag{2.65}$$

and

$$\left\langle \nabla \cdot \left\langle \frac{\nabla p}{\rho} \right\rangle \right\rangle_i = B_i : \left\{ 2 \sum_j^{n_b} V_j r_{ij} \otimes \nabla W_{ij} \left(\frac{p_i - p_j}{r_{ij}^2 \overline{\rho_{ij}}} - \frac{r_{ij}}{r_{ij}^2} \cdot \left\langle \frac{\nabla p}{\rho} \right\rangle_i \right) \right\} \tag{2.66}$$

B_i refers to the normalization matrix defined from solving the Eq. (2.54) and $\left\langle \frac{\nabla p}{\rho} \right\rangle_i$ is the first order consistent gradient formulation of the quantity $\left(\frac{p}{\rho} \right)$.

In a parallel way, Molteni and Colagrossi [238] have proposed another diffusive term into the conservation of mass equation. Unfortunately, this term was incompatible with a hydrostatic equilibrium problem. To fix this shortcoming, Antuono et al [239] have improved this term by including a correction term designed to deal better with problems involving free surface flows, calling it δ-SPH. This diffusive term is written as:

$$D_i^{\delta - SPH} = \delta \; h_i \; c_0 \sum_j^{n_b} \Psi_{ij} \nabla W_{ij} V_j \tag{2.67}$$

The vector Ψ_{ij} is written as

$$\Psi_{ij} = 2 \left(\rho_i - \rho_j \right) \frac{r_{ij}}{r_{ij}^2} - \left\{ \langle \nabla \rho \rangle_i^L + \langle \nabla \rho \rangle_j^L \right\} \tag{2.68}$$

The symbol $\langle \nabla \rho \rangle_i^L$ denotes renormalized density gradient calculated through the Laplacian operator equation. For more details about these diffusive terms, readers can refer to [doi.org/10.1016/j.apm.2016.05.016].

To summarize, the Smoothed Particle Hydrodynamics (SPH) method has undergone a significant improvement over the years. Advances in numerical methods and computing power have allowed for more accurate simulations and the ability to handle increasingly complex problems. Additionally, the development of new kernel functions, better treatment of governing equations, and improved diffusive terms have further enhanced the robustness

and accuracy of the SPH method. As a result, SPH is now widely used in a variety of fields and continues to be a subject of active research and development.

2.4 Neighboring particles search in SPH simulations

In Smoothed Particle Hydrodynamics (SPH) simulations, determining the neighboring particles of a target particle i is crucial for accurately calculating fluid dynamics interactions. To do this, it is necessary to find all the particles j that are within a specified smoothing length h from the target particle. This information is then used to perform calculations such as density estimation and pressure forces. There are several methods to search for neighboring particles, including:

2.4.1 Brute Force Method

In this method, the distance between each pair of particles i and j is calculated using a distance metric such as Euclidean distance or Manhattan distance [59, 240]. If the distance between two particles is less than or equal to h, they are considered neighbors. This method is simple but computationally expensive as the number of calculations grows quadratically with the number of particles.

2.4.2 Linked-list Method

The main idea behind this method is to divide the simulation space into cells, and then use a linked-list data structure to store the particles in each cell [241, 71]. When searching for the neighbors of a target particle i, only the particles in the same cell and surrounding cells need to be considered. This reduces the number of particles that need to be compared to the target particle, making the search more efficient than the Brute Force method [242]. This method can also handle dynamic changes in the particle positions, as particles can be added or removed from the linked-list as needed. This makes the linked-list method well-suited for simulations that involve fluid-structure interaction dynamics, where particles are constantly moving and changing position and physical properties.

2.4.3 Tree-based Method

This method involves the use of a tree data structure, such as a K-D Tree or an Octree, to organize the particles [243–246]. The tree is constructed by recursively dividing the simulation space into smaller regions until each region contains only a few particles. During

the neighbor search, the tree is traversed to find particles j within a distance of h from particle i. This method is more efficient than the Brute Force method, but can be more complex to implement and may require more memory to store the tree structure.

2.4.4 Adaptive Kernel Method

In this method, the smoothing length h is allowed to vary depending on the local particle density [213, 247]. This reduces the number of particles considered as neighbors in low-density regions, leading to more efficient neighbor search. This method can also prevent particle clustering and ensure an even distribution of particles. However, the determination of h and the calculation of the density can be computationally expensive.

It's worth noting that the choice of method depends on the specific requirements of the simulation, such as the number of particles, the size of the simulation space, and the desired accuracy. Some methods may be more suitable for certain applications, while others may be more efficient in others.

2.5 Boundary conditions in SPH simulations

Boundary conditions play a crucial role in the accuracy and validity of any numerical simulation, including Smoothed Particle Hydrodynamics (SPH) simulations. In SPH, the governing equations are discretized into a set of particles, and the solution of the equations is obtained by considering the interactions between these particles. The presence of boundaries in a simulation introduces a set of unique challenges as the behavior of the particles near these boundaries can have a significant impact on the overall solution. As a result, it is of utmost importance to impose appropriate boundary conditions that accurately capture the physical behavior of the system being modeled. There are several techniques for implementing boundary conditions in SPH and the choice of which to be used among them depends on the problem being solved and the type of simulation being performed.

2.5.1 Immovable boundary conditions

Immovable boundary conditions in SPH simulations refer to a scenario where the properties or characteristics of the particles near the boundaries are static to a known value. This approach is often used when the boundaries represent solid objects, such as walls or containers, where the flow or movement of particles is restricted. In such cases, it is important to ensure that

the boundary conditions are properly implemented to avoid unrealistic results or errors in the simulation.

There are different approaches used to enforce immovable boundary conditions in SPH simulations. One of the most widely used methods is the ghost particle technique, which involves introducing additional particles near the boundary that act as a "ghost" to prevent the fluid from flowing through the boundary. These ghost particles are usually given a mass, velocity and density that is equal to that of the fluid particles, but their positions are adjusted so that they are positioned exactly at the boundary. The concept of the Ghost Particles technique was initially introduced by Libersky et al. [248] as a means to enforce symmetrical conditions by imparting opposing velocities to reflected particle images. The Fixed Ghost Particles technique, proposed by Marrone et al. [249, 250], utilizes fixed layers of ghost particles placed around solid boundaries. These particles are used to interpolate fluid properties with a high-order accuracy kernel function.

Another approach is the reflective boundary condition, where the particles near the boundary are reflected back into the fluid domain, mimicking the behavior of a solid wall. Colagrossi and Landrini [175] expanded upon the technique of ghost particle to accommodate rigid boundaries, incorporating density, pressure, and velocity reflections into the ghost particles.

A third approach is the no-slip boundary condition, introduced by J.P. Morris [112], involving the introduction of virtual velocities within the ghost particles. This approach ensures robust support near boundaries and allows SPH simulations to better capture fluid behavior. However, challenges arise when dealing with complex boundary geometries, particularly in scenarios involving corners.

The Coupled Dynamic Solid Boundary Treatment technique, introduced by Liu et al. [251], involves the use of two types of virtual particles: repulsive particles and fixed particles to represent solid boundaries. Repulsive particles are placed directly on the solid boundary, while fixed particles are positioned outside the solid boundary area.

The repulsive force method, initially introduced by Monaghan [170], relies on the application of Lennard-Jones forces between fluid particles and solid walls. While this technique is straightforward to implement, it can lead to significant numerical oscillations near solid boundaries, as observed in studies such as those by Liu et al. [95] and [252]. Subsequently, a milder variant of the repulsive force approach was developed by Rogers and Dalrymple [253] for the purpose of simulating tsunami waves using the SPH method.

The Dummy Particles method, initially introduced by Takeda et al. [254], involves the placement of fixed layers of particles to represent solid boundaries and ensure a compact

support region near them. This technique offers an advantage over the Ghost Particle method by being capable of handling complex geometric boundary shapes. Issa et al. [255] extended this approach to investigate turbulence modeling within the SPH framework. Adami et al. [209] further improved the Dummy Particle technique by introducing a generalized formulation that provides accurate pressure approximations on the boundary particles based on local force balance. Krimi et al. [21] expanded this technique, based on Adami et al.'s work [209], to be applicable in the context of multiphase fluid flow with varying densities and viscosities.

A semi-analytical wall boundary condition was developed in 2D by Ferrand et al. [256], building upon the works of Kulasegaram et al. [257] and De Leffe et al. [258]. This method discretizes wall boundaries using boundary elements such as segments and vertices. It overcomes the limitations of kernel support near boundaries by computing surface integrals and using renormalization factors in the weakly compressible SPH (WCSPH) discrete interpolation. Macia et al. [259] and Leroy et al. [260] applied this method in the context of incompressible SPH (ISPH), while Mayrhofer et al. [261, 262] extended it to 3D applications. Although this method yields reasonable results, it is known to be challenging to implement and can significantly increase simulation time, as noted by Valizadeh and Monaghan [263].

An innovative approach was proposed by Fatehi and Manzari [164] for modeling wall boundary conditions using a single layer of solid particles. This method ensures accurate pressure calculations at the wall, effectively preventing particle penetration. It demonstrates strong performance, especially in scenarios involving complex geometries. Hashemi et al. [264] successfully applied this technique to simulate the motion of rigid bodies within Newtonian fluid flows.

2.5.2 Free boundary conditions

In Smoothed Particle Hydrodynamics (SPH) simulations, Free boundary conditions are used to model physical systems with boundaries that allow fluid or solid particles to move freely in and out of the computational domain [265, 209, 266].The width of the buffer zones for inflow and outflow, depending on the flow direction, is set to be equal to or greater than the kernel function's support radius ($\geq kh$). This is done to ensure that the kernel's support is fully encompassed. This type of boundary condition is particularly important in simulations of problems such as flow over porous media, filtration, and flow in porous pipes, among others.

The main challenge in modeling free boundary conditions in SPH is to ensure that the continuity of the fluid or solid phase is maintained, while avoiding any artificial mass or

momentum transport across the boundary. This is achieved by using specific boundary conditions that mimic the physics of the physical system being modeled.

One common approach to modeling free boundary conditions in SPH is the use of ghost particles. This method involves placing additional particles outside the computational domain, with properties that match those of the fluid or solid particles inside the domain. These ghost particles are then used to maintain the continuity of the fluid or solid phase and to avoid any artificial mass or momentum transport across the boundary.

Another approach to modeling free boundary conditions in SPH is the use of a pressure-velocity coupling scheme. In this method, the velocity of the fluid or solid phase is explicitly set to zero at the boundary, while the pressure is calculated using a boundary condition that mimics the physics of the physical system. This method is particularly useful in simulations of problems such as flow over porous media, where the fluid or solid phase is expected to be stagnant at the boundary.

The unified semi-analytical wall boundary condition method introduced by Ferrand et al. [256] has been extended by Leroy et al [267] and Ferrand et al. [268] to be applicable to open boundary conditions (inflow/outflow boundaries) within the context of incompressible and weakly compressible Smoothed Particle Hydrodynamics (ISPH and WCSPH). This extended method eliminates the need for buffer zones when modeling inflow and outflow conditions. For a more comprehensive understanding of this technique, readers are encouraged to refer to [269, 268, 270].

2.5.3 Moving boundary conditions

In SPH simulations, moving boundary conditions refer to the situation where the boundary of the fluid or solid system is in motion. Modeling these types of boundary conditions requires the ability to accurately track the movement of the boundary and to make adjustments to the simulation accordingly [271].

One approach for dealing with moving boundary conditions is to use a marker particle method, where a separate set of particles is used to represent the boundary. These marker particles can be used to track the movement of the boundary and to communicate the boundary position to the fluid or solid particles in the simulation. The movement of the marker particles can be determined through the use of an external solver or through the integration of their motion within the SPH simulation itself.

Another approach for dealing with moving boundary conditions is to use an interface-capturing technique, where the fluid and solid are treated as separate phases and the interface

between the two is captured using an additional set of variables. This approach can be used to handle both free and immovable boundaries, and can be used to model more complex fluid-structure interaction scenarios.

2.5.4 Treatment of Free Surface boundary Conditions

Dealing with a free surface boundary necessitates the application of both kinetic and dynamic boundary conditions. The kinetic condition ensures that the initial free surface particles remain on the boundary. This condition is inherently satisfied in both WCSPH and ISPH schemes, as particles follow their Lagrangian velocities [266].

The dynamic condition involves enforcing a null-pressure condition $(p = 0)$ at the free surface. For WCSPH, this condition is implicitly met due to the use of the equation of state [272–274]. In contrast, for the ISPH scheme, correctly detecting the free surface particles is essential for imposing the null-pressure condition. Various methods have been employed in the literature for identifying these particles.

The conventional technique involves evaluating the intermediate densities ρ^* of particles. If $(\rho_i^* < 0.99\rho_0)$, particle i is considered to be at the free surface [165, 275–279]. A similar volume-based approach was introduced in [231].

An alternative free surface detection method was proposed in [280], which relies on calculating the divergence of particle positions and comparing it to a threshold value adjusted according to the number of space dimensions n.

A straightforward geometric-based technique was suggested by [281]. A more advanced and accurate algorithm for free surface detection, based on SPH interpolations, was developed by Marrone [282]. Implementing this algorithm does not require intricate geometrical procedures.

2.5.5 Reflecting boundary conditions

Reflecting boundary conditions in SPH simulations refer to a type of boundary treatment in which fluid particles that encounter the boundary are reflected back into the fluid domain. This type of boundary condition is used to model flows in which the fluid cannot penetrate the boundary and instead bounces back into the fluid domain [283, 284].

Unlike immovable boundary conditions, where the boundary is treated as a solid and the fluid particles are prevented from crossing it, reflecting boundary conditions allow the fluid to interact with the boundary and change its velocity, density and pressure. This makes it a more realistic boundary condition for many fluid flow problems.

The implementation of reflecting boundary conditions in SPH simulations is relatively straightforward [285, 286]. When a fluid particle crosses the boundary, it is reflected back into the fluid domain by reflecting its velocity vector. The particle's velocity is flipped about the normal to the boundary, which allows it to continue its motion in the fluid domain. Additionally, the pressure and density of the particle are updated to account for the change in velocity.

In comparison to other types of boundary conditions, such as free or moving boundary conditions, reflecting boundary conditions are relatively simple to implement. However, they can lead to unphysical behaviour if not used carefully. For example, if the fluid is approaching the boundary with a high velocity, it may bounce back into the fluid domain and create an unrealistic high-pressure region. To prevent this, a damping term is often added to the velocity update equation, which gradually reduces the velocity of the fluid as it approaches the boundary.

2.5.6 Periodic Boundary Conditions

Periodic boundary conditions are a well-established concept in fluid mechanics and find extensive use in SPH simulations, as demonstrated in works such as [112, 209]. In this condition, particles near a periodic boundary interact with particles situated near the corresponding open periodic boundary on the opposite side of the computational domain. This bidirectional interaction facilitates the exchange of information.

Additionally, when a particle crosses the computational fluid domain through a periodic boundary, the same particle re-enters the domain via the complementary boundary. If a particle's kernel function support is truncated by an open periodic boundary, the SPH interpolation for this particle is completed using the remaining portion of its clipped support, which is applied at the complementary open periodic boundary [287].

Another approach for SPH interpolation near open periodic boundaries is to employ buffer zones with a width equal to or greater than the radius of the kernel support ($\geq kh$). These buffer zones contain mirrored computational fluid particles near the complementary boundaries

2.5.7 Combination of boundary conditions

In many simulations, a combination of different boundary conditions can be used to more accurately represent the real scenario being modeled [288–290]. When a combination of boundary conditions is required, it is important to carefully consider the implications of

each type of boundary condition on the overall simulation. For example, the presence of a immovable boundary may restrict the movement of fluid particles, while a reflecting boundary may cause the fluid particles to bounce back into the simulation domain.

2.6 Solid-Fluid Interaction in SPH

Solid-Fluid Interaction in Smoothed Particle Hydrodynamics (SPH) is a crucial aspect of simulating scenarios where solid objects interact with surrounding fluids.

2.6.1 Rigid bodies

In cases involving rigid bodies, the motion of the rigid body's center of mass and its angular velocity are determined by the forces and torques acting on it. These forces include hydrodynamic forces exerted by the surrounding fluid. In this section, we examine a scenario involving a fluid system containing a floating rigid body with a center of mass represented as R and a velocity at R denoted as V. The equation of motion governing the center of mass of the discretized rigid body is given by [291, 292, 291]:

$$M\frac{\mathrm{d}V}{\mathrm{d}t} = \sum_{k}^{n_k} m_k f_k \tag{2.69}$$

Here, k refers to the k^{th} rigid particle constituting the entire rigid body. The term f_k represents the hydrodynamics force per unit mass acting on the boundary particle k, m_k represents the mass of rigid particle k, and n_k is the total number of rigid body particles. The force f_k can be expressed as:

$$f_k = \sum_{l}^{n_{FPs}} f_{kl} \tag{2.70}$$

In this equation, f_{kl} is the force per unit mass exerted by the fluid particle l on the boundary particle k. In other hand, the rotational motion of the rigid body is described by the equation:

$$I\frac{\mathrm{d}\Omega}{\mathrm{d}t} = \sum_{k}^{n_k} m_k (r_k - R) \times f_k \tag{2.71}$$

Here, Ω represents the angular velocity, I is the moment of inertia, and r_k is the position of the rigid particle k. The $\times$ symbol denotes the cross product.

The values of V and Ω are determined through the integration of equations (2.69) and (2.71). As the rigid body boundary particles move as part of the rigid body, the position of boundary particle k can be expressed as:

$$\frac{\mathrm{d}r_k}{\mathrm{d}t} = v_k = V + \Omega \times (r_k - R) \tag{2.72}$$

It is worth noting that this technique conserves both linear and angular momentum [293, 88]. Additionally, Hashemi et al [264] have explored an alternative approach for modeling body motion by employing surface integration on pressure and viscosity forces applied to the body elements.

2.6.2 Fluid-Structure Interaction (FSI) Approaches

Fluid-Structure Interaction (FSI), deals with the mutual interaction between solid bodies (like rigid or deformable objects) and the surrounding fluid. This interaction is prevalent in various real-world scenarios, such as ship hulls moving through water, debris in a river, or objects submerged in a fluid. Within the Smoothed Particle Hydrodynamics (SPH) method, two distinct approaches are employed for coupling fluid and structure interactions: Weak coupling (partitioned) and Strong coupling (monolithic) strategies (refer to [294, 295] for more details).

In the case of weak coupling, the behavior of one material is independent of the other, allowing separate analysis. Typically, one material is solved first, followed by the other. For example, in the work of Shi et al. [296], the fluid dynamics are resolved initially using a Navier-Stokes solver, treating the structure as a rigid moving wall. Subsequently, the structure is addressed using its designated constitutive equation, accounting for the forces exerted on it by the fluid. An issue with this approach is that it can lead to particle interpenetration between both materials, necessitating very small time steps for accurate simulations. Weak coupling strategies are commonly employed for fluid-rigid body interactions [297, 293, 88]. In these scenarios, the fluid treats the rigid body as a dynamic wall boundary, while the motion of the rigid bodies is determined by the forces imparted by the fluid using equations described in Section 2.6.1. Coupling algorithms in fluid-structure interactions that explicitly enforce continuity conditions at the fluid-structure interface (continuity of normal stress and velocity) may fall under the category of weak coupling, as observed in [298].

In strong coupling, both the fluid and structure are solved simultaneously. The Lagrangian nature of the SPH method makes this approach straightforward and robust. It involves considering the contribution of all particles to the summation in the SPH discretized equations, regardless of their nature. In this approach, coupling conditions at the interface are naturally

satisfied [172, 178, 299]. Several works have successfully implemented strong coupling in various contexts [300–307, 299].

The described fluid-structure coupling strategies primarily pertain to SPH-SPH applications, where both the fluid and structure are modeled using the SPH method. However, in the broader framework of fluid-structure interactions, other numerical methods can also be coupled, such as SPH-FEM (SPH for fluid and Finite Elements Method for structure) [308–311]. These couplings are typically categorized as weak (partitioned) due to the distinct natures of the methods and solvers involved.

2.7 Advanced time integration algorithms in SPH Simulations

In Smoothed Particle Hydrodynamics (SPH) simulations, time integration algorithms play a crucial role in determining the accuracy and stability of the simulation. The time integration algorithm updates the particle positions and velocities and other variables at successive time steps. There are several time integration algorithms used in SPH, each with its own advantages and disadvantages. Some of the commonly used time integration algorithms include:

2.7.1 Verlet Algorithm

This is a simple and efficient algorithm that uses particle positions and velocities at two consecutive time steps to calculate the position at the next time step. It is often used in molecular dynamics simulations and is suitable for systems with simple boundary conditions [312, 209].

2.7.2 Leapfrog Algorithm

This algorithm uses particle positions and velocities at two consecutive time steps to calculate the velocity at the next time step and the position at the following time step [313, 314]. It is a popular choice for SPH simulations due to its stability and efficiency.

2.7.3 Predictor-Corrector Algorithms

These algorithms involve a prediction step, where the particle positions and velocities are estimated, followed by a correction step, where the values are refined based on the estimated

values. Predictor-corrector algorithms [234] can be more accurate than Verlet or Leapfrog algorithms but are also more computationally expensive.

2.7.4 Symplectic Integrators

These are a class of algorithms that are designed to preserve the symplectic structure of the equations of motion. They are particularly suitable for Hamiltonian systems and are commonly used in celestial mechanics simulations [88].

2.7.5 Runge-Kutta Algorithms

Runge-Kutta algorithms are a family of time integration methods that are widely used in SPH simulations [315, 175, 316]. They are very popular due to their ability to handle complex physical systems and their ability to adapt to changing time steps.

2.7.6 Forward Euler method

The Forward Euler method is the simplest time integration algorithm used in SPH [317, 318]. It updates the particle position and velocity by using the current values and the acceleration calculated from the forces. However, it is known to be unstable for large time steps and therefore, not commonly used in SPH simulations.

2.7.7 Multi-Step Algorithms

Multi-step algorithms are used to improve the stability of the simulation [319, 320]. They work by using information from multiple time steps to update the current state of the system. A common multi-step algorithm used in SPH is the Adams-Bashforth algorithm.

2.8 Numerical stability criteria

The stability of an SPH simulation is closely related to the time-stepping scheme used to advance the system in time [110]. To ensure accurate and meaningful results, there are several stability conditions that must be satisfied. These conditions, which are based on the physical processes involved in the simulation, are used to determine the maximum allowed time step for advancing the system. The stability of an SPH simulation is dependent on

the choice of time integration algorithms, as well as the numerical viscosity and boundary conditions.

2.8.1 Courant-Friedrichs-Lewy (CFL) condition

One of the key stability constraints for SPH simulations is the CFL condition, which states that the time step must be smaller than the ratio of the smoothing length to the fluid velocity. This condition is necessary to prevent numerical instabilities from developing in the solution. In practice, the time step is often chosen to be a fraction of the CFL time step, depending on the desired accuracy and stability of the solution. According to [177], the CFL time-step condition for ISPH and EISPH methods is expressed as follows:

$$\delta t \leq 0.25 \frac{h}{\max(\|v_i\|)} \tag{2.73}$$

For WCSPH the CFL condition is expressed as follows:

$$\delta t \leq 0.25 \frac{h}{\max(c_{0_i}) + \max(\|v_i\|)} \tag{2.74}$$

where δt is the time step, h is the smoothing length, and v_i is the velocity of particle i. The coefficient of 0.25 is a safety factor that is used to ensure stability.

2.8.2 Artificial viscosity condition

Another important time-step criterion is the artificial viscosity condition, which is necessary when the artificial viscosity is introduced to capture shock waves and prevent inter-particle penetration. According to Monaghan [234], the time-step criterion for the artificial viscosity is given by Equation 2.75:

$$\delta t \leq 0.3 \min \frac{h_i}{c_{0_i} + 1.2(\alpha c_{0_i} + \beta \max \phi_{ij})} \tag{2.75}$$

where α and β are the coefficients of the artificial viscosity term, ϕ_{ij} is the magnitude of the relative velocity between particle i and j, and c_{0_i} is the sound speed of particle i.

2.8.3 Viscous-Diffusion Condition

In simulations involving viscous fluids, it is necessary to ensure that the time step is small enough to accurately capture the effects of viscosity [321]. This is achieved through the viscous-diffusion condition, which takes the following form:

$$\delta t \leq 0.125 \frac{h^2}{\max(\frac{\mu_i}{\rho_{0_i}})} \tag{2.76}$$

where μ_i is the dynamic viscosity and ρ_{0_i} is the reference density of particle i.

2.8.4 Body force condition

In some cases, the fluid flow is subjected to external body forces, such as gravity. The body force condition ensures that the time step is small enough to resolve the effect of these forces [209]. This condition can be expressed as:

$$\delta t \leq 0.25 \left(\frac{h}{\|F^b\|} \right)^{1/2} \tag{2.77}$$

where F^b is the external body force.

2.8.5 Surface tension condition

In the case of interfacial multiphase SPH fluid flow, it is necessary to take into account the surface tension between the different fluid phases. The surface tension condition ensures that the time step is small enough to resolve the effect of surface tension [322, 203]. This condition can be expressed as:

$$\delta t \leq 0.25 \left(\frac{\min(\rho_k, \rho_l) h^3}{2\pi \sigma^{k-l}} \right)^{1/2} \tag{2.78}$$

the term σ^{k-l} represents the surface tension coefficient between the two phases.

All these time-step criteria must be satisfied in each iteration to ensure a stable SPH computation. In practice, the smallest of the above criteria is used as the actual time-step.

In conclusion, this chapter has provided a comprehensive overview of the numerical techniques essential for utilizing Smooth Particle Hydrodynamics (SPH) in simulating complex problems, especially those involving fluid-structure interaction (FSI). We have highlighted SPH's proficiency in handling intricate geometries and substantial deformations, rendering it a versatile tool for a wide array of applications. By delving into the governing

equations, their discretization, multiphysics coupling strategies, interpolation smoothing kernels, boundary condition treatments, as well as methods for enhancing accuracy, stability, and time integration, we have laid a solid foundation for the subsequent application of SPH in diverse scenarios. Armed with this knowledge, we are poised to embark on practical implementations and simulations in the following chapters, confident in our understanding of the numerical underpinnings of this powerful method.

Chapter 3

Modelling of fluid-granular material interaction using Smoothed Particle Hydrodynamics

In recent decades, modeling of fluid-structure interactions has attracted the attention of many researchers, scientists, and engineers since these phenomena occur in many realistic natural and industrial fields (see, e.g., [323, 324]). The interaction between fluids and granular materials is a prime example of fluid-structure interaction and is crucial in a wide variety of processes spanning from geophysical hazards to industrial operations. Because of the numerous ways fluids and granular materials can interact, many numerical studies using both mesh-based and mesh-less methods for modeling, predicting, and mitigating their expected damage have been proposed [325, 17, 326, 327, 323, 328–331].

In the context of mesh-based methods, some studies have used single phase models to track the dynamical behavior of fluids and granular materials as a mixture [332]. However, these models have been shown to be inadequate in capturing many important behavior aspects due to the complex and evolving nature of solid-fluid interactions, as discussed by Pudasaini and Mergili [333]. To overcome the limitations of single-phase models, two-phase mass flow models were extensively use in the literature for simulating fluid-granular material interactions within mesh-based methods [334–338]. Furthermore, the two-phase models have been extended to accommodate multi-phase flows, demonstrating its versatility and broad applicability [333, 339]. In mesh-based methods, it is often necessary to track the interface between solid and fluid phases. Common techniques used for this purpose include volume of fluid [340], the immersed boundary method [337], and level set method [341]. While these techniques are effective, they can be computationally expensive and difficult to

implement, requiring algorithms or specific treatments that further increase the computational cost [29].

Alternatively, in the framework of mesh-less methods, smoothed particle hydrodynamics (SPH) has emerged as a promising approach for modeling fluid-structure interactions, including those involving fluid-granular material interactions. To model a physical phenomenon, the SPH method splits the computational domain into a set of independent particles and then allocates to each one separately its physical properties (density, mass, pressure, etc.), according to the governing equations of motion. Thus, no connected grid topology is required to compute the physical quantities of nodes or mesh [89]. Mathematically, it relies on numerical approximations of the integrals and derivatives of continuous functions in terms of their values reproduced in a discrete form. One of the primary advantages of the SPH approach in modeling fluid-granular material interaction fields is its inherent ability to naturally track the interface between phases, without the need for additional algorithms or specific treatments. This is achieved through the Lagrangian nature of the particles, utilizing the differences in densities and viscosities between each phase [342]. Consequently, the SPH method has proved its success in a variety of applications [5, 307, 343, 344, 202].

Regarding the dynamic behavior and the complex nature of water-granular material interaction, extensive research has been conducted to model this kind of fluid-structure interaction (FSI) phenomenon as multiphase flow problem using the SPH method [222, 345, 264]. However, most of them are limited within the scope of assuming Newtonian fluid rheology for both water and granular material (where a high viscosity for granular material was used). Within such a framework, an inappropriate choice of the viscosity is a notorious bottleneck that might significantly affect the granular material rheology, modify its deformation, and thus cause difficulties in accurately reproducing the coupled water-granular material dynamic behavior. This problem comes from the fact that the complex behavior of granular materials is modeled as a deformable solid that moves like an extremely viscous liquid. Non-Newtonian rheology, such as viscoplastic models, provides a suitable approach to capture the complex behavior of granular materials by incorporating a yield stress criterion [346]. These models take into account various physical properties of the granular material, including densities, frictions, viscosities, porosities, and their corresponding mechanical responses [333]. This kind of rheology requires the implementation of some constitutive laws, such as, Bingham, Herschel-Bulkley, or Casson models [347]. However, directly utilizing these models under their original discontinuous mathematical formulations within the context of SPH method can lead to numerical instabilities when simulating complex flows [21, 348, 24, 10].

This work aims to comprehensively investigate the impact of the widely utilized Bingham model [349–353, 279], along with the less commonly employed Casson model [354, 10], on simulating the dynamic behavior of water, granular material, and their interaction using the Weakly Compressible Smoothed Particle Hydrodynamics (WCSPH) method. We generalize and incorporate the models, while considering the pressure-dependent Mohr-Coulomb yielding criterion. Since the rheological models utilized in this study are sensitive to pressure, the presence of spurious numerical high-frequency oscillations in the pressure field due to the weakly compressible flow assumption can significantly affect the simulation results. To address and mitigate these numerical artifacts, we incorporate an artificial multi-phase diffusive term ($D^{\delta-MSPH}$) developed in [21] into the WCSPH model. By applying these models to various materials, we effectively assess their performance in simulating different material behaviors.

3.1 Mathematical models

3.1.1 Governing equations

In this study, we employ a Weakly Compressible Smoothed Particle Hydrodynamics (WCSPH) approach, which is specifically suited for scenarios involving significant deformations in water-granular material interactions. To effectively model the interaction between the granular material and water, we consider the granular material as a fluid-like mass within a multiphase flow problem. The motion of both the granular material and fluid phases is governed by the continuity, Navier-Stokes, and displacement equations [355]. We assume the multiphase flow to be a single continuum with multiple densities and viscosities, weakly compressible, and flowing under isothermal conditions. By incorporating these assumptions, we can express the governing equations system for each particle i within a Lagrangian framework as follows:

$$\begin{cases} \frac{\mathrm{d}\rho_i}{\mathrm{d}t} = -\rho_i \nabla . v_i \\ \frac{\mathrm{d}v_i}{\mathrm{d}t} = \frac{-\nabla p_i}{\rho_i} + \frac{\nabla . \tau_i}{\rho_i} + g_i \\ \frac{\mathrm{d}r_i}{\mathrm{d}t} = v_i \end{cases} \tag{3.1}$$

where, ρ_i, p_i, v_i, r_i and g_i represent the density, pressure, reference density at rest, velocity vector, position vector, and the gravitational acceleration vector, respectively. τ_i is the deviatoric part of the Cauchy stress tensor, also known as the viscous tensor for fluids. The

subscript "i" in the variables refers to the Lagrangian domain particles, which can belong to either the fluid or solid (granular material) phases.

To close the above system of equations (Eq. (3.1)), according to a weakly compressible fluid, the addition of an equation of state that computes the pressure in terms of the density is required instead of solving the Poisson equation as in the case of ISPH schemes [279, 24]. In this work, we employ an equation of state which is expressed in the pressure-density domain [167] in the form:

$$p_i = p_r \left\{ \left(\frac{\rho_i}{\rho_{0i}} \right) - 1 \right\} \tag{3.2}$$

where ρ_{0i} and p_r are the reference density and the reference pressure, respectively. In this simulation case, the reference pressure is checked depending on the reference density and the reference speed of sound c_0 using the following equation

$$p_r = \rho_{0i} {c_{0i}}^2 \tag{3.3}$$

To choose an adequate time step for the simulations, the reference pseudo-sound speed c_0 must satisfy the following equation:

$$c_0^2 \geq max \left\{ \frac{U_0^2}{\delta\rho}, \frac{\|g\| L_0}{\delta\rho}, \frac{\mu_{eff} U_0}{\rho_0 L_0 \delta\rho} \right\} \tag{3.4}$$

where U_0, $\delta\rho$, L_0, and μ_{eff} are the reference velocity, the ratio of density variation, the reference length, and the effective dynamic viscosity, respectively. In this study, $\delta\rho = 0.01$ is adopted to ensure weakly compressible assumptions.

Maintaining a smooth pressure field at the interface between the fluid and solid phases (water and granular phases) is crucial for the stability of our system. This requirement arises from the need for a continuous pressure field to accurately approximate its gradient. The choice of reference pressure p_r plays a critical role in achieving this smoothness. Based on the findings of Colagrossi and Landrini [175], it is recommended to set the reference pressure equal for all particle phases. Since the phases have different densities ρ_i, we introduce different artificial speeds of sound c_{0i} to ensure the equality of reference pressure. Then, Eq. (3.3) is extended to satisfy the conservation of reference pressures for each flow phase as follows:

$$p_r = p_{r_s} = p_{r_f} \tag{3.5}$$

$$p_r = \rho_s {c_s}^2 = \rho_f {c_f}^2. \tag{3.6}$$

here, p_r is the reference pressure, p_{r_s} is the reference pressure in the solid phase, p_{r_f} is the reference pressure in the fluid phase, ρ_s is the density of the solid phase, c_s is the pseudo-sound speed in the solid phase, ρ_f is the density of the fluid phase, and c_f is the pseudo-sound speed in the fluid phase. The numerical stability of the computations will be significantly improved by the above conditions (Eqs. (3.4) and (3.6)) [175].

3.1.2 Viscoplastic constitutive laws

For modeling water-granular material interactions, it should be noted that the computational domain consists of two phases, each with its own rheology and thus its specific dynamic behavior. Under real conditions, the fluid phase (water in our case) can deviate significantly from an ideal fluid (pure water with negligible viscosity) due to the presence of various constituents like silt and fine particles [333, 328]. However, for simplicity and to facilitate the mathematical modeling, we assume that the water in our study behaves as a Newtonian fluid with constant viscosity, which is a reasonable approximation [25, 94]. In this case, the shear stress is directly proportional to the shear rate, and the unique parameter that relates to them is the constant viscosity of the fluid. The granular material, on the other hand, has a more complex dynamic behavior because it has the physical properties of a solid but flows like a liquid under certain conditions. The shear stress is related to the shear rate via a non-constant parameter, which is the apparent viscosity [183] (see Fig. 3.1). Consequently, non-Newtonian rheologies are practically adopted to model granular material flows.
The shear stress (deviatoric tensor) for Newtonian fluids can be expressed as:

$$\tau = \mu\, D \tag{3.7}$$

where D denotes the shear rate and it is defined as $D = \nabla v + (\nabla v)^T$, with ∇v signifying the velocity gradient tensor, and the superscript T is the transpose tensor symbol. All materials that do not obey Eq. (3.7) are categorized as non-Newtonian fluids [183]. Several viscoplastic constitutive laws can be employed in describing the non-Newtonian rheology of granular materials. Two laws are devoted to this work: the Bingham and Casson models, [354].

The Bingham plastic model [356] is one of the simplest and most extensively used among viscoplastic constitutive laws. In this two-parameter linear model, the granular material behaves like a Newtonian fluid above a limit stress value called the yield stress (τ_y). Otherwise, it exhibits rigid body behavior. Namely, when τ_y is exceeded, the structure undergoes deformations and behaves as a fluid, otherwise it maintains a stiff body structure (see Fig. 3.1). Mathematically, it can be represented as:

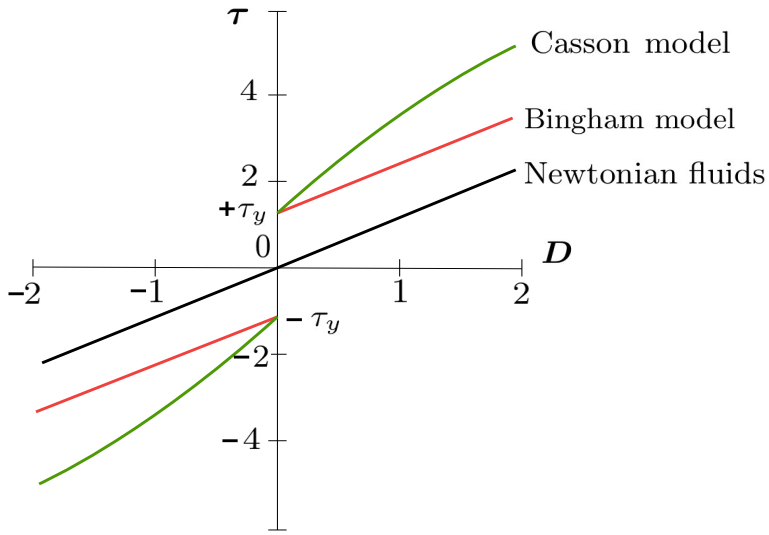

Fig. 3.1 Shear stress vs. shear rate for Newtonian fluids, Bingham and Casson rheological models. Figure based on that presented by Mitsoulis [27]

$$\begin{cases} \tau = \left\{ \frac{\tau_y}{\|D\|_F} + \mu \right\} D & \|\tau\|_F \geq \tau_y \\ D = 0 & \|\tau\|_F < \tau_y \end{cases} \tag{3.8}$$

The notation $\|.\|_F$ refers to Frobenius norm, thus:

$$\|D\|_F = \left(\frac{1}{2} D : D \right)^{\frac{1}{2}} \tag{3.9}$$

$$\|\tau\|_F = \left(\frac{1}{2} \tau : \tau \right)^{\frac{1}{2}} \tag{3.10}$$

On the other hand, under the Casson model [357, 358], the material behaves exactly as with the Bingham plastic model, but after exceeding the yield stress, it follows a non-linear (power law) viscoplastic model instead of the Newtonian (linear) one (see Fig. 3.1). Mathematically, it can be represented as:

$$\begin{cases} \tau^{\frac{1}{2}} = \left\{ \frac{\tau_{yc}^{\frac{1}{2}}}{\|D\|_F^{\frac{1}{2}}} + \mu_c^{\frac{1}{2}} \right\} D^{\frac{1}{2}} & \|\tau\|_F \geq \tau_{y_c} \\ D = 0 & \|\tau\|_F < \tau_{y_c} \end{cases} \tag{3.11}$$

where τ_{y_c} is the Casson yield stress and μ_c is the Casson plastic viscosity.

While the formulations (Eqs. 3.8 and 3.11) are commonly employed as constitutive laws to describe the rheology of granular materials, both models suffer from mathematical discontinuities, making them impractical for numerical simulations [354]. To address this issue in our study, we have opted to utilize the Bercovier and Engelman (BE) model [187]. By smoothing out the constitutive laws of both Bingham and Casson, we aim to facilitate their implementation in our Smoothed Particle Hydrodynamics (SPH) model, enabling us to accurately predict the non-Newtonian rheological behavior of granular materials.

Herein, both constitutive laws are adjusted to be mathematically continuous by implementing a corrective deformation ($\varepsilon_D > 0$) that is infinitesimally small, which makes the approximation of the discontinuous model possible without influencing any of the other computations. Hence, Eq. (3.8) is expressed as:

$$\tau = \left\{ \frac{\tau_y}{\sqrt{\|D\|_F^2 + \varepsilon_D^2}} + \mu \right\} D \tag{3.12}$$

When ($\varepsilon_D = 0$) in Eq. (3.12) with $\|D\|_F \neq 0$, Eq. (3.12) is reverted to the basic Bingham constitutive law (3.8). Thus, ε_D must be selected as small as possible to be appropriate in numerical simulations. Since we ensure a positive value for the infinitesimal deformation term ($\varepsilon_D > 0$), Eq. (3.12) can well describe the effective viscosity of the matter even if the material does not undergo any deformation (null rate of strain tensor $D = 0$) without any numerical troublesome or difficulties.

By introducing the effective viscosity (μ_{eff}) concept [183], Eq. (3.12) is then written:

$$\tau = \mu_{eff}(\|D\|_F) D \tag{3.13}$$

where the Bingham effective viscosity is expressed as:

$$\mu_{eff}(\|D\|_F) = \frac{\tau_y}{\sqrt{\|D\|_F^2 + \varepsilon_D^2}} + \mu \tag{3.14}$$

When the steps followed to reproduce the continuous form of the Bingham plastic model are applied to the Casson model, then the shear stress is expressed as:

$$\tau = \mu \left\{ \sqrt{\frac{\tau_y}{\mu(\|D\|_F + \varepsilon_D)}} + 1 \right\}^2 D \tag{3.15}$$

where the Casson effective viscosity is expressed as:

$$\mu_{eff}(\|D\|_F) = \mu \left\{ \sqrt{\frac{\tau_y}{\mu(\|D\|_F + \varepsilon_D)}} + 1 \right\}^2 \tag{3.16}$$

The effective viscosity is inversely proportional to the rate of strain tensor, so the maximum value of the effective viscosity μ_{eff} in both Eqs. (3.14 and 3.16) is attained when the shear rate tends to zero ($D = 0$).

Physically, a very high value of the effective viscosity, corresponds to the rigid part of the material in terms of structural behaviors (non-sheared region). However, numerically, a stable simulation time step can greatly be affected by the value of the maximum effective viscosity. An inappropriate choice of the effective viscosity can significantly increase the simulation duration as discussed in the Subsection 3.2.2. As a result, using the bi-viscosity model, the Casson-Papanastasiou model [359], or even both proposed models (Eqs. 3.12 and 3.15), may enormously affect the rate of accuracy/efficiency of our numerical SPH code.

To address this issue, additional regularization is applied to Eqs. 3.12 and 3.15, respectively. Therefore, two new constitutive laws based on the continuous forms of the Bingham and Casson models, respectively, are proposed. Prior selection, control of the simulation time step, and rheological proprieties are assumed using these new models.

– For the continuous Bingham model: Let us suppose that $\max(\mu_{eff}) = \alpha_\mu \mu$, where α_μ is a positive parameter that is proposed to adjust the maximum apparent viscosity value. Assuming obviously that the maximum apparent viscosity corresponds with the undeformable part of the material ($\|D\|_F \to 0$), therefore from equation (3.14), the infinitesimal deformation term ε_r results in $\varepsilon_r = \frac{\tau_y}{(\alpha_\mu - 1)\mu}$. Hence, the equation (3.12) becomes:

$$\tau = \left\{ \frac{\mu(\alpha_\mu - 1)\tau_y}{\sqrt{\left(\mu(\alpha_\mu - 1)\|D\|_F\right)^2 + \tau_y^2}} + \mu \right\} D \tag{3.17}$$

– For the continuous Casson model: by following the above steps that were applied to Bingham model, we find

$$\tau = \mu \left\{ \sqrt{\frac{\tau_y}{\mu(\|D\|_F + \frac{\tau_y}{\mu(\alpha_\mu - 1)^2})}} + 1 \right\}^2 D \tag{3.18}$$

Both the constitutive models presented by Eqs. (3.17 and 3.18) are well suited to numerical simulations since both of them avoid singularities and can be applied to sheared or non-sheared regions. Furthermore, when ($\tau_y = 0$), both laws are reduced

to the Newtonian fluid model, and when the parameter is large enough ($\alpha_\mu >> 0$), they are reduced to the original constitutive laws of Bingham and Casson, respectively. So, one can say that Eqs. (3.17 and 3.18) are smooth approximations of Bingham and Casson constitutive laws, respectively.

Yield stress computations

In order to culminate our model, we have to identify the yield stress τ_y value, since it is a crucial rheological criterion to characterize the dynamical behavior of the granular material which is generally specified by the use of pressure dependent yield criteria. The Mohr-Coulomb and Drucker-Prager yield criteria are pressure-dependent models that are commonly adopted for determining the yield stress [360, 361]. It is worth noting that the Mohr-Coulomb and Drucker-Prager criteria are the same in 2D space [361, 21]. As stated by Domnik et al. [361], the pressure-dependent Mohr-Coulomb criterion for computing yield stress is a good rheological model for granular flows since it includes the frictional nature of the granular material, based on the angle of repose (ϕ) (also known as the angle of internal friction), on one hand and ensures adding a constant tensile stress to include the cohesion (c) of the material on the other hand. Overall, Mohr-Coulomb criterion uses a linear failure envelope and the material properties (yield condition) to associate the shear and normal stresses (τ, σ) as follows:

$$\tau = c - \sigma \tan\phi \tag{3.19}$$

Therefor, the yield stress τ_y of a material which yields under the Mohr-Coulomb criterion can be expressed as:

$$\tau_y = p \sin\phi + c\cos\phi \tag{3.20}$$

The yield stress of a granular flow is determined by the cohesion (c) and the internal friction angle (ϕ) between the grains, as described in Eq. (3.20). This equation, which includes the effect of cohesion, was first proposed by Domnik et al [361] and has since been widely adopted in numerous studies on granular flows, including those by Krimi et al [29], Si et al [362], and Han et al [363]. More details about how we use the Mohr-Coulomb criterion for calculating the The yield stress are available in the Appendix A.
By merging Eqs.3.20 into Eqs.(3.17, and 3.18) we find for the Bingham model:

$$\tau = \left\{ \frac{\mu(\alpha_\mu - 1)\left(p\sin\phi + c\cos\phi\right)}{\sqrt{\left(\mu(\alpha_\mu - 1)\|D\|_F\right)^2 + \left(p\sin\phi + c\cos\phi\right)^2}} + \mu \right\} D \tag{3.21}$$

and for the Casson model

$$\tau = \mu \left\{ \sqrt{\frac{(p\sin\phi + c\cos\phi)}{\mu(\|D\|_F + \frac{(p\sin\phi + c\cos\phi)}{\mu(\alpha_\mu - 1)^2})}} + 1 \right\}^2 D \tag{3.22}$$

When we apply the equation of state (Eq. (3.2)) to identify the pressure value from the density, a negative pressure can arise if the density value of the weakly compressible flow is smaller than the reference density for any positive reference pressure. Here, to avoid this negative pressure which subsequently leads to the tensile instability ((**author?**) 29), an alternative positive pressure $\{p\}_+ = \max\{0, p\}$ is employed rather than p. Thus, Eq. (3.21) and Eq. (3.22), respectively, become:

$$\tau = \left\{ \frac{\mu(\alpha_\mu - 1)(\{p\}_+ \sin\phi + c\cos\phi)}{\sqrt{\left(\mu(\alpha_\mu - 1)\|D\|_F\right)^2 + (\{p\}_+ \sin\phi + c\cos\phi)^2}} + \mu \right\} D \tag{3.23}$$

$$\tau = \mu \left\{ \sqrt{\frac{(\{p\}_+ \sin\phi + c\cos\phi)}{\mu(\|D\|_F + \frac{(\{p\}_+ \sin\phi + c\cos\phi)}{\mu(\alpha_\mu - 1)^2})}} + 1 \right\}^2 D \tag{3.24}$$

To sum up, we have provided two regularized constitutive laws, which we call R_B_RCL (Regularized Bingham Rheological Constitutive Law) and R_C_RCL (Regularized Casson Rheological Constitutive Law), respectively. The main numerical advantages of the R_B_RCL and R_C_RCL models over the original rheological models may be highlighted in the following points:

- The shear stress is a continuous function that only depends on the physical properties of the material, as we have already discussed.
- Numerical singularities are avoided by using the R_B_RCL and R_C_RCL models, which could be easily implemented for use in existing codes.
- The R_B_RCL and R_C_RCL models can be applied to any fluid-like material where both sheared and non-sheared regions are easily handled.

The R_B_RCL and R_C_RCL constitutive laws (equations (3.23) and (3.24)) can be adapted to other rheological models by modifying the following parameters:

- For Newtonian fluid (e.g., water), set $(c = \phi = 0)$ in equations (3.23) and (3.24) use the dynamic viscosity of the Newtonian fluid as μ.

- For cohesionless or purely frictional materials, set $c = 0$ in equations (3.23) and (3.24)).
- For Bingham and Casson fluids (non-frictional/purely cohesional materials), use the yielding stress value τ_y as the material cohesion c ($\tau_y = c$) and set the frictional angle to zero ($\phi = 0$).

According to Vardis et al. [364] and Xenakis et al. [28], good numerical results can be achieved when the value of the maximum effective viscosity $max(\mu_{eff})$ at the unyielding region is 1000 times greater than the value of the plastic viscosity μ at the highest shearing region ($max(\mu_{eff}) = 1000\mu$). Moreover, according to Ionescu et al. [365], using a constant value of the plastic viscosity is found to not significantly alter the material rheology if it is estimated correctly.

3.2 SPH approximation forms of governing equations

To calculate the physical properties of a particle i in the SPH framework, a smoothing kernel function W is defined to approximate the continuous function at this particle and its derivatives in discrete form. Namely, this kernel function W determines exactly all neighboring particles j that have an influence on the particle i and evaluates the contribution of each particle based on the distance r among particle i and other particles j within the kernel function support domain, depending on a smoothing length h [109]. Hence, any function $f(r_i)$, defined in the distance between two particles $r = r_i - r_j$, is approximated by the Lagrangian integral interpolation as:

$$f(r_i) \approx \int_{\Omega(kh)} W(r_i - r_j, h) f(r_j) \mathrm{d}r_j^n \tag{3.25}$$

where r_i and r_j denote the position of particles i and j, respectively, and $\Omega(kh)$ is the compact support domain.

The smoothing kernel function used in this study is the quintic spline (Eq. (3.26)) since it fulfills the normalization condition, spherical symmetry, and compactness of its support [102]. Also, it is sufficiently smooth and does not allow a high disorder in the particle distribution [366].

$$W(r,h) = \alpha_d \begin{cases} (3-\frac{r}{h})^5 - 6(2-\frac{r}{h})^5 + 15(1-\frac{r}{h})^5 & 0 \leq \frac{r}{h} < 1 \\ (3-\frac{r}{h})^5 - 6(2-\frac{r}{h})^5 & 1 \leq \frac{r}{h} < 2 \\ (3-\frac{r}{h})^5 & 2 \leq \frac{r}{h} < 3 \\ 0 & \frac{r}{h} \geq 3 \end{cases} \tag{3.26}$$

where $\alpha_d = \frac{1}{120h}$, $\alpha_d = \frac{7}{478h^2\pi}$ and $\alpha_d = \frac{3}{359h^3\pi}$ for 1D, 2D, and 3D cases, respectively. In this work, we choose the smoothing length h as a constant relative to the initial inter-particular spacing ($h = 1.33\delta x$) and the constant α_d for the 2D case is used.

3.2.1 SPH discretization

According to Adami et al. [208], the discretized forms of governing equations in the framework of the SPH approach are based almost on the approximations of mass conservation and momentum conservation equations.

Mass conservation (Continuity equation)

The discretized form of the continuity equation is given by:

$$\frac{\mathrm{d}\rho_i}{\mathrm{d}t} = \rho_i \sum_j^{n_b} \frac{m_j}{\rho_j} v_{ij} \nabla W_{ij} \tag{3.27}$$

where ρ_i and ρ_j are the densities of particles i and j, respectively. m_j is the mass of the particle j. $W_{ij} = W(r_{ij},h)$ is the Kernel function and $r_{ij} = r_i - r_j$ is the distance between the particle i and its neighbors j. The number of particles in the neighborhood of particle i is denoted as n_b. The term $\nabla W_{ij} = \frac{\partial W}{\partial r_{ij}} e_{ij}$ is the gradient of the kernel function, and $e_{ij} = \frac{r_{ij}}{r_{ij}} = \frac{r_i - r_j}{r_{ij}}$ is the unit inter-particle vector. $v_{ij} = v_i - v_j$ is the relative velocity between the particle i and j.

For WCSPH formulations, the pressure field generally presents instabilities and spurious numerical oscillations due to the approximation of density. Especially, these issues can be critical in the present case due to the use of a Mohr-Coulomb criterion through which the effective viscosity of the material and pressure are explicitly coupled (Eqs. (3.23 and 3.24)). To deal with this problem, Molteni and Colagrossi [238] have developed the δ-SPH method where a diffusive term is added to the continuity equation in Eq. (3.27). Unfortunately, the use of δ-SPH method is only valid for single phase fluid flows. For multiphase flows, including water-granular material interactions, the δ-SPH term can cause important numerical difficulties, especially at the interface between granular material and water. These issues are

principally generated by the repulsive forces exerted between the particles of each material and others due to the difference in densities and vscosities between different phases. In order to mitigate these problems, [21] have proposed to use the $\mathscr{D}_i^{\delta-MSPH}$ formulation which is able to deal with both single and multiphase flow applications.

In this work, we propose the implementation of this multiphase diffusive term $\mathscr{D}_i^{\delta-MSPH}$ in Eq. (3.27) instead of $\mathscr{D}^{\delta-SPH}$ to deal with water-granular material interactions as a multi-phase continuum flows. Applying this implementation on the continuity equation in Eq. (3.27), we find:

$$\frac{\mathrm{d}\rho_i}{\mathrm{d}t} = \rho_i \sum_j^{n_b} \frac{m_j}{\rho_j} v_{ij} \nabla W_{ij} + \mathscr{D}_i^{\delta-MSPH} \tag{3.28}$$

where, the multiphase diffusive term can be written as:

$$\mathscr{D}_i^{\delta-MSPH} = 2\delta\ h_i\ c_0 \sum_j^{n_b} \left(\beta_{\rho_i} - \beta_{\rho_j}\right) \rho_{0_i} \frac{r_{ij}}{r_{ij}^2} \nabla W_{ij} V_j \tag{3.29}$$

δ is a dimensionless parameter defining the magnitude of density diffusion usually taken as $\delta = 0.1$. β_{ρ_i} and β_{ρ_j} are the density ratio of particles i and j to their original reference density, respectively ($\beta_{\rho_i} = \frac{\rho_i}{\rho_{0_i}}$ and $\beta_{\rho_j} = \frac{\rho_j}{\rho_{0_j}}$).

The multiphase numerical diffusive term $\mathscr{D}_i^{\delta-MSPH}$ described in Eq. (3.29) is added to the basic continuity equation to enhance the simulation results since it allows the reduction of tensile instabilities and spurious numerical oscillations due to the enhancement in the estimation of the density and the pressure values. Moreover, this term is well suited to water-granular material interaction problems involving multiphase processes [10].

Momentum conservation (Navier-Stokes equations)

The acceleration of particle due to a Cauchy stress tensor is approximated as:

$$\begin{aligned} \frac{\mathrm{d}v_i}{\mathrm{d}t} = &-\frac{1}{m_i} \sum_j^{n_b} \left(V_i^2 + V_j^2\right) \frac{\rho_j p_i + \rho_i p_j}{\rho_i + \rho_j} \nabla W_{ij} + \\ &\frac{1}{m_i} \sum_j^{n_b} \left(V_i^2 + V_j^2\right) \frac{\rho_j \tau_i + \rho_i \tau_j}{\rho_i + \rho_j} \nabla W_{ij} + g_i \end{aligned} \tag{3.30}$$

where m_i is the mass of the particle i. $V_i = \frac{m_i}{\rho_i}$ and $V_j = \frac{m_j}{\rho_j}$ are volumes of particles i and j, respectively. v_i is the velocity vector of the particle i. In this work, the initial particle volume $V_0 = \delta {x_0}^d$ is defined, where d is the number of spatial dimensions. The mass m of

any particle i is taken as a constant value equal to $m = \rho_{0_{Phase}} V_0$ in our numerical simulation, whether for the granular material or for water.
The gradient of the viscous tensor ($\nabla \cdot \tau_i$) in Eq. (3.1) can be expressed using Eq. (3.13) as follows:

$$\begin{aligned} \nabla \cdot \tau_i &= \frac{1}{m_i} \sum_j^{n_b} \left(V_i^2 + V_j^2\right) \frac{\rho_j \tau_i + \rho_i \tau_j}{\rho_i + \rho_j} \nabla W_{ij} \\ &= \frac{1}{V_i} \sum_j^{n_b} \left(V_i^2 + V_j^2\right) \frac{\rho_i \mu_{eff_j} + \rho_j \mu_{eff_i}}{\rho_i + \rho_j} D\, \nabla W_{ij} \end{aligned} \tag{3.31}$$

The term $\left(D\, \nabla W_{ij}\right)$ can be also simplified as:

$$\begin{aligned} D\, \nabla W_{ij} &= (\nabla v + (\nabla v)^T) \nabla W_{ij} \\ &= \frac{1}{r_{ij}^2} \left(v_{ij} \otimes r_{ij}\right) \nabla W_{ij} + \frac{1}{r_{ij}^2} \left(r_{ij} \otimes v_{ij}\right) \nabla W_{ij} \\ &= \frac{1}{r_{ij}^2} \left\{ v_{ij} \left(r_{ij} \cdot \nabla W_{ij}\right) + r_{ij} \left(v_{ij} \cdot \nabla W_{ij}\right) \right\} \end{aligned} \tag{3.32}$$

where $\otimes$ defines the outer product. Finally, the gradient of the viscous tensor is described as:

$$\nabla \cdot \tau_i = \frac{1}{V_i} \sum_j^{n_b} \left\{ \frac{V_i^2 + V_j^2}{r_{ij}^2} \right\} \frac{\rho_i \mu_{eff_j} + \rho_j \mu_{eff_i}}{\rho_i + \rho_j} \left\{ v_{ij} \left(r_{ij} \cdot \nabla W_{ij}\right) + r_{ij} \left(v_{ij} \cdot \nabla W_{ij}\right) \right\} \tag{3.33}$$

This attained formulation is analogous to that found by [222] in the framework of ISPH. Moreover, the effective viscosity is then calculated via Eqs. (3.14 and 3.16).
The gradient of the pressure (∇p_i) in Eq. (3.1) is approximated according [208] as

$$\frac{1}{\rho_i} \nabla p_i = \frac{1}{m_i} \sum_j^{n_b} \left(V_i^2 + V_j^2\right) \widetilde{p_{ij}} \nabla W_{ij} \tag{3.34}$$

The term $\widetilde{p_{ij}}$ is defined to ensure the continuity of pressure even for the case of discontinuous density between fluid particles (for example, when they belongs to different phases). Following [166] this term reads as

$$\widetilde{p_{ij}} = \frac{\rho_j p_i + \rho_i p_j}{\rho_i + \rho_j} \tag{3.35}$$

Also, from the equation of state The pressure field is approximated as:

$$p_i = \rho_{0_i} c_{0_i}^2 \left\{ \left(\frac{\rho_i}{\rho_{0_i}} \right) - 1 \right\} \tag{3.36}$$

Displacement equation

The velocity vector is discritized as:

$$\frac{\mathrm{d}r_i}{\mathrm{d}t} = v_i \tag{3.37}$$

In 2D, the velocity vector components are $v = [u\ w]^T$, thus the Frobenius norm of the shear rate $\|D\|_F$ is written:

$$\|D\|_F = \sqrt{2\left(\left(\frac{\partial u}{\partial x}\right)^2 + \left(\frac{\partial w}{\partial y}\right)^2\right) + \left(\frac{\partial u}{\partial y} + \frac{\partial w}{\partial y}\right)^2} \tag{3.38}$$

More details about how the form of the Frobenius norm in Eq. (3.38) is found are available in the Appendix B. To fulfill a first order consistency approximation derivative of the velocity components [208], we write:

$$\left\langle \nabla u \right\rangle = \left[\frac{\partial u}{\partial x} \ \frac{\partial u}{\partial y} \right]^T = 2 \frac{\sum_j^{n_b} V_j (u_i - u_j) \nabla W_{ij}}{\sum_j^{n_b} V_j r_{ij} \frac{\partial W}{\partial r_{ij}}} \tag{3.39}$$

$$\left\langle \nabla w \right\rangle = \left[\frac{\partial w}{\partial x} \ \frac{\partial w}{\partial y} \right]^T = 2 \frac{\sum_j^{n_b} V_j (w_i - w_j) \nabla W_{ij}}{\sum_j^{n_b} V_j r_{ij} \frac{\partial W}{\partial r_{ij}}} \tag{3.40}$$

where the symbol $\left\langle . \right\rangle$ refers to the first order consistency approximation of the quantity $\{.\}$.

3.2.2 Boundary conditions and time integration techniques

In our algorithm, the "three-layers of dummy particles for multi-phase flows" technique validated by Krimi at al. [29] is implemented as wall boundary conditions. This technique can be applied to multi-phase flows in general, and it is particularly well suited for water-granular material interactions under free-slip or no-slip boundary conditions. Readers can also refer to [21] for more information.

Lastly, the second-order Predictor-Corrector scheme is adopted in our code to integrate the governing equations over time. According to Monaghan [88], the time step is chosen to satisfy the following equation:

$$\delta t \leq \left\{ 0.25 \frac{h}{\max\{c_{0_i} + \|v_i\|\}}, 0.25 \left(\frac{h}{\|g\|} \right)^{1/2}, CFL \frac{\rho h^2}{\max\{\mu_{eff}\}} \right\} \tag{3.41}$$

The Courant number ($CFL = 0.2$) is chosen for this work because it provides a time step δt that is twice as large as that used in the previous formulation [367]. In Eq. 3.41, picking the right maximum effective viscosity $\max\{\mu_{eff}\}$ value is still a big challenge because it can affect the time step δt, which is important for numerical stability and efficiency.

In conclusion, this chapter has significantly contributed to our understanding of fluid-granular material interaction modeling using the SPH approach. By successfully integrating the Bingham and Casson constitutive laws into the SPH framework, we have enhanced our capabilities in simulating and analyzing complex phenomena in various fields, from geophysical processes to industrial applications. The insights gained from this chapter not only extend our knowledge of SPH as a versatile numerical tool but also open doors to explore novel research avenues in fluid-structure interaction involving granular materials. As we move forward, armed with these valuable modeling techniques, we are better equipped to tackle the challenges posed by fluid-granular interactions and contribute to advancements in science and engineering.

Chapter 4

Validation of the SPH Model for Fluid-Granular Material Interaction: Applications, Results, and Discussion

In this chapter, we rigorously assess the performance and accuracy of our proposed Smoothed Particle Hydrodynamics (SPH) model in the context of fluid flows, granular material flows, and their dynamic interaction. The validity of the model is evaluated through a comprehensive series of simulations that encompass a diverse range of scenarios, allowing us to examine its capabilities across various physical phenomena.

To establish the robustness of our SPH model, we undertake a meticulous comparison of our simulation results with both experimental data and outcomes obtained from other numerical models. This benchmarking process serves as a critical step in the validation process, ensuring that our SPH model faithfully reproduces real-world observations.

Furthermore, this chapter conducts an in-depth comparative analysis of two pivotal rheological models integrated within our SPH framework: the generalized Casson model (R_C_RCL) and the Bingham model (R_B_RCL). Through this meticulous examination, we seek to discern the strengths and limitations of each model and ascertain their suitability for accurately simulating fluid-granular material interactions.

The ensuing sections of this chapter will elucidate the specific applications, present the obtained results, and engage in a comprehensive discussion of the implications and insights gleaned from our validation efforts. By addressing these key aspects, we aim to provide a nuanced evaluation of the SPH model's applicability and efficacy in capturing the intricate dynamics of fluid-granular material interactions.

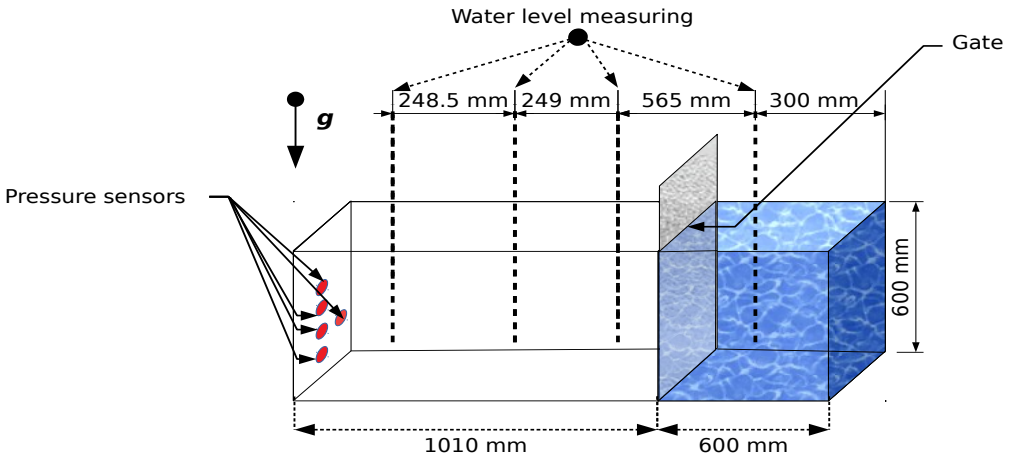

Fig. 4.1 Geometrical details and material descriptions of dam break configuration

4.1 Dam-break benchmark

The famous dam-break benchmark, also known as column water collapse, has been extensively tested in experimental and SPH numerical studies [368–371], among others. Therefore, this benchmark is adopted in this study to test how well our SPH model deals with such complex single-phase flows involving significant free surface profile deformations where the water is considered as a Newtonian fluid. Here, we reproduce the experiment of Lobovskỳ et al. [368] because it provides a lot of clear and usable data, including detailed snapshots of how water behaves over time.

The experimental setup was designed as depicted in Fig. 4.1. To summarize, a water column collapse was performed using an initial water depth $H_0 = 600$ mm. A movable gate, initially obstructing the flow of water, was placed 600 mm from the left bottom edge of a prismatic tank with internal dimensions of $1610 \times 600 \times 150$ mm. Upon removal of the gate, the water starts to flow downstream under the effect of gravity. The starting time $t = 0$ was assigned at the release of the gate. The water level was measured at four specific locations (300 mm, 865 mm, 1114 mm, and 1362.5 mm from the left side of the tank, respectively), while the pressure signal was captured using pressure sensors (see Fig. 4.1). The entire scene was recorded using a digital camera.

The present simulation is performed with an inter-particle distance of $\delta x = 0.005$, resulting in 1704 SPH boundary particles and 14400 SPH water particles. The pseudo speed of sound is selected to satisfy $c_0 = 10\sqrt{2gH}$ [342]. Based on the experiment of Lobovskỳ et al. [368], our simulation assumes that water is a Newtonian fluid with a density of $\rho_w = 997$ kg/m^3 and a constant dynamic viscosity $\mu_w = 8.9 \times 10^-4$ pa.s. Therefore, the specific values

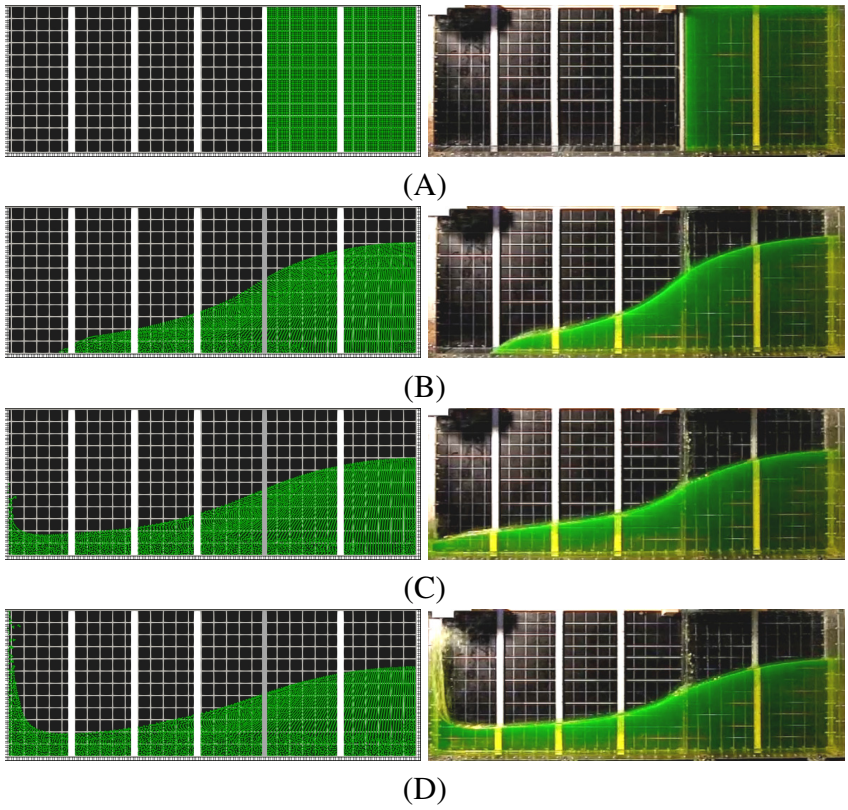

Fig. 4.2 Dam-break problem: comparison between our numerical results (left column) and the experimental results of Lobovskỳ et al. [368] (right column) at t: (A)=0 s, (B)=0.32 s, (C)=0.41 s, (D)=0.46 s

of cohesion ($c = 0$) and angle of internal friction ($\phi = 0$) are chosen to align the R_B_RCL and R_C_RCL rheological models with Newtonian behavior.

In Fig. 4.2, the experimental recording scenes for the initial water depth $H_0 = 600$ mm (right column) and the simulated ones using our SPH code (left column) are given at four different times $t = \{0.0, 316.7, 413.4, 463.3\}$ s. After the gate lift-up, the water is advected in the x direction (the spreading direction) by its kinetic energy, and the free surface is evolved gradually downward, creating a wive front. After that, the water bumps the inner right side of the tank wall where large deformations and complex flow occur. The overall behavior of the dam-break flow in the experiment and that obtained by the current SPH numerical model, describing water with Newtonian rheology, is qualitatively very similar. Despite this, the experiment reveals a somewhat slower rate compared to the numerical results.

For a quantitative assessment of this discrepancy, the water wavefront evolution is investigated in Fig 4.3, where our results are compared with the experimental data obtained by Lobovskỳ et al. [368] and the numerical results obtained by Vaucorbeil et al. [372] using the

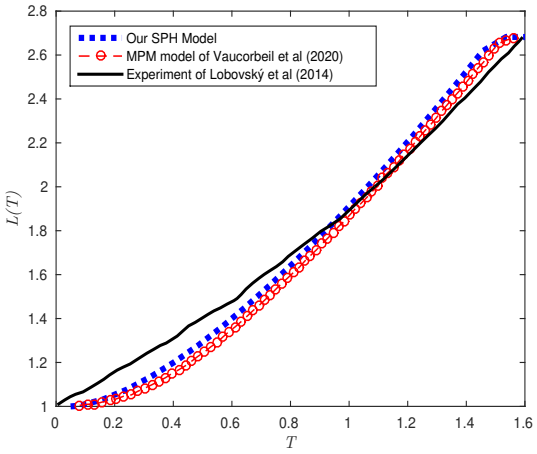

Fig. 4.3 Dam-break problem: comparison between the water wave front evolution obtained by our numerical results (blue points), numerical results of Vaucorbeil et al. [372] (red dashed circles) and experimental results of Lobovskỳ et al. [368] (black line)

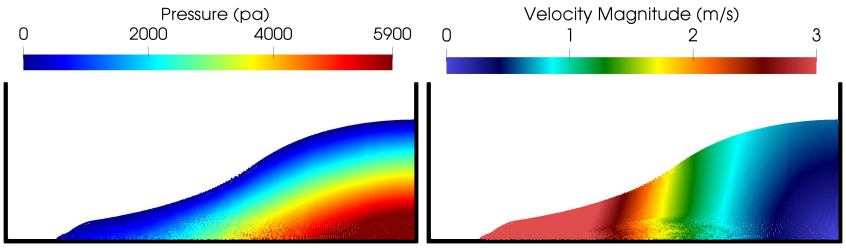

Fig. 4.4 Dam break problem: Snapshots of numerical results presenting the pressure (left side) and velocity (right) fields

Material Point Method (MPM). To achieve the same fit as in previous works, the adimensional parameters $X(T) = x(t)/H_0$ and $T = t\sqrt{g/H_0}$ for position and time, respectively, are assigned. Obviously, both numerical models agree with the experimental data. The slight forward movement that occurred in the numerical results can be due to the influence of the gate removal, which is not considered in this simulation [373], as well as the bottom wall roughness. Fig 4.4 depicts the velocity and pressure fields using our SPH code. It should be noted that the implementation of the multiphase numerical diffusive term $\mathscr{D}_i^{\delta-MSPH}$ serves to stabilize pressure by reducing the frequency of oscillations inherited from weakly compressible assumptions and density approximations [29, 10, 249].

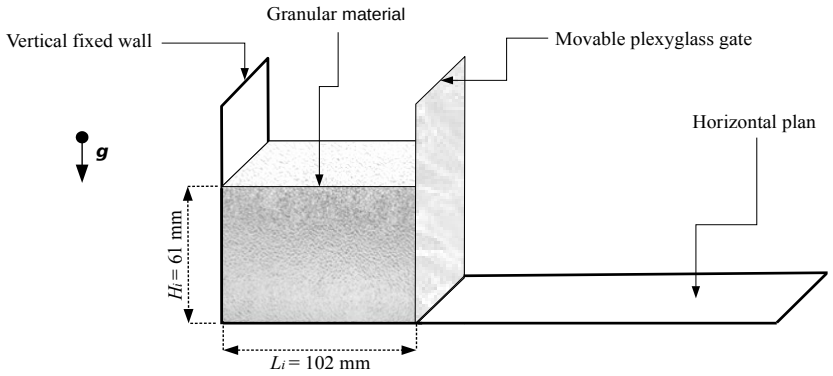

Fig. 4.5 Granular material collapse: Geometrical details of the experimental configuration

4.2 Granular material collapse

Many experimental and numerical studies were conducted to investigate granular material dynamics processes [374–377]. The granular column collapse test has been provided as a relatively straightforward benchmark through which the non-Newtonian rheology of granular material can be numerically investigated [378]. To verify the effectiveness of the proposed models in reproducing the granular material dynamic behavior, the rectangular granular column collapse experiment conducted by Lajeunesse et al. [375] is devoted to this work. This benchmark consists of a granular mass (glass beads) that is confined inside a transparent glass tank. In this experimental configuration, once the column of the granular mass is released, it suddenly undergoes a collapse and spreads in the horizontal plane until it eventually reaches a frozen deposit.

The experimental set up is depicted in Fig. 4.5. It is similar to a rectangular dam-break flow that spreads on one side with an initial height of $H_i = 61$ mm and a length of $L_i = 102$ mm, resulting in an aspect ratio of $a = H_i/L_i = 0.6$. The granular material had a mass of $m = 470$ g with a grain density of $\rho_g = 2500$ kg/m^3 (bulk density $\rho_s = \rho_g(1 - n_{por}) = 1675$ kg/m^3 with a porosity $n_{por} = 0.33$ according to Lajeunesse et al. [375], and an angle of repose $\phi = 22 \pm 0.5^\circ$. The overall dynamic process of the configuration was recorded using a digital camera.

The simulation is performed in 2-D using an inter-particle spacing of $\delta x = 0.002$, leading to 1582 SPH granular material particles. The pseudo speed of sound $c_0 = 10\sqrt{2gH_i}$ is selected. The dynamic viscosity $\mu = 10^{-2}$ pa.s and the maximum effective viscosity $\max\{\mu_{eff}\} = 10$ pa.s are assigned to the granular material. In order to properly compare how well the two generalized constitutive laws work, the same simulation parameters are used for both of them.

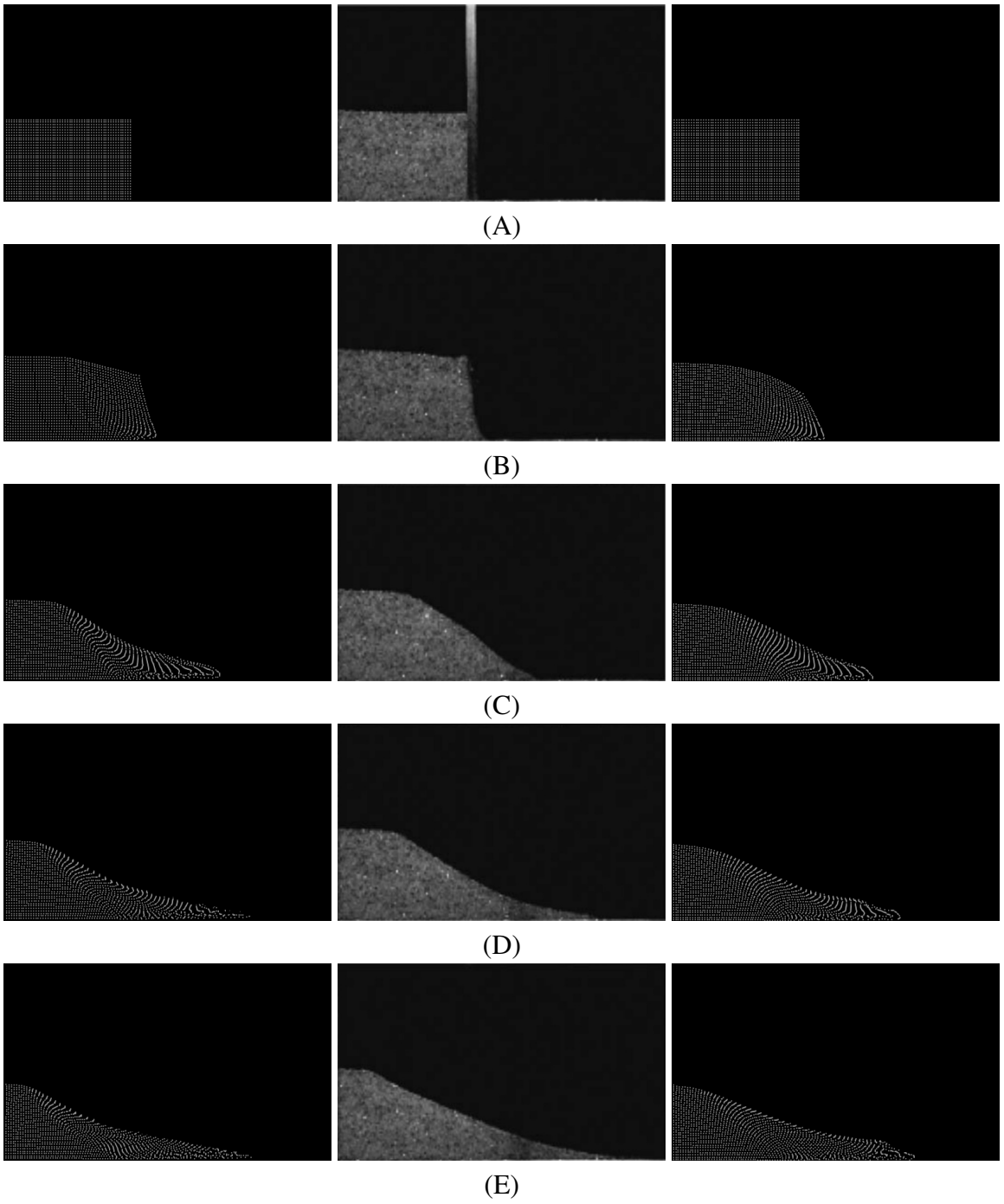

Fig. 4.6 Granular material collapse: comparison between the numerical results from R_C_RCL rheological model (left column), R_B_RCL rheological model (right column) and the experimental results of Lajeunesse et al. [375] (middle column), at t: (A)=0 s, (B)=0.08 s, (C)=0.16 s, (D)=0.24 s, and (E)=0.32 s

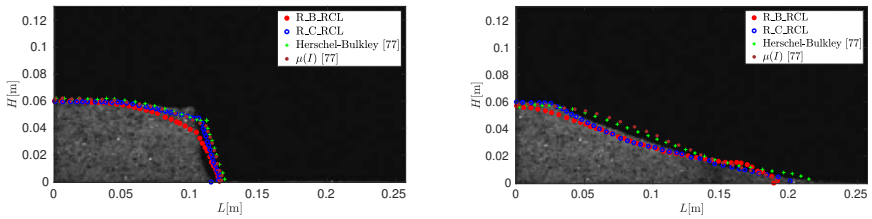

Fig. 4.7 Granular material collapse: Comparison of R_B_RCL (red) and R_C_RCL (blue) rheological models presented in this work, along with Herschel-Bulkley (green) and $\mu(I)$ (brown) models used by Kheirkhahan and Hosseini [379], overlaid on the original experiment PIV snapshots by Lajeunesse et al. [375]. The snapshots were taken at two different instants: (a) t = 0.08 s and (b) t = 0.32 s.

In Fig. 4.6, a comparison between the laboratory results and our numerical ones at different times is shown. Overall, both the R_B_RCL and R_C_RCL models can relatively predict how the shape of the rectangular granular column collapse changes as the material accelerates and then slows down in the x direction until it reaches a point where there is no more kinetic energy and a steady deposit is formed. Nevertheless, the R_C_RCL model proved to be more effective than the R_B_RCL model in predicting the dynamic behavior of the collapse process. This result was expected because the R_C_RCL model is an extension of Casson's original constitutive law, which suggests a more gradual change from Newtonian flow to the yield zone under the conditions of the high and low-rate strain tensors, unlike Bingham's constitutive model, which shows sudden changes [347].

Fig. 4.7, depicts a comparison between numerical results achieved using different rheological models, including R_B_RCL and R_C_RCL models developed in this work, and Herschel-Bulkley and $\mu(I)$ models used by Kheirkhahan and Hosseini [379], overlaid on the original experiment PIV snapshots by Lajeunesse et al. [375]. At time t = 0.08 s , we can observe the performance of different rheological models in capturing the collapse process. Overall, all the rheological models show a reasonable level of agreement with the experimental data in terms of reproducing the deformation of the granular material. However, there are notable discrepancies, particularly at the upper shoulder of the collapse. these discrepancies may be due to the effect of the withdrawing of the gate which is not considered in the numerical results. R_B_RCL and R_C_RCL models, presented in our work, demonstrate relatively good agreement with the experimental data, with acceptable fitting of the granular material behavior. However, the generalized Bingham (R_B_RCL) model appears to be less accurate in reproducing the collapsing granular material's shape compared to the other models.

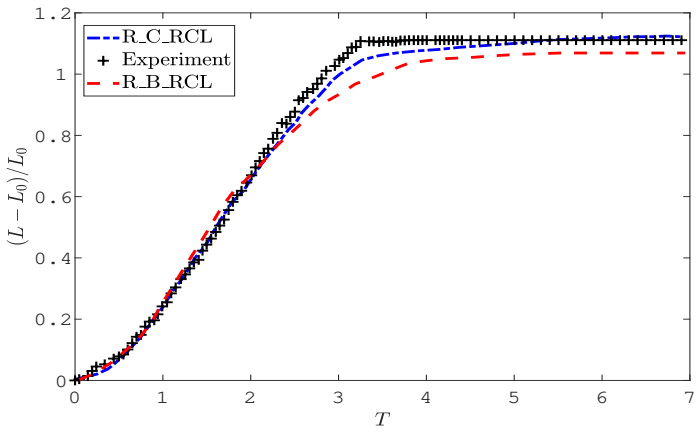

Fig. 4.8 Granular material collapse: comparison between the distance traveled by the material obtained with the numerical results from R_C_RCL (blue dash-dotted line), R_B_RCL (red dashed line) rheological models , and the experimental results of Lajeunesse et al. [375] (black plus sign)

.

At time t = 0.24 s, all the rheological models demonstrate a reasonable agreement with the experimental data in terms of the overall trend of the collapse process. However, the Bingham model consistently exhibits less accuracy compared to the other models.

Of particular interest is the performance of the Casson model, which proves to be the most appropriate in reproducing the trapezoidal shape observed in the granular material deposit. The Casson model aligns well with the conclusion of Lajeunesse et al., who noted that for aspect ratios $a = H_i/L_i < 0.74$ (in our case, $a = H_i/L_i = 0.6$), the final deposit forms a trapezoidal shape with a constant maximum height throughout the collapsing process. These findings emphasize the significance of selecting an appropriate rheological model to accurately reproduce the shape and behavior of the collapsing granular material. The Casson model, in this case, demonstrates its suitability for capturing the trapezoidal shape and better aligning with experimental observations.

In Fig 4.8, the time evolution of the normalized distance traveled by the granular material $L(T) = L(t) - L_i/L_i$, with $T = t\sqrt{H_i/g}$, is depicted. Both numerical models, R_C_RCL and R_B_RCL, are compared with the experimental data obtained by Lajeunesse et al. [375] in order to verify which rheological model can better reproduce the dynamic process of the granular collapse.

At $T \leq 2.5$, both numerical models match well with the experimental data. After that, at $2.5 \leq T \leq 4$, a discrepancy between the numerical models and experimental results is observed where the distance traveled by the granular material was longer in the experiment compared to the numerical results. Then, at $T \geq 4$, the flow front comes to rest in the

experiment while it continues to spread in the numerical cases, where the flow front reaches a deposit form at almost $T = 5$, using both models R_C_RCL and R_B_RCL. Nevertheless, it is vividly observed that the distance traveled by the granular in the numerical simulation using the R_C_RCL model is closer to the experiment than the results of the R_B_RCL model, where the front of the flow traveled a shorter distance. The discrepancy in mass halt timing between the experimental results and our numerical simulation can be attributed to two main factors: the difference in dimensionality (3D in the experiment vs. 2D in the simulation) and the additional frictional effects on the horizontal plate due to the use of no-slip boundary condition in our SPH model.

4.3 Water-granular material interaction

Characterized by its complex dynamic behavior, the Fluid-Structure Interaction (FSI) phenomenon includes the coupling relations between two bodies with different physical states where a moving or a deformable structure interacts within or around the fluid flow [6]. Given its multi-physics character, landslides interacting with water bodies are an integral part of FSI problems. Landslides can occur above water (subaerial) or under-water (submarine). Accordingly, the potential energy that arises from landslide-water interactions may generate impulse waves and it is also likely to induce significant catastrophes. For instance, the tsunamis that occurred in Lituya Bay in Alaska on July 1958 [380] and Papua New Guinea in 1998 [381] were the results of a subaerial and a submarine landslide, respectively. Indeed, these disasters have illustrated the high fatality, the big damage, and the massive destruction of these natural phenomena. Therefore, theoretical, experimental, and numerical studies have focused on landslide-water interactions problems for effectively predicting tsunamis, assessing their hazards, and proposing their prevention measures. The purpose of the following examples is to investigate and demonstrate the ability of the proposed SPH model to simulate multi-phase problems related to landslide-water interaction problems. The two coupled phenomena chosen are a subaerial and a submarine landslide in 2D space.

4.3.1 Subaerial landslide induced generated water waves

The validation test case selected in this study is a rapid subaerial deformable landslide. Herein, we reproduce an experimental case of Fritz et al. [382] where both numerical models, R_B_RCL and R_C_RCL, are therefore confronted to simulate the collapse of a granular material that interacts with a water body.

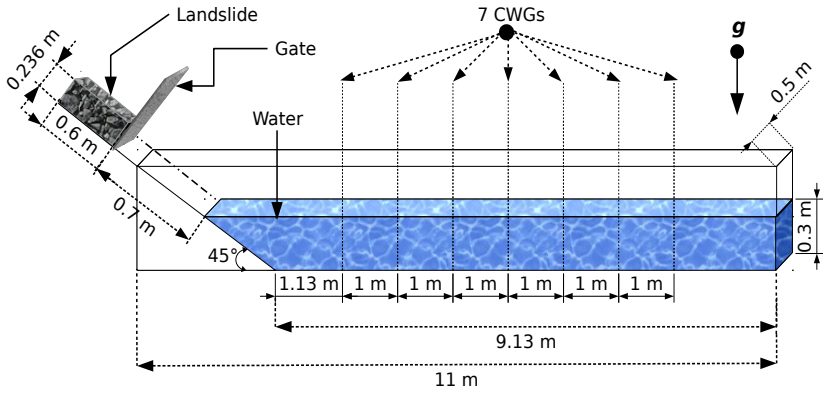

Fig. 4.9 Water-granular material interaction: Geometrical details and material descriptions of subaerial landslide-tsunami experimental benchmark. Figure based on that presented in [10]

In the original experimental setup by Fritz et al. [382], a water body of $h = 0.30$ m initial depth was placed in a rectangular tank that was 11 m long, 0.5 m wide, and 1 m deep. A 45° inclination ramp is fitted to the front of the tank where a granular material mass ($m_s = 108$ kg), which had the starting form and dimensions of a rectangular box with l = $l = 0.6$ m length, $b = 0.5$ m width, and $d = 0.236$ m depth, was placed as shown in Fig. 4.9. The density $\rho_w = 1000$ kg/m^3 and the dynamic viscosity $\mu_w = 0.001$ pa.s are devoted to the water.

The granular material was characterized by an effective internal friction angle $\phi = 43°$, a bed friction angle $\delta = 24°$, a grain diameter $dg = 4$ mm, and a grain density of $\rho_g = 2640$ kg/m^3 with a porosity $n_{por} = 0.39$. In our simulation, we focused on the initial stage of the landslide entering the water. To simplify the analysis, we considered the landslide material and water as separate and immiscible fluid phases. The bulk density of the granular landslide (taking into account the porosity of the air present within the material) is formulated as $\rho_s = \rho_g(1 - n_{por}) = 1620$ kg/m^3. This assumption is based on the physical characteristics of the phenomenon, such as the high velocity of the landslide (Fr = 4.1) and the resulting momentum of the sliding land. These factors contribute to the separation between the land and water at the entry stage, preventing immediate mixing. This assumption aligns with the findings observed in the experimental work of Fritz et al. [382], where flow separation on the slide shoulder resulted in hydrodynamic impact craters at high impact velocities. It is also consistent with the numerical simulations conducted by Shi et al. [296], who obtained relatively good results using a different SPH model that treated the land bulk as not mixing with water in the case of rapid subaerial landslide.

The granular material deformation, water free-surface evolution, and their interfaces were captured by the Particle Image Velocimetry (PIV) technique. A pneumatic landslide generator was initially used to provide the following dimensionless parameters at the impact [382]: $F = v_s/\sqrt{gh} = 4.1$, $V = V_s/bh^2 = 1.57$, and $S = s/h = 0.56$, where F is the Froude number, v_s is the slide impact velocity, $g = 9.81$ m/s^2 is the gravitational acceleration, V is the dimensionless slide volume, $V_s = l \times \mathrm{b} \times d = 0.0708$ m^3 is the rectangular box volume, and S is the relative landslide thickness. All values of these parameters have been determined through laboratory measurements conducted by Fritz et al., [382] and will be directly incorporated into the simulation. For more details about the benchmark setup, we refer readers to [382].

In order to ensure a fair and meaningful comparison between the R_B_RCL and R_C_RCL models in reproducing the granular material deformation and water tsunami waves, the same numerical simulation parameters are used for both models. Namely, the inter-particle distance of $\delta x = 0.0025$ m was determined to capture the small-scale interactions between particles, allowing for an accurate representation of the particles of granular material and water at an adequate resolution. The reference speed of sound (c_0) is set to 30 m/s based on the relationship $c_0 = 10\sqrt{2gH_i}$, ensuring it is at least 10 times higher than the maximum velocity in the flow field. This choice limits density variations to less than 1%, assuming an acceptable compressibility that aligns with the WCSPH approach [383]. The plastic viscosities $\mu_b = \mu_c = 0.01$ Pa·s (as in the work of Ionescu et al [365]) are employed for both the R_B_RCL and R_C_RCL models, where μ_b represents the Bingham plastic viscosity, and μ_c represents the Casson plastic viscosity. In addition to the chosen plastic viscosities, the maximum effective viscosity ($\max(\mu_{eff})$) plays a crucial role in capturing the flow behavior of the granular material and its interaction with the surrounding water. To represent the upper limit of the material's resistance to flow, a value of 10 Pa·s was selected for $\max(\mu_{eff})$. Notably, $\max(\mu_{eff})$ is set to be 1000 times greater than the plastic viscosity (μ) at the highest shearing region ($\max(\mu_{eff}) = 1000\mu$), which ensures the halt of the granular particles at the unyielding region, as reported in [364, 28].

Figure 4.10 displays snapshots of a laboratory experiment on rapid subaerial landslide with water-granular material interactions conducted by Fritz et al. [382] (middle column) compared to numerical results obtained using the R_C_RCL (left column) and R_B_RCL (right column) rheological models at different relative times $T = t(gh)^{0.5}$ (0.18, 0.56, 1.33, and 3.61, respectively). Overall, both the R_C_RCL and R_B_RCL models satisfactorily reproduce the dynamic process of this water-granular material interaction. However, there are noticeable differences between the experimental snapshots and the numerical models. Particularly, at times $T = 0.18$ and 0.56, the numerical results from both rheological models closely resemble the experiment, with similar profiles of the granular material and generated

water waves. As time progresses ($T = 1.33$ and 3.61), the numerical results obtained using the R_C_RCL rheological model align more closely with the experimental results than those from the R_B_RCL model. One significant contributing factor to this discrepancy is the difference in dimensionality between the experimental setup and our numerical simulation. The experimental flow is inherently three-dimensional (3D), while our simulation is conducted in a two-dimensional (2D) setting. Additionally, the friction effect of the sliding bed is simplified as a no-slip boundary condition in our simulation. Moreover, the simulation models consider the granular material and water as separated flows without accounting for mixing, and pore pressure is not incorporated into the constitutive laws equations. It is important to acknowledge that in real mass flows, granular fluid mixing can be more complex and may not strictly conform to the separated or unseparated flow assumptions. Practical situations involve various factors such as turbulence, particle size distribution, and interparticle interactions that can influence the mixing behavior between the granular material and fluid. The effect of these differences is investigated in Figure 4.11, which compares the experimental snapshot with the numerical results obtained using the R_C_RCL and R_B_RCL rheological models. In Figure 4.11 (A), it is observed that the granular material evolution using the R_B_RCL model shows a thicker deposit and less traveled distance compared to the R_C_RCL model. However, the R_C_RCL model better reproduces the dynamic process of the granular material. A similar observation can be made for the evolution of the water free-surface in Figure 4.11 (B). This difference may arise because the linear R_B_RCL model struggles to accurately predict the maximum effective viscosity of the unyielding zone, which is non-constant within the physical case due to changing shear rates. This discrepancy is not solely attributed to the 2D effect and no-slip boundary assumption used in our work. At $T = 3.61$ (as shown in Figure 4.11), the flow becomes more complex as water starts to submerge the granular material. In such cases, pore pressure should be considered in the constitutive laws to account for the intricate pore filling patterns, where some regions are fully filled with water, some are partially filled, and others do not have water penetration. However, in our simulation, we continue to treat the granular material and water as immiscible and do not incorporate pore pressure effects. We believe this is the primary reason why the differences between experimental and numerical simulations become more pronounced for both the Bingham and Casson models at this stage. Nevertheless, it is worth noting that even with this assumption, the Casson model provides better agreement with the experimental observations, both in terms of the granular shape and water wave shape.

The velocity vector fields, acquired through the use of Particle Image Velocimetry (PIV) [382], offer a detailed depiction of fluid motion within the area of interest. Additionally, numerical simulations employing the R_C_RCL model further enable the visualization of

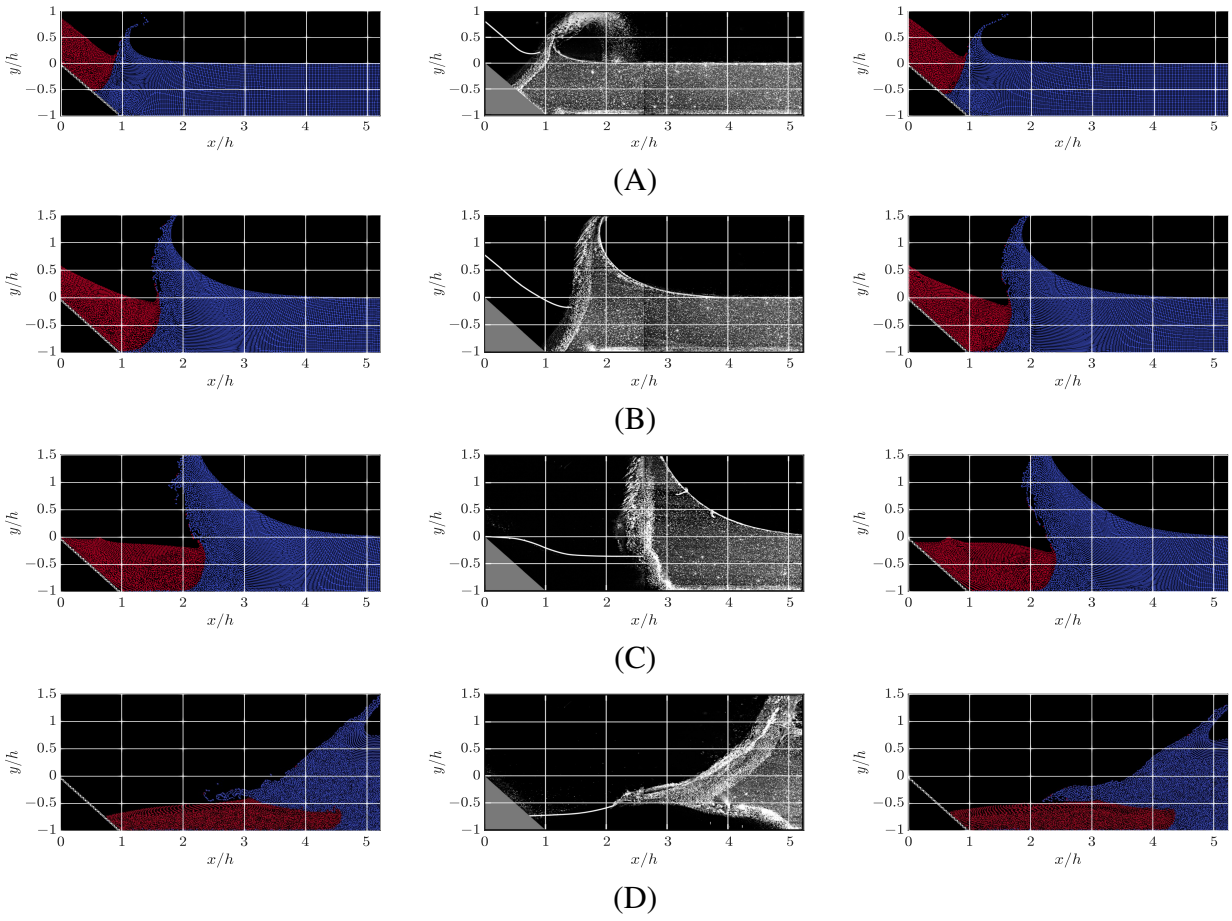

Fig. 4.10 Water-granular material interaction: comparison between the numerical results from R_C_RCL rheological model (left column), R_B_RCL rheological model (right column) and the experimental results of Fritz et al. [382] (middle column), at T: (A)=0.18 , (B)=0.56 , (C)=1.33 , (D)=3.61

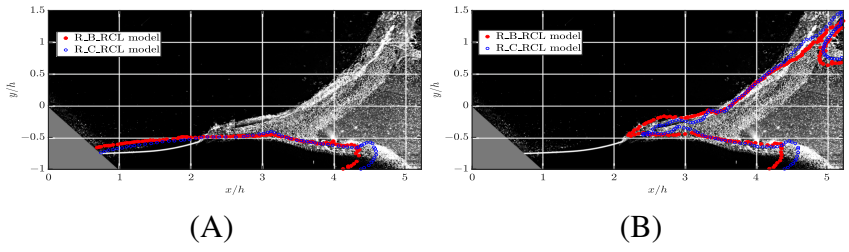

Fig. 4.11 Water-granular material interaction: confrontation between R_C_RCL (red point) and R_B_RCL (blue circle) rheological models overlaid on the original experiment PIV snapshot of Fritz et al. [382] at $T = 3.61$. (A): represent the granular material profile and (B) the water wave profile

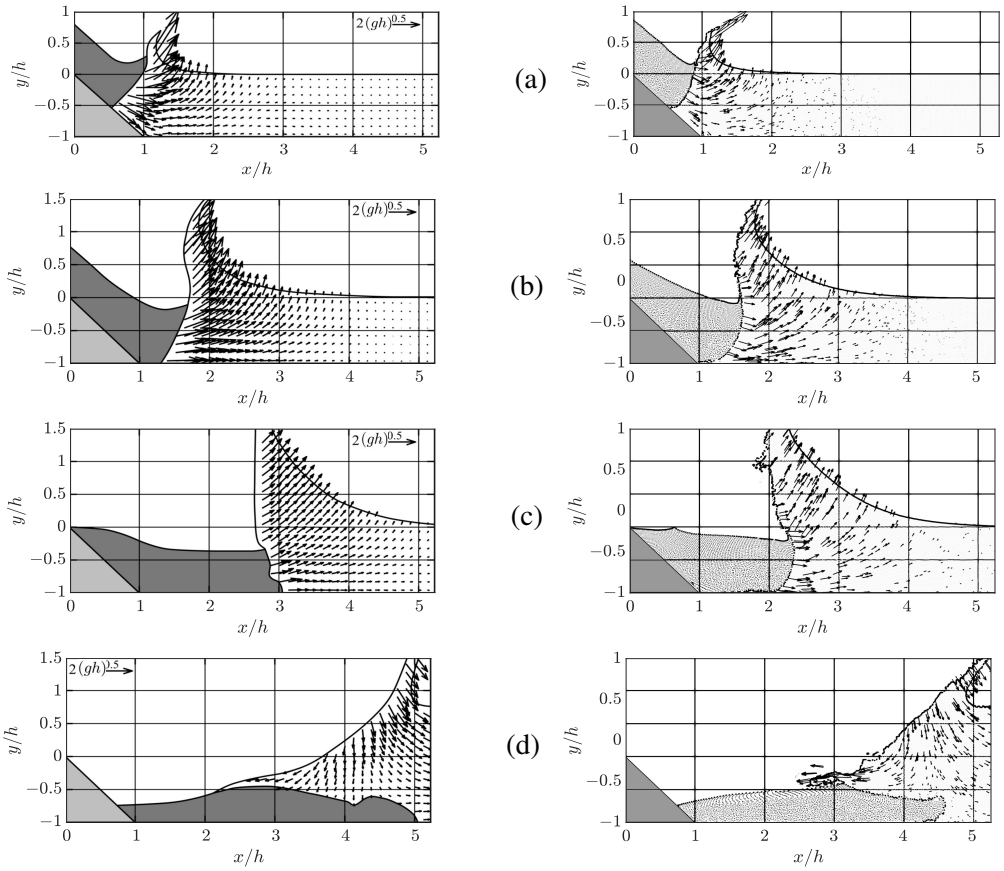

(A)

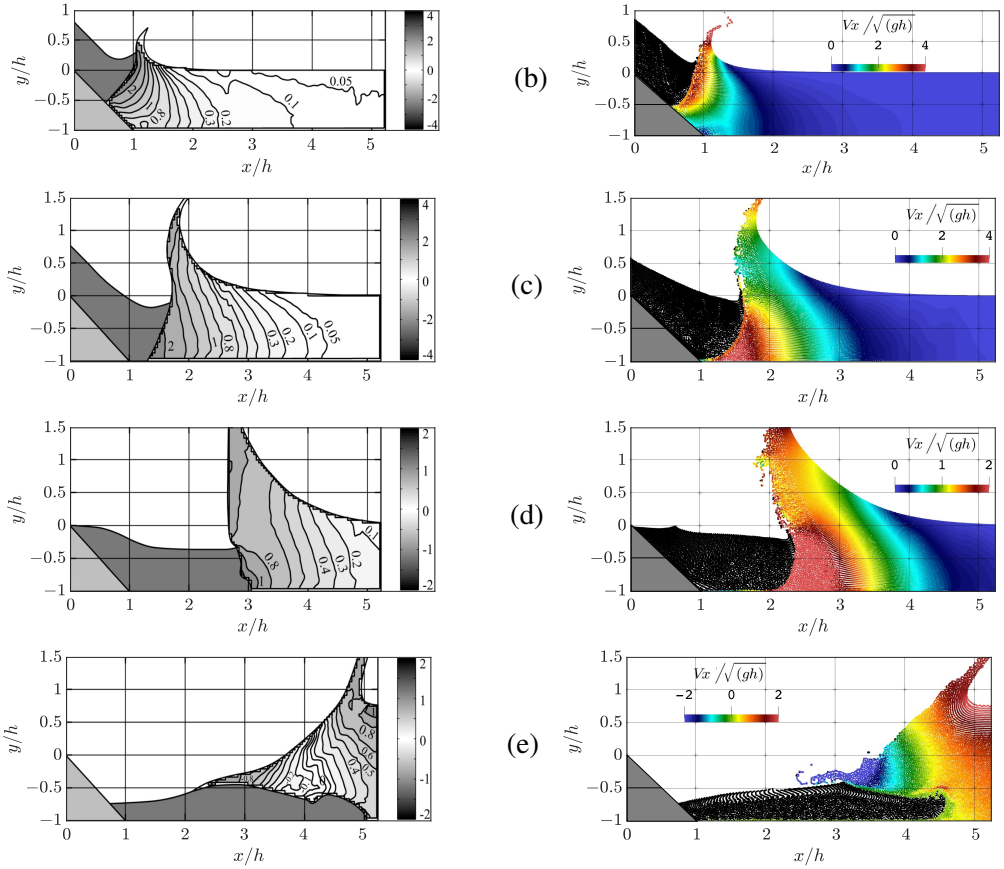

(B)

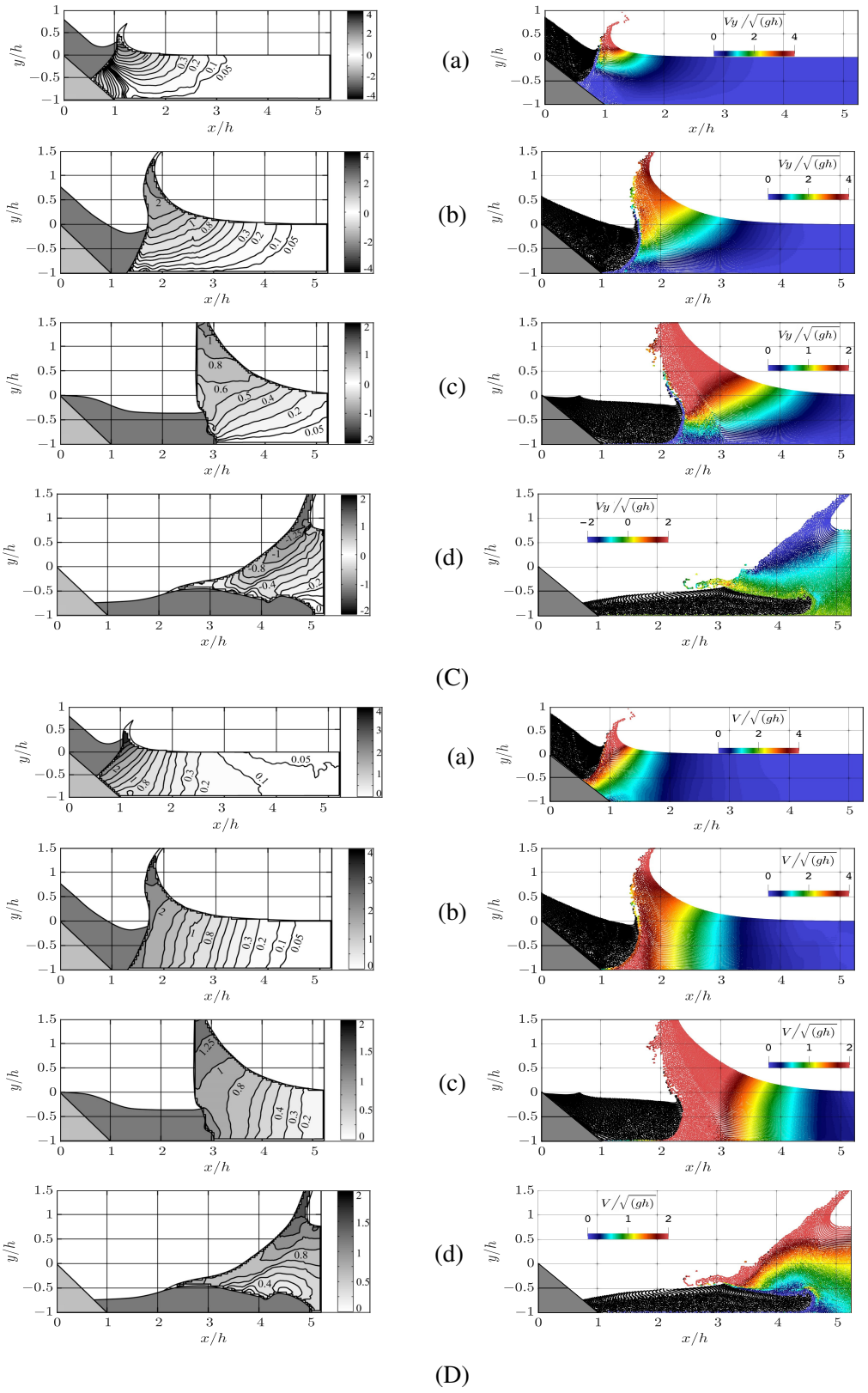

Fig. 4.11 Subaerial landslide-tsunamis: comparison between the numerical results of R_C_RCL model (right column) and the experimental results of [382] (left column) at relative time $t(gh)^{0.5}$: (a)=0.18, (b)=0.56, (c)=1.33, (d)=3.61; with: (A) Velocity vector fields; (B) Horizontal particle velocity fields; (C) Vertical particle velocity fields; (D) Absolute particle velocity fields

fluid flow patterns. As illustrated in Fig. 4.11 (A), these vector fields vividly represent the intricate directional flow dynamics of the water. It is noteworthy that the highest velocities are concentrated around the shoulder of the landslide, particularly where it makes contact with the water surface. This observation holds true for both experimental findings and numerical simulations.

The comparisons presented in Fig. 4.11 (B), (C), and (D) shed light on the agreement between the simulated horizontal, vertical, and magnitude particle velocity fields, obtained using our SPH model with the R_C_RCL constitutive law, and the empirically measured results from [382]. The interaction between the landslide material and the water surface leads to a significant transfer of kinetic energy. This energy is predominantly absorbed by the water body, manifesting in heightened velocity levels and the generation of a substantial propagating wave. This phenomenon underscores the intricate interplay between granular material and fluid dynamics, a critical aspect in understanding and predicting natural events like subaerial landslides.

4.3.2 Submarine landslide induced generated water waves

Submarine landslide along an inclined plane (Grilli et al. benchmark [13])

The following validation test case is a submarine deformable landslide. Herein, we reproduce the experiment of [13] where our numerical approach, using R_C_RCL SPH model, is applied to model the collapse of a fully submerged granular material. The experiment was conducted in a 6.27 m long, 0.25 m wide tank with an initial water depth of 0.33 m. The water free-surface evolutions were measured by four resistive gauges placed at 0.6, 1.6, 2.6, 3.6 m from a movable vertical gate which was initially used to retain the landslide material before starting to flow down an inclined ramp of 35°. A high-speed video camera was used to record the dynamic behavior of the water, landslide, and their interactions. The landslide mass consisted of glass beads with an effective internal friction angle $\phi = 34°$, a dynamic bed friction angle $\delta = 24°$, a grain diameter $dg = 4$ mm, and a grain density 2500 kg/m^3. Herein, the bulk density is used as a mix $\rho_s = \rho_w(1 - n_{por}) + \rho_g(n_{por}) = 1951$ kg/m^3 with a porosity of $n_{por} = 0.634$.

In contrast to the subaerial case, where the landslide was accelerated to get a high impact velocity, here the landslide mass ($m_s = 2$ kg) with an initially triangle shape placed on an inclined slope of 35° and with a cross-section of 0.12 m $\times$ 0.084 m, collapsed inertially, once the vertical gate was withdrawn. The initial slide submergence was 0.0422 m. The submarine landslide benchmark setup with more geometrical details and material descriptions is shown in Fig. 4.12.

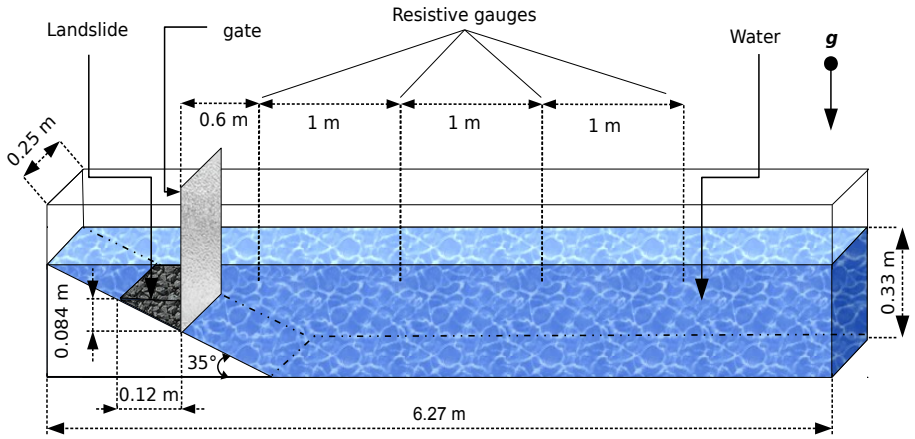

Fig. 4.12 Water-granular material interaction: Geometrical details and material descriptions of submarine landslide-tsunami experimental benchmark. Figure based on that presented in [10]

The density $\rho_w = 1000$ kg/m^3 and the dynamic viscosity $\mu_w = 0.001$ pa.s are used for the water. The Casson plastic viscosity of the landslide is chosen to be equal to the water dynamic viscosity $\mu = \mu_s = \mu_w = 0.001$ pa.s and the maximum effective viscosity $\max(\mu_{eff}) = 10$ pa.s, corresponding to the value of $\alpha_\mu = 100$, is used accordingly to $\max(\mu_{eff}) = \alpha_\mu^2 \mu$.

The numerical simulation for this benchmark is adapted with an initial inter-particle spacing of $\delta x = 0.0025$ m that returns a total number of 293803 SPH particles (285605 particles for water, 797 particles for the landslide, and 7401 particles for boundaries). The reference speed of sound $c_0 = 30$ m/s is selected, and a no-slip boundary condition is adopted for all tank channel walls.

Fig. 4.13 shows snapshots of laboratory experiments on submarine landslide-water interactions conducted by [13] compared to the simulation results performed by the SPH model of the current study and those found by [384] using SPH with a Coulomb friction wall boundary condition model. At time $t = 0.02$ s, the result obtained by the SPH model of [384] is somewhat closer to the experimental snapshot than our SPH model. This result is expected since we did not take into account the withdrawing of the gate effects in the current work. However, for the times $t = 0.17$, 0.32, and 0.47 s, our SPH model reproduces results that are more consistent with experimental ones, where the landslide profile has exhibited a thick front and a thin trailing as previously discussed by [17], compared to the model of [384] in which the landslide particles were significantly scattered in the water body, especially with advancing in time ($t = 0.32$ and 0.47 s). Nevertheless, a notable delay and an amplitude shift are observed between the two numerical landslides and the experimental results that slided faster than in both SPH models. This issue could be due to the use of a constant value for the

bulk density while the porosity is changing within the physical case; it could also be due to 3D effects.

Submarine landslide along an inclined plane (Rzadkiewicz et al. benchmark [13])

The laboratory-scale investigation established by Rzadkiewicz et al. [385] stands as one of the most renowned experiments on submarine landslides, extensively recreated numerically due to its ability to vividly illustrate the dynamic processes inherent to such flow phenomena.

In this benchmark, water was introduced into a reservoir with dimensions of 0.3 m in width, 4 m in length, and 2 m in height, reaching an initial level of 1.6 m. Positioned over a sloped plane inclined at 45° and supported by a retractable gate, A triangular-shaped sand mass, with dimensions spanning 0.65 m in both length and width, was positioned. The sand, possessing a volume of 63 dm^3, was initially positioned 10 cm below the horizontal water surface (depicted in Fig. 4.14). While the water's density is 1000 kg/m^3, the sand's mean apparent density amounts to 1950 kg/m^3.

The numerical model employs a discretization scheme, where the physical domain is partitioned with an inter-particle separation of $\delta x = 0.001$, leading to a total of 35,680 particles for the fluid and 2,145 particles for the granular material. The water behavior is modeled using a Newtonian fluid rheology, with a constant dynamic viscosity of $\mu_w = 10^{-3}$ Pa·s, while the sand is initially considered as a Newtonian fluid (with $\mu_s = 10^{-3}$ Pa·s and $\tau_y = 0$ Pa) and subsequently as a non-Newtonian fluid obeying the generalized Casson constitutive law. This shift is performed to evaluate the effectiveness of the proposed rheological model. In the latter case, the rheological parameters utilized align with those chosen by [385], specifically $\tau_y = 200$ Pa and 1000 Pa, respectively.

In Fig. 4.15, we compare the dynamic behaviors of the granular flow using three different rheological parameters: a Newtonian fluid model with $\tau_y = 0$ (Fig. 4.15(B)), a generalized Casson model with $\tau_y = 200$ (Fig. 4.15(C)), and a generalized Casson model with $\tau_y = 1000$ (Fig. 4.15(D)). These simulations are contrasted with the experimental results (Fig. 4.15(A)), which originally captured the granular mass positions at two different times, $t = 0.4$ and 0.8 s. In all scenes, we observe that upon lifting the gate, the sand mass freely descends into the water, generating water waves. However, each simulation case depicts distinct granular flow deformations, resulting in water waves with varying amplitudes and free surface profiles.

The Newtonian model (Fig. 4.15(B)) indicates that the granular material at the interface erodes and scatters significantly within the water body over time. This model's accuracy is limited due to its lack of mechanical characteristics to adequately represent the granular flow. Conversely, the generalized Casson rheological model depicts a more rigid granular mass, with its deformation proportional to the yield stress criterion τ_y. As seen in Figs. 4.15(C) and

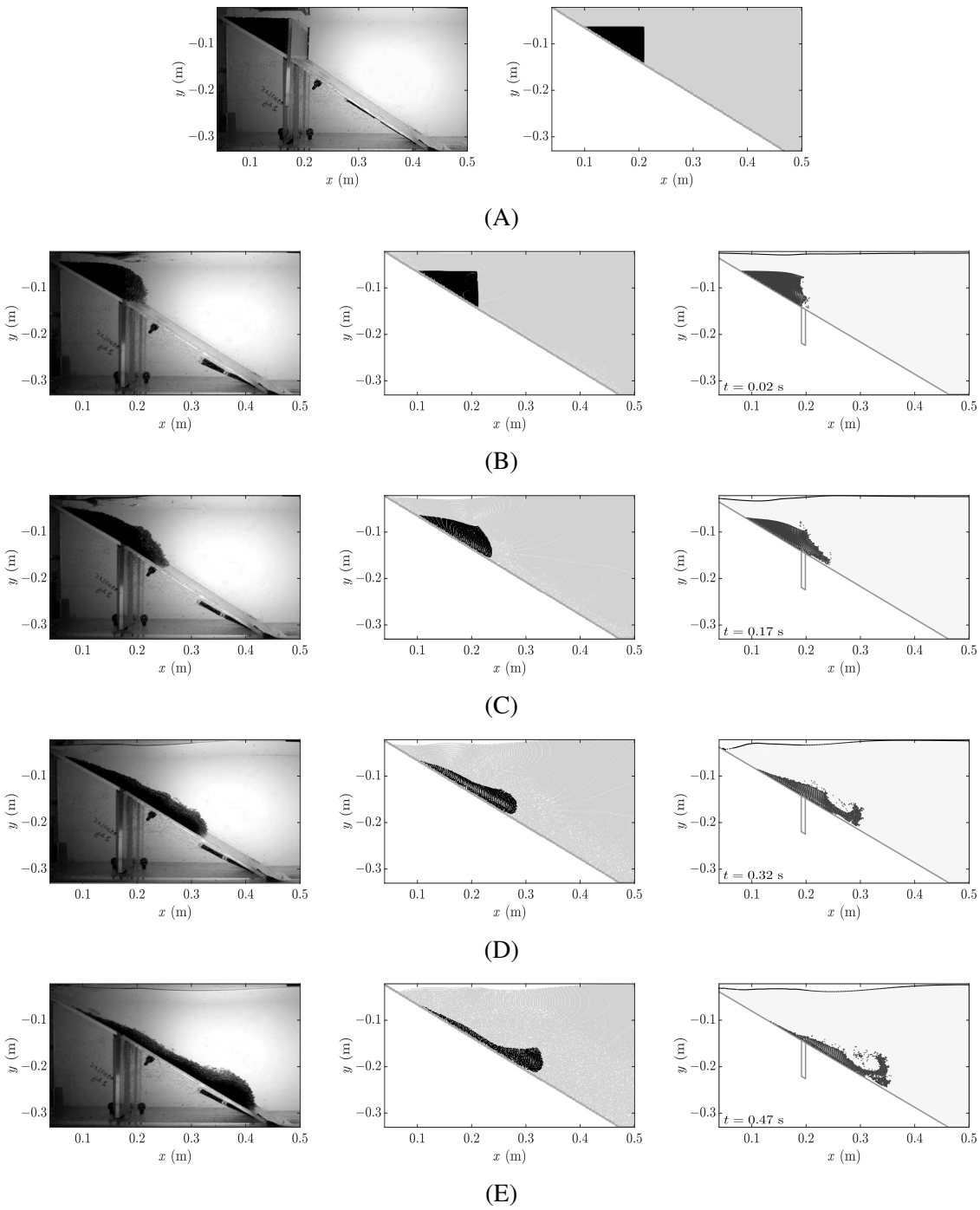

Fig. 4.13 Submarine landslide-tsunamis: comparison between the numerical results of the present work (middle column), the experimental results of Grilli et al. [13] (left column), and the numerical results of Ghaitanellis et al. [384] (right column) at t: (A)=0 s, (B)=0.02 s, (C)=0.17 s, (D)=0.32 s and (E)=0.47 s

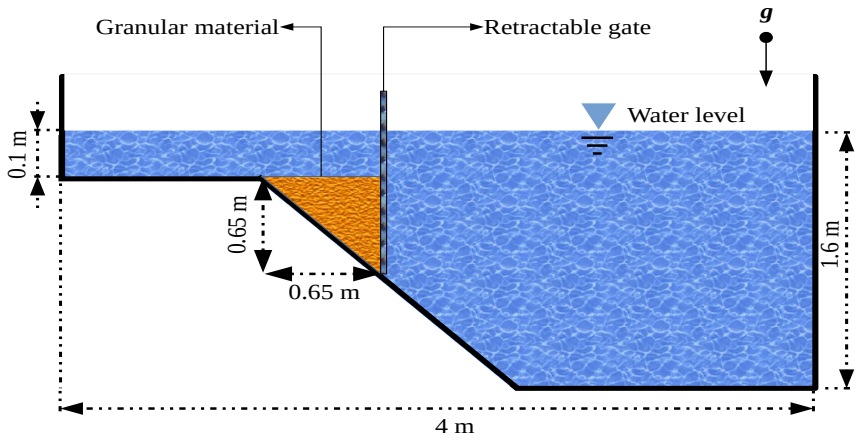

Fig. 4.14 Description of the initial configuration of the submarine landslide along an inclined plane

4.15(D), the granular flow demonstrates more shear strain with a yield stress of $\tau_y = 200$ Pa compared to $\tau_y = 1000$ Pa.

Given that the experiment's screenshots describing the underwater granular flow's overall behavior lacked clarity, we undertake a quantitative comparison. Specifically, we compare the experimental water wave profiles at the free surface with those computed using our model with the three aforementioned rheological models: $\tau_y = 0$, 200, and 1000 Pa, respectively (Fig. 4.16). At $t = 0.4$ s, the Newtonian rheology ($\tau_y = 0$ Pa) deviates more from the experimental results compared to the generalized Casson rheological model, which closely aligns with the experimental outcomes, particularly with $\tau_y = 1000$ Pa. Over time, at $t = 0.8$, the inadequacy of the Newtonian rheology becomes more apparent, progressively diverging from the experimental results. In contrast, the generalized Casson rheological model effectively predicts the water wave profiles, contingent upon the appropriate yield stress value. For instance, the generalized Casson rheological model with $\tau_y = 1000$ Pa closely matches the experimental wave amplitude, in contrast to $\tau_y = 200$ Pa, which exhibits less significant viscous effects. Similar observations about yield stress value were noted by [386] and [387] using other numerical approaches.

In Fig. 4.17, a comparison is made between the numerical predicted granular mass shapes at times $t = 0.4$ and 0.8 s, utilizing the generalized Casson rheological model from our current work with $\tau_y = 1000$ Pa, to the results obtained by [25] and [150] using the $\mu(I)$ and Herschel-Bulkley rheological models, respectively. At $t = 0.4$ s, a noticeable agreement is observed among all the numerical results. However, at $t = 0.8$ s, substantial quantitative

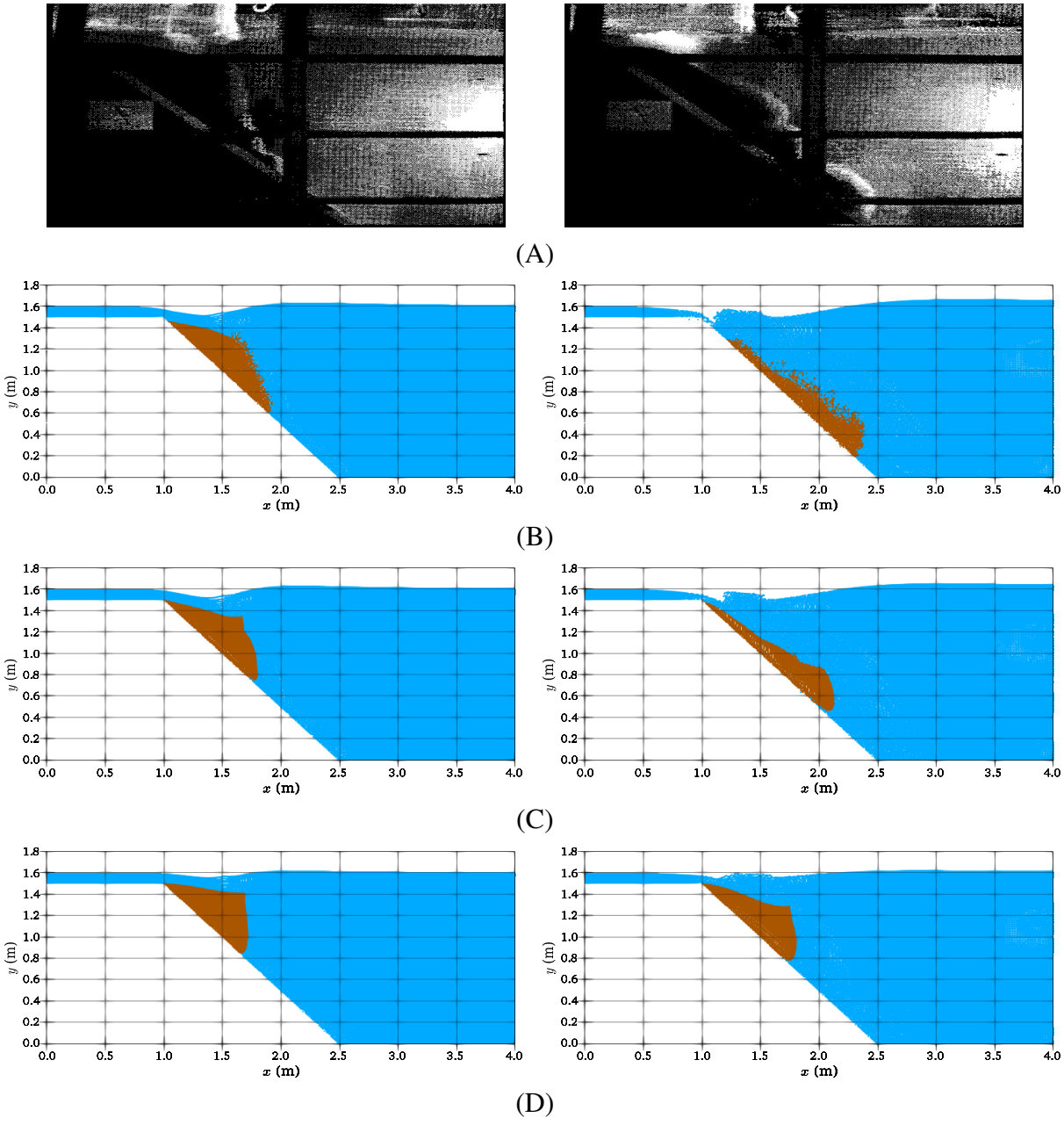

Fig. 4.15 Submarine landslide: comparison between the experimental sequences ((A) row) and the numerical results achieved using the generalized Casson rheological model of the current study, with $\tau_y = 0$ pa ((B) row), $\tau_y = 200$ pa ((C) row), and $\tau_y = 1000$ pa ((D) row), at t=0.4 s (left) and t=0.8 s (right)

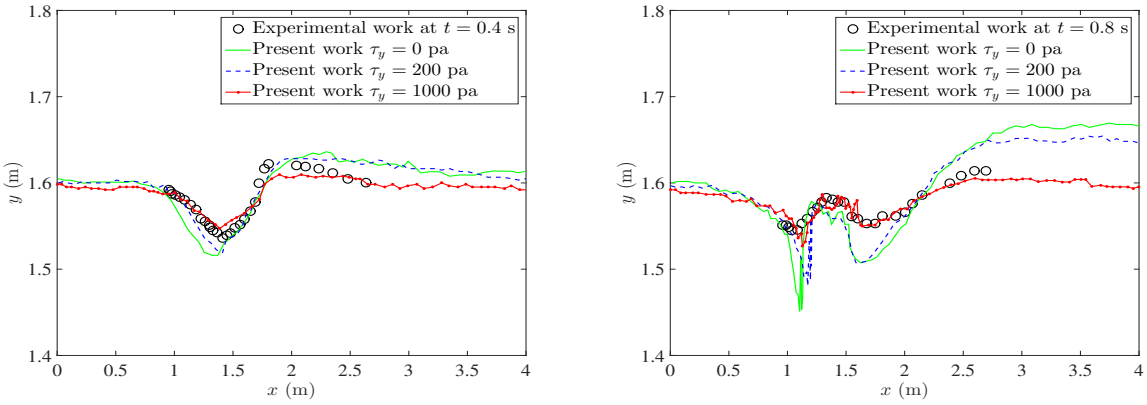

(A) (B)

Fig. 4.16 Submarine landslide: comparison between the experimental water waves profiles (black circles) and the numerical results achieved using the generalized Casson rheological model of the current study, with $\tau_y = 0$ pa (green line), $\tau_y = 200$ pa (dashed blue line), and $\tau_y = 1000$ pa (dotted red line), at t=0.4 s (left) and t=0.8 s (right)

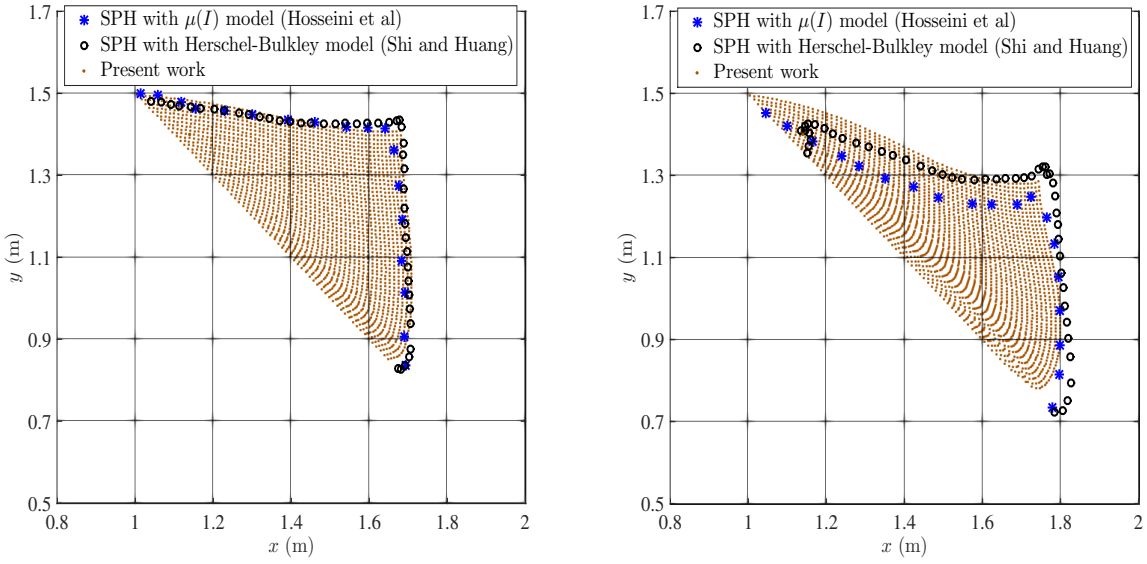

(A) (B)

Fig. 4.17 Submarine landslide: comparison between the numerical granular material profiles achieved using the generalized Casson rheological model of the current study (brown points), the $\mu(I)$ rhological model of Hosseini et al. [25] (blue stars), and the Herschel-Bulkley rhological model of Shi and Huang [150] (black circles), with $\tau_y = 1000$ pa at t=0.4 s (left) and t=0.8 s (right)

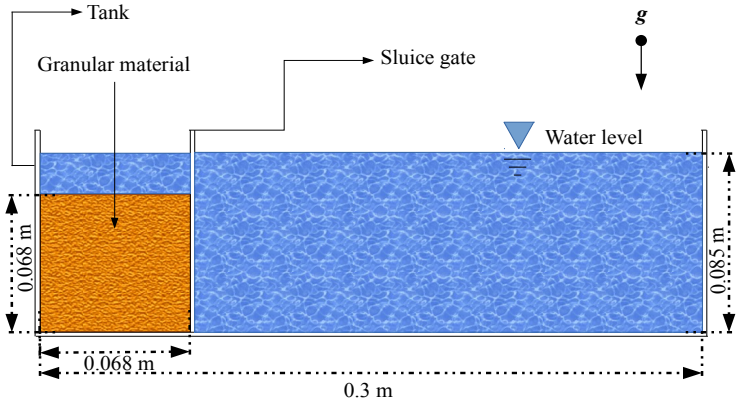

Fig. 4.18 Description of the initial configuration of the immersed granular column collapse benchmark

changes have occurred in the granular mass shapes, leading to notable discrepancies across the models. Although all numerical models predict an almost identical flow front profile, distinct deviations are evident. Regrettably, the absence of experimental results for this comparison prevents us from determining the most suitable model for replicating the granular flow behavior.

Immersed granular column collapse

In this segment, we employ the SPH model proposed in our study to replicate the gravity-driven experimental benchmark conducted by [388]. The experiment took place within a rectangular cross-hatched tank, measuring 0.1 m in width, 0.3 m in length, and 0.1 m in height. The initial setup involved partially filling the tank with water, forming a parallelepiped with dimensions $L_w \times H_w \times W_w = 0.3 \times 0.08 \times 0.1$ m^3. Inside this configuration, a pile of granular mass, featuring a squared cross-section of $L_g \times H_g = 0.068 \times 0.068$ m^2, was retained by a sluice gate, as depicted in Fig. 4.18. The granular material consisted of glass beads, characterized by a grain density of $\rho_g = 2470$ kg/m^3, a mean grain diameter of $d_g = 0.0008$ m, and a friction angle $\theta = 22°$, and a volume fraction of the grains $\phi = 0.64$. Water's dynamic viscosity is $\mu_w = 0.001$ Pa·s, and its density is $\rho_w = 1000$ kg/m^3, yielding a bulk density of $\rho_s = \rho_w(1-\phi) + \rho_g(\phi) = 1940.8$ kg/m^3 for the granular mass. The starting time is set to $t = 0$ when the sluice gate is definitively opened. At this point, the granular mass begins to undergo inertial collapse under the effect of gravitational acceleration.

The simulation setup involves an inter-particle spacing of $\delta x = 0.002$ m, leading to the placement of 5294 SPH particles for fluid phase and 1156 for granular material phase. The artificial sound speed is prescribed as $c_0 = 10$ m/s, derived through computation in accordance with the equation provided in Eq. 3.4. Water's behavior adheres to the conventional Newtonian rheology, while the granular material adopts a non-Newtonian rheology characterized by the generalized Casson constitutive law. For the granular material, the Casson dynamic viscosity is specified as $\mu_s = \mu_w = 0.001$ Pa·s.

In Figure 4.19, a comparison is presented between the simulation findings of our current study, utilizing the SPH model, and simulated outcomes of [388], where the Moving Particle Semi-implicit (MPS) Scheme was employed for depicting the evolving deformation of the collapsed granular mass and the dynamic patterns of the resulting water waves.

These results are juxtaposed with the experimental findings at different time instances: $t = 0$, 0.17, 0.33, and 0.49 seconds. On the whole, the simulations of gravity-driven flows during submerged granular collapse using both the SPH and MPS approaches correspond well to the experimental observations. In these simulations, the sliding granular mass accelerates and disperses initially, subsequently decelerating until it comes to a halt, eventually forming a granular deposit with a triangular shape and a diminished final height compared to the initial one. This pattern concurs with conclusions from other studies in a similar context([389–391]). The sole discrepancy lies in the fact that the morphology of the granular mass in both our SPH and MPS models appears slightly thicker than that observed in the experiment.

In Figure 4.20, additional evidence is presented, showcasing the strong compatibility between the numerical outcomes of both the SPH and MPS models and the experimental snapshots. This is achieved through a comparison of the distance traversed by the front of the granular particles when contrasting experimental data with the results from both the SPH and MPS methods. The normalized displacement $L(T) = (L(t) - L_g)/L_g$ is plotted against the normalized time evolution $T = t\sqrt{H_g/g}$. Remarkably, the curves of both the experimental and numerical results exhibit significant similarity, with the SPH model displaying a slight advantage in its proximity to the experimental findings compared to the MPS model.

This advantage of the current SPH model becomes notably evident when comparing the shapes of the granular mass at various time instances, as depicted in Figure 4.21. In this visualization, the numerical outcomes of the MPS model as presented by [388] exhibit broader profiles compared to both the SPH model and the experimental data. Despite this, neither of the two numerical models effectively predicted the shape of the granular material front at $t = 0.33$ s. This discrepancy could potentially arise from 3D effects and the variations in the actual sizes of the granules constituting the granular material, which might not be exactly uniform in the real-world scenario.

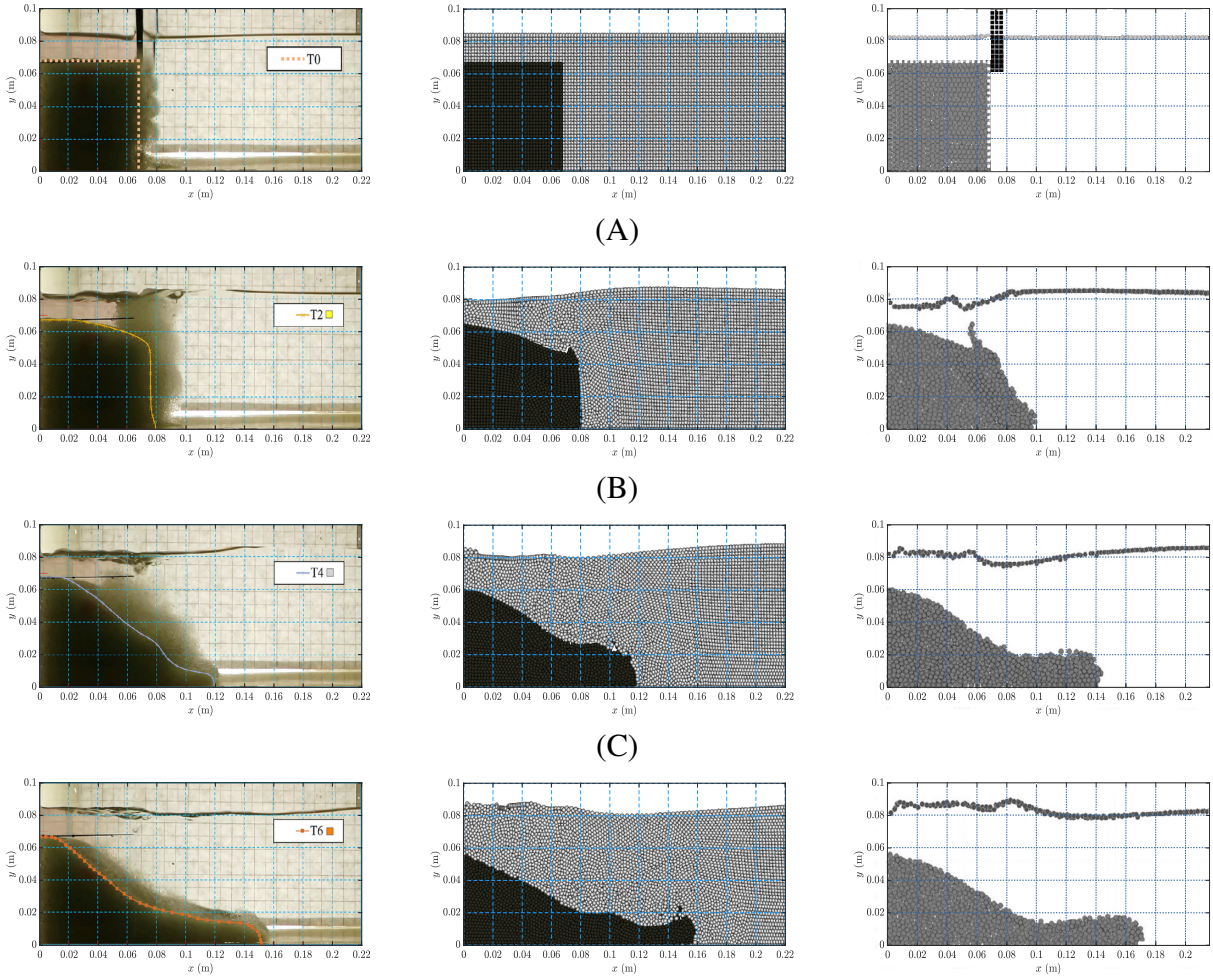

Fig. 4.19 Immersed granular column collapse: Comparison between the temporal evolution of the experimental results of Jandaghian et al. [388](left column),the numerical results of Jandaghian et al. [388] using MPS model (right column), and the present SPH model results (middle column) at times t: (A)=0 s, (B)=0.17 s, (C)=0.33s, and (D)=0.49 s

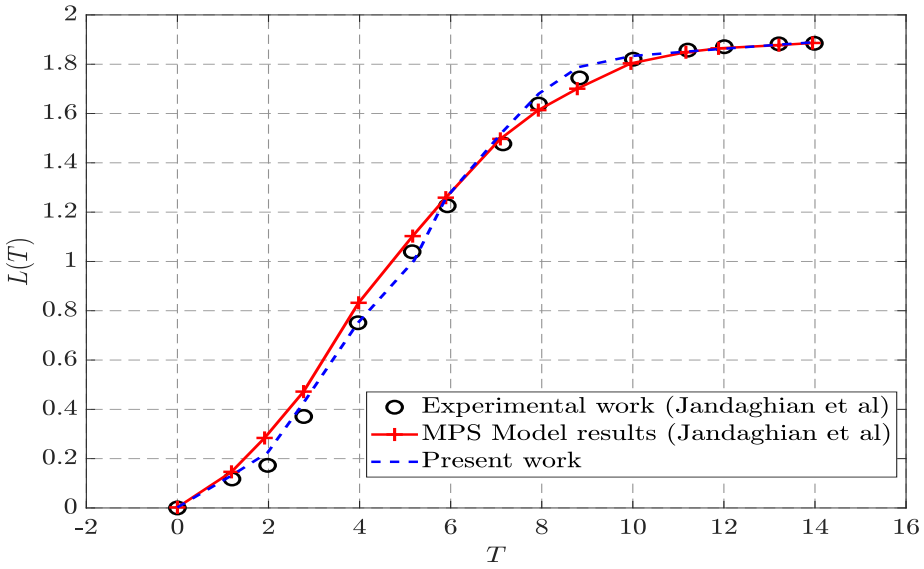

Fig. 4.20 Immersed granular column collapse: Comparison between the temporal evolution of the normalized traveled distance by the front of the granular material obtained in the experimental results of Jandaghian et al. [388](black circles),the numerical results of Jandaghian et al. [388] using MPS model (the red lines with + signs), and the present SPH model results (dashed blue line)

To gain insight into how the movement of the granular particles influences the development of water free surface, Figure 4.22 offers a comparison among the water waves generated. It includes data extracted from the experimental records, the numerical results provided by [388] utilizing the MPS model, and the simulated outcomes generated by the current SPH model at different time points ($t = 0.17$, 0.33, and 0.49 s). Although some disparities exist between the experimental data and the numerical simulations, particularly evident at $t = 0.17$ s, the SPH model presented in this work yields outcomes that are closer to the experimental observations when compared to the MPS model. This trend is more pronounced as time progresses ($t = 0.33$ and 0.49 s). The dissimilarities could potentially stem from factors such as the mechanics of the gate removal process, the estimation of bulk density in the real-world scenario, or the influence of three-dimensional effects, which were not taken into consideration in the simulation setups. Overall, this test case effectively demonstrates that the proposed numerical SPH model can aptly reproduce the core dynamic phenomena exhibited in gravity-driven flows during submerged granular collapses.

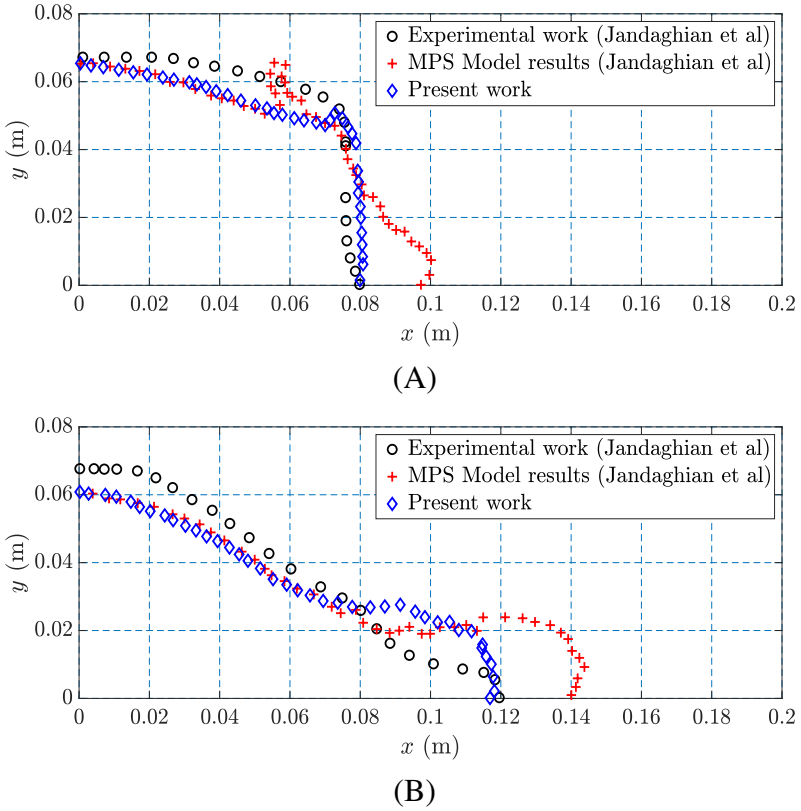

Fig. 4.21 Immersed granular column collapse: comparison between the experimental granular material profiles of Jandaghian et al. [388](black circles), the numerical results of Jandaghian et al. [388] using MPS model (the red + signs), and the present SPH model results (blue diamond) at times t: (A)=0.17 s, and (B)=0.33 s

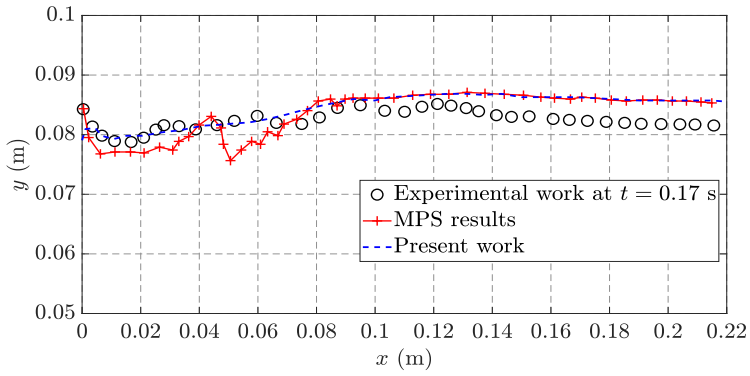

(A)

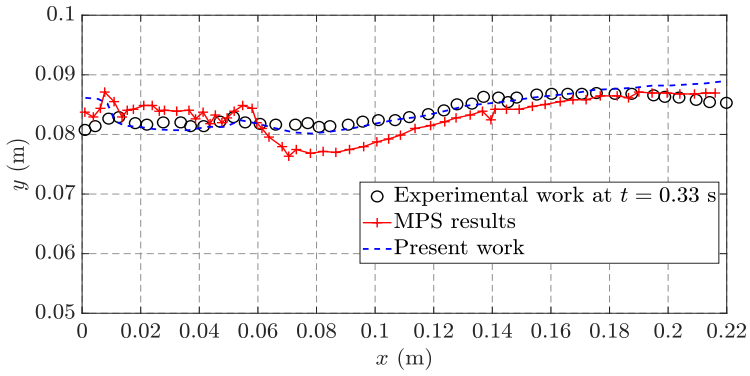

(B)

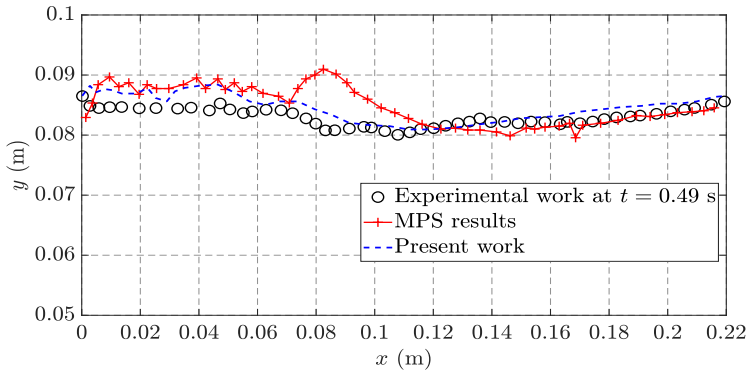

(C)

Fig. 4.22 Immersed granular column collapse: Comparison between the evolution of the water free surface obtained in the experimental results of [388](black circles),the numerical results of [388] using MPS model (the red lines with + signs), and the present SPH model results (dashed blue line) at t: (A)=0.17 s, (B)=0.33 s, and (C)=0.49 s

Conclusions and Perspectives

In conclusion, this thesis represents a significant advancement in the field of Fluid-Structure Interaction (FSI) modeling and simulation, particularly focusing on the interaction between fluids and granular materials through the application of the Smoothed Particle Hydrodynamics (SPH) method. The work underscores the critical role of rheological models, specifically the Bingham and Casson constitutive laws, in describing the behavior of granular materials within the SPH framework. A noteworthy contribution lies in the generalization of these rheological models, a process aimed at mitigating numerical discontinuities inherent in the original laws. This novel implementation substantially enhances the accuracy and robustness of simulation outcomes. The detailed exposition of the implementation process, encompassing the equations and numerical methods employed, provides a valuable resource for researchers and practitioners in the field.

The thesis rigorously validates the implemented models through a series of comprehensive numerical simulations, involving the interaction between fluids and granular materials. These results are thoughtfully compared with experimental data and outcomes from other numerical approaches, establishing a solid foundation for the validity and reliability of the proposed methodology. Moreover, a sensitivity analysis of the numerical parameters within the SPH method offers critical insights into their impact on simulation outcomes, further refining our understanding of this powerful computational technique. In addition to the specific contributions mentioned above, this research also brings forth a spectrum of key advancements in the SPH methodology itself. These encompass improvements in SPH method algorithms, a diversity of SPH algorithms for governing equation discretization, the development of a dedicated weakly compressible SPH code tailored for complex water-granular material interactions, and the introduction of innovative constitutive laws to address coupled dynamics. Additionally, the incorporation of a multiphase diffusive term and generalized wall boundary conditions significantly expands the applicability of SPH simulations. A comprehensive comparison of rheological models and rigorous validation studies further augment the robustness of the SPH model.

Overall, this research demonstrates the efficacy of the SPH method in modeling fluid-granular material interaction, highlighting the pivotal role of generalized non-Newtonian rheological models. The contributions made in this thesis are poised to significantly influence and advance future research in the domain of fluid-structure interaction modeling and simulation.

From the perspectives of advancing SPH modeling in the framework of FSI, there lie several avenues for further exploration and refinement. The following are potential areas of interest for future research:

- Multi-Physics Phenomena Simulation: Augment the computational framework to include the modeling of other physical natures, such as the interaction of rigid bodies with fluids, as well as elastic and elasto-plastic models. This expansion will enable the simulation of multi-physics phenomena, providing a more comprehensive representation of complex real-world FSI scenarios.

- Multi-Phase FSI Modeling: Extend the current framework to encompass scenarios involving multiple phases, such as air-liquid-solid interactions. This could involve developing specialized rheological models and numerical techniques tailored to these complex scenarios.

- Solid-Solid SPH Particle Interactions: Incorporate solid-solid interactions using SPH particles to model the behavior of different granular materials in contact. This extension will enable the simulation of interactions between solid particles, further enhancing the versatility of the computational framework.

- Extension to 3D Simulations: Expand the existing 2D SPH model into a 3D framework. This enhancement will allow for the simulation of more complex and realistic scenarios, providing a more accurate representation of 3D phenomena.

- Advanced Material Models: Explore the incorporation of more sophisticated material models to capture the behavior of complex granular materials, including those exhibiting non-Newtonian, viscoelastic, or viscoplastic properties.

- Interactive Interface Development: Create an interactive interface for the developed code used in this thesis. This interface will facilitate user-friendly interactions with the computational framework, making it accessible to a wider range of researchers and engineers for various applications.

References

[1] Josef Ballmann. *Flow Modulation and Fluid—Structure Interaction at Airplane Wings: Research Results of the Collaborative Research Center SFB 401 at RWTH Aachen, University of Technology, Aachen, Germany*, volume 84. Springer Science & Business Media, 2012. 1

[2] Edwin Kreuzer. *IUTAM Symposium on Fluid-Structure Interaction in Ocean Engineering: Proceedings of the IUTAM Symposium Held in Hamburg, Germany, July 23-26, 2007*, volume 8. Springer Science & Business Media, 2008.

[3] François Axisa and Jose Antunes. *Modelling of mechanical systems: Fluid-structure interaction*, volume 3. Elsevier, 2006.

[4] Giovanni Paolo Galdi and Rolf Rannacher. *Fundamental trends in fluid-structure interaction*, volume 1. World Scientific, 2010.

[5] Z. Dai, Y. Huang, H. Cheng, and Q. Xu. SPH model for fluid-structure interaction and its application to debris flow impact estimation. *Landslides*, 14(3):917–928, 2017. https://doi.org/10.1007/s10346-016-0777-4. 1, 80

[6] H-J. Bungartz and M. Schäfer. *Fluid-structure interaction modelling, simulation, optimisation*, volume 53. Springer Science & Business Media, 2006. 1, 5, 103

[7] Wen-Jie Xu, Xue-Yang Dong, and Wen-Tao Ding. Analysis of fluid-particle interaction in granular materials using coupled sph-dem method. *Powder Technology*, 353:459–472, 2019. 1

[8] Lu Liu, Jie Wu, and Shunying Ji. Dem–sph coupling method for the interaction between irregularly shaped granular materials and fluids. *Powder Technology*, 400:117249, 2022.

[9] Farhang Radjai, Jean-Noël Roux, and Ali Daouadji. Modeling granular materials: century-long research across scales. *Journal of engineering mechanics*, 143(4):04017002, 2017. 1

[10] Abderrahmane Mahallem, Mohamed Roudane, Abdelkader Krimi, and Sid Ahmed Gouri. Smoothed particle hydrodynamics for modelling landslide–water interaction problems. *Landslides*, 19(5):1249–1263, 2022. https://doi.org/10.1007/s10346-021-01807-1. 1, 29, 46, 80, 81, 91, 98, 104, 111

[11] A. Romano, J. L. Lara, G. Barajas, B. Di Paolo, G. Bellotti, M. Di Risio, I. J. Losada, and P. De Girolamo. Tsunamis generated by submerged landslides: numerical analysis of the near-field wave characteristics. *Journal of Geophysical Research: Oceans.*, 125(7):e2020JC016157, july 2020. https://doi.org/10.1029/2020JC016157.

[12] . Qiu, L-C., F. Jin, . Lin, P-Z., Y. Liu, and Y. Han. Numerical simulation of submarine landslide tsunamis using particle based methods. *Journal of Hydrodynamics*, 29(4):542–551, 2017. https://doi.org/10.1016/S1001-6058(16)60767-9.

[13] S. T. Grilli, M. Shelby, O. Kimmoun, G. Dupont, D. Nicolsky, G. Ma, J. T. Kirby, and F. Shi. Modeling coastal tsunami hazard from submarine mass failures: Effect of slide rheology, experimental validation, and case studies off the US East Coast. *Natural Hazards*, 86:353–391, 2017. https://doi.org/10.1007/s11069-016-2692-3. 110, 111, 112, 113

[14] A Najafi-Jilani and B Ataie-Ashtiani. Estimation of near-field characteristics of tsunami generation by submarine landslide. *Ocean Engineering*, 35(5-6):545–557, 2008. https://doi.org/10.1016/j.oceaneng.2007.11.006. 1

[15] et al. Higman, B. The 2015 landslide and tsunami in taan fiord, alaska. *Scientific reports*, 8:12993, 2018. 1

[16] Cheng-Hsien Lee and Zhenhua Huang. Multi-phase flow simulation of impulsive waves generated by a sub-aerial granular landslide on an erodible slope. *Landslides*, 18(3):881–895, 2021. https://doi.org/10.1007/s10346-020-01527-y. 1, 29, 38

[17] S Yavari-Ramshe and Behzad Ataie-Ashtiani. A rigorous finite volume model to simulate subaerial and submarine landslide-generated waves. *Landslides*, 14(1):203–221, 2017. https://doi.org/10.1007/s10346-015-0662-6. 79, 111

[18] S. Yavari-Ramshe and B. Ataie-Ashtiani. Numerical modeling of subaerial and submarine landslide-generated tsunami waves–recent advances and future challenges. *Landslides*, 13(6):1325–1368, 2016. https://doi.org/10.1007/s10346-016-0734-2.

[19] S. Viroulet, D. Cébron, O. Kimmoun, and C. Kharif. Shallow water waves generated by subaerial solid landslides. *Geophysical Journal International*, 193(2):747–762, 2013. https://doi.org/10.1093/gji/ggs133. 1

[20] Nikhil Prakash, Andrea Manconi, and Simon Loew. A new strategy to map landslides with a generalized convolutional neural network. *Scientific reports*, 11(1):9722, 2021. 1

[21] Abdelkader Krimi, Sofiane Khelladi, Xesús Nogueira, Michael Deligant, Riadh Ata, and Mehdi Rezoug. Multiphase smoothed particle hydrodynamics approach for modeling soil–water interactions. *Advances in Water Resources*, 121:189–205, 2018. https://doi.org/10.1016/j.advwatres.2018.08.004. 1, 2, 47, 57, 59, 68, 80, 81, 87, 91, 93

[22] Hamzah M Beakawi Al-Hashemi and Omar S Baghabra Al-Amoudi. A review on the angle of repose of granular materials. *Powder technology*, 330:397–417, 2018.

[23] Tore Børvik, Sumita Dey, and L Olovsson. Penetration of granular materials by small-arms bullets. *International Journal of Impact Engineering*, 75:123–139, 2015. 1

[24] A. M. Xenakis, S. J. Lind, P. K. Stansby, and B. D Rogers. Landslides and tsunamis predicted by incompressible smoothed particle hydrodynamics (SPH) with application to the 1958 Lituya Bay event and idealized experiment. *Proceedings of The Royal Society A: Mathematical, Physical and Engineering Sciences*, 473(2199):20160674, 2017. https://doi.org/10.1098/rspa.2016.0674. 1, 80, 82

[25] K. Hosseini, P. Omidvar, M. Kheirkhahan, and S. Farzin. Smoothed particle hydrodynamics for the interaction of Newtonian and non-Newtonian fluids using the $\precneqq(I)$ model. *Powder Technology*, 351:325–337, 2019. https://doi.org/10.1016/j.powtec.2019.02.045. 1, 83, 114, 116

[26] Ha H Bui and Giang D Nguyen. Smoothed particle hydrodynamics (sph) and its applications in geomechanics: From solid fracture to granular behaviour and multiphase flows in porous media. *Computers and Geotechnics*, 138:104315, 2021. 1

[27] E. Mitsoulis. Flows of viscoplastic materials: models and computations. *Rheology Reviews*, pages 135–178, 2007. 2, 84

[28] Antonios M Xenakis, Steven J Lind, Peter K Stansby, and Benedict D Rogers. An incompressible smoothed particle hydrodynamics scheme for newtonian/non-newtonian multiphase flows including semi-analytical solutions for two-phase inelastic poiseuille flows. *International Journal for Numerical Methods in Fluids*, 92(7):703–726, 2020. https://doi.org/10.1002/fld.4802. 2, 89, 105

[29] Abdelkader Krimi, Mehdi Rezoug, Sofiane Khelladi, Xesús Nogueira, Michael Deligant, and Luis Ramírez. Smoothed particle hydrodynamics: a consistent model for interfacial multiphase fluid flow simulations. *Journal of Computational Physics*, 358:53–87, 2018. https://doi.org/10.1016/j.jcp.2017.12.006. 2, 18, 20, 80, 87, 88, 93, 98

[30] Yuri Bazilevs, Kenji Takizawa, and Tayfun E Tezduyar. *Computational fluid-structure interaction: methods and applications*. John Wiley & Sons, 2013. 5

[31] Xia Wu, Shuhao Niu, and Changjun Li. The study of the dynamic response of the natural gas pipeline aerial crossing during pigging process: A review. *Journal of Fluids and Structures*, 105:103339, 2021. 5

[32] Yuri Bazilevs and Kenji Takizawa. *Advances in computational fluid-structure interaction and flow simulation*. Springer, 2017. 5

[33] Alessandro Franci. *Unified Lagrangian formulation for fluid and solid mechanics, fluid-structure interaction and coupled thermal problems using the PFEM*. Springer, 2016. 5

[34] Rajeev K Jaiman and Vaibhav Joshi. *Computational Mechanics of Fluid-Structure Interaction*. Springer, 2022. 5, 6

[35] Jean-François Sigrist. *Fluid-structure interaction: an introduction to finite element coupling*. John Wiley & Sons, 2015. 5

[36] Thuan Lieu, Charbel Farhat, and Michel Lesoinne. Reduced-order fluid/structure modeling of a complete aircraft configuration. *Computer methods in applied mechanics and engineering*, 195(41-43):5730–5742, 2006. 5

[37] Ramji Kamakoti and Wei Shyy. Fluid–structure interaction for aeroelastic applications. *Progress in Aerospace Sciences*, 40(8):535–558, 2004. 5

[38] You-sheng Wu, Ming-song Zou, TIAN Chao, SIMA Can, Li-bo Qi, DING Jun, Zhi-wei Li, and LU Ye. Theory and applications of coupled fluid-structure interactions of ships in waves and ocean acoustic environment. *Journal of Hydrodynamics, Ser. B*, 28(6):923–936, 2016. 5

[39] Zhe Tian, Fushun Liu, Lin Zhou, and Changfeng Yuan. Fluid-structure interaction analysis of offshore structures based on separation of transferred responses. *Ocean Engineering*, 195:106598, 2020. 5

[40] Mhamed Souli and Jonathan Gabrys. Fluid structure interaction for bird impact problem: experimental and numerical investigation. *Computer Modeling in Engineering and Sciences*, 85(2):177, 2012. 6

[41] Zhijing Xu and Hongde Qin. Fluid-structure interactions of cage based aquaculture: From structures to organisms. *Ocean Engineering*, 217:107961, 2020. 6

[42] Alejandro Cornejo, Alessandro Franci, Francisco Zárate, and Eugenio Oñate. A fully lagrangian formulation for fluid-structure interaction problems with free-surface flows and fracturing solids. *Computers & Structures*, 250:106532, 2021. 6

[43] Chongqiang Zhu, Zhiyi Chen, and Yu Huang. Coupled moving particle simulation–finite-element method analysis of fluid–structure interaction in geodisasters. *International Journal of Geomechanics*, 21(6):04021081, 2021. 6

[44] Abdelkader Krimi. *Modélisation des écoulements fluide multiphasiques avec une approche SPH*. PhD thesis, Ecole nationale supérieure d'arts et métiers-ENSAM, 2018. 6, 13, 55

[45] Michael Griebel, Marc Alexander Schweitzer, et al. *Meshfree methods for partial differential equations II*. Springer, 2005.

[46] Gui-Rong Liu and Yuan-Tong Gu. *An introduction to meshfree methods and their programming*. Springer Science & Business Media, 2005. 6, 7

[47] Tayfun E Tezduyar. *Frontiers in Computational Fluid-Structure Interaction and Flow Simulation: Research from Lead Investigators under Forty–2018*. Springer, 2018. 6

[48] Olek C Zienkiewicz and Robert L Taylor. *The finite element method for solid and structural mechanics*. Butterworth-heinemann, 2005. 6

[49] Yong Zhao and Xiaohui Su. *Computational fluid-structure interaction: Methods, models, and applications*. Academic Press, 2018. 6

[50] Friedrich-Karl Benra, Hans Josef Dohmen, Ji Pei, Sebastian Schuster, Bo Wan, et al. A comparison of one-way and two-way coupling methods for numerical analysis of fluid-structure interactions. *Journal of applied mathematics*, 2011, 2011. 6

[51] M Ahamed, Sharmin Atique, M Munshi, and Tuomas Koiranen. A concise description of one way and two way coupling methods for fluid-structure interaction problems. *Imperial Journal of Interdisciplinary Research*, 3(3), 2017. 6

[52] Tetsuya Takahashi and Christopher Batty. Frictionalmonolith: a monolithic optimization-based approach for granular flow with contact-aware rigid-body coupling. *ACM Transactions on Graphics (TOG)*, 40(6):1–20, 2021. 6

[53] Qun Zhang and Toshiaki Hisada. Analysis of fluid–structure interaction problems with structural buckling and large domain changes by ale finite element method. *Computer methods in applied mechanics and engineering*, 190(48):6341–6357, 2001. 6

[54] T. Xiao, N. Qin, Z. Lu, X. Sun, M. Tong, and Z. Wang. Development of a smoothed particle hydrodynamics method and its application to aircraft ditching simulations. *Aerospace Science and Technology*, 66:28–43, 2017. https://doi.org/10.1016/j.ast.2017.02.022. 7

[55] MS Shadloo, G Oger, and David Le Touzé. Smoothed particle hydrodynamics method for fluid flows, towards industrial applications: Motivations, current state, and challenges. *Computers & Fluids*, 136:11–34, 2016. 7, 9, 58

[56] Woowon Jeong and Jaehoon Seong. Comparison of effects on technical variances of computational fluid dynamics (cfd) software based on finite element and finite volume methods. *International Journal of Mechanical Sciences*, 78:19–26, 2014. 7

[57] Jiun-Shyan Chen, Michael Hillman, and Sheng-Wei Chi. Meshfree methods: progress made after 20 years. *Journal of Engineering Mechanics*, 143(4):04017001, 2017. 7

[58] Timon Rabczuk, Jeong-Hoon Song, Xiaoying Zhuang, and Cosmin Anitescu. *Extended finite element and meshfree methods*. Academic Press, 2019. 7

[59] Gui-Rong Liu and Moubin B Liu. *Smoothed particle hydrodynamics: a meshfree particle method*. World Scientific, 2003. 7, 13, 63, 65

[60] GR3543275 Liu. An overview on meshfree methods: for computational solid mechanics. *International Journal of Computational Methods*, 13(05):1630001, 2016. 7

[61] Alessandra Monteleone, Guido Borino, Enrico Napoli, and Gaetano Burriesci. Fluid–structure interaction approach with smoothed particle hydrodynamics and particle–spring systems. *Computer Methods in Applied Mechanics and Engineering*, 392:114728, 2022. 8

[62] Wing Kam Liu, Y Chen, S Jun, JS Chen, T Belytschko, C Pan, RA Uras, and CT1379414 Chang. Overview and applications of the reproducing kernel particle methods. *Archives of Computational Methods in Engineering*, 3:3–80, 1996. 7

[63] Tsung-Hui Huang, Haoyan Wei, Jiun-Shyan Chen, and Michael C Hillman. Rkpm2d: an open-source implementation of nodally integrated reproducing kernel particle method for solving partial differential equations. *Computational particle mechanics*, 7:393–433, 2020. 7

[64] Francis H Harlow. The particle-in-cell computing method for fluid dynamics. *Methods Comput. Phys.*, 3:319–343, 1964. 7

[65] N Sukumar, Brian Moran, T Black, and T Belytschko. An element-free galerkin method for three-dimensional fracture mechanics. *Computational Mechanics*, 20:170–175, 1997. 7

[66] Apiwish Thongraksa, Pornkasem Jongpradist, Pruettha Nanakorn, and Jukkrawut Tunsakul. Shear fracture propagation in quasi-brittle materials by an element-free galerkin method. *Theoretical and Applied Fracture Mechanics*, 123:103713, 2023. 7

[67] PJ Hoogerbrugge and JMVA Koelman. Simulating microscopic hydrodynamic phenomena with dissipative particle dynamics. *EPL (Europhysics Letters)*, 19(3):155, 1992. 7

[68] Pep Espanol. Fluid particle model. *Physical Review E*, 57(3):2930, 1998. 7

[69] Marino Arroyo and Michael Ortiz. Local maximum-entropy approximation schemes: a seamless bridge between finite elements and meshfree methods. *International journal for numerical methods in engineering*, 65(13):2167–2202, 2006. 7

[70] Sreehari Peddavarapu and Raghuraman Srinivasan. Local maximum-entropy approximation based stabilization methods for the convection diffusion problems. *Engineering Analysis with Boundary Elements*, 146:531–554, 2023. 7

[71] Roger W Hockney and James W Eastwood. *Computer simulation using particles*. crc Press, 1988. 7, 65

[72] GR Liu, KY Dai, KM Lim, and YT Gu. A radial point interpolation method for simulation of two-dimensional piezoelectric structures. *Smart Materials and Structures*, 12(2):171, 2003. 7

[73] Omar Askour, Said Mesmoudi, and Bouazza Braikat. On the use of radial point interpolation method (rpim) in a high order continuation for the resolution of the geometrically nonlinear elasticity problems. *Engineering Analysis with Boundary Elements*, 110:69–79, 2020. 7

[74] Stephen Wolfram. Cellular automata. *Los Alamos Science*, 9:2–27, 1983. 7

[75] Leo P Kadanoff, Guy R McNamara, and Gianluigi Zanetti. From automata to fluid flow: comparisons of simulation and theory. *Physical Review A*, 40(8):4527, 1989. 7

[76] Piotr Breitkopf, Alain Rassineux, and Pierre Villon. An introduction to moving least squares meshfree methods. *Revue européenne des éléments finis*, 11(7-8):825–867, 2002. 7

[77] Jiangshuang Wan and Xiaolin Li. Analysis of a superconvergent recursive moving least squares approximation. *Applied Mathematics Letters*, 133:108223, 2022. 7

[78] Natarajan Sukumar, Brian Moran, and Ted Belytschko. The natural element method in solid mechanics. *International journal for numerical methods in engineering*, 43(5):839–887, 1998. 7

[79] Ping Lu, Shiyuan Guo, Yang Shu, Bin Liu, Peifeng Li, Wei Cao, and Kaiyong Jiang. A local search scheme in the natural element method for the analysis of elastic-plastic problems. *Advances in Engineering Software*, 176:103403, 2023. 7

[80] Jörg Kuhnert. An upwind finite pointset method (fpm) for compressible euler and navier-stokes equations. In *Meshfree methods for partial differential equations*, pages 239–249. Springer, 2003. 7

[81] Jörg Kuhnert, Isabel Michel, and Reiner Mack. Fluid structure interaction (fsi) in the meshfree finite pointset method (fpm): Theory and applications. *Meshfree Methods for Partial Differential Equations IX 9*, pages 73–92, 2019. 7

[82] Francis H Harlow. The particle-in-cell method for numerical solution of problems in fluid dynamics. Technical report, Los Alamos Scientific Lab., N. Mex., 1962. 7

[83] Richard A Gentry, Robert E Martin, and Bart J Daly. An eulerian differencing method for unsteady compressible flow problems. *Journal of Computational Physics*, 1(1):87–118, 1966. 7

[84] Seiichi Koshizuka, Atsushi Nobe, and Yoshiaki Oka. Numerical analysis of breaking waves using the moving particle semi-implicit method. *International Journal for Numerical Methods in Fluids*, 26(7):751–769, 1998. 8

[85] Leon B Lucy. A numerical approach to the testing of the fission hypothesis. *The astronomical journal*, 82:1013–1024, 1977. https://doi.org/10.1086/112164. 8, 9, 61

[86] Joseph J Monaghan. An introduction to sph. *Computer physics communications*, 48(1):89–96, 1988. 8

[87] Robert A Gingold and Joseph J Monaghan. Smoothed particle hydrodynamics: theory and application to non-spherical stars. *Monthly notices of the royal astronomical society*, 181(3):375–389, 1977. https://doi.org/10.1093/mnras/181.3.375. 8, 9, 11

[88] Joe J Monaghan. Smoothed particle hydrodynamics. *Reports on progress in physics*, 68(8):1703, 2005. 8, 10, 53, 73, 75, 93

[89] Steven J Lind, Benedict D Rogers, and Peter K Stansby. Review of smoothed particle hydrodynamics: towards converged lagrangian flow modelling. *Proceedings of the royal society A*, 476(2241):20190801, 2020. https://doi.org/10.1098/rspa.2019.0801. 9, 15, 80

[90] Xiufeng Yang and Song-Charng Kong. Smoothed particle hydrodynamics method for evaporating multiphase flows. *Physical Review E*, 96(3):033309, 2017.

[91] Yusuke Imaeda and Shu-ichiro Inutsuka. Shear flows in smoothed particle hydrodynamics. *The Astrophysical Journal*, 569(1):501, 2002. 9

[92] Joe J Monaghan. Smoothed particle hydrodynamics. *Annual review of astronomy and astrophysics*, 30(1):543–574, 1992. 9, 10, 13, 51, 52, 53, 54, 55

[93] Jérôme Limido, Christine Espinosa, Michel Salaün, and Jean-Luc Lacome. Sph method applied to high speed cutting modelling. *International journal of mechanical sciences*, 49(7):898–908, 2007.

[94] Ting Ye, Dingyi Pan, Can Huang, and Moubin Liu. Smoothed particle hydrodynamics (sph) for complex fluid flows: Recent developments in methodology and applications. *Physics of Fluids*, 31(1):011301, 2019. https://doi.org/10.1063/1.5068697. 10, 83

[95] MB Liu and GR Liu. Smoothed particle hydrodynamics (sph): an overview and recent developments. *Archives of computational methods in engineering*, 17(1):25–76, 2010. 9, 16, 67

[96] Damien Violeau and Reza Issa. Numerical modelling of complex turbulent free-surface flows with the sph method: an overview. *International Journal for Numerical Methods in Fluids*, 53(2):277–304, 2007. 9, 56

[97] Jean-Christophe Marongiu, Francis Leboeuf, Joëlle Caro, and Etienne Parkinson. Free surface flows simulations in pelton turbines using an hybrid sph-ale method. *Journal of Hydraulic Research*, 48(sup1):40–49, 2010. 9

[98] Alexandre Lavrov, Paal Skjetne, Bjørnar Lund, Erik Bjønnes, Finn Olav Bjørnson, Jan Ove Busklein, Térence Coudert, Pascal Klebert, Kjetil Olsen Lye, Jan Erik Olsen, et al. Density-consistent initialization of sph on a regular cartesian grid: Comparative numerical study of 10 smoothing kernels in 1, 2 and 3 dimensions. *Procedia IUTAM*, 18:85–95, 2015. 10

[99] Lars Hernquist and Neal Katz. Treesph-a unification of sph with the hierarchical tree method. *The Astrophysical Journal Supplement Series*, 70:419–446, 1989. 10

[100] Joseph J Monaghan and John C Lattanzio. A refined particle method for astrophysical problems. *Astronomy and astrophysics*, 149:135–143, 1985. 11

[101] Joseph Peter Morris. A study of the stability properties of sph. *arXiv preprint astro-ph/9503124*, 1995. 11

[102] Joseph Peter Morris. *Analysis of smoothed particle hydrodynamics with applications*. Monash University Australia, 1996. 11, 89

[103] Holger Wendland. Piecewise polynomial, positive definite and compactly supported radial functions of minimal degree. *Advances in computational Mathematics*, 4(1):389–396, 1995. 11

[104] Matt P Wand and M Chris Jones. *Kernel smoothing*. CRC press, 1994. 12

[105] Stephan Rosswog. Sph methods in the modelling of compact objects. *Living Reviews in Computational Astrophysics*, 1(1):1–109, 2015. 12

[106] Moncho Gomez-Gesteira, Benedict D Rogers, Robert A Dalrymple, and Alex JC Crespo. State-of-the-art of classical sph for free-surface flows. *Journal of Hydraulic Research*, 48(S1):6–27, 2010. 12, 59

[107] Carlos Alberto Dutra Fraga Filho, Carlos Alberto Dutra Fraga Filho, and Castro. *Smoothed Particle Hydrodynamics*. Springer, 2019. 13

[108] David A Fulk and Dennis W Quinn. An analysis of 1-d smoothed particle hydrodynamics kernels. *Journal of Computational Physics*, 126(1):165–180, 1996. 13

[109] MB Liu, GR Liu, and KY Lam. Constructing smoothing functions in smoothed particle hydrodynamics with applications. *Journal of Computational and applied Mathematics*, 155(2):263–284, 2003. https://doi.org/10.1016/S0377-0427(02)00869-5. 13, 89

[110] Jeff W Swegle, Darrell L Hicks, and Steve W Attaway. Smoothed particle hydrodynamics stability analysis. *Journal of computational physics*, 116(1):123–134, 1995. 14, 75

[111] L Brookshaw. A method of calculating radiative heat diffusion in particle simulations. *Publications of the Astronomical Society of Australia*, 6(2):207–210, 1985. 14

[112] Joseph P Morris, Patrick J Fox, and Yi Zhu. Modeling low reynolds number incompressible flows using sph. *Journal of computational physics*, 136(1):214–226, 1997. 14, 15, 55, 67, 71

[113] JJ Monaghan. Heat conduction with discontinuous conductivity. *Applied Mathematics Reports and Preprints*, 95(18):7–1, 1995. 14

[114] Paul W Cleary and Joseph J Monaghan. Conduction modelling using smoothed particle hydrodynamics. *Journal of Computational Physics*, 148(1):227–264, 1999. 15

[115] Alexandre M Tartakovsky, Kim F Ferris, and Paul Meakin. Lagrangian particle model for multiphase flows. *Computer Physics Communications*, 180(10):1874–1881, 2009. 15

[116] Alejandro JC Crespo, José M Domínguez, Benedict D Rogers, Moncho Gómez-Gesteira, S Longshaw, R Canelas, Renato Vacondio, A Barreiro, and O García-Feal. Dualsphysics: Open-source parallel cfd solver based on smoothed particle hydrodynamics (sph). *Computer Physics Communications*, 187:204–216, 2015. 15

[117] Alejandro Jacobo Cabrera Crespo. *Application of the smoothed particle hydrodynamics model SPHysics to free-surface hydrodynamics*. PhD thesis, PhD Thesis, Departamento De Fisica Aplicada, Universidade De Vigo, 2008. 15, 58

[118] Jean Luc Lacome. Smooth particle hydrodynamics (sph): a new feature in ls-dyna. In *6th International LS-Dyna Users Conference, Detroit, USA*, 2000. 15

[119] José M Domínguez, Alejandro JC Crespo, Daniel Valdez-Balderas, Benedict D Rogers, and Moncho Gómez-Gesteira. New multi-gpu implementation for smoothed particle hydrodynamics on heterogeneous clusters. *Computer Physics Communications*, 184(8):1848–1860, 2013. 15

[120] Renato Vacondio, Corrado Altomare, Matthieu De Leffe, Xiangyu Hu, David Le Touzé, Steven Lind, Jean-Christophe Marongiu, Salvatore Marrone, Benedict D Rogers, and Antonio Souto-Iglesias. Grand challenges for smoothed particle hydrodynamics numerical schemes. *Computational Particle Mechanics*, 8:575–588, 2021. 16

[121] Fei Xu, Jiayi Wang, Yang Yang, Lu Wang, Zhen Dai, and Ruiqi Han. On methodology and application of smoothed particle hydrodynamics in fluid, solid and biomechanics. *Acta Mechanica Sinica*, 39(2):722185, 2023. 16

[122] Chi Zhang, Yu-jie Zhu, Dong Wu, Nikolaus A Adams, and Xiangyu Hu. Smoothed particle hydrodynamics: Methodology development and recent achievement. *Journal of Hydrodynamics*, 34(5):767–805, 2022. 16

[123] Xiufeng Yang, Song-Charng Kong, and Qingquan Liu. Smoothed particle hydrodynamics with adaptive spatial resolution for multiphase flows with large density ratio. *Physical Review E*, 104(5):055308, 2021. 16, 17

[124] Michael Blank, Prapanch Nair, and Thorsten Pöschel. Modeling surface tension in smoothed particle hydrodynamics using young–laplace pressure boundary condition. *Computer Methods in Applied Mechanics and Engineering*, 406:115907, 2023. 16, 17

[125] Paul W Cleary and Yoshihiro Serizawa. A coupled discrete droplet and sph model for predicting spray impingement onto surfaces and into fluid pools. *Applied Mathematical Modelling*, 69:301–329, 2019. 16, 18

[126] M. Antuono, P.N. Sun, S. Marrone, and A. Colagrossi. The δ-ale-sph model: An arbitrary lagrangian-eulerian framework for the δ-sph model with particle shifting technique. *Computers & Fluids*, 216:104806, 2021. 17, 19

[127] Shuoguo Zhang, Wenbin Zhang, Chi Zhang, and Xiangyu Hu. A lagrangian free-stream boundary condition for weakly compressible smoothed particle hydrodynamics. *arXiv preprint arXiv:2206.06875*, 2022. 18, 21, 22

[128] Satori Tsuzuki. Theoretical framework bridging classical and quantum mechanics for the dynamics of cryogenic liquid helium-4 using smoothed-particle hydrodynamics. *Physics of Fluids*, 34(12):127116, 2022. 18, 23

[129] Dong Wu, Chi Zhang, Xiaojing Tang, and Xiangyu Hu. An hourglass-free formulation for total lagrangian smoothed particle hydrodynamics. *arXiv preprint arXiv:2212.00753*, 2022. 18, 24

[130] Ondřej Kincl, Ilya Peshkov, Michal Pavelka, and Václav Klika. Unified description of fluids and solids in smoothed particle hydrodynamics. *Applied Mathematics and Computation*, 439:127579, 2023. 19, 25

[131] Mohammad Naqib Rahimi and Georgios Moutsanidis. A smoothed particle hydrodynamics approach for phase field modeling of brittle fracture. *Computer Methods in Applied Mechanics and Engineering*, 398:115191, 2022. 19, 25

[132] Muhammad N Nawaz, Sohaib Z Khan, Muhammad Asif, Abdulrahman Aljabri, Asad A Zaidi, and Essam RI Mahmoud. Comparison of machining simulations of aerospace alloy al6061-t6 using lagrangian and smoothed particle hydrodynamics techniques. *Lubricants*, 10(11):310, 2022. 21, 26

[133] Stefan Fabbro, Mohamadreza Afrasiabi, Lucas Marra, Michal Kuffa, Markus Bambach, and Konrad Wegener. Experimental study and smoothed particle hydrodynamics simulation of synthetic diamond grit scratching on steel. *International Journal of Solids and Structures*, 259:112038, 2022. 21, 26

[134] Lei Li, Md Reza-E-Rabby, Nicole Overman, Tianhao Wang, Scott Whalen, Glenn Grant, Suveen Mathaudhu, and Ayoub Soulami. Analysis of contact conditions and microstructure evolution in shear assisted processing and extrusion using smoothed particle hydrodynamics method. *Materials & Design*, 221:111010, 2022. 21, 27

[135] Chengzhi Xia, Zhenming Shi, Hongchao Zheng, and Xiaohan Wu. Kernel broken smooth particle hydrodynamics method for crack propagation simulation applied in layered rock cells and tunnels. *Underground Space*, 2023. 22, 27

[136] Nhu HT Nguyen, Ha H Bui, and Giang D Nguyen. Effects of material properties on the mobility of granular flow. *Granular Matter*, 22:1–17, 2020. 22, 28

[137] Chengwei Zhu, Chong Peng, and Wei Wu. Lagrangian meshfree particle method (sph) based simulation for granular flow in a rotating drum with regularized μ (i) elastoplastic model. *Powder Technology*, 408:117699, 2022. 23, 29

[138] Sebastian L Fuchs, Christoph Meier, Wolfgang A Wall, and Christian J Cyron. A novel smoothed particle hydrodynamics and finite element coupling scheme for fluid–structure interaction: The sliding boundary particle approach. *Computer Methods in Applied Mechanics and Engineering*, 383:113922, 2021. 23, 30

[139] Chi Zhang, Massoud Rezavand, and Xiangyu Hu. A multi-resolution sph method for fluid-structure interactions. *Journal of Computational Physics*, 429:110028, 2021. 24, 31

[140] Chi Zhang, Yujie Zhu, Xiuxiu Lyu, and Xiangyu Hu. An efficient and generalized solid boundary condition for sph: Applications to multi-phase flow and fluid–structure interaction. *European Journal of Mechanics-B/Fluids*, 94:276–292, 2022. 24, 32

[141] ZL Zhang, MSU Khalid, T Long, MB Liu, and C Shu. Improved element-particle coupling strategy with δ-sph and particle shifting for modeling sloshing with rigid or deformable structures. *Applied Ocean Research*, 114:102774, 2021. 26, 33

[142] Marko Topalovic, Aleksandar Nikolic, Vladimir Milovanovic, Snezana Vulovic, and Milos Ivanovic. Smoothed particle hydrodynamics for blood flow analysis: development of particle lifecycle algorithm. *Computational Particle Mechanics*, pages 1–17, 2022. 26, 33

[143] Harry Duckworth, David J Sharp, and Mazdak Ghajari. Smoothed particle hydrodynamic modelling of the cerebrospinal fluid for brain biomechanics: Accuracy and stability. *International Journal for Numerical Methods in Biomedical Engineering*, 37(4):e3440, 2021. 27, 34

[144] Mark A Woodgate, George N Barakos, Nigel Scrase, and Tim Neville. Simulation of helicopter ditching using smoothed particle hydrodynamics. *Aerospace Science and Technology*, 85:277–292, 2019. 28, 35

[145] Yu-Xiang Peng, A-Man Zhang, and Shi-Ping Wang. Coupling of wcsph and rkpm for the simulation of incompressible fluid–structure interactions. *Journal of Fluids and Structures*, 102:103254, 2021. 28, 36

[146] Jie Cui, Xin Chen, and Pengnan Sun. Numerical investigation on the hydrodynamic performance of a new designed breakwater using smoothed particle hydrodynamic method. *Engineering Analysis with Boundary Elements*, 130:379–403, 2021. 28, 37

[147] B Bouscasse, A Colagrossi, S Marrone, and M Antuono. Nonlinear water wave interaction with floating bodies in sph. *Journal of Fluids and Structures*, 42:112–129, 2013. 28, 37

[148] Guibin Zhang, Jianyun Chen, Youting Qi, Jing Li, and Qiang Xu. Numerical simulation of landslide generated impulse waves using a δ+-les-sph model. *Advances in Water Resources*, 151:103890, 2021. 29, 38

[149] Zili Dai, Jinwei Xie, Shiwei Qin, and Shuyang Chen. Numerical investigation of surge waves generated by submarine debris flows. *Water*, 13(16):2276, 2021. 29, 39

[150] Hao Shi and Yu Huang. A gpu-based δ-plus-sph model for non-newtonian multiphase flows. *Water*, 14(11):1734, 2022. 29, 40, 114, 116

[151] W Michael Lai, David Rubin, and Erhard Krempl. *Introduction to continuum mechanics*. Butterworth-Heinemann, 2009. 42

[152] Junuthula Narasimha Reddy. *Principles of continuum mechanics: a study of conservation principles with applications*. Cambridge University Press, 2010. 50

[153] Sergei K Godunov and Evgenii Romenskii. *Elements of continuum mechanics and conservation laws*. Springer Science & Business Media, 2013. 42, 50

[154] Anthony James Merrill Spencer. *Continuum mechanics*. Courier Corporation, 2004. 42

[155] Xavier Oliver and C Agelet de Saracibar. Continuum mechanics for engineers. *Theory and problems*, 2017. 42

[156] Faith A Morrison. *An introduction to fluid mechanics*. Cambridge University Press, 2013. 43, 48

[157] Sven Gross and Arnold Reusken. *Numerical methods for two-phase incompressible flows*, volume 40. Springer Science & Business Media, 2011. 43, 48

[158] Alexandre Joel Chorin. Numerical solution of the navier-stokes equations. *Mathematics of computation*, 22(104):745–762, 1968. 44

[159] Alexandre Joel Chorin. On the convergence of discrete approximations to the navier-stokes equations. *Mathematics of computation*, 23(106):341–353, 1969. 44

[160] Sharen J Cummins and Murray Rudman. An sph projection method. *Journal of computational physics*, 152(2):584–607, 1999. 44

[161] Massoud Rezavand, Mohammad Taeibi-Rahni, and Wolfgang Rauch. An isph scheme for numerical simulation of multiphase flows with complex interfaces and high density ratios. *Computers & Mathematics with Applications*, 75(8):2658–2677, 2018. 44

[162] SJ Lind, Rui Xu, PK Stansby, and Benedict D Rogers. Incompressible smoothed particle hydrodynamics for free-surface flows: A generalised diffusion-based algorithm for stability and validations for impulsive flows and propagating waves. *Journal of Computational Physics*, 231(4):1499–1523, 2012. 45

[163] Rui Xu, Peter Stansby, and Dominique Laurence. Accuracy and stability in incompressible sph (isph) based on the projection method and a new approach. *Journal of Computational Physics*, 228(18):6703–6725, 2009. 45

[164] R Fatehi and MT Manzari. A consistent and fast weakly compressible smoothed particle hydrodynamics with a new wall boundary condition. *International Journal for Numerical Methods in Fluids*, 68(7):905–921, 2012. 45, 63, 68

[165] Songdong Shao and Edmond YM Lo. Incompressible sph method for simulating newtonian and non-newtonian flows with a free surface. *Advances in water resources*, 26(7):787–800, 2003. 45, 70

[166] XY Hu and Nikolaus A Adams. An incompressible multi-phase sph method. *Journal of computational physics*, 227(1):264–278, 2007. 45, 92

[167] JJ Monaghan. Smoothed particle hydrodynamics and its diverse applications. *Annual Review of Fluid Mechanics*, 44:323–346, 2012. https://doi.org/10.1146/annurev-fluid-120710-101220. 46, 55, 82

[168] Joseph P Morris. Simulating surface tension with smoothed particle hydrodynamics. *International journal for numerical methods in fluids*, 33(3):333–353, 2000. 46, 58

[169] Rakulan Sivanesapillai, Nadine Falkner, Alexander Hartmaier, and Holger Steeb. A csf-sph method for simulating drainage and imbibition at pore-scale resolution while tracking interfacial areas. *Advances in Water Resources*, 95:212–234, 2016. 46

[170] Joe J Monaghan. Simulating free surface flows with sph. *Journal of computational physics*, 110(2):399–406, 1994. 46, 67

[171] JP Gray, JJ Monaghan, and RP Swift. Sph elastic dynamics. *Computer methods in applied mechanics and engineering*, 190(49):6641–6662, 2001. 46

[172] Carla Antoci, Mario Gallati, and Stefano Sibilla. Numerical simulation of fluid–structure interaction by sph. *Computers & structures*, 85(11-14):879–890, 2007. 48, 74

[173] C Schäfer, Sven Riecker, Thomas I Maindl, Roland Speith, Samuel Scherrer, and Wilhelm Kley. A smooth particle hydrodynamics code to model collisions between solid, self-gravitating objects. *Astronomy & Astrophysics*, 590:A19, 2016. 46, 63

[174] Salvatore Marrone, Andrea Colagrossi, Matteo Antuono, G Colicchio, and Giorgio Graziani. An accurate sph modeling of viscous flows around bodies at low and moderate reynolds numbers. *Journal of Computational Physics*, 245:456–475, 2013. 47

[175] Andrea Colagrossi and Maurizio Landrini. Numerical simulation of interfacial flows by smoothed particle hydrodynamics. *Journal of computational physics*, 191(2):448–475, 2003. https://doi.org/10.1016/S0021-9991(03)00324-3. 47, 67, 75, 82, 83

[176] SM Hosseini, MT Manzari, and SK Hannani. A fully explicit three-step sph algorithm for simulation of non-newtonian fluid flow. *International Journal of Numerical Methods for Heat & Fluid Flow*, 17(7):715–735, 2007. 47, 48

[177] Edoardo Daly, Stefania Grimaldi, Ha Hong Bui, et al. Explicit incompressible sph algorithm for free-surface flow modelling: A comparison with weakly compressible schemes. *Advances in Water Resources*, 97:156–167, 2016. https://doi.org/10.1016/j.advwatres.2016.09.008. 76

[178] Ashkan Rafiee and Krish P Thiagarajan. An sph projection method for simulating fluid-hypoelastic structure interaction. *Computer Methods in Applied Mechanics and Engineering*, 198(33):2785–2795, 2009. 74

[179] DA Barcarolo, D Le Touzé, and F de Vuyst. Incompressible smoothed particle hydrodynamics: proposition and validation of a fully-explicit algorithm. In *Proc. Seventh International SPHERIC Workshop, Prato, Italy*, 2012.

[180] Daniel Afonso Barcarolo. *Improvement of the precision and the efficiency of the SPH method: theoretical and numerical study*. PhD thesis, Ecole Centrale de Nantes (ECN)(ECN)(ECN)(ECN), 2013. 47

[181] Ronald L Panton. *Incompressible flow*. John Wiley & Sons, 2006. 48

[182] Rajendra P Chhabra. Non-newtonian fluids: an introduction. In *Rheology of Complex Fluids*, pages 3–34. Springer, 2010. 48

[183] Robert Byron Bird, Robert Calvin Armstrong, and Ole Hassager. *Dynamics of polymeric liquids. Vol. 1: Fluid mechanics*. John Wiley and Sons Inc., New York, NY, 1987. 48, 57, 83, 85

[184] Ko Fei Liu and Chiang C Mei. Slow spreading of a sheet of bingham fluid on an inclined plane. *Journal of fluid mechanics*, 207:505–529, 1989. 48

[185] R von Mises. Mechanik der plastischen formänderung von kristallen. *ZAMM-Journal of Applied Mathematics and Mechanics/Zeitschrift für Angewandte Mathematik und Mechanik*, 8(3):161–185, 1928. 48

[186] Tasos C Papanastasiou. Flows of materials with yield. *Journal of Rheology*, 31(5):385–404, 1987. 48

[187] Michel Bercovier and Michael Engelman. A finite-element method for incompressible non-newtonian flows. *Journal of Computational Physics*, 36(3):313–326, 1980. https://doi.org/10.1016/0021-9991(80)90163-1. 48, 85

[188] VC Kelessidis and R Maglione. Modeling rheological behavior of bentonite suspensions as casson and robertson–stiff fluids using newtonian and true shear rates in couette viscometry. *Powder technology*, 168(3):134–147, 2006. 49

[189] Rafał Wiśniowski, Krzysztof Skrzypaszek, and Tomasz Małachowski. Selection of a suitable rheological model for drilling fluid using applied numerical methods. *Energies*, 13(12):3192, 2020. 49

[190] Walter P Walawender, Te Yu Chen, and David F Cala. An approximate casson fluid model for tube flow of blood. *Biorheology*, 12(2):111–119, 1975. 49

[191] Arild Saasen and Jan David Ytrehus. Viscosity models for drilling fluids—herschel-bulkley parameters and their use. *Energies*, 13(20):5271, 2020. 49

[192] Xin Huang and Marcelo H Garcia. A herschel–bulkley model for mud flow down a slope. *Journal of fluid mechanics*, 374:305–333, 1998. 49

[193] Allan BG Motta, Roney L Thompson, Mateus P Schwalbert, Luiz FLR Silva, Jovani L Favero, Rodrigo AC Dias, and Raphael J Leitão. Effects of intra-rev pore distribution modeling in the flow of non-newtonian fluids in porous media. *Transport in Porous Media*, 145(2):505–525, 2022. 49

[194] Jin Hyun Lee, Jae Hong Kim, and Jin Young Yoon. Prediction of the yield stress of concrete considering the thickness of excess paste layer. *Construction and Building Materials*, 173:411–418, 2018.

[195] Sreelakshmi Sandeep and SR Shine. Effect of stenosis and dilatation on the hemodynamic parameters associated with left coronary artery. *Computer Methods and Programs in Biomedicine*, 204:106052, 2021. 49

[196] Ashutosh Mujumdar, Antony N Beris, and Arthur B Metzner. Transient phenomena in thixotropic systems. *Journal of Non-Newtonian Fluid Mechanics*, 102(2):157–178, 2002. 50

[197] Houxing Teng and Jinjun Zhang. A new thixotropic model for waxy crude. *Rheologica Acta*, 52(10-12):903–911, 2013. 50

[198] Rajinder Pal. Rheology of polymer-thickened emulsions. *Journal of Rheology*, 36(7):1245–1259, 1992. 50

[199] A Rafiee, MT Manzari, and M Hosseini. An incompressible sph method for simulation of unsteady viscoelastic free-surface flows. *International Journal of Non-Linear Mechanics*, 42(10):1210–1223, 2007. 50

[200] Ali A Rashaida. *Flow of a non-Newtonian Bingham plastic fluid over a rotating disk*. PhD thesis, University of Saskatchewan, 2005. 50

[201] G Thomas Mase, Ronald E Smelser, and George E Mase. *Continuum mechanics for engineers*. CRC press, 2009. 50

[202] Yujie Zhu, Chi Zhang, and Xiangyu Hu. A consistency-driven particle-advection formulation for weakly-compressible smoothed particle hydrodynamics. *Computers & Fluids*, 230:105140, 2021. https://doi.org/10.1016/j.compfluid.2021.105140. 50, 80

[203] Xiang Yu Hu and Nikolaus A Adams. A multi-phase sph method for macroscopic and mesoscopic flows. *Journal of Computational Physics*, 213(2):844–861, 2006. 52, 54, 77

[204] Andrea Colagrossi. A meshless lagrangian method for free-surface and interface flows with fragmentation. *These, Universita di Roma*, 2005. 53

[205] JP Vila. On particle weighted methods and smooth particle hydrodynamics. *Mathematical models and methods in applied sciences*, 9(02):161–209, 1999. 53, 55

[206] PW Randles and LD Libersky. Smoothed particle hydrodynamics: some recent improvements and applications. *Computer methods in applied mechanics and engineering*, 139(1-4):375–408, 1996. 53, 55

[207] S Adami, XY Hu, and NA Adams. A conservative sph method for surfactant dynamics. *Journal of Computational Physics*, 229(5):1909–1926, 2010. 54

[208] S Adami, XY Hu, and NA Adams. A new surface-tension formulation for multi-phase sph using a reproducing divergence approximation. *Journal of Computational Physics*, 229(13):5011–5021, 2010. 54, 90, 92, 93

[209] S Adami, XY Hu, and NA Adams. A generalized wall boundary condition for smoothed particle hydrodynamics. *Journal of Computational Physics*, 231(21):7057–7075, 2012. 54, 59, 68, 71, 74, 77

[210] JK Chen, JE Beraun, and CJ Jih. An improvement for tensile instability in smoothed particle hydrodynamics. *Computational Mechanics*, 23(4):279–287, 1999. 55

[211] Marco Ellero, Martin Kröger, and Siegfried Hess. Viscoelastic flows studied by smoothed particle dynamics. *Journal of Non-Newtonian Fluid Mechanics*, 105(1):35–51, 2002. 55

[212] Mihai Basa, Nathan J Quinlan, and Martin Lastiwka. Robustness and accuracy of sph formulations for viscous flow. *International Journal for Numerical Methods in Fluids*, 60(10):1127–1148, 2009. 56

[213] RA Gingold and JJ Monaghan. Kernel estimates as a basis for general particle methods in hydrodynamics. *Journal of Computational Physics*, 46(3):429–453, 1982. 56, 66

[214] Paul W Cleary. Modelling confined multi-material heat and mass flows using sph. *Applied Mathematical Modelling*, 22(12):981–993, 1998. 56

[215] XY Hu and NA Adams. Angular-momentum conservative smoothed particle dynamics for incompressible viscous flows. *Physics of Fluids*, 18(10):101702, 2006. 57

[216] Nicolas Grenier, Matteo Antuono, Andrea Colagrossi, David Le Touzé, and B Alessandrini. An hamiltonian interface sph formulation for multi-fluid and free surface flows. *Journal of Computational Physics*, 228(22):8380–8393, 2009. 57

[217] Nicolas Grenier. *Modélisation numérique par la méthode SPH de la séparation eau-huile dans les séparateurs gravitaires*. PhD thesis, Ecole Centrale de Nantes (ECN), 2009.

[218] N Grenier, D Le Touzé, A Colagrossi, G Colicchio, and M Antuono. Sph multiphase simulation of bubbly flows: Towards oil and water separation. In *ASME 2013 32nd International Conference on Ocean, Offshore and Arctic Engineering*, pages V007T08A083–V007T08A083. American Society of Mechanical Engineers, 2013.

[219] N Grenier, D Le Touzé, A Colagrossi, M Antuono, and G Colicchio. Viscous bubbly flows simulation with an interface sph model. *Ocean Engineering*, 69:88–102, 2013. 57

[220] D Vola, F Babik, and J-C Latché. On a numerical strategy to compute gravity currents of non-newtonian fluids. *Journal of computational physics*, 201(2):397–420, 2004. 57

[221] X-J Fan, RI Tanner, and R Zheng. Smoothed particle hydrodynamics simulation of non-newtonian moulding flow. *Journal of Non-Newtonian Fluid Mechanics*, 165(5):219–226, 2010. 57

[222] AM Xenakis, SJ Lind, PK Stansby, and BD Rogers. An incompressible sph scheme with improved pressure predictions for free-surface generalised newtonian flows. *Journal of Non-Newtonian Fluid Mechanics*, 218:1–15, 2015. https://doi.org/10.1016/j.enganabound.2015.12.014. 57, 80, 92

[223] Prapanch Nair and Gaurav Tomar. Volume conservation issues in incompressible smoothed particle hydrodynamics. *Journal of Computational Physics*, 297:689–699, 2015. 58

[224] Zhi-Bin Wang, Rong Chen, Hong Wang, Qiang Liao, Xun Zhu, and Shu-Zhe Li. An overview of smoothed particle hydrodynamics for simulating multiphase flow. *Applied Mathematical Modelling*, 40(23-24):9625–9655, 2016. 58

[225] Leonardo Di G Sigalotti, Jaime Klapp, Otto Rendón, Carlos A Vargas, and Franklin Peña-Polo. On the kernel and particle consistency in smoothed particle hydrodynamics. *Applied Numerical Mathematics*, 108:242–255, 2016. 58

[226] Donald Shepard. A two-dimensional interpolation function for irregularly-spaced data. In *Proceedings of the 1968 23rd ACM national conference*, pages 517–524. ACM, 1968. 58

[227] RA Dalrymple and BD Rogers. Numerical modeling of water waves with the sph method. *Coastal engineering*, 53(2):141–147, 2006. 59

[228] SJ Lind, PK Stansby, and Benedict D Rogers. Incompressible–compressible flows with a transient discontinuous interface using smoothed particle hydrodynamics (sph). *Journal of Computational Physics*, 309:129–147, 2016. 59

[229] Joe J Monaghan and Jules B Kajtar. Sph particle boundary forces for arbitrary boundaries. *Computer Physics Communications*, 180(10):1811–1820, 2009. 59

[230] JJ Monaghan. Sph and riemann solvers. *Journal of Computational Physics*, 136(2):298–307, 1997. 60

[231] Hans F Schwaiger. An implicit corrected sph formulation for thermal diffusion with linear free surface boundary conditions. *International journal for numerical methods in engineering*, 75(6):647–671, 2008. 60, 70

[232] R Fatehi and MT Manzari. Error estimation in smoothed particle hydrodynamics and a new scheme for second derivatives. *computers & Mathematics with Applications*, 61(2):482–498, 2011. 60

[233] JJ Monaghan and RA Gingold. Shock simulation by the particle method sph. *Journal of computational physics*, 52(2):374–389, 1983. 61

[234] JJ Monaghan. On the problem of penetration in particle methods. *Journal of Computational physics*, 82(1):1–15, 1989. 62, 75, 76

[235] M Gómez-Gesteira and Robert A Dalrymple. Using a three-dimensional smoothed particle hydrodynamics method for wave impact on a tall structure. *Journal of waterway, port, coastal, and ocean engineering*, 130(2):63–69, 2004. 63

[236] Angela Ferrari, Michael Dumbser, Eleuterio F Toro, and Aronne Armanini. A new 3d parallel sph scheme for free surface flows. *Computers & Fluids*, 38(6):1203–1217, 2009. 63

[237] Joel H Ferziger and Milovan Perić. Solution of the navier-stokes equations. In *Computational Methods for Fluid Dynamics*, pages 157–216. Springer, 2002. 63

[238] Diego Molteni and Andrea Colagrossi. A simple procedure to improve the pressure evaluation in hydrodynamic context using the sph. *Computer Physics Communications*, 180(6):861–872, 2009. https://doi.org/10.1016/j.cpc.2008.12.004. 64, 90

[239] Matteo Antuono, Andrea Colagrossi, Salvatore Marrone, and Diego Molteni. Free-surface flows solved by means of sph schemes with numerical diffusive terms. *Computer Physics Communications*, 181(3):532–549, 2010. 64

[240] Daniel Winkler, Massoud Rezavand, and Wolfgang Rauch. Neighbour lists for smoothed particle hydrodynamics on gpus. *Computer Physics Communications*, 225:140–148, 2018. 65

[241] JJ Monaghan. Particle methods for hydrodynamics. *Computer Physics Reports*, 3(2):71–124, 1985. 65

[242] David A Fulk. A numerical analysis of smoothed particle hydrodynamics. Technical report, AIR FORCE INST OF TECH WRIGHT-PATTERSON AFB OH, 1994. 65

[243] Andrew W Appel. An efficient program for many-body simulation. *SIAM Journal on Scientific and Statistical Computing*, 6(1):85–103, 1985. 65

[244] Josh Barnes and Piet Hut. A hierarchical o (n log n) force-calculation algorithm. *nature*, 324(6096):446–449, 1986.

[245] Lars Hernquist. Vectorization of tree traversals. *Journal of Computational Physics*, 87(1):137–147, 1990.

[246] Junichiro Makino. Vectorization of a treecode. *Journal of Computational Physics*, 87(1):148–160, 1990. 65

[247] Wei-Kang Sun, Lu-Wen Zhang, and KM Liew. Adaptive particle refinement strategies in smoothed particle hydrodynamics. *Computer Methods in Applied Mechanics and Engineering*, 389:114276, 2022. 66

[248] Larry D Libersky, Albert G Petschek, Theodore C Carney, Jim R Hipp, and Firooz A Allahdadi. High strain lagrangian hydrodynamics: a three-dimensional sph code for dynamic material response. *Journal of computational physics*, 109(1):67–75, 1993. 67

[249] Salvatore Marrone, M Antuono, A Colagrossi, G Colicchio, D Le Touzé, and G Graziani. δ-sph model for simulating violent impact flows. *Computer Methods in Applied Mechanics and Engineering*, 200(13):1526–1542, 2011. https://doi.org/10.1016/j.cma.2010.12.016. 67, 98

[250] S Marrone, A Colagrossi, M Antuono, C Lugni, and MP Tulin. A 2d+t sph model to study the breaking wave pattern generated by fast ships. *Journal of Fluids and Structures*, 27(8):1199–1215, 2011. 67

[251] MouBin Liu, JiaRu Shao, and JianZhong Chang. On the treatment of solid boundary in smoothed particle hydrodynamics. *Science China Technological Sciences*, 55(1):244–254, 2012. 67

[252] Mou-Bin Liu and Gui-Rong Liu. *Particle methods for multi-scale and multi-physics*. World Scientific, 2015. 67

[253] Benedict D Rogers and Robert A Dalrymple. Sph modeling of tsunami waves. *Advanced numerical models for simulating tsunami waves and runup*, 10:75–100, 2008. 67

[254] Hidenori Takeda, Shoken M Miyama, and Minoru Sekiya. Numerical simulation of viscous flow by smoothed particle hydrodynamics. *Progress of Theoretical Physics*, 92(5):939–960, 1994. 67

[255] R Issa, D Violeau, ES Lee, and H Flament. Modelling nonlinear water waves with rans and les sph models. *Advances in numerical simulation of nonlinear water waves*, 11, 2010. 68

[256] Martin Ferrand, DR Laurence, Benedict D Rogers, Damien Violeau, and Christophe Kassiotis. Unified semi-analytical wall boundary conditions for inviscid, laminar or turbulent flows in the meshless sph method. *International Journal for Numerical Methods in Fluids*, 71(4):446–472, 2013. 68, 69

[257] S Kulasegaram, J Bonet, RW Lewis, and M Profit. A variational formulation based contact algorithm for rigid boundaries in two-dimensional sph applications. *Computational Mechanics*, 33(4):316–325, 2004. 68

[258] M De Leffe, D Le Touzé, and B Alessandrini. Normal flux method at the boundary for sph. In *4th Int. SPHERIC Workshop (SPHERIC 2009)*, 2009. 68

[259] Fabricio Macia, Leo M González, Jose L Cercos-Pita, and Antonio Souto-Iglesias. A boundary integral sph formulation: consistency and applications to isph and wcsph. *Progress of Theoretical Physics*, 128(3):439–462, 2012. 68

[260] Agnes Leroy, Damien Violeau, Martin Ferrand, and Christophe Kassiotis. Unified semi-analytical wall boundary conditions applied to 2-d incompressible sph. *Journal of Computational Physics*, 261:106–129, 2014. 68

[261] Arno Mayrhofer, Benedict D Rogers, Damien Violeau, and Martin Ferrand. Investigation of wall bounded flows using sph and the unified semi-analytical wall boundary conditions. *Computer Physics Communications*, 184(11):2515–2527, 2013. 68

[262] Arno Mayrhofer, Martin Ferrand, Christophe Kassiotis, Damien Violeau, and François-Xavier Morel. Unified semi-analytical wall boundary conditions in sph: analytical extension to 3-d. *Numerical Algorithms*, 68(1):15–34, 2015. 68

[263] Alireza Valizadeh and Joseph J Monaghan. A study of solid wall models for weakly compressible sph. *Journal of Computational Physics*, 300:5–19, 2015. 68

[264] MR Hashemi, R Fatehi, and MT Manzari. A modified sph method for simulating motion of rigid bodies in newtonian fluid flows. *International Journal of Non-Linear Mechanics*, 47(6):626–638, 2012. https://doi.org/10.1016/j.ijnonlinmec.2011.10.007. 68, 73, 80

[265] R Vacondio, BD Rogers, PK Stansby, and P Mignosa. Sph modeling of shallow flow with open boundaries for practical flood simulation. *Journal of Hydraulic Engineering*, 138(6):530–541, 2011. 68

[266] Damien Violeau and Benedict D Rogers. Smoothed particle hydrodynamics (sph) for free-surface flows: past, present and future. *Journal of Hydraulic Research*, 54(1):1–26, 2016. 68, 70

[267] Agnès Leroy, Damien Violeau, Martin Ferrand, Louise Fratter, and Antoine Joly. A new open boundary formulation for incompressible sph. *Computers & Mathematics with Applications*, 72(9):2417–2432, 2016. 69

[268] Martin Ferrand, Antoine Joly, Christophe Kassiotis, Damien Violeau, Agnès Leroy, François-Xavier Morel, and Benedict D Rogers. Unsteady open boundaries for sph using semi-analytical conditions and riemann solver in 2d. *Computer Physics Communications*, 210:29–44, 2017. 69

[269] Martin Ferrand. *Unified semi-analytical wall boundary conditions for inviscid, laminar and turbulent slightly compressible flows in SPARTACUS-2D combined with an improved time integration scheme on the continuity equation*. The University of Manchester (United Kingdom), 2011. 69

[270] Domenica Mirauda, Raffaele Albano, Aurelia Sole, and Jan Adamowski. Smoothed particle hydrodynamics modeling with advanced boundary conditions for two-dimensional dam-break floods. *Water*, 12(4):1142, 2020. 69

[271] Aaron English, JM Domínguez, Renato Vacondio, AJC Crespo, PK Stansby, SJ Lind, Luca Chiapponi, and M Gómez-Gesteira. Modified dynamic boundary conditions (mdbc) for general-purpose smoothed particle hydrodynamics (sph): Application to tank sloshing, dam break and fish pass problems. *Computational Particle Mechanics*, 9(5):1–15, 2022. 69

[272] Andrea Colagrossi, Matteo Antuono, and David Le Touzé. Theoretical considerations on the free-surface role in the smoothed-particle-hydrodynamics model. *Physical Review E*, 79(5):056701, 2009. 70

[273] Andrea Colagrossi, Matteo Antuono, Antonio Souto-Iglesias, and David Le Touzé. Theoretical analysis and numerical verification of the consistency of viscous smoothed-particle-hydrodynamics formulations in simulating free-surface flows. *Physical Review E*, 84(2):026705, 2011.

[274] Guillaume Oger. *Aspects théoriques de la méthode SPH et applications à l'hydrodynamique à surface libre*. PhD thesis, Nantes, 2006. 70

[275] Songdong Shao. Incompressible sph simulation of wave breaking and overtopping with turbulence modelling. *International Journal for Numerical Methods in Fluids*, 50(5):597–621, 2006. 70

[276] A Khayyer, H Gotoh, and SD Shao. Corrected incompressible sph method for accurate water-surface tracking in breaking waves. *Coastal Engineering*, 55(3):236–250, 2008.

[277] Abbas Khayyer, Hitoshi Gotoh, and Songdong Shao. Enhanced predictions of wave impact pressure by improved incompressible sph methods. *Applied Ocean Research*, 31(2):111–131, 2009.

[278] Abbas Khayyer and Hitoshi Gotoh. Modified moving particle semi-implicit methods for the prediction of 2d wave impact pressure. *Coastal Engineering*, 56(4):419–440, 2009.

[279] B Ataie-Ashtiani and G Shobeyri. Numerical simulation of landslide impulsive waves by incompressible smoothed particle hydrodynamics. *International Journal for numerical methods in fluids*, 56(2):209–232, 2008. https://doi.org/10.1002/fld.1526. 70, 81, 82

[280] E-S Lee, Charles Moulinec, Rui Xu, Damien Violeau, Dominique Laurence, and Peter Stansby. Comparisons of weakly compressible and truly incompressible algorithms for the sph mesh free particle method. *Journal of computational physics*, 227(18):8417–8436, 2008. 70

[281] Agra Barecasco, Hanifa Terissa, and Christian Fredy Naa. Simple free-surface detection in two and three-dimensional sph solver. *arXiv preprint arXiv:1309.4290*, 2013. 70

[282] Salvatore Marrone, Andrea Colagrossi, David Le Touzé, and Giorgio Graziani. Fast free-surface detection and level-set function definition in sph solvers. *Journal of Computational Physics*, 229(10):3652–3663, 2010. 70

[283] Pingping Wang, A-Man Zhang, Furen Ming, Pengnan Sun, and Han Cheng. A novel non-reflecting boundary condition for fluid dynamics solved by smoothed particle hydrodynamics. *Journal of Fluid Mechanics*, 860:81–114, 2019. 70

[284] Frank Bierbrauer, Peter Charles Bollada, and Timothy Nigel Phillips. A consistent reflected image particle approach to the treatment of boundary conditions in smoothed particle hydrodynamics. *Computer Methods in Applied Mechanics and Engineering*, 198(41-44):3400–3410, 2009. 70

[285] Diego Molteni, Rosario Grammauta, and Enrico Vitanza. Simple absorbing layer conditions for shallow wave simulations with smoothed particle hydrodynamics. *Ocean engineering*, 62:78–90, 2013. 71

[286] Pawan Negi and Prabhu Ramachandran. How to train your solver: Verification of boundary conditions for smoothed particle hydrodynamics. *Physics of Fluids*, 34(11), 2022. 71

[287] Moncho Gomez-Gesteira, Benedict D Rogers, Alejandro JC Crespo, Robert A Dalrymple, Muthukumar Narayanaswamy, and José M Dominguez. Sphysics–development of a free-surface fluid solver–part 1: Theory and formulations. *Computers & Geosciences*, 48:289–299, 2012. 71

[288] Simone Elke Hieber and Petros Koumoutsakos. An immersed boundary method for smoothed particle hydrodynamics of self-propelled swimmers. *Journal of Computational Physics*, 227(19):8636–8654, 2008. 71

[289] Kamil Szewc, Jacek Pozorski, and J-P Minier. Analysis of the incompressibility constraint in the smoothed particle hydrodynamics method. *International Journal for Numerical Methods in Engineering*, 92(4):343–369, 2012.

[290] Thomas Douillet-Grellier, Ranjan Pramanik, Kai Pan, Abdulaziz Albaiz, Bruce D Jones, and John R Williams. Development of stress boundary conditions in smoothed particle hydrodynamics (sph) for the modeling of solids deformation. *Computational Particle Mechanics*, 4:451–471, 2017. 71

[291] Pengnan Sun, Furen Ming, and Aman Zhang. Numerical simulation of interactions between free surface and rigid body using a robust sph method. *Ocean Engineering*, 98:32–49, 2015. 72

[292] Bing Ren, Ming He, Ping Dong, and Hongjie Wen. Nonlinear simulations of wave-induced motions of a freely floating body using wcsph method. *Applied Ocean Research*, 50:1–12, 2015. 72

[293] JJ Monaghan, Andrew Kos, and Nader Issa. Fluid motion generated by impact. *Journal of waterway, port, coastal, and ocean engineering*, 129(6):250–259, 2003. 73

[294] Moubin Liu and Zhilang Zhang. Smoothed particle hydrodynamics (sph) for modeling fluid-structure interactions. *Science China Physics, Mechanics & Astronomy*, 62:1–38, 2019. 73

[295] KC Ng, A Alexiadis, and YL Ng. An improved particle method for simulating fluid-structure interactions: The multi-resolution sph-vcpm approach. *Ocean Engineering*, 247:110779, 2022. 73

[296] Chuanqi Shi, Yi An, Qiang Wu, Qingquan Liu, and Zhixian Cao. Numerical simulation of landslide-generated waves using a soil–water coupling smoothed particle hydrodynamics model. *Advances in Water Resources*, 92:130–141, 2016. https://doi.org/10.1016/j.advwatres.2016.04.002. 73, 104

[297] Guiyong Zhang, Shuangqiang Wang, Zhixiang Sui, Lei Sun, Zhiqian Zhang, and Zhi Zong. Coupling of sph with smoothed point interpolation method for violent fluid-structure interaction problems. *Engineering Analysis with Boundary Elements*, 103:1–10, 2019. 73

[298] M Lahooti, A Pishevar, and MS Saidi. A novel 2d algorithm for fluid solid interaction based on the smoothed particle hydrodynamics (sph) method. *Scientia Iranica*, 18(3):358–367, 2011. 73

[299] Xiaojing Tang, Chi Zhang, Oskar Haidn, and Xiangyu Hu. An integrative sph method for heat transfer problems involving fluid-structure interaction. *Acta Mechanica Sinica*, 39(2):722248, 2023. 74

[300] M Khanpour, AR Zarrati, M Kolahdoozan, A Shakibaeinia, and SM Amirshahi. Mesh-free sph modeling of sediment scouring and flushing. *Computers & Fluids*, 129:67–78, 2016. 74

[301] Ahmad Shakibaeinia and Yee-Chung Jin. A mesh-free particle model for simulation of mobile-bed dam break. *Advances in Water Resources*, 34(6):794–807, 2011.

[302] Sauro Manenti, Stefano Sibilla, Mario Gallati, Giordano Agate, and Roberto Guandalini. Sph simulation of sediment flushing induced by a rapid water flow. *Journal of Hydraulic Engineering*, 138(3):272–284, 2011.

[303] G Fourtakas and BD Rogers. Modelling multi-phase liquid-sediment scour and resuspension induced by rapid flows using smoothed particle hydrodynamics (sph) accelerated with a graphics processing unit (gpu). *Advances in Water Resources*, 92:186–199, 2016.

[304] Christian Ulrich, Marzia Leonardi, and Thomas Rung. Multi-physics sph simulation of complex marine-engineering hydrodynamic problems. *Ocean Engineering*, 64:109–121, 2013.

[305] Dong Wang, Shaowu Li, Taro Arikawa, and Hayao Gen. Isph simulation of scour behind seawall due to continuous tsunami overflow. *Coastal Engineering Journal*, 58(03):1650014, 2016.

[306] Akhmad Adi SULIANTO and Keisuke MURAKAMI. Sph simulation of local scouring on rubble mound due to tsunami overflow. *strain*, 2(2):4, 2015.

[307] Luhui Han and Xiangyu Hu. Sph modeling of fluid-structure interaction. *Journal of Hydrodynamics*, 30(1):62–69, 2018. https://doi.org/10.1007/s42241-018-0006-9. 74, 80

[308] Ting Long, Dean Hu, Gang Yang, and Detao Wan. A particle-element contact algorithm incorporated into the coupling methods of fem-isph and fem-wcsph for fsi problems. *Ocean Engineering*, 123:154–163, 2016. 74

[309] Ting Long, Dean Hu, Detao Wan, Chen Zhuang, and Gang Yang. An arbitrary boundary with ghost particles incorporated in coupled fem–sph model for fsi problems. *Journal of Computational Physics*, 350:166–183, 2017.

[310] Cristiano Fragassa, Marko Topalovic, Ana Pavlovic, and Snezana Vulovic. Dealing with the effect of air in fluid structure interaction by coupled sph-fem methods. *Materials*, 12(7):1162, 2019.

[311] Cheng Chen, Wen-Kui Shi, Yan-Ming Shen, Jian-Qiang Chen, and A-Man Zhang. A multi-resolution sph-fem method for fluid–structure interactions. *Computer Methods in Applied Mechanics and Engineering*, 401:115659, 2022. 74

[312] Loup Verlet. Computer" experiments" on classical fluids. i. thermodynamical properties of lennard-jones molecules. *Physical review*, 159(1):98, 1967. 74

[313] MB Liu, GR Liu, Z Zong, and KY Lam. Computer simulation of high explosive explosion using smoothed particle hydrodynamics methodology. *Computers & Fluids*, 32(3):305–322, 2003. 74

[314] Ha H Bui, K Sako, and R Fukagawa. Numerical simulation of soil–water interaction using smoothed particle hydrodynamics (sph) method. *Journal of Terramechanics*, 44(5):339–346, 2007. 74

[315] Antony Jameson, Wolfgang Schmidt, Eli Turkel, et al. Numerical solutions of the euler equations by finite volume methods using runge-kutta time-stepping schemes. *AIAA paper*, 1259:1981, 1981. 75

[316] Jean-Marc Cherfils, G Pinon, and Elie Rivoalen. Josephine: A parallel sph code for free-surface flows. *Computer Physics Communications*, 183(7):1468–1480, 2012. 75

[317] Michael Meister, Daniel Winkler, Massoud Rezavand, and Wolfgang Rauch. Integrating hydrodynamics and biokinetics in wastewater treatment modelling by using smoothed particle hydrodynamics. *Computers & Chemical Engineering*, 99:1–12, 2017. 75

[318] J Feng, P Chen, Q Zhou, K Dai, E An, and Y Yuan. Numerical simulation of explosive welding using smoothed particle hydrodynamics method. *The International Journal of Multiphysics*, 11(3):315–326, 2017. 75

[319] SJ Lind, PK Stansby, BD Rogers, and PM Lloyd. Numerical predictions of water–air wave slam using incompressible–compressible smoothed particle hydrodynamics. *Applied Ocean Research*, 49:57–71, 2015. 75

[320] Salvatore Marrone, Andrea Di Mascio, and David Le Touzé. Coupling of smoothed particle hydrodynamics with finite volume method for free-surface flows. *Journal of Computational Physics*, 310:161–180, 2016. 75

[321] Stefano Sibilla. An algorithm to improve consistency in smoothed particle hydrodynamics. *Computers & Fluids*, 118:148–158, 2015. 77

[322] JU Brackbill, Douglas B Kothe, and Charles Zemach. A continuum method for modeling surface tension. *Journal of computational physics*, 100(2):335–354, 1992. 77

[323] Parameshwari Kattel, Jeevan Kafle, Jan-Thomas Fischer, Martin Mergili, Bhadra Man Tuladhar, and Shiva P. Pudasaini. Interaction of two-phase debris flow with obstacles. *Engineering Geology*, 242:197–217, 2018. https://doi.org/10.1016/j.enggeo.2018.05.023. 79

[324] Shiva P Pudasaini and Jan-Thomas Fischer. A mechanical model for phase separation in debris flow. *International Journal of Multiphase Flow*, 129:103292, 2020. https://doi.org/10.1016/j.ijmultiphaseflow.2020.103292. 79

[325] P. Si, H. Shi, and X Yu. A general numerical model for surface waves generated by granular material intruding into a water body. *Coastal Engineering.*, 142:42–51, 2018. https://doi.org/10.1016/j.coastaleng.2018.09.001. 79

[326] F. M. Evers, V. Heller, H. Fuchs, W. H. Hager, and R. M. Boes. Landslide generated impulse waves in reservoirs: basics and computation. 2nd edn. *VAW Mitteilung 254, ETH Zurich, Switzerland*, 2019. https://doi.org/10.3929/ethz-b-000413216. 79

[327] V. Heller and J. Spinneken. Improved landslide-tsunami prediction: Effects of block model parameters and slide model. *Journal of Geophysical Research: Oceans.*, 118(3):1489–1507, March 2013. https://doi.org/10.1002/jgrc.20099. 79

[328] Shiva P Pudasaini. A general two-phase debris flow model. *Journal of Geophysical Research: Earth Surface*, 117(F3), 2012. https://doi.org/10.1029/2011JF002186. 79, 83

[329] Chongqiang Zhu, Yu Huang, and Liang-tong Zhan. Sph-based simulation of flow process of a landslide at hongao landfill in china. *Natural Hazards*, 93:1113–1126, 2018. https://doi.org/10.1007/s11069-018-3342-8.

[330] M Pastor, Thomas Blanc, B Haddad, S Petrone, Mila Sanchez Morles, V Drempetic, D Issler, GB Crosta, L Cascini, G Sorbino, et al. Application of a sph depth-integrated model to landslide run-out analysis. *Landslides*, 11:793–812, 2014. https://doi.org/10.1007/s10346-014-0484-y.

[331] GR Liu, Zirui Mao, and Yu Huang. Sph modeling for soil mechanics with application to landslides. In *Modeling in Geotechnical Engineering*, pages 257–289. Elsevier, 2021. https://doi.org/10.1016/B978-0-12-821205-9.00004-6. 79

[332] Tamotsu Takahashi and Dilip K Das. *Debris flow: mechanics, prediction and countermeasures*. CRC press, 2014. 79

[333] Shiva P Pudasaini and Martin Mergili. A multi-phase mass flow model. *Journal of Geophysical Research: Earth Surface*, 124(12):2920–2942, 2019. https://doi.org/10.1029/2019JF005204. 79, 80, 83

[334] Huicong An, Chaojun Ouyang, and Dongpo Wang. A new two-phase flow model based on coupling of the depth-integrated continuum method and discrete element method. *Computers & Geosciences*, 146:104640, 2021. https://doi.org/10.1016/j.cageo.2020.104640. 79

[335] Wei Liu, Shuaixing Yan, and Siming He. A simple method to evaluate the performance of an intercept dam for debris-flow mitigation. *Engineering Geology*, 276:105771, 2020. https://doi.org/10.1016/j.enggeo.2020.105771.

[336] Wei Liu, Zongji Yang, and Siming He. Modeling the landslide-generated debris flow from formation to propagation and run-out by considering the effect of vegetation. *Landslides*, 18:43–58, 2021. https://doi.org/10.1007/s10346-020-01478-4.

[337] Yong Kong, Xingyue Li, and Jidong Zhao. Quantifying the transition of impact mechanisms of geophysical flows against flexible barrier. *Engineering Geology*, 289:106188, 2021. https://doi.org/10.1016/j.enggeo.2021.106188. 79

[338] Daniel H Shugar, Mylène Jacquemart, David Shean, Shashank Bhushan, Kavita Upadhyay, Ashim Sattar, Wolfgang Schwanghart, S McBride, M Van Wyk De Vries, M Mergili, et al. A massive rock and ice avalanche caused the 2021 disaster at chamoli, indian himalaya. *Science*, 373(6552):300–306, 2021. https://doi.org/10.1126/science.abh4455. 79

[339] Yin-Fu Jin and Zhen-Yu Yin. Two-phase pfem with stable nodal integration for large deformation hydromechanical coupled geotechnical problems. *Computer Methods in Applied Mechanics and Engineering*, 392:114660, 2022. 79

[340] Linda Gesenhues, José J Camata, Adriano MA Côrtes, Fernando A Rochinha, and Alvaro LGA Coutinho. Finite element simulation of complex dense granular flows using a well-posed regularization of the μ (I)-rheology. *Computers & Fluids*, 188:102–113, 2019. https://doi.org/10.1016/j.compfluid.2019.05.012. 79

[341] Jia Mao, Lanhao Zhao, Yingtang Di, Xunnan Liu, and Weiya Xu. A resolved cfd–dem approach for the simulation of landslides and impulse waves. *Computer Methods in Applied Mechanics and Engineering*, 359:112750, 2020. https://doi.org/10.1016/j.cma.2019.112750. 79

[342] Youting Qi, Jianyun Chen, Guibin Zhang, Qiang Xu, and Jing Li. An improved multi-phase weakly-compressible sph model for modeling various landslides. *Powder Technology*, 397:117120, 2022. https://doi.org/10.1016/j.powtec.2022.117120. 80, 96

[343] Kai Gong, Songdong Shao, Hua Liu, Benlong Wang, and Soon-Keat Tan. Two-phase sph simulation of fluid–structure interactions. *Journal of Fluids and Structures*, 65:155–179, 2016. https://doi.org/10.1016/j.jfluidstructs.2016.05.012. 80

[344] Martin Robinson, Marco Ramaioli, and Stefan Luding. Fluid–particle flow simulations using two-way-coupled mesoscale sph–dem and validation. *International journal of multiphase flow*, 59:121–134, 2014. 80

[345] HF Schwaiger and B Higman. Lagrangian hydrocode simulations of the 1958 lituya bay tsunamigenic rockslide. *Geochemistry, Geophysics, Geosystems*, 8(7), 2007. https://doi.org/10.1029/2007gc001584. 80

[346] Shijie Xie, Hang Lin, Yixian Wang, Rihong Cao, Rui Yong, Shigui Du, and Jiangteng Li. Nonlinear shear constitutive model for peak shear-type joints based on improved harris damage function. *Archives of Civil and Mechanical Engineering*, 20(3):1–14, 2020. https://doi.org/10.1007/s43452-020-00097-z. 80

[347] Folayan J Adewale, Anawe P Lucky, Abioye P Oluwabunmi, and Elehinafe F Boluwaji. Selecting the most appropriate model for rheological characterization of synthetic based drilling mud. *Int. J. Appl. Eng. Res*, 12:7614–7629, 2017. https://doi.org/10.1016/j.jcp.2010.03.022. 80, 101

[348] Guibin Zhang, Jianyun Chen, Youting Qi, Jing Li, and Qiang Xu. A WCSPH two-phase mixture model for tsunami waves generated by granular landslides. *Computers and Geotechnics*, 144:104657, 2022. https://doi.org/10.1016/j.compgeo.2022.104657. 80

[349] Shiyin Sha, Ashley P Dyson, Gholamreza Kefayati, and Ali Tolooiyan. Simulation of debris flow-barrier interaction using the smoothed particle hydrodynamics and coupled eulerian lagrangian methods. *Finite Elements in Analysis and Design*, 214:103864, 2023. 81

[350] Erwan Bertevas, Thien Tran-Duc, Khoa Le-Cao, Boo Cheong Khoo, and Nhan Phan-Thien. A smoothed particle hydrodynamics (sph) formulation of a two-phase mixture model and its application to turbulent sediment transport. *Physics of Fluids*, 31(10):103303, 2019.

[351] Mohsen Abdolahzadeh, Ali Tayebi, and Pourya Omidvar. Mixing process of two-phase non-newtonian fluids in 2d using smoothed particle hydrodynamics. *Computers & Mathematics with Applications*, 78(1):110–122, 2019.

[352] H Mahardima, E Bahsan, and RRDR Marthanty. Development of smoothed particle hydrodynamics (sph) method to model the interaction of sand and water during liquefaction with bingham fluid model adaptation. *IOP Conference Series: Earth and Environmental Science*, 622(1):012009, 2021.

[353] Abdelraheem M Aly, Mitsuteru Asai, and Ehab Mahmoud Mohamed. Simulation of water-soil-structure interactions using incompressible smoothed particle hydrodynamics. *CMC-computers materials and continua*, 65(1):205–224, 2020. 81

[354] M Jabbari, Regina Bulatova, AIY Tok, CRH Bahl, E Mitsoulis, and Jesper Henri Hattel. Ceramic tape casting: A review of current methods and trends with emphasis on rheological behaviour and flow analysis. *Materials Science and Engineering: B*, 212:39–61, 2016. https://doi.org/10.1016/j.mseb.2016.07.011. 81, 83, 85

[355] Valentin Heller, Mark Bruggemann, Johannes Spinneken, and Benedict D Rogers. Composite modelling of subaerial landslide-tsunamis in different water body geometries and novel insight into slide and wave kinematics. *Coastal Engineering*, 109:20–41, 2016. https://doi.org/10.1016/j.coastaleng.2015.12.004. 81

[356] Eugene Cook Bingham. *Fluidity and plasticity*, volume 2. McGraw-Hill, 1922. 83

[357] N. Casson. A flow equations for pigment-oil suspensions of the printing ink type. *In: Mill, C.C., Ed., Rheology of Disperse Systems. Pergamon Press, Oxford,*, pages 84–104, 1959. 84

[358] Anastasios Skiadopoulos, Panagiotis Neofytou, and Christos Housiadas. Comparison of blood rheological models in patient specific cardiovascular system simulations. *Journal of Hydrodynamics*, 29(2):293–304, 2017. https://doi.org/10.1016/S1001-6058(16)60739-4. 84

[359] W. Elsaady, S. O. Oyadiji, and A. Nasser. A review on multi-physics numerical modelling in different applications of magnetorheological fluids. *Journal of Intelligent Material Systems and Structures*, 31(16):1855–1897, 2020. https://doi.org/10.1177/1045389X20935632. 86

[360] Qiang Fu, Wenrui Xu, Daguan Huang, Jiaqi He, Lu Zhang, Hailei Kou, and Ditao Niu. Dynamic non-linear mohr–coulomb strength criterion for hybrid basalt–polypropylene fibre-reinforced concrete under impact loading. *Archives of Civil and Mechanical Engineering*, 21(3):1–19, 2021. https://doi.org/10.1007/s43452-021-00248-w. 87

[361] Birte Domnik, Shiva P Pudasaini, Rolf Katzenbach, and Stephen A Miller. Coupling of full two-dimensional and depth-averaged models for granular flows. *Journal of Non-Newtonian Fluid Mechanics*, 201:56–68, 2013. https://doi.org/10.1016/j.jnnfm.2013.07.005. 87

[362] Pengfei Si, Huabin Shi, and Xiping Yu. Development of a mathematical model for submarine granular flows. *Physics of Fluids*, 30(8):083302, 2018. https://doi.org/10.1063/1.5030349. 87

[363] Zheng Han, Bin Su, Yange Li, Wei Wang, Weidong Wang, Jianling Huang, and Guangqi Chen. Numerical simulation of debris-flow behavior based on the sph method incorporating the herschel-bulkley-papanastasiou rheology model. *Engineering Geology*, 255:26–36, 2019. https://doi.org/10.1016/j.enggeo.2019.04.013. 87

[364] GC Vradis and MV O¨tu¨gen. The axisymmetric sudden expansion flow of a non-Newtonian viscoplastic fluid. *Journal of Fluids Engineering*, 119(1):193–200, 1997. https://doi.org/10.1115/1.2819108. 89, 105

[365] Ioan R Ionescu, Anne Mangeney, François Bouchut, and Olivier Roche. Viscoplastic modeling of granular column collapse with pressure-dependent rheology. *Journal of Non-Newtonian Fluid Mechanics*, 219:1–18, 2015. https://doi.org/10.1016/j.jnnfm.2015.02.006. 89, 105

[366] K Pan, RHA IJzermans, BD Jones, A Thyagarajan, BWH Van Beest, and JR Williams. Application of the sph method to solitary wave impact on an offshore platform. *Computational Particle Mechanics*, 3(2):155–166, 2016. https://doi.org/10.1007/s40571-015-0069-0. 89

[367] M. Tajnesaie, A. Shakibaeinia, and K. Hosseini. Meshfree particle numerical modelling of sub-aerial and submerged landslides. *Computers & Fluids*, 172:109–121, 2018. https://doi.org/10.1016/j.compfluid.2018.06.023. 94

[368] Libor Lobovskỳ, Elkin Botia-Vera, Filippo Castellana, Jordi Mas-Soler, and Antonio Souto-Iglesias. Experimental investigation of dynamic pressure loads during dam break. *Journal of Fluids and Structures*, 48:407–434, 2014. https://doi.org/10.1016/j.jfluidstructs.2014.03.009. 96, 97, 98

[369] Bastiaan Buchner. *Green water on ship-type offshore structures*. PhD thesis, Delft University of Technology Delft, The Netherlands, 2002.

[370] Selahattin Kocaman and Kaan Dal. A new experimental study and SPH comparison for the sequential dam-break problem. *Journal of Marine Science and Engineering*, 8(11):905, 2020. https://doi.org/10.3390/jmse8110905.

[371] Xi Yang, Zhifan Zhang, Guiyong Zhang, Song Feng, and Zhe Sun. Simulating multi-phase sloshing flows with the SPH method. *Applied Ocean Research*, 118:102989, 2022. https://doi.org/10.1016/j.apor.2021.102989. 96

[372] Alban de Vaucorbeil, Vinh Phu Nguyen, and Chi Nguyen-Thanh. Karamelo: an open source parallel C++ package for the material point method. *Computational Particle Mechanics*, 8(4):767–789, 2021. https://doi.org/10.1007/s40571-020-00369-8. 97, 98

[373] Zhouteng Ye, Xizeng Zhao, and Zhengzhi Deng. Numerical investigation of the gate motion effect on a dam break flow. *Journal of Marine Science and Technology*, 21(4):579–591, 2016. https://doi.org/10.1007/s00773-016-0374-1. 98

[374] Gert Lube, Herbert E Huppert, R Stephen J Sparks, and Armin Freundt. Collapses of two-dimensional granular columns. *Physical Review E*, 72(4):041301, 2005. https://doi.org/10.1103/PhysRevE.72.041301. 99

[375] E Lajeunesse, JB Monnier, and GM Homsy. Granular slumping on a horizontal surface. *Physics of fluids*, 17(10):103302, 2005. https://doi.org/10.1063/1.2087687. 99, 100, 101, 102

[376] Ha H Bui, Ryoichi Fukagawa, Kazunari Sako, and Shintaro Ohno. Lagrangian meshfree particles method (sph) for large deformation and failure flows of geomaterial using elastic–plastic soil constitutive model. *International Journal for Numerical and Analytical Methods in Geomechanics*, 32(12):1537–1570, 2008. https://doi.org/10.1002/nag.688.

[377] Hao Xiong, Zhen-Yu Yin, François Nicot, Antoine Wautier, Miot Marie, Félix Darve, Guillaume Veylon, and Pierre Philippe. A novel multi-scale large deformation approach for modelling of granular collapse. *Acta Geotechnica*, 16(8):2371–2388, 2021. https://doi.org/10.1007/s11440-020-01113-5. 99

[378] Tibing Xu and Yee-Chung Jin. Two-dimensional continuum modelling granular column collapse by non-local peridynamics in a mesh-free method with rheology. *Journal of Fluid Mechanics*, 917, 2021. https://doi.org/10.1017/jfm.2021.320. 99

[379] Mehran Kheirkhahan and Khosrow Hosseini. Comparison of the μ (i) and hbp models for simulating granular media. *International Journal of Modern Physics C*, 29(07):1850050, 2018. https://doi.org/10.1142/S012918311850050X. 101

[380] DJ Miller. Giant waves in lituya bay, alaska, geological survey professional paper 354-c. *US Government Printing Office, Washington DC*, 354-C, 1960. https://doi.org/10.3133/pp354C. 103

[381] D. R. Tappin, P. Watts, and S. T. Grilli. The Papua New Guinea tsunami of 17 July 1998: anatomy of a catastrophic event. *Natural Hazards and Earth System Sciences*, 8(2):243–266, 2008. https://doi.org/10.5194/nhess-8-243-2008. 103

[382] H. M. Fritz, W. H. Hager, and . Minor H-E. Landslide generated impulse waves. 1. Instantaneous flow fields. *Experiments in Fluids*, 35:505–519, Novebmer/December 2003. https://doi.org/10.1007/s00348-003-0659-0. 103, 104, 105, 106, 107, 109, 110

[383] Stefan Adami, XY Hu, and Nikolaus A Adams. A transport-velocity formulation for smoothed particle hydrodynamics. *Journal of Computational Physics*, 241:292–307, 2013. https://doi.org/10.1016/j.jcp.2013.01.043. 105

[384] A. Ghaïtanellis. *Modelling bed-load sediment transport through a granular approach in SPH. Dynamique, vibrations*. PhD thesis, Université Paris-Est, 2017. English. NNT : 2017PESC1087. 111, 113

[385] S Assier Rzadkiewicz, C Mariotti, and Philippe Heinrich. Numerical simulation of submarine landslides and their hydraulic effects. *Journal of Waterway, Port, Coastal, and Ocean Engineering*, 123(4):149–157, July,August 1997. https://doi.org/10.1061/(ASCE)0733-950X(1997)123:4(149). 112

[386] Mohammad Amin Nabian and Leila Farhadi. Multiphase mesh-free particle method for simulating granular flows and sediment transport. *Journal of Hydraulic Engineering*, 143(4):04016102, 2017. 114

[387] B. E. Snelling, G. S. Collins, M. D. Piggott, and S. J. Neethling. Improvements to a smooth particle hydrodynamics simulator for investigating submarine landslide generated waves. *International Journal for Numerical Methods in Fluids*, 92(7):744–764, 2020. https://doi.org/10.1002/fld.4804. 114

[388] Mojtaba Jandaghian, Abdelkader Krimi, and Ahmad Shakibaeinia. Enhanced weakly-compressible MPS method for immersed granular flows. *Advances in Water Resources*, 152:103908, 2021. 117, 118, 119, 120, 121, 122

[389] Anouk Riffard and Miltiadis V Papalexandris. Numerical study of the collapse of columns of sand immersed in water using two-phase flow modeling. *International Journal of Multiphase Flow*, page 104143, 2022. 118

[390] Cheng-Hsien Lee, Zhenhua Huang, and Ming-Lan Yu. Collapse of submerged granular columns in loose packing: Experiment and two-phase flow simulation. *Physics of Fluids*, 30(12):123307, 2018.

[391] Chun Wang, Yongqi Wang, Chong Peng, and Xiannan Meng. Two-fluid smoothed particle hydrodynamics simulation of submerged granular column collapse. *Mechanics Research Communications*, 79:15–23, 2017. 118

Appendix A

Determination of the yield stress τ_y

The Mohr-Coulomb criterion defines a linear failure envelope that combines the normal and shear stresses (σ, τ) on the failure plane. It is given by the equation:

$$\tau = c - \sigma \tan\phi \tag{A.1}$$

Here, c and ϕ represent the cohesion and angle of internal friction (repose angle) of the material, respectively. These parameters characterize the material's physical properties.

The yielding behavior of materials governed by the Mohr-Coulomb criterion occurs when the Mohr's circle is tangent to the failure envelope (see Figure A.1). This relationship can be expressed in terms of principal stresses as:

$$\frac{\sigma_1 - \sigma_2}{2} = -\frac{\sigma_1 + \sigma_2}{2}\sin\phi + c\cos\phi \tag{A.2}$$

The second invariant J_2 of the deviatoric stress tensor can be expressed in terms of principal stresses in two-dimensional space as:

$$\begin{aligned} J_2 &= \frac{1}{2}\tau : \tau \\ &= \frac{1}{2}\mathrm{tr}\left(\tau^2\right) \\ &= \frac{1}{2}\mathrm{tr}\left(\left\{\sigma - \frac{I_1}{2}I\right\}^2\right) \\ &= \frac{1}{2}\left(\mathrm{tr}(\sigma^2) - \frac{I_1^2}{2}\right) \\ &= \frac{1}{4}\left(\sigma_1 - \sigma_2\right)^2 \end{aligned} \tag{A.3}$$

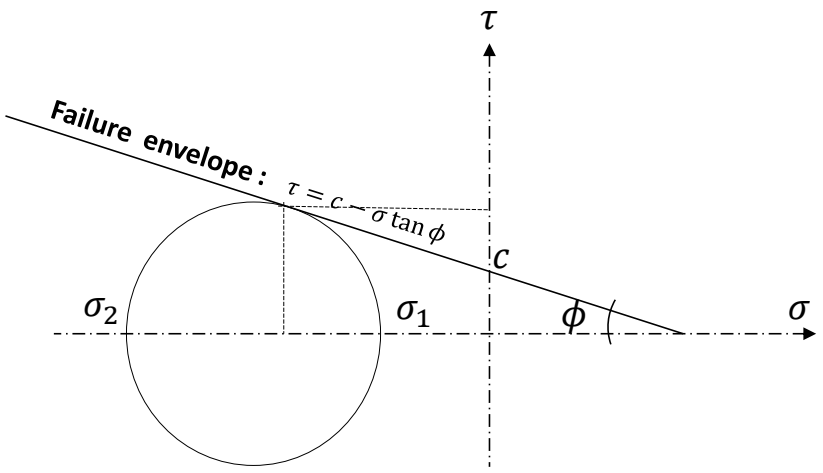

Fig. A.1 Mohr-Coulomb yield criterion. The Mohr circle is based on the principal stresses σ_1 and σ_2. Yielding occurs when the Mohr circle is tangent to the failure envelope.

In the above equation, $tr(A)$ denotes the trace of the square matrix A. The terms σ_1 and σ_2 represent the largest and smallest principal stresses of the Cauchy stress tensor σ ($\sigma_1 > \sigma_2$), respectively. The first invariant I_1 of the Cauchy stress tensor in a two-dimensional space is given by:

$$I_1 = \sigma_1 + \sigma_2 \tag{A.4}$$

The hydrostatic pressure p can be expressed in terms of the first invariant I_1 or principal stresses as:

$$p = -\frac{I_1}{2} = -\frac{\sigma_1 + \sigma_2}{2} \tag{A.5}$$

Hence, the Mohr-Coulomb criterion envelope can also be written in terms of the hydrostatic pressure p and the second invariant J_2 as:

$$\sqrt{J_2} = p\sin\phi + c\cos\phi \tag{A.6}$$

For materials that yield under the Mohr-Coulomb criterion, the yielding stress τ_y can be expressed as:

$$\tau_y = p\sin\phi + c\cos\phi \tag{A.7}$$

This equation represents the yield stress τ_y for materials that follow the Mohr-Coulomb criterion.

Appendix B

Frobenius norm of the shear rate tensor

In 2D, the velocity vector components are $v = [u\ w]^T$ and the velocity gradient tensor can be expressed as:

$$\nabla v = \begin{bmatrix} \frac{\partial u}{\partial x} & \frac{\partial u}{\partial y} \\ \frac{\partial w}{\partial x} & \frac{\partial w}{\partial y} \end{bmatrix} \tag{B.1}$$

Taking the transpose of this tensor, we have:

$$(\nabla v)^T = \begin{bmatrix} \frac{\partial u}{\partial x} & \frac{\partial w}{\partial x} \\ \frac{\partial u}{\partial y} & \frac{\partial w}{\partial y} \end{bmatrix} \tag{B.2}$$

The shear rate tensor, denoted as D, is given by the sum of the velocity gradient tensor and its transpose:

$$D = \nabla v + (\nabla v)^T = \begin{bmatrix} \frac{\partial u}{\partial x} & \frac{\partial u}{\partial y} \\ \frac{\partial w}{\partial x} & \frac{\partial w}{\partial y} \end{bmatrix} + \begin{bmatrix} \frac{\partial u}{\partial x} & \frac{\partial w}{\partial x} \\ \frac{\partial u}{\partial y} & \frac{\partial w}{\partial y} \end{bmatrix} \tag{B.3}$$

Simplifying this expression, we get:

$$D = \begin{bmatrix} 2\frac{\partial u}{\partial x} & \frac{\partial u}{\partial y} + \frac{\partial w}{\partial x} \\ \frac{\partial u}{\partial y} + \frac{\partial w}{\partial x} & 2\frac{\partial w}{\partial y} \end{bmatrix} \tag{B.4}$$

Now, let's calculate the Frobenius norm of D, denoted as $\|D\|_F$. The Frobenius norm is defined as:

$$\|D\|_F = \left(\frac{1}{2} D : D\right)^{\frac{1}{2}} \tag{B.5}$$

where the colon (:) denotes the double-dot product. In this case, the double-dot product can be computed as:

$$D : D = \sum_{i=1}^{2} \sum_{j=1}^{2} D_{ij} D_{ij} \tag{B.6}$$

Substituting the components of D from (B.4) into (B.6), we have:

$$D : D = \left(2\frac{\partial u}{\partial x}\right)^2 + \left(\frac{\partial u}{\partial y} + \frac{\partial w}{\partial x}\right)^2 + \left(\frac{\partial u}{\partial y} + \frac{\partial w}{\partial x}\right)^2 + \left(2\frac{\partial w}{\partial y}\right)^2 \tag{B.7}$$

Simplifying further:

$$D : D = 4\left(\frac{\partial u}{\partial x}\right)^2 + 2\left(\frac{\partial u}{\partial y} + \frac{\partial w}{\partial x}\right)^2 + 4\left(\frac{\partial w}{\partial y}\right)^2 \tag{B.8}$$

Finally, by substituting the equation (B.8) into (B.5) , we can express the Frobenius norm of D as:

$$\|D\|_F = \sqrt{2\left(\left(\frac{\partial u}{\partial x}\right)^2 + \left(\frac{\partial w}{\partial y}\right)^2\right) + \left(\frac{\partial u}{\partial y} + \frac{\partial w}{\partial y}\right)^2} \tag{B.9}$$

This expression represents the Frobenius norm of the shear rate tensor in the 2D case.